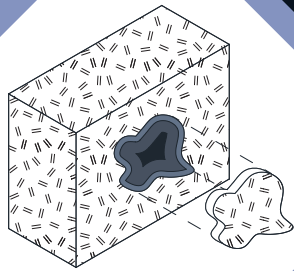


Matteo De Poli

# Fire dynamics and spalling mechanism in tunnel infrastructures



Delft, 29 October 2018



# **FIRE DYNAMICS AND SPALLING MECHANISM IN TUNNEL INFRASTRUCTURES**

**Matteo DE POLI**

Delft University of Technology  
Faculty of Civil Engineering and Geosciences  
MASTER: Structural Engineering  
TRACK: Concrete Structures  
Stevinweg 1, Delft, The Netherlands

*Delft, 29 October 2018*

Author: Matteo De Poli  
student number: 4621913

The following Master thesis has been carried out in collaboration with the consultancy and engineering firm, Witteveen+Bos.



Master thesis committee:

Prof. dr. ir. D.A. Hordijk,	Technische Universiteit Delft
Dr. ir. C.B.M. Blom,	Technische Universiteit Delft/Gemeente Rotterdam
Dr. ir. G.J.P. Ravenshorst,	Technische Universiteit Delft

*Members from the company:*

Dr. ir. B.B.G. Lottman,	Witteveen+Bos
Ir. A.J.M. Snel,	Witteveen+Bos

Copyright © 2018 by M. De Poli

An electronic version of this MSc thesis is available at  
<http://repository.tudelft.nl/>.

*The problem in this business isn't to keep people from stealing your ideas;  
it's making them steal them!*

Howard Aiken



# CONTENTS

<b>Abstract</b>	<b>vii</b>
<b>Acknowledgements</b>	<b>ix</b>
<b>List of Symbols</b>	<b>xiii</b>
<b>1 Introduction</b>	<b>1</b>
<b>2 Problem statement, Research question, objectives and Methodology</b>	<b>3</b>
<b>3 State of the art</b>	<b>7</b>
3.1 Tunnels: general introduction . . . . .	7
3.2 Tunnels: fire and structural design . . . . .	9
3.3 Fire scenarios . . . . .	9
3.3.1 Fire progress . . . . .	10
3.3.2 Tunnel Fires . . . . .	12
3.4 Computational Fluid Dynamics . . . . .	14
3.5 Spalling mechanism . . . . .	15
3.5.1 Pore pressure and imposed thermal deformations. . . . .	17
3.5.2 Buckling Instability . . . . .	17
3.5.3 Influencing Parameters . . . . .	18
3.6 Laws and Regulations . . . . .	23
3.6.1 Fire regulations . . . . .	24
3.6.2 Spalling regulations . . . . .	25
<b>4 Fire dynamics</b>	<b>29</b>
4.1 Vehicles . . . . .	29
4.1.1 HRR . . . . .	29
4.1.2 Dimensions . . . . .	32
4.1.3 Temperature development. . . . .	32
4.2 Pool fires . . . . .	38
4.2.1 Fire development. . . . .	38
4.2.2 Pool dimensions . . . . .	40
4.3 Horizontal flame length . . . . .	43
4.4 Temperature decay in the tunnel . . . . .	43
4.5 Smoke layer instability along the tunnel . . . . .	45
4.6 Fire spread and increased ambient temperature. . . . .	46
4.7 Temperature Heat Maps . . . . .	47
4.8 Lining temperature profile. . . . .	48
4.8.1 Numerical solution. . . . .	49
4.8.2 Versions . . . . .	50
4.9 Results. . . . .	52
4.9.1 Temperature development. . . . .	52
4.9.2 Pool dimensions . . . . .	52
4.9.3 Fire development. . . . .	54

4.9.4	Horizontal Flame length . . . . .	55
4.9.5	Temperature decay . . . . .	55
4.9.6	Smoke layer instability . . . . .	57
4.9.7	Fire spread . . . . .	60
4.9.8	Temperature heat maps . . . . .	62
4.9.9	Lining Temperature profile . . . . .	62
4.10	Conclusions. . . . .	66
<b>5</b>	<b>Fire Dynamics Simulator</b>	<b>67</b>
5.1	Inputs . . . . .	67
5.2	Outputs . . . . .	69
5.2.1	Fuel vs Ventilation controlled fire . . . . .	71
5.3	Results. . . . .	73
5.3.1	HGV simulation (no ventilation) . . . . .	73
5.3.2	Pool simulation (no ventilation) . . . . .	79
5.3.3	Pool simulation (v=2.5 m/s) . . . . .	85
5.3.4	Pool simulation (v=3.5 m/s) . . . . .	85
5.3.5	Discussion and comparison with previous simulations . . . . .	91
5.4	Conclusions. . . . .	95
<b>6</b>	<b>NSC spalling mechanism - 1st version</b>	<b>97</b>
6.1	Spalling test results. . . . .	97
6.2	Preliminary approach . . . . .	98
6.2.1	Column spalling model . . . . .	98
6.3	Detailed approach . . . . .	105
6.3.1	Stress model. . . . .	105
6.3.2	Optimal thickness model . . . . .	105
6.3.3	Crack model. . . . .	108
6.4	Spalling mechanism calculations overview . . . . .	112
6.5	Results. . . . .	112
6.6	Conclusions. . . . .	117
<b>7</b>	<b>Spalling mechanism: 2nd version and HSC/PPFRC</b>	<b>119</b>
7.1	Spalling mechanism improvements (2ns version) . . . . .	119
7.1.1	Results. . . . .	120
7.2	HSC and PPFRC . . . . .	123
7.2.1	High Strength Concrete . . . . .	125
7.2.2	Polypropylene Fibre Reinforcement Concrete . . . . .	125
7.2.3	Parametric study . . . . .	126
7.3	Crack failure . . . . .	129
7.4	Conclusions. . . . .	134
<b>8</b>	<b>Conclusions and recommendations</b>	<b>135</b>
8.1	Conclusions. . . . .	135
8.2	Recommendations . . . . .	137
8.2.1	Recommendations for future research . . . . .	137
8.2.2	Recommendations for practice . . . . .	138
	<b>Reference list</b>	<b>140</b>
<b>A</b>	<b>Appendix</b>	<b>145</b>

# ABSTRACT

Underground infrastructures and the importance of the people's safety and structures robustness are relevant and contemporary issues in the civil engineering industry. The demand for this infrastructural typology has developed to such an extent that the need for a better and cost-beneficial knowledge of the risks is necessary.

This thesis aims at bridging and developing further the knowledge on Fire safety engineering and structural engineering on the particular topic of spalling failure. Another objective of this thesis is the discussion over the possible replacement of the used procedures used to assess and guarantee tunnel safety. Both from a fire safety and structural engineering point of view, prescriptive measures and solutions are mostly proposed to accomplish a safe tunnel design. This causes the design to be non optimised and in some cases more costly than what is actually needed.

From the fire safety side, the use of pre-given fire curves is put under discussion. Research has been conducted to assess which are the origins of the most widely used curves. Studies have also been performed to develop a practical analytical engineering method to analyse and estimate the consequences of a given fire scenario tailored to the specific tunnel under consideration. Subsequently the results of the analytical models have been compared with the results obtained with advanced Computational Fluid Dynamics tools. Finally, more complicated scenarios have been studied with the use of this software.

On the other hand, from a structural engineering point of view, a new model able to describe the spalling mechanism has been proposed. The model predicts the spalling time for NSC elements and at the same time verifies which is the optimal thickness for the piece to spall. On top of that the possibilities for further use of the model in the description of the spalling mechanism for HSC and PPFRC elements have been investigated.

Finally this two topics have been combined together and conclusion have been drawn.



# ACKNOWLEDGEMENTS

My gratitude goes to all the people that contributed to the realization of this thesis.

From the university, I wish to thank Kees for proposing me this topic in the first place: academically appealing but at the same intrinsically related to the current engineering practice and its challenges. It was a pleasure to work with him as a supervisor, starting from mentioning the help and guidance given thorough the thesis till the methodology and work approach that he has taught me. I am also very thankful to Dick and Geert for the insightful help and suggestions that I received during the meetings where I exposed my work progress.

I would like to express my gratitude to Witteveen+Bos because it believed in my proposal and gave me the opportunity to work on this topic while experiencing the work environment in its offices. In particular, I would like to show my gratitude to three colleagues I collaborated with: Bas for being there every week, helping me out in all the aspects of the thesis. From guiding me through the possibilities and drawbacks of the different aspects I was researching till helping me in my academic writing and referencing. I would like to thank Aryan for the experienced and detailed help given to me in relation to the tunnel fire safety “world”. Finally, I would like to thank Marina for the help that she gave with the use of a relatively new tool to me, such as FDS.

My thanks go to all my friends, which are many and it is a hard task to properly thank in this context. Starting from my childhood friends till my classmates in school, I am grateful to them. What is more, these two years could not have been the same without the friends I made in such an international environment as Delft university. They made me grow and contributed in expanding my points of view and cultural background. I want also to thank Vaggy, that during this last year “shook” my life and supported me from the first moment, bringing joy whenever the mood was low.

Last, but not least I will never stop to be thankful to my parents. Their love, support and encouragement throughout my education has never vanished. They taught me what is the meaning of sacrifice and that every achievement is built upon a journey accomplished step after step and resulting in the definition of a person.



## LIST OF SYMBOLS

$\%_{rad}$	Radiation fraction	–
$\alpha_r$	Radiative heat transfer coefficient	$W/m^2/K^4$
$\alpha_c$	Convective heat transfer coefficient	$W/m^2/K$
$\alpha_{tot}$	Lumped heat transfer coefficient	$W/m^2/K$
$\Delta H_c$	Net calorific value	$Jkg^{-1}$
$\dot{m}$	Burning rate	$kg/m^2/s$
$\dot{m}_a$	Mass flow rate of supplied air	$kg/m^2/s$
$\dot{m}_f$	Fuel mass rate loss	$kg/m^2/s$
$\lambda_c$	Concrete thermal conductivity	$Wm^{-1}K^{-1}$
$\Phi$	Air/Fuel equivalence ratio	–
$\rho_a$	Air density	$kg/m^3$
$\rho_c$	Concrete density	$kg/m^3$
$\sigma_n$	Stefan-Boltzmann	–
$\sigma_{ext}$	External stress	MPa
$\sigma_t$	Tensile stress	MPa
$\varepsilon_c$	Concrete thermal elongation	–
$\varepsilon_{cT}$	PPFRC thermal elongation	–
$\rho_s$	Smoke density	$kg/m^3$
$\zeta$	Sectional coefficient	–
$A$	Tunnel cross sectional area	$m^2$
$A^*$	Original heat content of the smoke stream	$Wm^{-1}K^{-1}$
$b$	Spalled piece width	mm
<i>BLEVE</i>	Boiling Liquid Expanding Vapour Explosion	–
$c_a$	Air specific heat capacity	$kJkg^{-1}K^{-1}$
$c_c$	Concrete specific heat capacity	$Jkg^{-1}K^{-1}$
<i>CFD</i>	Computational Fluid Dynamics	–
$D$	Equivalent fire diameter	m

$d_I$	Smoke layer thickness close to fire location	m
$E_c$	Concrete Young's-Modulus	MPa
$E_{PPFRC}$	PPFRC Young's Modulus	MPa
$f_{ctk,0.05}$	Concrete tensile strength	MPa
$f_{cm}$	Mean value of concrete cylinder compressive strength	MPa
$F_{s-c}$	Smoke-concrete view factor	–
$FFFS$	Fixed Fire Fighting Systems	–
$g$	Gravitational acceleration	m/s <sup>2</sup>
$H$	Tunnel height	m
$h_{cut}$	'Cut-off' flame length	m
$H_{eff}$	Effective height	m
$h_{free}$	Flame height in open space	m
$h_{hor}$	Horizontal flame length	m
$HGV$	Heavy Goods Vehicle	–
$HRR$	Heat Release Rate	MW
$HRR_*$	Convective Heat Release Rate	MW
$HSC$	High Strength Concrete	–
$i_l$	Pavement longitudinal inclination	%
$i_t$	Pavement transversal inclination	%
$l_{buc}$	Spalled piece length	mm
$MD$	Smoke production rate	kg s <sup>-1</sup>
$n$	Air entrainment ratio	mol(air)/mol(hep)
$NSC$	Normal Strength Concrete	–
$PPFRC$	Polypropylene Fibre Reinforcement Concrete	–
$q_s$	Smoke flow rate	m <sup>3</sup> /s
$q_{cond}$	Conductive heat	W/m <sup>-2</sup>
$q_{conv}$	Convective heat	W/m <sup>-2</sup>
$q_{rad}$	Radiative heat	W/m <sup>-2</sup>
$r$	Equivalent fire radius	m
$S$	Pool Area	m <sup>2</sup>

---

$T$	Concrete temperature	°C
$t$	Spalled piece thickness	mm
$T - avg$	Average temperature over spalled piece thickness	°C
$T_a$	Air ambient temperature	K
$T_r$	Smoke temperature	K
$T_{avg}$	Average gas temperature over the entire tunnel cross-section	K
$t_{opt}$	Optimal spalled piece thickness	mm
$T_{r0}$	Maximum smoke temperature	K
$u$	Ventilation velocity	$m s^{-1}$
$u_{avg}$		$m s^{-1}$
$V_f$	Fibers volume fraction	%
$v_{cr}$	Critical velocity	$m s^{-1}$
$VCE$	Vapour Cloud Explosion	–
$W$	Tunnel width	m
$z$	Effective height	m



# 1

## INTRODUCTION

In the last few years there has been a growing interest in underground infrastructures and in particular tunnels. These constructions play a fundamental role in the development of the infrastructural and economical networks of a country. The continuous growth of urban areas and the increased need of living and working space facilities within the cities boundary push in the direction of an increase in the need for underground transport links. Within this context, two main categories can be mentioned, which namely are underground infrastructures for road vehicles or rail vehicles. Within the underground infrastructures field, one of the main issues of concern is *Fire Safety*. An increase in their use is demanding a better understanding of the dynamics involved, in order to successfully achieve a balance between safety and economical sustainability of the project.

Fire Safety focuses its attention towards 2 main directions:

- *Users tunnel safety*, which can, for example, be met with sufficient time to escape from the fire within a tunnel;
- *Structural tunnel safety*, which is concerned with maintaining a sufficient structural performance during fire. This may vary depending on the stakeholders demands which, for instance, can be related to the limitation of the time needed for repairing the damages.

The issues under consideration present significant challenges. One of the last reported fire accident, as shown in Fig. 1.1, occurred in 2018 in one of the main highways connecting France and Italy, causing kilometers of jams and big delays to the users of the highway. In Appendix A a list of some of the main road tunnel fire accidents in the last years is reported [6]. As can be seen there were fortunately no casualties in the last accidents, but for all the tunnels severe damage to the structure was recorded.



**Figure 1.1**

*Fire accident (A10). Article screenshot retrieved from <sup>a</sup> in May 2018*

<sup>a</sup>= <https://tg24.sky.it/cronaca>

Scientific research and regulations are currently tackling the numerous topics related to this field driven by the need to reach safer and more economical



Figure 1.2

Article showing the relevance of the topic. Retrieved from Cobouw newspaper of 30 August 2018

ways to design and use underground infrastructures. The newspaper article shown in Fig.1.2 outlines the major interest for this topic of the civil engineering industry.

The focus of recent research has been on fire scenarios that should be used in order to assess the safety of tunnels and the spalling mechanism endangering the capacity of the concrete structure. Spalling is only one of the main failure modes that needs to be addressed in the check of a structure subjected to fire and, at the moment of this thesis, is not fully understood. According to the fib bulletin 38 [11], together with spalling, bending failure, buckling/compression failure, anchorage/bond failure, shear or torsional failure need to be checked.

In particular, spalling affects the structural performance of a tunnel endangering the capacity of the infrastructure to keep standing. In the literature, several theories have been proposed to explain the spalling mechanism. However, a definitive explanation has not yet been found.

# 2

## PROBLEM STATEMENT, RESEARCH QUESTION, OBJECTIVES AND METHODOLOGY

### PROBLEM STATEMENT

Based on the aspects mentioned in the introduction, the focus in Fire Safety Engineering is on two main areas. Namely, Users Tunnel Safety and Structural Tunnel Safety. In the former the use of advanced tools, such as Computational Fluid Dynamics software and performance-based design, is applied, whereas that is not happening in the case of the latter, since Prescriptive Design is mainly used. Structural Tunnel Safety is also related to structural engineering which involves failure modes calculation. In case of fire these need to incorporate the temperature dependent variation of mechanical and cross sectional properties. This is usually carried out with the help of specific software's such as FEM tools.

Taking that into consideration, the present thesis aims at further improving the knowledge in Structural Safety, mainly addressing tunnel fire dynamics, the spalling mechanism and their relation. The problem stems from mainly two factors. Namely, the method implemented so far which makes use of standard fire curves prescribed by regulations without taking into account the specific design under consideration. At the same time, the spalling mechanism is insufficiently understood and simplistic check methodologies are often applied or more elaborate full-scale fire testing is adopted. The two above mentioned aspects highlight the lack in comprehension of the governing mechanisms and their relation. This might lead to a highly conservative design and as a consequence an unnecessary rise of the costs.

Stressing the relevance of this topic and taking a look in what is happening in actual practice, one could see that fire scenarios and structural checks, like spalling, appear to be most of the times disconnected topics within the field of Fire Safety. More specifically, this disconnection is due to the fact that the two topics are being treated separately and the results coming from the one are often not being directly used by the other.

This disconnection between both topics, in the view of the author, raises urgency for relevant research, both scientific and practical. This involves analysis of the key aspects and the relevant relationships. The goal is to obtain an optimized and better design approach intended to improve the cost benefits.

## RESEARCH QUESTION

*Within the actual state of the art in tunnels engineering, under which conditions is it advantageous to incorporate real fire scenario in combination with a spalling mechanism model in the structural safety checks of road tunnels?*

2

### Sub-questions:

- Which parameters are mainly influencing the fire scenarios? How can they be taken into account to calculate a temperature profile in the tunnel, and what is subsequently a worst case fire curve based on an actual scenario?
- How can the spalling mechanism be described and modelled at a structural level? Can such a model follow spalling test results and describe effects such the prevention of the spalling mechanism by the addition of PP-fibers into concrete mixture?

## RESEARCH OBJECTIVES

**The research objective is** the comparison of tunnel structural safety checks between the actual method, making use of standard fire curves and spalling test procedures, and a new site-based one (method) to be developed. **That will come as a result after** deriving the most probable occurring fire scenario and developing a spalling mechanism model at structural level **in order to** understand if cost-benefits and a better understanding in tunnels design-phase using the site-based approach can be obtained.

The research objectives of this thesis can be summarized in the following main points:

1. derive the most probable fire scenarios;
2. develop a new spalling mechanism model;
3. compare the standard design fire curves used in practice with the derived fire scenarios;
4. compare the spalling test procedures with the derived spalling model.

## METHODOLOGY

The methodology applied to carry out the work in this master thesis is graphically synthesized in Fig.2.1. The work has been conducted using three different approaches throughout the thesis:

1. theoretical approach;
2. analytical approach;
3. numerical approach.

After the definition of the research inputs, research about the fire dynamics and spalling mechanism has been conducted in parallel. In the final stage of the thesis, the interaction between these two aspects has been investigated.

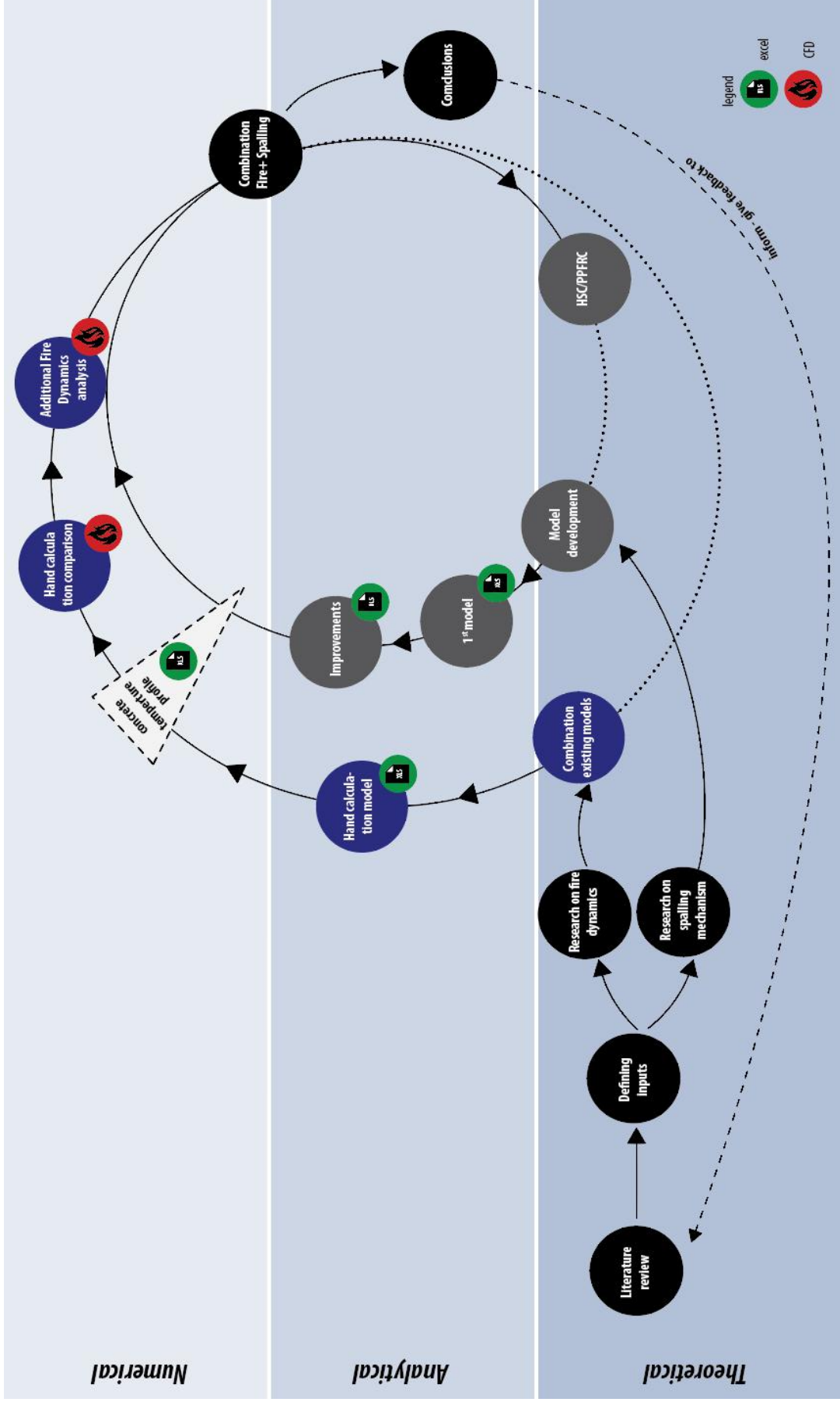


Figure 2.1  
Methodology diagram



# 3

## STATE OF THE ART

*This chapter aims at making the reader familiar with the concepts explained further in the thesis. A literature overview over fire dynamics, spalling mechanism and their relations is exposed. Moreover additional topics such as a general overview of tunnel design and use, computational fluid dynamics and laws and regulations are highlighted.*

### 3.1. TUNNELS: GENERAL INTRODUCTION

A tunnel is an underground passageway characterized by the presence of an enclosed space with the exception of the entrance and the exit. In general, a tunnel can be built with the purpose of serving as utility tunnel, aqueduct, sewer, etc. In this master thesis focus will be given to road tunnels.

Many tunnel typologies exist. The main ones, as reported in [16] are: cut and cover, cast in situ, tunnels excavated through rock and immersed tunnels. The width of the tunnel varies depending on the tunnel use. A tunnel can be uni-directional or bi-directional. Additional space for emergency lanes in some cases needs to be taken into account.

Emergency exits are present, depending on the tunnel specific configuration, in accordance with the tunnel user safety rules. As an example, NFPA[3] and LTS(*Landelijke Tunnel Standaard*) provide indications on how to meet these safety requirements.

A tunnel is provided with numerous technical installations such as road signs, emergency signs and lighting systems. Two installations worth mentioning more in detail are the ventilation system and the Fixed Fire Fighting System (FFFS).

Ventilation is a measure adopted in order to control and regulate fire, smoke, air pollutant, heat and evacuation procedures. Ventilation can be divided into two categories: *natural ventilation* and *mechanical ventilation*. Natural ventilation relies on meteorological and traffic conditions and is rarely applied due to the unpredictability in meeting the required safety conditions at every moment in time [16]. Short tunnels make sometimes use of natural ventilation [27]. In general, especially for long tunnels, mechanical ventilation systems are applied. Various mechanical systems exist, but the focus will be on the two most widely used systems: *Longitudinal ventilation* and *Transverse ventilation*. Longitudinal ventilation is used to create a longitudinal flow of air with the help of either jet fans, nozzles, shafts or a combination of them as reported in [27]. Fig.3.1 shows two tunnels examples making use of longitudinal ventilation. Transverse ventilation is used to create a transversal air flow with the help of supply and exhaust vents. In Fig.3.2 an example of it is shown.

FFFS are piping systems supplying extinguishing agents or water to regulate and mitigate the effect of fire and its by-products (heat, smoke, etc.) in a tunnel [18]. Water FFFS are widely used and have been extensively studied during the large scale fire tests carried out during SOLIT [42],[12] and

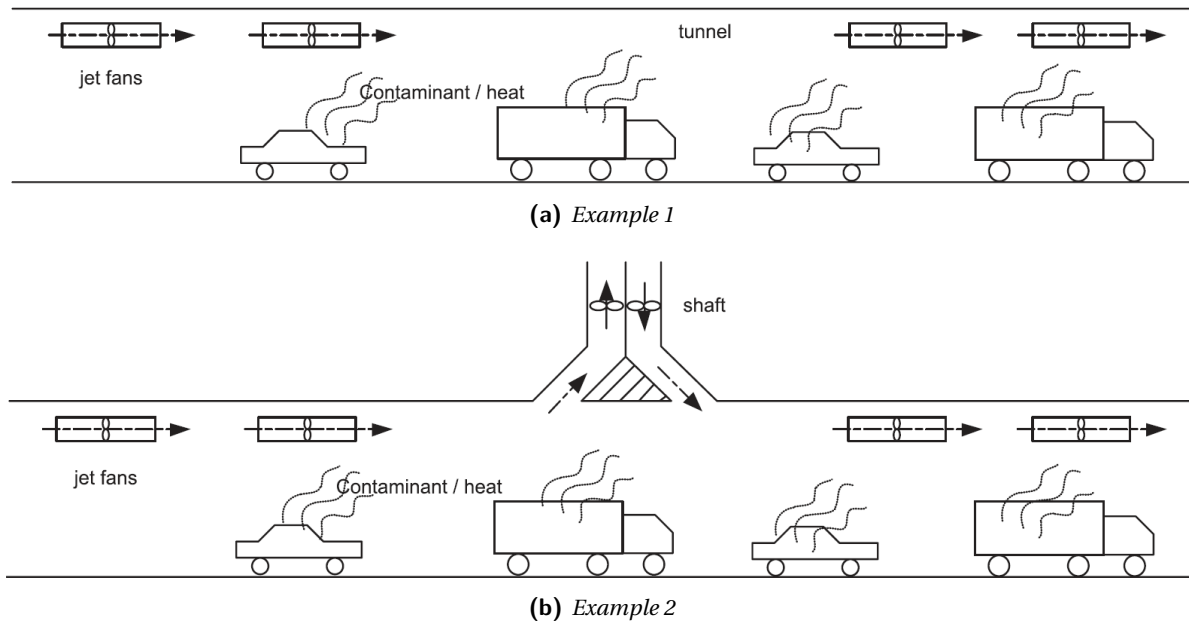


**Figure 3.1**

*Longitudinal ventilation examples. Retrieved from [27]*

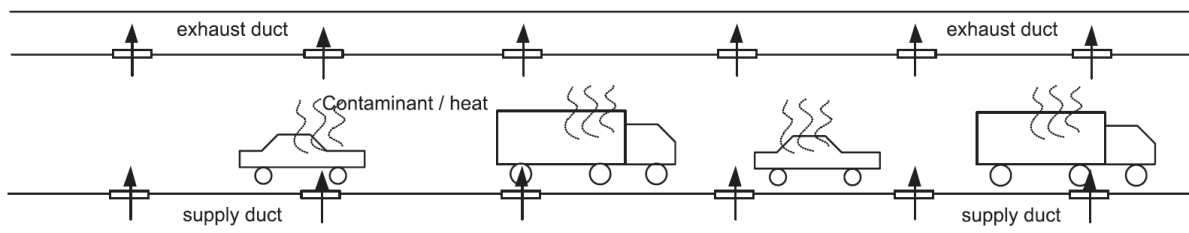


**Figure 3.2**

*Transverse ventilation example. Retrieved from [27]*

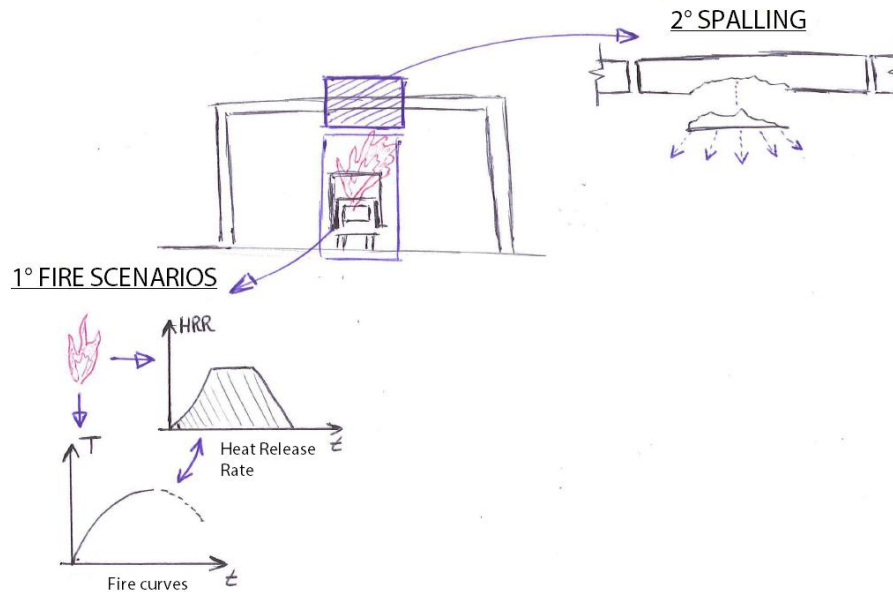


**Figure 3.3**  
*Thesis aim*

UPTUN [43] research projects. In these tests the water mist systems have been studied. Water mist systems are defined as systems which, for 99% of the water volume, release droplets with a diameter less than 1 mm [18]. Droplets can be released with different water pressure causing different response of the fire development.

### 3.2. TUNNELS: FIRE AND STRUCTURAL DESIGN

For a tunnel various possible fire scenarios can be considered based on, for instance, location, geometry and traffic. All these scenarios are characterized by a Heat Release Rate (HRR) referring to a single or multiple objects burning. The HRR can be seen as the basic component of a fire and is not only an intrinsic characteristic of the object, but it is also influenced by the surrounding environment. Based on the thermal energy development, expressed by the HRR, a certain temperature response at a given location will take place. In particular, fire curves represent the temperature development in time. Regulations often impose the use of Design Fire curves, which represent the worst scenario in terms of thermal impact for a given location. The curves adopted are mainly based on experimental data which have the consensus of technical committees. A fire curve will usually describe the temperature development for the first 60 to 180 minutes after the ignition phase [27].

Spalling, on the other hand, is the detachment of pieces of concrete from the tunnel lining caused by fire exposure. Concrete characteristics influence this mechanism, but also the typology of the fire exposure play a major role. The fire is the necessary ingredient for spalling to occur. At the same time, the structural geometry influences how the fire affects the concrete and the concrete characteristics influence how the temperature rise progresses into the cross section.

In order to visualize the two topics (Fire dynamics and Spalling mechanism) on which this thesis focuses and to understand the relation between them, reference is given to Fig.3.3.

### 3.3. FIRE SCENARIOS

A combination of theoretical background and well-known results used in practice have been combined together in this section in order to give a broad overview of the issues related to the fire mech-

anism in a tunnel. This is needed in order to be able to analyse the fire dynamics in a tunnel and capture the aspects relevant for the spalling mechanism.

Fire scenarios can consist of an infinite number of cases, but some indications on the most realistic ones can be looked up in a fire historical accidents record. From Appendix A it can be seen that collision as well as fire spreading from one vehicle are possible fire scenarios. It has, in any case, to be noted that the *fire progress*, spreading from a single vehicle, is a key ingredient for tunnel fire dynamics. On top of that, this influence the fire spread. As reported by Ingason [6, ch. 13] a tunnel fire develops and involves completely different aspects compared to a fire occurring in a building or in the open air. In this thesis attention is specific on fire in road tunnels. This allows for a larger variety in both tunnel cross-sections as well as fire scenarios.

### 3.3.1. FIRE PROGRESS

A fire can take place only if Oxygen, Fuel and Heat are all present (Fig.3.4a). The optimal fire combustion in air occurs if oxygen and fuel amount are present in accordance to the stoichiometric combustion reaction relation [6]. At the same time, pyrolysis occurs for the organic fuel material present. Pyrolysis is a decomposition reaction affecting the organic materials exposed to heat and does not necessitate of supply of oxygen [4]. The combination of these two phenomenon determines a certain fire progress which can be divided into stages.

The Fire stages are schematically shown in Fig.3.4b and are: *Ignition, Fire growth, Flash-over, Fire development*.

**Ignition:** the necessary first step for a fire to start. Several are the causes for a fire to start. Among them, there are the ignition from a vehicle, collision/explosion and crash due to accidents. Martin in [6, ch. 3] indicates that some of the main causes of vehicle ignition for a HGV are:

- *Fuel leak*, if a fuel leak reaches the engine or other hot surfaces, such as the exhaust parts, cause this fuel vaporisation which can subsequently ignite to form the combustion process. Similarly fuel vaporised and ignited from a big tanker truck leak can cause a significant pool fire in a tunnel;
- *Oil vaporisation*, if a rupture occurs in the hydraulic system and lubricant gets into contact with hot surfaces;
- *Electrical defect*, is a persistent heat source that might lead to the ignition if it enters into contact with the fuel;
- *Friction of internal mechanical parts*, similarly to an electrical defect this is a persistent heat source.

**Fire spread:** the early phase development of a fire.

Fire spread can be examined only after the heat transfer mechanisms have been highlighted. In practice oxygen and fuel are available before the start of a vehicle fire. The heat is the missing component and cause of a fire ignition and spread. According to Bonacina et al. [7], the heat can be transferred in the following ways:

- *conduction*, transfer of kinetic energy from molecules from a high temperature zone to a lower temperature zone ( $q_{cond}$ );
- *convection*, relative movement of fluid particles ( $q_{conv}$ );
- *radiation*, electromagnetic waves propagation ( $q_{rad}$ ).

Eventually, fire spread is influenced by the heat transfer which, in a tunnel, depends mainly on its geometry and the ventilation conditions.

Fire spread is also the cause of ignition for vehicles in the proximity of a fire already occurring. The common cause of ignition is the heat reaching the fuel material through convective and radiative heat transfer. In the case of a multi-vehicle fire, as discussed by Ingason in [6, ch. 13], the main causes of ignition of a second or subsequent vehicle are:

- *Flame impingement*, flames can developed and might reach a vehicle in the vicinity. In a tunnel fire, the reduced height of the ceiling compared to the flame length, causes a flame to spread horizontally along the ceiling;
- *Surface Spread*;
- *Remote Ignition*, through radiative or convective heat transfer is one of the main heat transfer mechanism;
- *Fuel transfer*, after leakage of fuel from the first vehicle the fuel and subsequently the fire can spread to other vehicles;
- *Explosion*.

**Flash-over:** the moment in time when all the combustible material suddenly ignites.

Flash-over occurs due to the faster energy generation rate with temperature compared to the aggregated energy losses, which gives rise to thermal instability as reported by Ingason [6, ch. 13]. This instability occurs in particular in compartments. In tunnel fires the conventional flash-over does not usually take place, due to the presence of the two portal openings [27].

On the other hand, that is not the only possible mechanism occurring after the fire growth. Other possible situations are:

1. *Back draft*, can take place in the case there is a lack of oxygen already in the spread phase, the fire will continue burning at a reduced rate. In the case of a sudden supply of oxygen while the fuel is not fully burned, the combustion reaction will suddenly increase, causing a steep temperature increase that leads to flash-over;
2. *Smoke gas explosion*, can occur if a cold mix of combustible gasses fill a certain zone and at some point, in the same location, ignition occurs. In the case of hot gases, ignition might occur earlier and the fire progress explained before would occur. For cold combustible gases this is prevented and the compartment can be filled with an explosive mix, that will give rise to a smoke gas explosion as soon as there is ignition

**Fire Fuel controlled:** the case when a fire is governed by the amount of fuel due to the abundance of oxygen present.

In [6] it is reported that, after flash-over, this is the most recurrent case for a single car or Heavy Goods Vehicle (HGV) fire.

**Fire Ventilation controlled:** the situation when a fire is governed by the amount of oxygen reaching the fire location.

In such a case, there is not sufficient oxygen to burn all the available fuel according to the stoichiometric relation. In [6] it is highlighted that the above is the most recurrent case for a multi-vehicles tunnel fire.

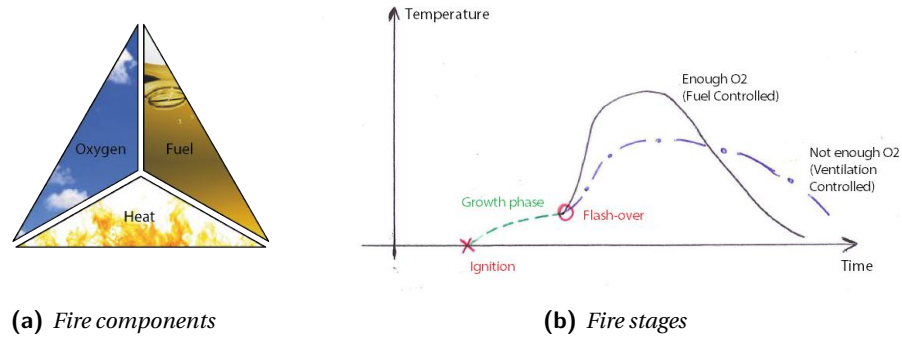


**Figure 3.4**  
Fire process basis

### 3.3.2. TUNNEL FIRES

In the following subsection tunnel fire dynamics and more in particular the main fire components are discussed. An example of the Gotthard tunnel fire occurred in 2001 is shown in Fig.3.7a. The concepts mentioned below are valid for vehicles fires and liquid pool fires. Other types of tunnel fire dynamics can involve, for instance, Boiling Liquid Expanding Vapour Explosion (BLEVE) or Vapour Cloud Explosion (VCE). These are however not in the scope of this thesis.

#### FUEL IN TUNNELS

In a tunnel, objects that are fuel components are the vehicles passing through it. The tunnel itself and its parts, such as the side barriers, are negligible. The following fuel typologies can be considered:

- Cars;
- Busses;
- HGV<sup>1</sup>;
- Tank vehicles which, in many cases, can be analysed as a pool fire due to the likely event of spillage of the liquid stored in it<sup>2</sup>. Pressurised tanker can also lead to a torch fire which is caused by the ignition of a leaking gas.

#### OXYGEN IN TUNNELS

Oxygen is the second basic parameter governing the fire process. For a tunnel fire there are multiple parameters influencing the oxygen supply as can be seen in Fig.3.5, which are:

- *Smoke*: it is a product of the combustion and mainly stratifies as a buoyant layer in the upper part of the tunnel cross section. It is mostly located above a cold layer of air which extends to the fire location. The two layers can mix with each other under unstable conditions which depends on many aspects such as ventilation and tunnel geometry as highlighted in [6]. This, indeed, affects oxygen supply;
- *Ventilation*: some of its main roles are control the smoke flow and and the removal of contaminants in a tunnel as reported in [27]. At the same time ventilation affects oxygen supply, smoke layer instability and HRR;

<sup>1</sup>the fire load of an HGV can vary significantly, depending on the type of goods transported

<sup>2</sup>as it applies for HGV, the fire load can vary significantly depending on the type of liquid transported

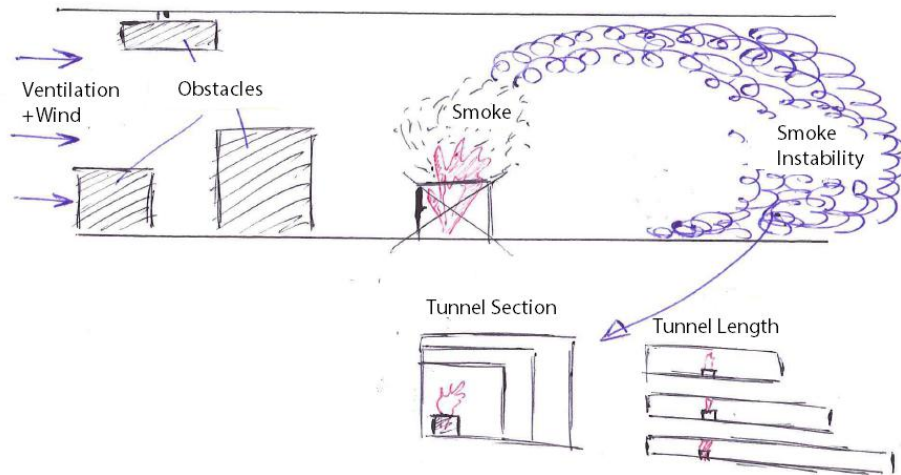


**Figure 3.5**

*Parameters influencing oxygen supply*

- *External conditions*; the ambient conditions at the portals such as wind determine the oxygen supply (higher input of oxygen per unit time) as well as the instability of the smoke layer (more turbulent mixing air/smoke in the inter-phase layer);
- *Tunnel dimensions*: regarded as length and cross section. These alter the amount of oxygen that reach the fire location;
- *Obstacles*: cause the reduction of the oxygen that can reach the fire.

### HEAT IN TUNNELS

The HRR is the basic parameter describing the heat produced in a fire and depends on a large amount of factors. The following parameters are in this respect mentioned:

- *Tunnel cross section*: for a smaller cross section the heat dissipates more slowly, resulting in a increased HRR at the fire location;
- *Tunnel length*: for a shorter tunnel, higher are the chances for environmental external conditions, such as wind, to alter the heat dispersion;
- *Ventilation*: for higher ventilation speeds, the HRR increases compared to the case without ventilation. Dependent on the ventilation the HRR can increase by a factor 10 times according to Ingason [25];
- *Oxygen/Fuel*: have both a direct influence on the HRR. In case of a lack of oxygen compared to the optimal combustion proportions, as already described for Ventilation Controlled fire, a reduced HRR will be present. At the same time, a fuel with the same calorific content, but different components materials might result in a different HRR as discussed in [6, ch. 14] and shown in the table of Fig.3.6 ;
- *Ambient conditions*: such as the ambient Temperature ( $T_a$ ) will influence the specific heat capacity ( $c_a$ ) and density of air ( $\rho_a$ ). These influence the heat development and the maximum temperature in a tunnel according to Heselden in [20] ;

Type of vehicle, model year, test number, longitudinal ventilation ( $u$ in m/s)	Tunnel (T) or calorimeter hood (C)	Tunnel cross-section: m <sup>2</sup>	Calorific content <sup>a</sup> : GJ	Peak HRR: MW	Time to peak HRR: minutes
Single passenger cars					
Ford Taunus 1.6, late 1970s, Test 1, NV	C		4	1.5	12
Datsun 160 J Sedan, late 1970s, Test 2, NV	C		4	1.8	10
Datsun 180 B Sedan, late 1970s, Test 3, NV	C		4	2	14
Fiat 127, late 1970s, $u=0.1$ m/s	T	8	NA	3.6	12
Renault Espace J11-II, 1988, Test 20, $u=0.5$ m/s	T	30	7	6	8
Citroën BX, 1986, NV <sup>b</sup>	C		5	4.3	15
Austin Maestro, 1982 <sup>b</sup>	C		4	8.5	16

**Figure 3.6**

*Passenger cars experimental HRR data. Retrieved from [25]*



**(a)** Tunnel fire. Retrieved from [34]



**(b)** Spalling. Retrieved from [61]

**Figure 3.7**

*Fire Dynamics and Spalling Mechanism*

- *Multiple Fire locations*: will influence the HRR, giving rise to a higher HRR compared to the case of a single fire of one of the vehicles;
- *Fixed Fire Fighting Systems (FFFS)*: are active fire protection measures, which influence the HRR, in a way such to suppress or control the fire development as stated by Håggkvist [18].

### 3.4. COMPUTATIONAL FLUID DYNAMICS

Tunnel fires are characterised by complex three dimensional flows. The energy release leads to buoyant forces governing the fire development. This development is influenced by turbulence and heat transfer which are themselves in relation with the tunnel geometry and ventilation conditions [6]. All these relations contribute to make a tunnel fire a complex phenomenon to understand and model.

Computational Fluid Dynamics (CFD) techniques have been developed to cope with situations involving such complexity. Fire and smoke behaviour in relation to safety assessment of tunnel infrastructures have been studied with the help of CFD software's. In the Performance Based Design these are quite often used by specialists in the industry.

CFD softwares solve the Navier-Stokes equations, consisting of a set of partial differential equations describing mass, energy and momentum conservation laws [16]. These are solved on a finite number of control volumes and require the definition of boundary conditions. In order to do so, the

tunnel under consideration has to be discretized through the definition of proper mesh volumes and boundary conditions. Different solutions methods characterize different CFD packages. Assumptions need to be made and inaccuracies can occur. Different CFD softwares focus on different aspects of fluid dynamics problems and are designed to model particular features [6].

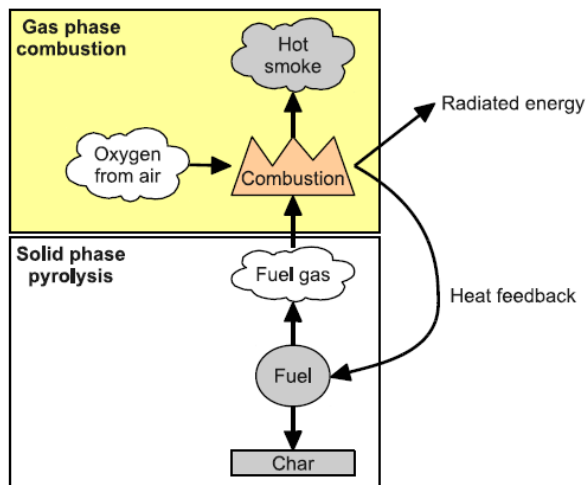


**Figure 3.8**

*FDS combustion models. Retrieved from [17]*

National Institute of Standards and Technology of the US Department of commerce (NIST) in cooperation with the VTT Technical Research Centre of Finland. It is a software which focus on fire smoke and heat transport phenomenon of low-speed thermally driven flows [16].

FDS has been used for many applications such as pyrolysis modelling, flame spread, fire growth and heat and combustion products transport. FDS makes use of a series of models and assumptions. The following aspects relevant to this thesis are here highlighted:

- *Hydrodynamic model:* the software allows both LES and RANS averaging techniques. The first one is the default option and requires a lower computational time compared to the RANS to obtain comparable accuracy;
- *Combustion model:* three combustion models are included. The first being a single step reaction whose products are the mass fraction of burned and unburned fuel and in which oxygen availability affects the reaction efficiency. A two step combustion model including the oxidation of fuel to carbon monoxide and the subsequent oxidation of the latter into carbon dioxide is also available. Lastly, a multiple step model can also be defined by the user. In FDS the fire can be prescribed specifying directly the Heat Release Rate on a surface, which is then used to model the fire as a gas phase combustion. This is possible using the one step combustion model. It is also possible to model both the solid phase pyrolysis and gas phase combustion when the multi-step model is used and the thermophysical properties of fuel materials are specified. In Fig.3.8 a representation of this two possibilities is shown;
- *Radiation model:* a gray gas transport equation solution is used to model the radiative heat transfer. The fire radiation from the fire is set as a fraction of the chemical energy released in a mesh cell by the flames.

### 3.5. SPALLING MECHANISM

Following the definition of Houry et al. [28], spalling (Fig.3.7b) is defined as:

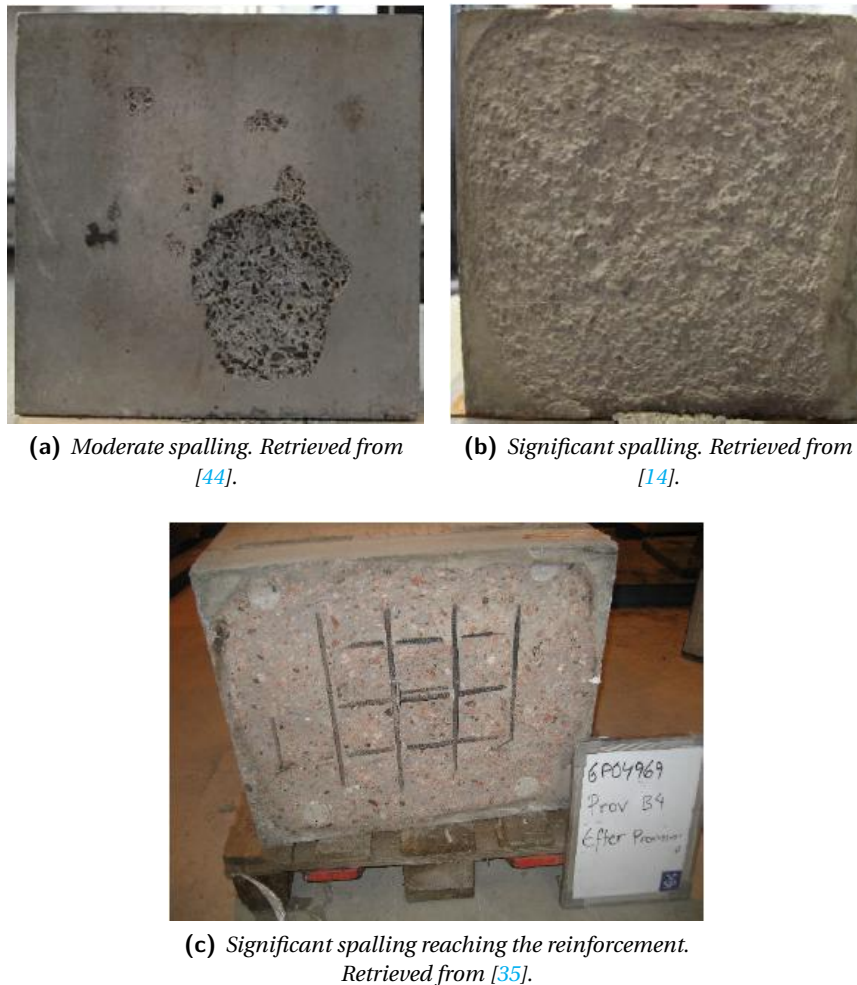


**Figure 3.9**  
Different degrees of spalling damage

*"The violent or non-violent breaking off of layers or pieces of concrete from the surface of a structural element when it is exposed to high and rapidly rising temperatures as experienced in fires"*

In Fig.3.9 different level of spalling damage are shown. The first evidence of spalling is reported by Khoury et al. [28] to occur within the first 5-30 min from the start of the fire. According to Mindeguia [38], typical lengths of the spalled pieces varies between 1 and 30 cm and the thickness can be equal to a couple of centimetres. The results obtained in the tests described in [31] show that the spalling mechanism can have a repetitive nature and occur frequently during a fire, causing multiple layers to be removed from the cross-section. Also more isolated, single occurrences reflecting spalling of larger pieces are reported in [28], causing sudden and sometimes significant damage to the cross-section.

The consequences for the concrete structure could be multiple, leading in extreme cases, to either the collapse of part of the structure or the redistribution of forces with associated deformations, as reported by Khoury et al. [28]. A main cause of collapse of the structure is the exposure of the reinforcement to fire due to the detachment of the concrete cover which act as protective layer. Exposure of the reinforcement bars to high temperatures cause the degradation of the mechanical properties and could ultimately lead to the failure of the whole structure.

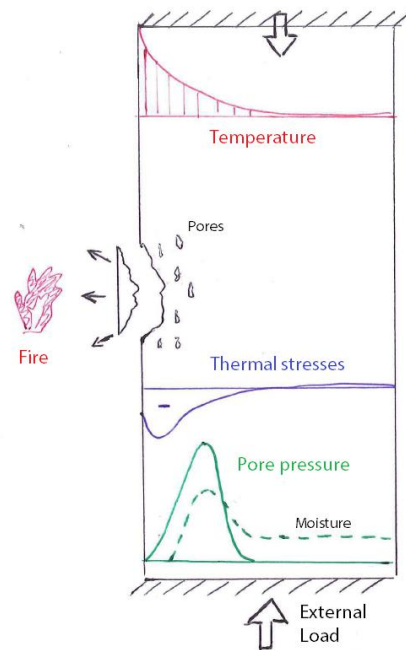


**Figure 3.10**

*Pore pressure - Thermal stresses Spalling mechanism*

In order to avoid the collapse and limitate the damage, protective measures are applied. In the fib technical report [11], for instance, polypropylene fibers in the concrete mix or thermal barriers applied to the fire exposed surface are indicated.

### 3.5.1. PORE PRESSURE AND IMPOSED THERMAL DEFORMATIONS

Many studies in order to explain the mechanism causing spalling phenomenon have been conducted.

**Imposed thermal deformations:** in 1963, Kordina [30] developed a theory describing spalling as the consequence of imposed deformations with corresponding thermal stresses caused by the temperature development in the element.

**Pore pressure:** a different approach was followed by Harmathy [19], who in 1965 developed a theory pointing the attention to moisture evaporation in the element causing pressure development in the pore system, leading to spalling. Following his work, Waubke [63] did one of the first calculations based on pore pressure development.

**Pore pressure and Imposed deformation combined:** Meyer-Ottens [36] and Zhukov [65] associated the possible causes of the spalling mechanism to a combination of pressure development and thermal stresses (Fig.3.10)

### 3.5.2. BUCKLING INSTABILITY

Recently, according to Lottman [34], an alternative possible explanation for the spalling mechanism has been proposed. The occurrence of spalling is linked to restrained thermal deformations with the instability of heated layers at the fire exposed surface being governed by a form of buckling. The thickness of the layer seems to be related to the crack pattern arising in the concrete and different behaviours have been recorded for High Strength Concrete (HSC) and Normal Strength Concrete (NSC).

The above mentioned theory is supported by the results of FEM analysis done on different conditions, such as structural loading, concrete type, fire scenarios. The FEM model was derived cou-

pling fracture mechanics and temperature/pore pressure developments. Comparison to various results from full-scale fire test have been made to assess and analyse the simulated behaviour.

The study furthermore suggests the idea that a pore pressure model is insufficient to describe the spalling mechanism. This is due to the fact that concrete, after structural loading or at the beginning of the fire exposure, will crack and create voids where moisture can expand. The model in particular showed that the connectivity of the crack pattern in the heated surface layer allows moisture to escape and mitigate the pore pressure development. The resultant influence on the local stress state was found to be limited in comparison to the stresses arising from the steep temperature gradient.

### 3.5.3. INFLUENCING PARAMETERS

Through mainly extensive full-scale testing various parameters have been found that influence the spalling phenomenon ([28],[21],[31],[38]). For the purpose of connecting to the topic involving fire scenarios, the influencing parameters can be separated in two categories, as shown in Fig.3.11. Namely, these are the *External parameters*, related to the fire load acting on the element, and the *Internal parameters* related to the intrinsic element characteristics.

The influencing parameters are highlighted below:

$$\left\{ \begin{array}{l} \text{EXTERNAL PARAMETERS} \quad \dashrightarrow \quad \text{SPALLING}(T_{max}, t_{Tmax}, \text{Exposed Area, Rad. \& Conv. Fluxes}) \\ \text{INTERNAL PARAMETERS} \quad \dashrightarrow \quad \text{SPALLING}(\text{Concrete, Reinforcements}) \end{array} \right.$$

In Khoury et al. report [28] and in related references it was observed that the maximum temperature ( $T_{max}$ ), the heating rate, which can simplistically be represented by the time needed to reach the maximum temperature ( $T_{Tmax}$ ), and the exposed surface are substantially affecting the spalling mechanism. In the tests carried out by SOLIT2 Research Program [12], the fundamental influence of radiative and conductive heat fluxes on the spalling occurrence is highlighted.

Whether spalling is considered as a result of pore pressures or thermal stress development, the temperature profile inside the concrete is of primary importance. One of the most widely used approaches to find the temperature profile is the use of Fourier unidirectional heat equation, mentioned for instance by van Breugel et al. in [8]. In the determination of the temperature outline, the following concrete parameters are of importance: Concrete density ( $\rho_c$ ), Concrete specific heat capacity ( $c_c$ ) and Concrete thermal conductivity ( $\lambda_c$ ). In case of considering the imposed thermal deformations and specifically the instability by buckling the following concrete characteristics are of importance: Young-Modulus ( $E_c(T)$ ) and thermal elongation ( $\varepsilon_c(T)$ ). In Austria a test series by the FSV found that the reinforcement set-up influence the detachment of concrete [31].

#### EXTERNAL PARAMETERS INFLUENCING FACTORS

In section 3.3, the complexity and the parameters involved in tunnel fires have been elaborated. Various of these parameters ( $T_{max}$ ,  $t_{Tmax}$ , Exposed Area, Rad. & Conv. Fluxes) govern the fire load and have an external influence on the spalling process. Through literature review it has been found that the following six influencing factors in relation with the external parameters can be mentioned: *Tunnel geometry, Scenarios, Ventilation, Portal openings, FFFS, Obstructions*. The implications between the external parameters and influencing factors will be explained and supported with relevant studies and experiments in the paragraphs below. In order to keep track of the relations between them, reference is made to Fig.3.12.

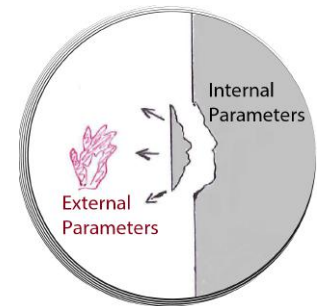


**Figure 3.11**  
*Spalling influencing parameters*

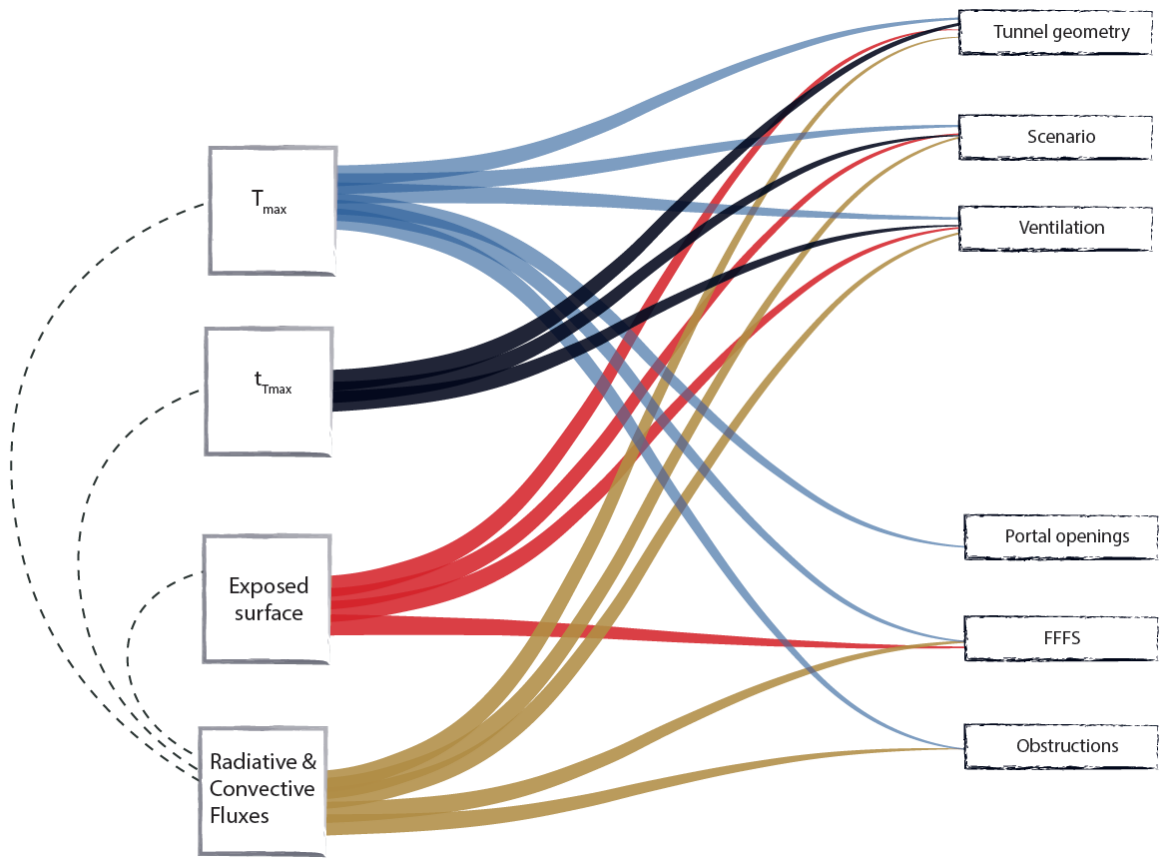


**Figure 3.12**  
*External parameters influencing spalling*

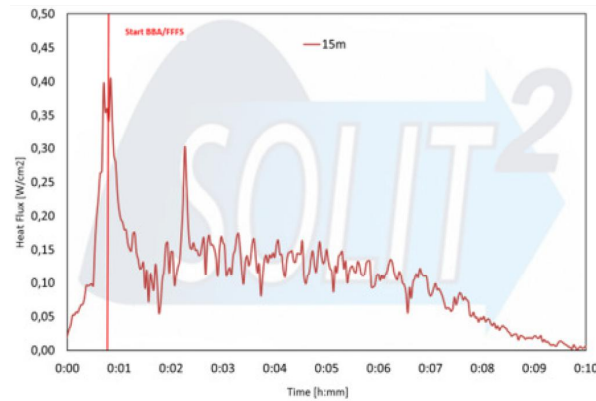


**Figure 3.13**

*Radiation Flux recordings (Water mist used). Retrieved from [12]*

**Radiative & Convective Fluxes:** these are the heat per unit area and per unit time that is carried away from the fire location via convection and radiation. Correlation with the other external parameters is as follows:

- *Maximum Temperature:* is related to the *Radiative & Convective Fluxes*. The fluxes surrounding the fire location greatly influence the HRR, which is directly related to the maximum temperature. For instance, in the model developed by Heselden in [20] the estimate of the maximum ceiling temperature is based on the smoke production in which the percentage of radiation that is able to leave the fire location has a great impact;
- *Time to maximum temperature:* has a direct relation with the *Radiative & Convective Fluxes* that determine the HRR in the post-flash-over fire growth phase as highlighted in [23];
- *Exposed surface:* the relation with the *Radiative & Convective Fluxes* is two-fold. First, the radiation in the proximity of the fire influences the amount of heat that reaches the surrounding surfaces. Secondly, radiation is one of the causes of fire spread. This affects the scenario and the locations at which the fire exposure occurs.

At the same time, many of the influencing factors have an impact on them. Namely those are:

- TUNNEL GEOMETRY and SCENARIO
- VENTILATION, it enters into play for the convective heat transfer. In particular, in proximity of the concrete elements the convective heat transfer coefficient is greatly dependent on the wind speed, as shown by van Breugel et al. in [8];
- FIXED FIRE FIGHTING SYSTEMS (FFFS), it has been proven by recent experimental results provided by SOLIT2 [12] that water mist, which is a FFFS, considerably reduce the radiation flux spreading in the vicinity of the fire. The results are shown in Fig.3.13;
- OBSTRUCTIONS, these define the fluxes spreading from the fire location and, perhaps act as shield for some parts of the tunnel from them.

**Maximum Temperature ( $T_{max}$ ):** is the highest temperature reached in the tunnel. This is usually below the ceiling in the proximity of the fire location. The main factors influencing the maximum temperature are:

- TUNNEL GEOMETRY, it affects the radiation and convection behaviour in the smoke/air mix;
- SCENARIO, it determines the global HRR as combination of all the HRR's of the vehicles involved in the fire at different moments in time and location;
- VENTILATION, it influences the HRR as mentioned by Ingason [25]. In the work of Li et al. [32], the combined effect of maximum ceiling temperature, HRR and ventilation is analysed. For instance, if the ventilation is above a certain critical value, the following two mechanisms occur:
  1. the maximum temperature increases linearly with the HRR;
  2. the maximum temperature decrease linearly with the ventilation.

At the same time, for a higher ventilation, as mentioned before, the HRR tends to grow. It is evident that all the three above mentioned effects are in relation and influence each other.

- PORTAL OPENINGS, it has been studied numerically by Huang et al. [22] the effect of totally or partially sealing the tunnel entrance during a fire. In this work, whose results are shown in Fig.3.14 , it has been found that for HRR below 50MW, the maximum temperature increase. On the other hand, for HRR above this value the maximum temperature is considerably reduced. Considering the fact that in a tunnel the HRR that is being considered in the design is greater than 50MW, the above-mentioned effect is of interest;
- FFFS, they greatly influence the temperature development in the tunnel. The results obtained in the SOLIT2 Research Program [12] suggest that the use of FFFS can stop the maximum temperature development, as can be seen from Fig.3.15a using water mist. As one of the causes of the previously mentioned effect, there is the effective contribution of the FFFS in blocking the HRR grow which in this case is kept limited to a constant value as shown in Fig.3.15b.
- OBSTRUCTIONS, those are the vehicles, but also the technical installations present inside the tunnel. They influence the ventilation reaching the fire location. The effect have been studied by Rojas Alva et al. [47] and it has been found that the vehicular blockage ratio affects the critical velocity ( $v_{cr}$ ), which is a key parameter in the fire behaviour and will be explained more in detail later on in Chap.4.

**Time to maximum Temperature ( $T_{Tmax}$ ):** is the time before the the maximum temperature is reached. The main factors influencing the time necessary for the highest temperature to be reached are:

- TUNNEL GEOMETRY and SCENARIO, the same reasons stated for the maximum temperature apply in this case;
- VENTILATION, it affects the HRR post-flash-over fire growth, as presented by Inganson in [25].

**Exposed surface:** is the surface that is exposed to the high temperatures caused by the fire. The main factors influencing the exposed surface are:

- TUNNEL GEOMETRY, the tunnel height greatly influence the development of flames. For low ceiling and/or high HRR, the flame will not only develop vertically, but it will also bend and spread horizontally along the ceiling [6]. In addition to that, as studied by Liu et al. the tunnel cross section has an impact on the temperature decay along the tunnel length [33]. For a

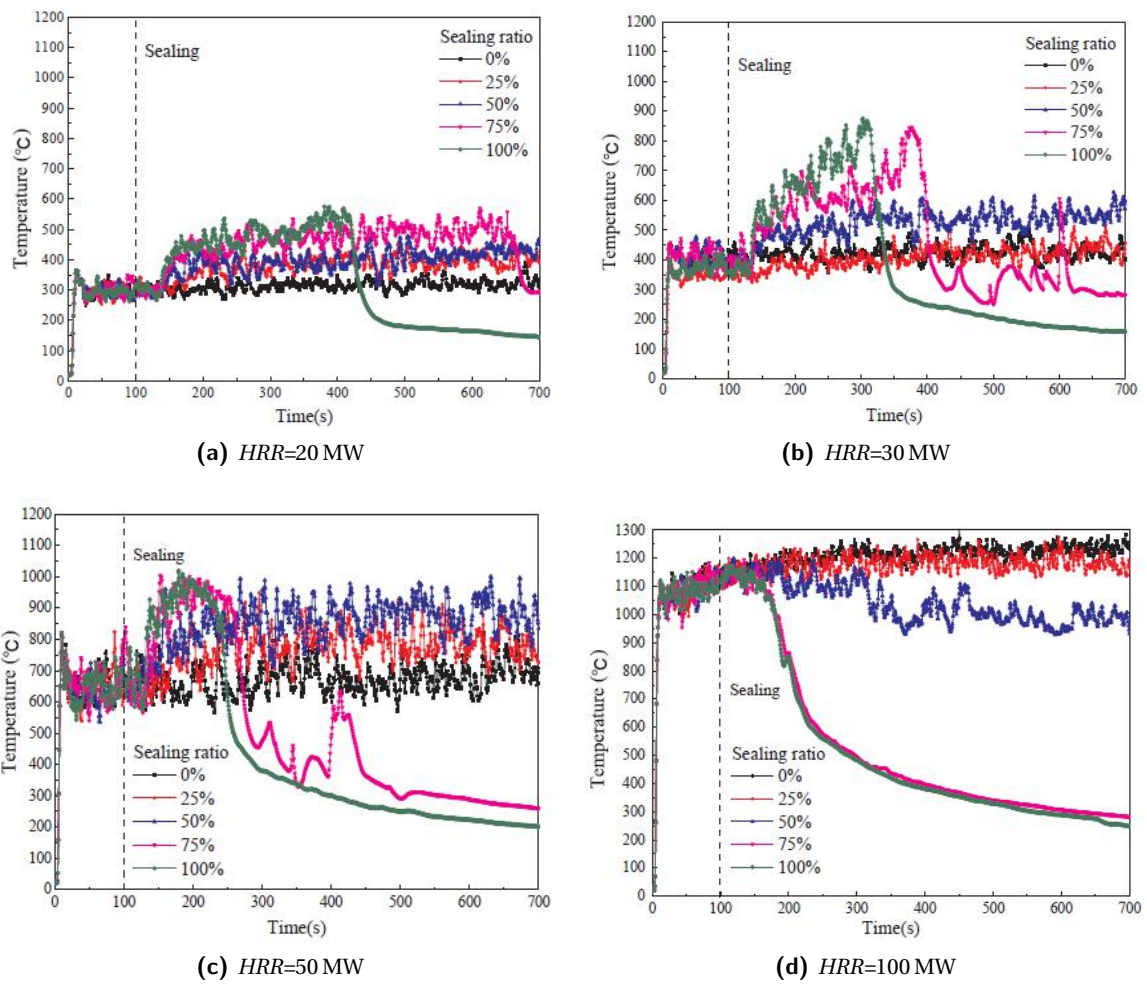


**Figure 3.14**  
Sealing ratio effect on maximum temperature. Retrieved from [22]

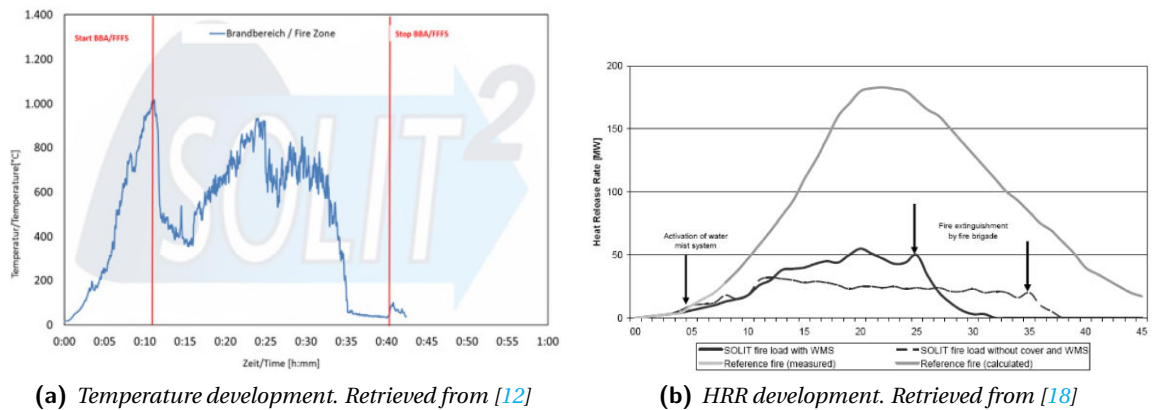


**Figure 3.15**  
FFFS influences on maximum ceiling Temperature

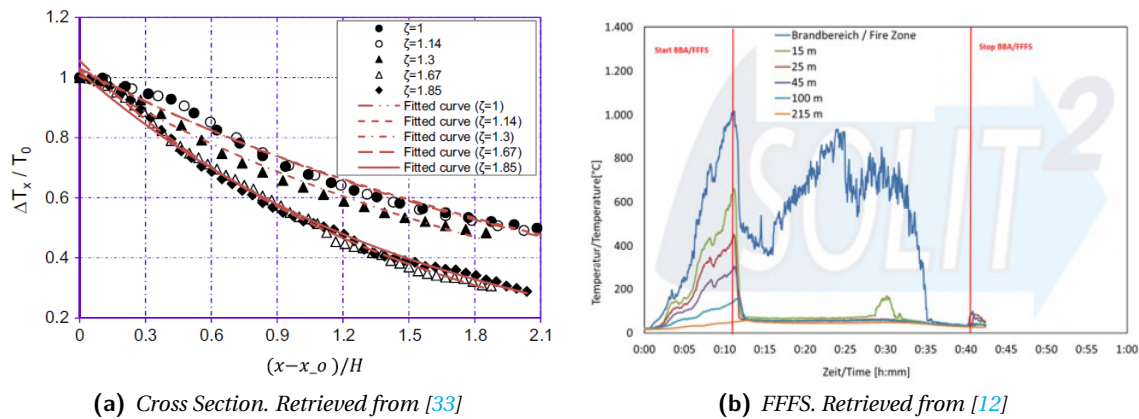


**Figure 3.16**  
Exposed Area influencing parameters

broader cross section, represented by a greater sectional coefficient ( $\zeta^3$ ), the temperature at the tunnel surface decreases more compared to a narrower section as depicted in Fig.3.16a ;

- SCENARIO, the vehicle position is, undoubtedly, of influence for the exposed area. In the case of a vehicle close to the tunnel side wall, the surface involved in the fire zone at high temperatures will involve both the ceiling and the wall;
- VENTILATION, it has an effect on the flame behaviour. For a higher ventilation, as stated in [6], the horizontal flame length tends to increase. Under these circumstances also the chances of fire spread due to flame impingement are higher;
- FFFS, the temperature in proximity of the fire is drastically reduced by the use of FFFS, such as water mist, as shown by the test carried out by SOLIT2 [12]. In Fig.3.16b, experimental results are shown about the temperature development in time at different distances from the fire.

### 3.6. LAWS AND REGULATIONS

Laws and Regulations regarding fire and spalling in concrete tunnel infrastructures will first be imposed by the European Union. The main specifications for the engineering practice are found in Eurocode 1, part 1-2 [50], Eurocode 2, part 1-1 [51], Eurocode 2, part 1-2 [52] and their National Annexes.

This thesis focuses on the procedures followed in The Netherlands for which the Dutch government imposes the laws (Bouwbesluit, WARVW, RARVW) whereas Rijkswaterstaat releases the majority of the directives (LTS, ROK). The additional regulations in The Netherlands for concrete tunnels are (Fig.3.17):

- WARVW (*Wet Aanvullende Regels Veiligheid Wegtunnels*), which is the Dutch road safety Law;
- RARVW (*Regeling Aanvullende Regels Veiligheid Wegtunnels*), which are the regulations for additional safety road tunnels;
- LTS (*Landelijke Tunnel Standaard*), which sets functional requirements and standard processes for construction and management of tunnels;

$${}^3\zeta = \frac{A}{H^2}$$

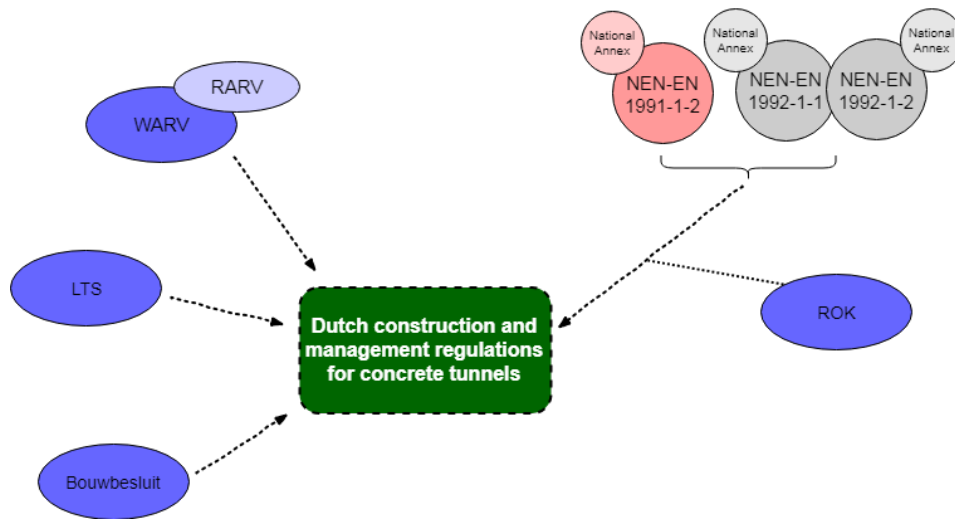


**Figure 3.17**  
Concrete tunnel regulations (NL)

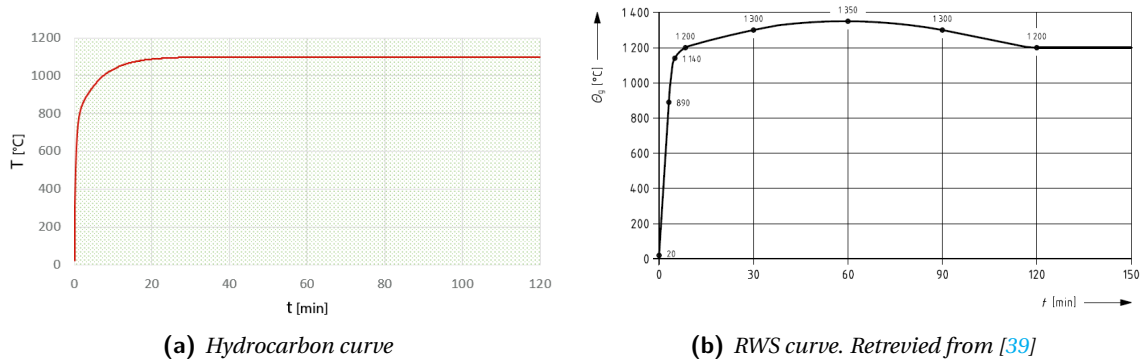


**Figure 3.18**  
Design fire curves (NL)

- *Bouwbesluit*, which sets requirements for health, safety, usability, energy efficiency and environment of constructions;
- *ROK* (*Richtlijnen Ontwerp Kunstwerken*), which are the guidelines for structures design;

In The Netherlands only tunnels longer than 250 m are designated as such. Whenever the length is longer than 500 m additional measures have to be met.

### 3.6.1. FIRE REGULATIONS

For a new tunnel in The Netherlands, unless specified otherwise in the contract, two main fire curves must be used to check the structural capacity (including spalling). For the closed part of the tunnel the temperature development in time according to the RWS-curve has to be resisted whereas for open parts, such as the access ramps, a slightly more moderate Hydrocarbon curve is used. In the case of under-water tunnels or tunnels with high economical significance the time frame of the temperature development has to be 120 minutes whereas for all the other cases is set at 60 minutes. These curves are depicted in Fig. 3.18.

The Hydrocarbon curve is highlighted in the European Standard [49] and describes the temperature profile for a standardised petroleum fire. Compared to the RWS-curve, it describes a situation

with a fire developing in a relatively open space from which the heat can escape. Secondly, for the Hydrocarbon curve the value of the Convective Heat Transfer Coefficient ( $\alpha_c = 50\text{W/m}^2\text{K}$ ) is prescribed in Eurocode 1, part 1-2 [50].

The RWS-curve was developed on the basis of the TNO scaled tests reported in [55] and [56] in 1979-1980. The tests were carried out in a scaled tunnel of 2x2 meters, with a length of 8 meters. Four steel containers aligned along the length of the tunnel, filled with gasoline, were set on fire. The gasoline supply was maintained constant with the help of an input supply system and temperatures were recorded at different locations along the roof. Fig.3.18 shows the test set-up and the recorded temperatures compared to the RWS curve and the Hydrocarbon curve.

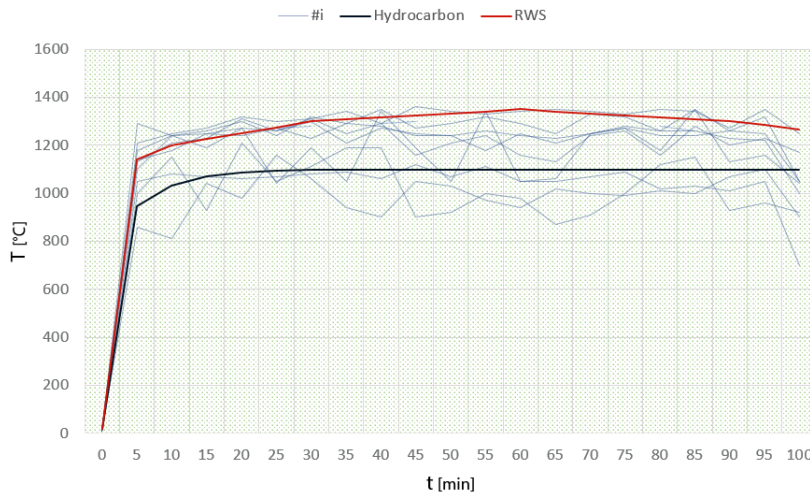
It is worth mentioning here that TNO, in 1992, carried out a series of Computational Fluid Dynamics calculations (CFD) for Rijkswaterstaat using as input a tunnel with a height of 5 m, width of 10 m and length of 600 m. Different scenarios were analysed, calculating as worst scenario temperature development a pool fire of  $142\text{m}^2$  caused by fuel leaking of a gasoline fuel tank with a capacity of 50 000 L and an HRR of 301 MW. A temperature development profile with an onset behaviour and maximum temperatures reaching and sometimes overshooting the RWS curve values were found. In Fig. 3.20a an example of temperature development of a pool fire ( $142\text{m}^2$ ) with a ventilation of  $1\text{ms}^{-1}$  is shown.

### 3.6.2. SPALLING REGULATIONS

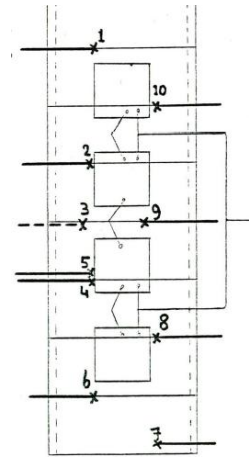
In the Dutch regulation [2] it is stated that spalling must be in any case avoided. The reason for stating "no-spalling" as well as temperature demands for concrete and structural reinforcement is that it should be possible to repair a tunnel after a fire has occurred.

In order to check whether a certain tunnel element is fulfilling the above-mentioned requirements, full-scale fire tests need to be done in accordance with the Efectis report [9]. These have to be representative for the tunnel (fire curve, loading and concrete). The addition of PP-fibers or use of protection measures are recommended due to the known beneficial effects in terms of spalling prevention and/or limitation. It is also common practice to increase the concrete cover thickness to meet the temperature demands. A new fire test is not compulsory in the case of a fire test carried out within the previous 3 years under the same conditions.

The previous version of the Richtlijnen Ontwerp Kunstwerken [1] contained indications of concrete mixes that were allowed to be used to avoid spalling. The Brawat test [57] led to a C28/35 mixture with a maximum cement CEM III B amount of  $340\text{kg/m}^3$ . In the Leidsche Rijn tunnel other 2 mixtures were allowed containing PP fibres and limestone. For these mixtures there was no need for full scale tests. The Brawat test were carried out during the construction of the second Benelux tunnel. In the test a partially protected concrete element was used as shown in Fig.3.20b. Minor damage occurred in the part of the wall that was unprotected and exposed to the RWS-curve.



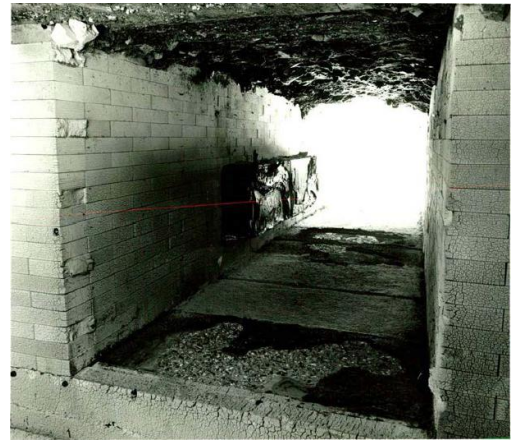
(a) Temperature profiles



(b) Experimental setup. Retrieved from [56]



(c) Conditions during fire. Retrieved from [56]

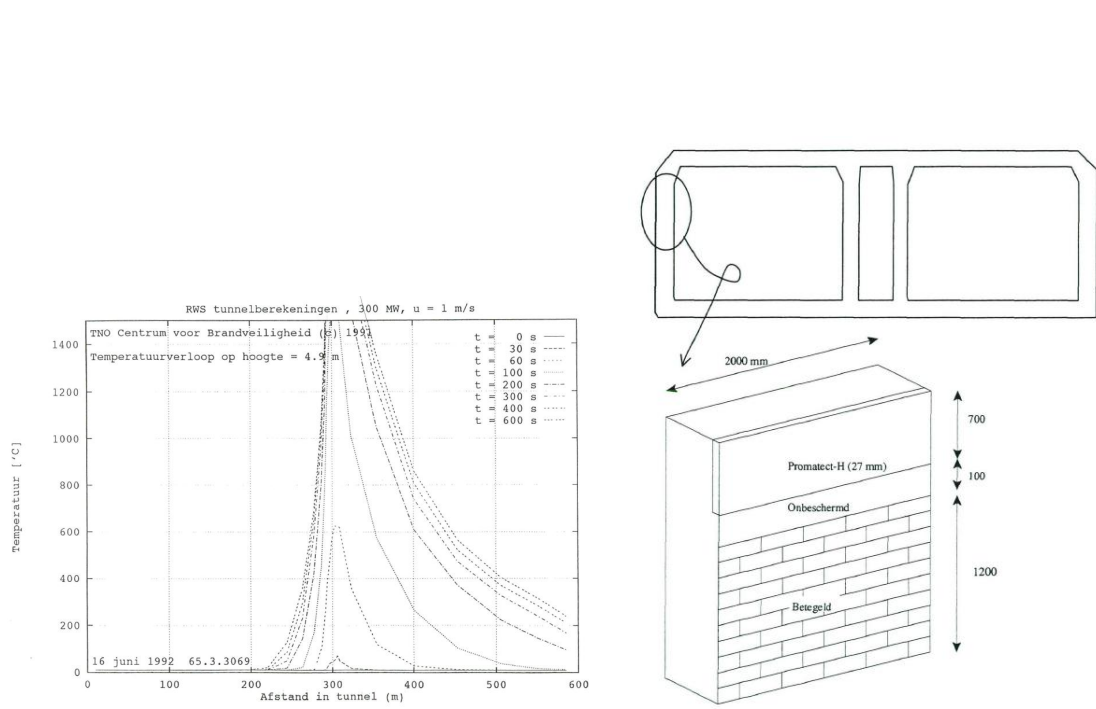


(d) Post-fire conditions. Retrieved from [56]



(e) Experiment location. Retrieved from [56]

**Figure 3.19**  
RWS curve full-scale experiments



(a) CFD Temperature results. Retrieved from [59]

(b) Experimental setup. Retrieved from [57]

**Figure 3.20**  
TNO fire tests and numerical simulations



# 4

## FIRE DYNAMICS

*In this chapter the basics of the fire dynamics that take place in a tunnel fire are analysed. Analytical models are proposed to calculate various aspects of the fire. The models focus mainly on two fire typologies which are the fire caused by the ignition of vehicles such as HGVS and pool fires. The aspects that have been treated are:*

- *Maximum temperature in the tunnel;*
- *Horizontal flame lengths;*
- *Temperature decay along the tunnel;*
- *Smoke layer instability;*
- *Fire spread between vehicles.*

*A numerical model able to estimate the temperature profile of a concrete element exposed on one side to the fire is also proposed. Finally results obtained using the above mentioned models are shown and discussed and subsequently conclusions drawn.*

The most common scenarios to be considered in a tunnel explosion/fire for different tunnels classification, in agreement with the ADR (European Agreement concerning the international carriage of Dangerous goods by Road) as reported by Vagiokas et al. in [62], are the ones shown in Fig.4.1. In this thesis we will focus on vehicles (Car and HGVS) fires and pool fires. These are among the most common fire scenarios in tunnels.

### 4.1. VEHICLES

The fires caused by vehicles are subdivided in this thesis into two main categories: *Cars* and *HGVS*.

#### 4.1.1. HRR

This subsection focuses on the HRR of the considered vehicles. Data of HRR in tunnel fires were found in literature [6]. These come from full-scale tests carried out in tunnels and are shown in Fig.4.2. Based on the available results the HGVS HRR were subdivided in two subcategories: HGVS with low and high fire load content ( $Q$ ). The tests results that were considered are the ones which involved no ventilation in the tunnel while the fire was burning. As mentioned in subsection 3.3.2,

	Scenario	Danger	Tunnel Categories				
			A	B	C	D	E
1	HGV fire 20 MW	Medium Fire	✓	✓	✓	✓	
2	HGV fire 100 MW	Large fire	✓	✓	✓		
3	BLEVE of LPG in cylinder	Small Explosion	✓	✓	✓	✓	
4	Motor spirit pool fire	Large Fire	✓	✓	✓		
5	VCE of motor spirit	Medium Size Explosion <sup>(1)</sup>	✓	✓	✓		
6	Chlorine release	Large Toxic Release	✓	✓			
7	BLEVE of LPG in bulk	Very Large Explosion	✓				
8	VCE of LPG in bulk	Very Large Explosion	✓				
9	Torch fire of LPG in bulk	Very Large Fire <sup>(2)</sup>	✓				
10	Ammonia release	Large Toxic Release	✓	✓			
11	Acrolein in bulk release	Large Toxic Release	✓	✓			
12	Acrolein in cylinder release	Medium Size Toxic Release	✓	✓	✓	✓	
13	BLEVE of carbon dioxide in bulk (not including toxic effects)	Large Explosion	✓	✓			

**Figure 4.1**

*Tunnel categories and scenarios. Retrieved in [62].*

ventilation strongly affects the HRR. The aim, in this stage, is to retrieve HRR data which are independent from the ventilation.

The hypothesis that are in common for all the retrieved data are the following:

- full-scale tests carried out in tunnels;
- no ventilation considered ( $v = 0,5 \text{ m s}^{-1}$ )<sup>1</sup>;

The HRR of the only available test carried out with HGV with high Q (Fig.4.2a) was set up with a ventilation of  $3 \text{ m s}^{-1}$  to  $6 \text{ m s}^{-1}$ . According to Ingason in [25], the HRR could increase of a factor of 4 for a longitudinal flow rate of  $3 \text{ m s}^{-1}$ . The maximum HRR of the HGV high Q was then reduced of 4 times to get rid of the effect of the ventilation, while the time to reach the maximum HRR was kept the same. The maximum HRR was subsequently fixed to 30MW.

The HRR development in time were modelled with simple shapes. From the tests results the following info were retrieved:

- maximum HRR ( $HRR_{max}$ );
- time till the maximum HRR ( $t_{HRRmax}$ );
- energy content.

For both cars and HGVs the energy content of the modelled HRR was kept equal to the one recorded in the tests. This results in a similar HRR development in time between tests and model. The car HRR was modelled as a triangular shape. The only info needed are the maximum HRR ( $HRR_{max}$ ) and the time needed to reach it ( $t_{HRRmax}$ ). Many tests data were available, so an average of all the quantities was taken. An example of a car HRR is shown in Fig.4.3b. On the other hand, the HGVs were modelled as a trapezoid. In addition to the knowledge of  $HRR_{max}$ ,  $t_{HRRmax}$ , further assumptions were needed. After reaching the maximum HRR and remaining constant for a given period of time, the HRR descending branch was assumed 3 times less steep compared to the ascending branch. An example of the trapezoidal HGV HRR is shown in Fig.4.3a.

<sup>1</sup>an exception has been made for the HGV-High Q. No data were available without ventilation for this type of vehicle. So, it was chosen to use the one with ventilation and adjust it based on considerations found in literature [25] over the influence of ventilation on the HRR.

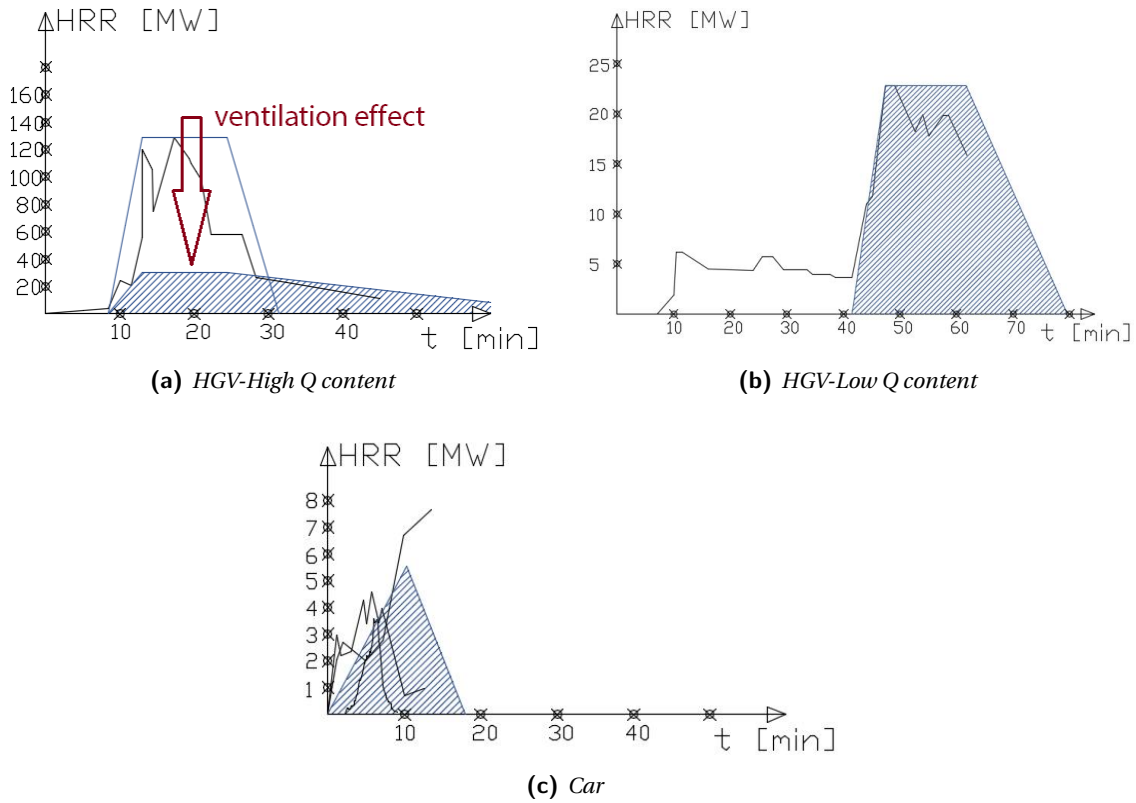


**Figure 4.2**  
Vehicle HRR data-Tunnel Full-scale Test. Retrieved from [25]

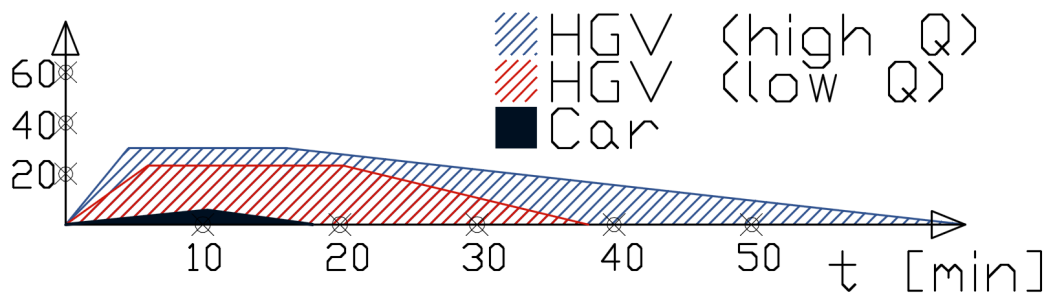
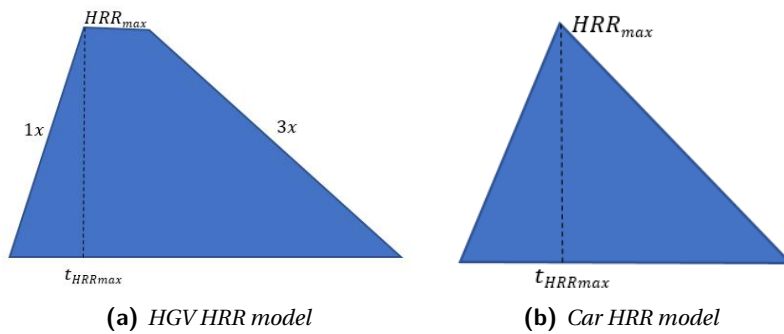


**Figure 4.3**  
HRR modelling

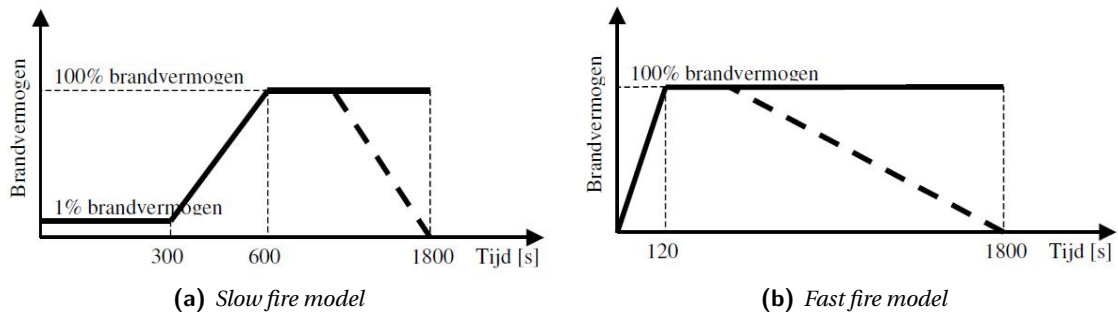


**Figure 4.4**

*QRA proposed HRR model. Retrieved from [46]*

4

In Fig.4.3c, the modelled HRR of all the vehicles are compared within each other. It is already visible that the car heat release rate is negligible in comparison with the heat that an HGV can release.

In order to check the modelled data, comparison between the modelled HRR (full scale tests based) and values contained in the theory document of the QRA software [46] is carried out. The QRA-tunnels (Quantitative Risk Analysis) is a software used in The Netherlands for the the risk assessment during the design of tunnels. In the QRA, the following maximum HRR for vehicle fires are proposed:

- single car fire: 5 MW;
- 2 cars accident fire: 10 MW;
- bus or truck with no inflammable goods: 25 MW.

In the software, indication of the HRR development for slow and fast fires are also available. The fast fire development is based on an Heptane liquid pool fire simulation carried out with a CFD software. It was chosen to take into account the great variety of cases showing a fast fire development. The two different fire development are shown in Fig.4.4.

Both the maximum HRR and the HRR development graphs, comparing the QRA and the one that have been proposed, are similar to each other and suggest similar development in time.

#### 4.1.2. DIMENSIONS

The dimensions of the vehicles were standardized. For the cars, it was chosen to average the dimensions of a common commercial car and a van (Fig.4.5a). For the HGVs the dimensional limits given in the European directive [41] were considered. An average between the modular configurations<sup>2</sup> allowed was used (Fig.4.5b).

#### 4.1.3. TEMPERATURE DEVELOPMENT

The temperature development in a tunnel and more in particular the maximum ceiling temperature has been extensively researched. Among the different theories and approaches, the most widely used are:

1. *Heselden work* [20]: based on experimental and theoretical work, it estimates a range of quantities among which there is the maximum ceiling temperature. The model is mainly related to the smoke production and movement. The following hypothesis apply:

<sup>2</sup>in general an HGV can be composed by a couple of short modules (swap bodies) or a long module (semi-trailer)

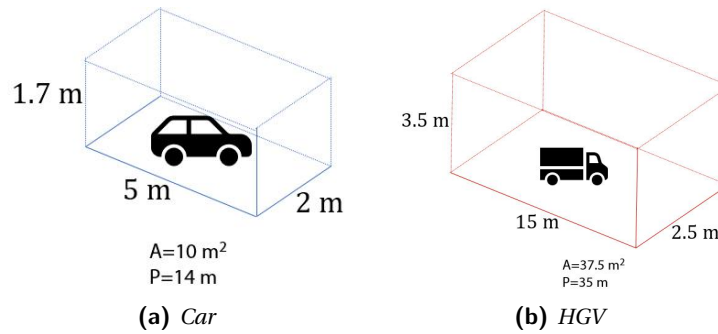


**Figure 4.5**  
Standardized vehicle dimensions

- horizontal tunnel;
  - fire away from the tunnel entrances;
  - HRR in the range 3-20 MW;
  - 25% radiation loss;
  - no longitudinal ventilation.
2. *Li et al. work* [32]: based on empirical equations compared to model-scale experimental tests, it estimates the maximum ceiling temperature. It takes into consideration HRR, ventilation velocity and tunnel geometry. It is valid only in the case of a flame length lower than the tunnel height.

**Heselden:** a visualization of the model used by Heselden to calculate the maximum ceiling temperature is schematically represented in Fig.4.6. The parameters involved in the tunnel fire are related to each other according to the following formulas:

$$v_{cr} = 0.8 \cdot \left( \frac{g HRR T_{r0}}{\rho_a c_a T_a^2 W} \right)^{1/3} \quad (4.1)$$

$$MD = 0.05 \cdot P \cdot (H - d_I)^{3/2} \cdot \rho_a \cdot \sqrt{g} \quad (4.2)$$

$$d_I = \frac{MD}{\rho_s v_{cr} W} \quad (4.3)$$

$$T_{r0} = T_a + (1 - \%_{rad}) \cdot \frac{HRR}{MD c_a} \quad (4.4)$$

with:

- $v_{cr}$ : Critical velocity ( $\text{ms}^{-1}$ ), defined as the ventilation velocity necessary to avoid any back-layering;
- HRR: Heat Release Rate (kW);
- $T_{r0}$ : Maximum Smoke temperature which in this case occurs above the fire location (K);
- $d_I$ : Smoke layer thickness close to fire location (m);
- MD: Smoke production rate ( $\text{kg s}^{-1}$ ).

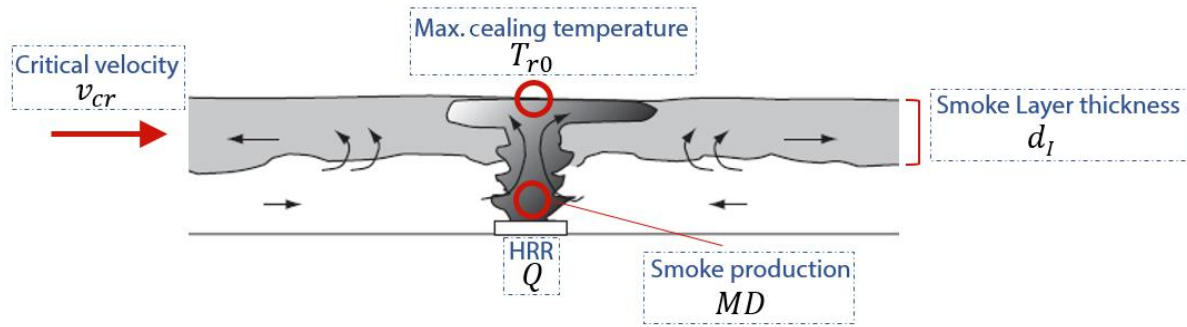


**Figure 4.6**

*Vehicle maximum temperature model. Retrieved from [6]*

4

The set of equations highlighted above has been slightly modified, in agreement with the modifications carried out in the TNO report [58]. The following aspects have been included:

- the smoke layer thickness at one side of the fire location ( $d_I$ ), in the case of absence of ventilation, is caused by the release of half of the available heat. The other half spreads on the opposite direction. This is the reason why the Heat Release Rate (HRR) is assumed equal to half of the  $HRR^*$  released by the vehicle on fire;

$$HRR = \frac{HRR^*}{2}$$

- the approach used by Heselden, uses the value of the smoke density ( $\rho_s$ ) as an input parameter. The assumption of a given value of the smoke density is really hard to do due to the fact that the density is temperature dependent [10]. The temperature is a value given as an output. It was chosen to relate the smoke density to a temperature proportional air density ( $\rho_a$ ) at ambient temperature ( $T_a$ ).

$$\frac{1}{\rho_s} = \frac{T_{r0}}{T_a \cdot \rho_a}$$

For a higher smoke temperature, the smoke density reduces. The same approach has been followed in [58]. Eq.4.3 modifies in the following way:

$$d_I = \frac{T_{r0}MD}{T_a \rho_a v_{cr} W} \quad (4.5)$$

- The tunnel height ( $H$ ) has been substituted with the effective height ( $H_{eff}$ ) which is the space between the fire source and the ceiling. For a vehicle fire it has been assumed as the distance between the ceiling and half of the vehicle height. Eq.4.2 modifies in the following way:

$$MD = 0.05 \cdot P \cdot (H_{eff} - d_I)^{3/2} \cdot \rho_a \cdot \sqrt{g} \quad (4.6)$$

In order to check the validity of the above proposed set of equations and better understand the relations existing between the different quantities, a parametric study has been conducted:

- in Fig.4.7 the relation between the critical velocity ( $v_{cr}$ ) and the HRR is shown. These quantities are related to each other in eq.4.1. An increased HRR has as a consequence a higher smoke production. This need to be counterbalanced by an higher critical velocity in order to avoid backlayering;

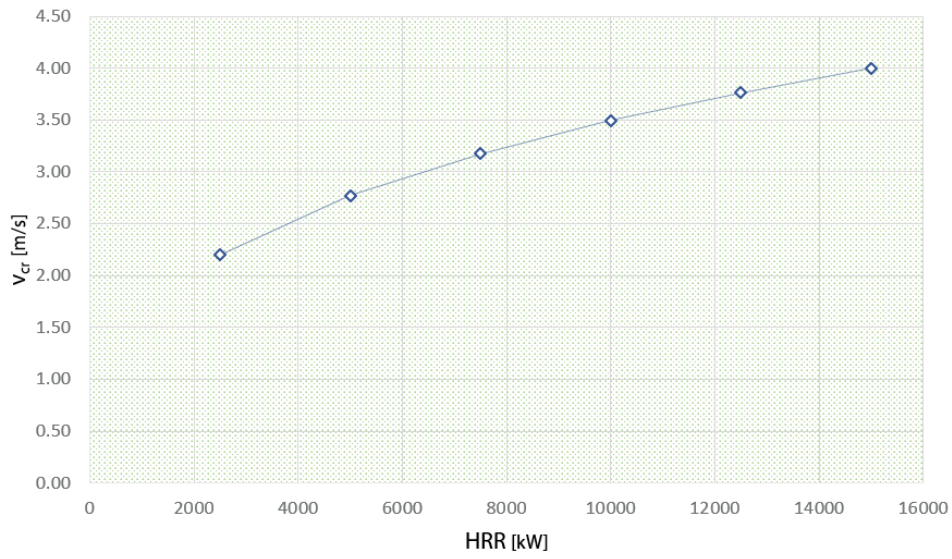


**Figure 4.7**  
*v<sub>cr</sub> vs HRR*

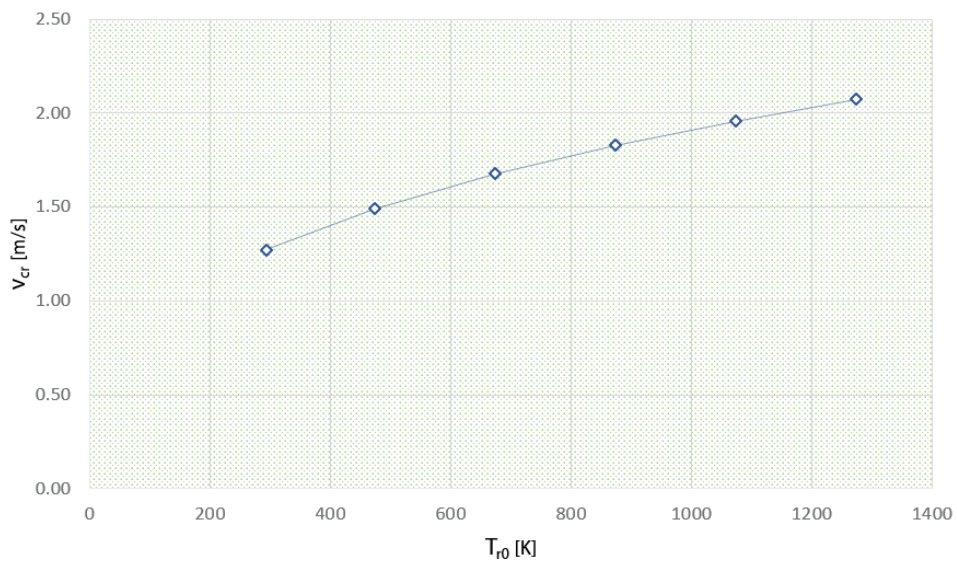


**Figure 4.8**  
*v<sub>cr</sub> vs T<sub>r0</sub>*

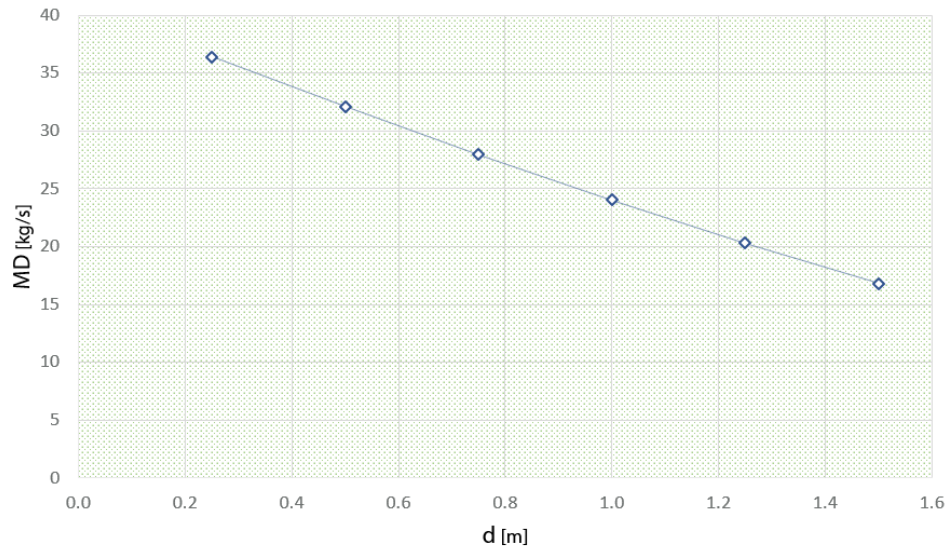


**Figure 4.9**  
*MD vs  $d_I$*

- in Fig.4.8 the relation between the critical velocity ( $v_{cr}$ ) and the smoke temperature ( $T_{r0}$ ) is shown. These quantities are related to each other in eq.4.1. A higher smoke temperature develops when a big quantity of smoke is produced. This, as highlighted at the previous point, has as a consequence a higher critical velocity needed;
- in Fig.4.9 the relation between the smoke production rate (MD) and the smoke layer thickness close to the fire location ( $d_I$ ) is shown. These quantities are related to each other in eq.4.6. For a greater smoke layer thickness less oxygen can reach the fire location and this cause the combustion to produce less combustion products;
- in Fig.4.10 the relation between the smoke layer thickness close to the fire location ( $d_I$ ) and the smoke production rate (MD) is shown. These quantities are related to each other in eq.4.5. For a higher smoke production rate, the smoke layer becomes thicker;
- in Fig.4.11 the relation between the smoke layer thickness close to the fire location ( $d_I$ ) and the critical velocity ( $v_{cr}$ ) is shown. These quantities are related to each other in eq.4.5. For a higher critical velocity more smoke is transported away from the fire location and the smoke layer thickness is smaller;
- in Fig.4.12 the relation between smoke production rate (MD) and the smoke temperature ( $T_{r0}$ ) is shown. These quantities are related to each other in eq.4.4. For a higher smoke production rate the smoke layer becomes thicker. This results in the heat been spread over a larger area and the local maximum smoke temperature been lower.

**Li et al.:** proposes a maximum ceiling temperature model dependent on a dimensionless ventilation velocity ( $u'$ ).

$$u' = \frac{u}{\left(\frac{gHRR}{r\rho_a c_a T_a}\right)^{1/3}}$$

For low values of the ventilation velocity, the fire plume is not deflected by the ventilation and the smoke production rate ( $MD$ ) is not affected. That's not the case for higher velocity where the air

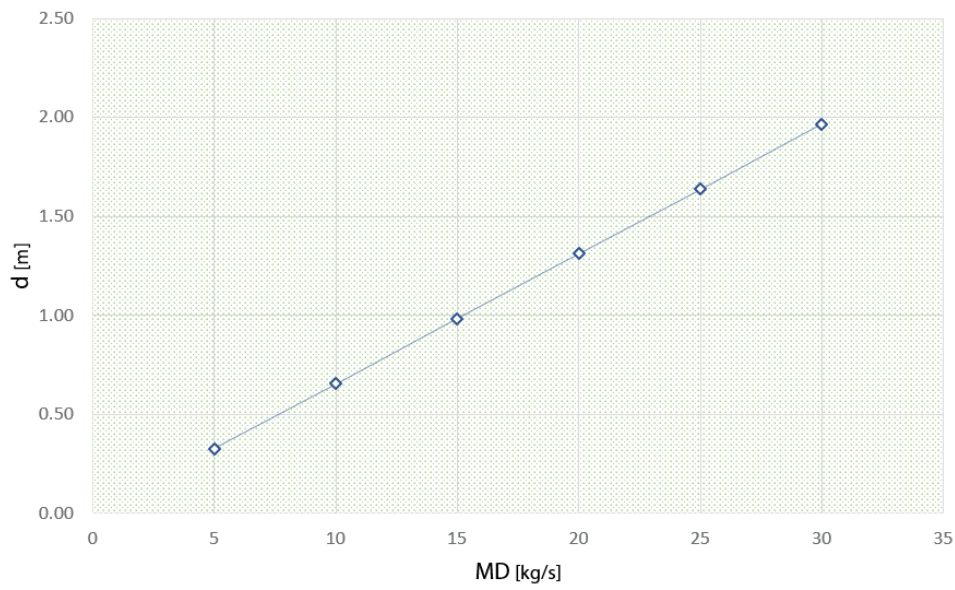


**Figure 4.10**  
 $d_I$  vs  $MD$

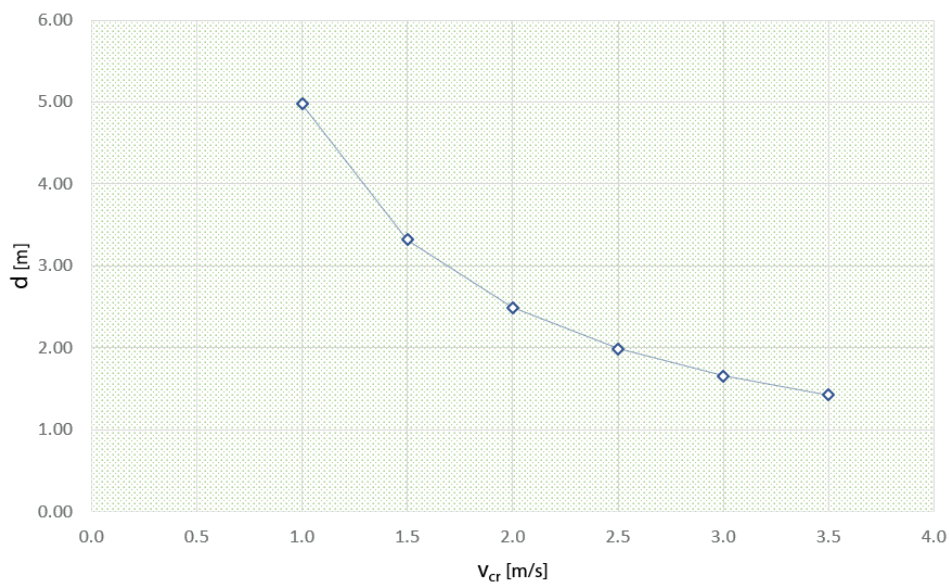


**Figure 4.11**  
 $d_I$  vs  $v_{cr}$

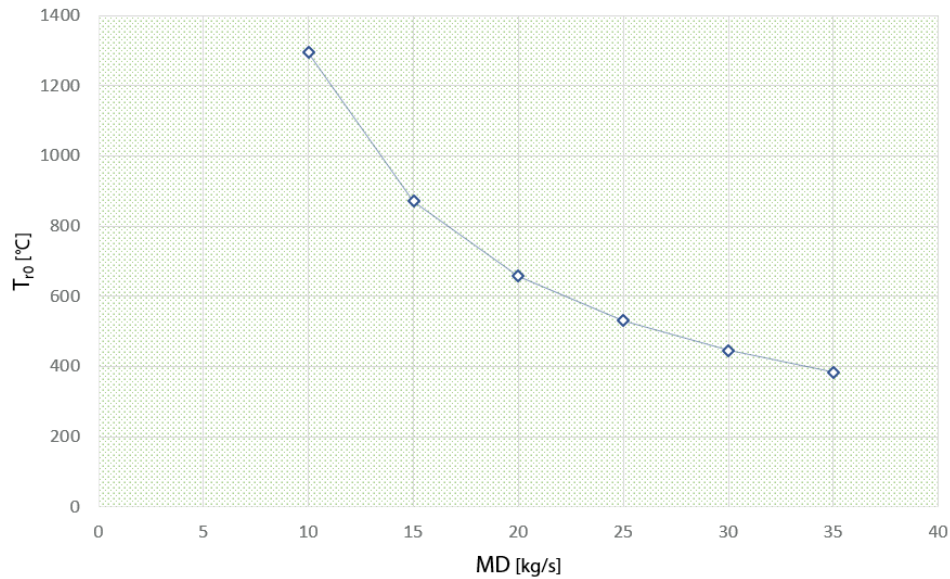


**Figure 4.12**  
*MD vs  $T_{r0}$*

entrainment ratio increases causing an increase in the smoke production. The maximum temperature ( $T_{r0}$ ) can be calculated as:

$$T_{r0} = \begin{cases} \frac{HRR}{vr^{1/3} H_{eff}^{5/3}} & u' > 0.19 \\ 17.5 \frac{HRR^{2/3}}{H_{eff}^{5/3}} & u' \leq 0.19 \end{cases} \quad (4.7)$$

## 4.2. POOL FIRES

In the case of a pool fire the model proposed by Heselden [20] could not be used, mainly for two reasons:

1. the pool fires under consideration resulted in HRR larger than the maximum allowed by Heselden model (20 – 30 MW);
2. the assumed radiation loss of 25% would not be valid for fires with such a high HRR.

It was chosen to follow a different approach and based on the combustion process of a given pool fire of fixed diameter, the HRR and subsequently the maximum ceiling temperature were derived.

### 4.2.1. FIRE DEVELOPMENT

The model used to determine the characteristics of pool fires in tunnels is semi-empirical and developed by Mégret et al. [37]. It considers the pool fire dynamics and extrapolate the values of the HRR and maximum smoke temperature. A scheme of the model is shown in Fig.4.13a and in Fig.4.13b an example of the predicted HRR based on an n-Heptane fire for different diameters of the pool is shown.

n-Heptane is considered a good candidate to simulate a generic pool fire according to Mégret et al. [37]. In order to calculate the HRR and maximum temperature of a fire of given diameter, the following procedure is followed:

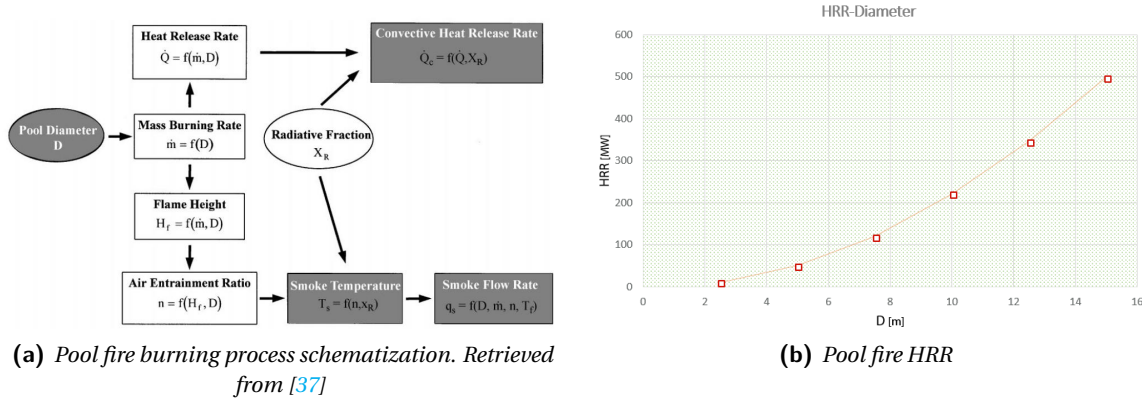


**Figure 4.13**  
Pool fire development

1. the convective part of the HRR is calculated ( $HRR_*$  [MW]). The convective part is the one considered as contributing to the temperature development of the fire:

$$HRR_* = (1 - \%_{rad}) \dot{m}_f S \Delta H_c$$

with:

- $S$ : Pool area ( $m^2$ );
- $\Delta H_c$ : *n*-Heptane net calorific value ( $44,9 \times 10^6 J kg^{-1}$ );
- the burning rate ( $\dot{m}_f$  [ $kg/m^2/s$ ]) of an *n*-Heptane pool fire is:

$$\dot{m}_f = 0.0784(1 - e^{-0.8D}) \quad (4.8)$$

2. the smoke flow rate ( $q_s$  [ $m^3/s$ ]):

$$q_s = [13.8 + 1.2n] S \dot{m}_f \frac{T_s}{T_a}$$

3. the smoke layer temperature ( $T_{r0}$ ). It is found through the sum of the released heat accumulated in the combustion products and requires the solution of a secondary order equation:

$$(30.7 + 2n)10^{-3} T_s^2 + (407 + 32.7n) T_s - (8.77 \cdot 10^5 + 9.9 \cdot 10^3 n) = 0$$

where

•

$$\begin{cases} \%_{rad} = 0.3 & D < 1 \text{ m} \\ \%_{rad} = 0.3 - \frac{0.1(D-1)}{9} & 1 \leq D \leq 10 \text{ m} \\ \%_{rad} = 0.2 & D > 10 \text{ m} \end{cases}$$

- the air entrainment ratio ( $n$  [mol(air)/mol(fuel)]), with a validity till a 15 meter diameter pool equal to:

$$11(2.13(z/R)^{0.53} - 1) \quad z/R > 0.5$$

and the effective height ( $z$  [m])

$$z = H + \frac{(h_{free} - H)}{2}$$

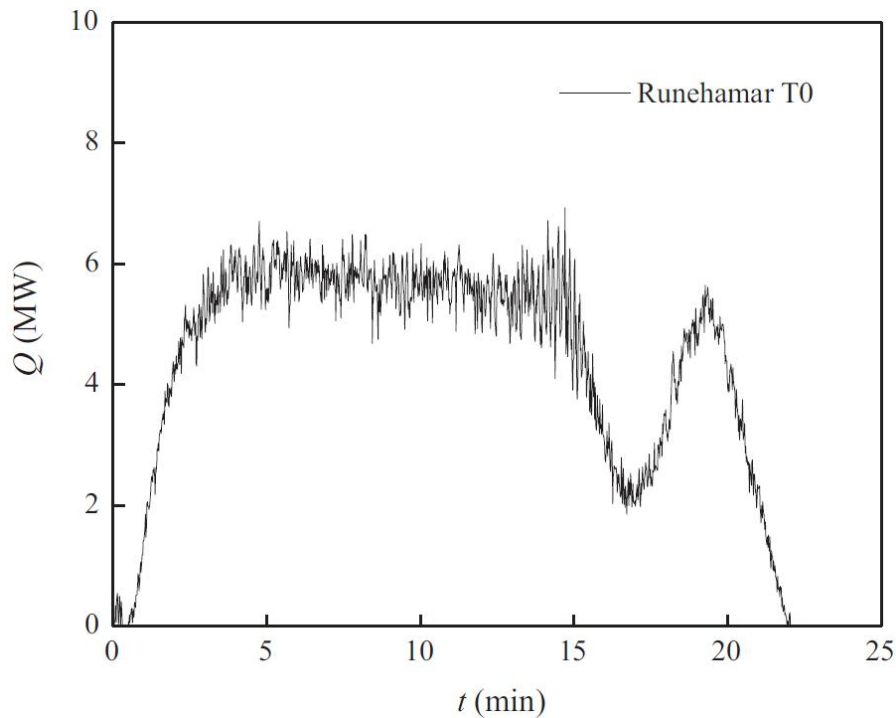


**Figure 4.14**  
*Runehamar pool fire test*

The model proposed above addresses the maximum values of HRR and ceiling temperature, nonetheless there are no info related to the early development of the fire. Pool fires can be related to the hydrocarbon fire curve. This is considered the most appropriate curve to describe the fire caused by hydrocarbon fuels. In EN1363-2 [49] the hydrocarbon curve was firstly introduced, but no relation describing the early development depending on the characteristics of the fire and geometrical configuration is present.

One of the few pool fire analysed in detail after a full-scale test is the one of the Runehamar tunnel fire test [26]. In Fig.4.14 the HRR is shown. This was estimated based on measurements of downstream gas concentrations. The test was conducted with a 200 L Diesel pool of 2,27 m diameter. The HRR takes approximately 3,75 min to reach its maximum value, which is 6 MW.

This result has been compared to the HRR prediction of the model of Mégret et al. [37] using the same inputs. The model predicts an HRR of 8,52 MW. Considering that the model assumes a perfect combustion process, which is not the case in a real situation, this is considered a good estimate.

The results predicted by Mégret et al. model [37] was compared with the indications given in the QRA [46]. In the QRA the worst scenario considered is a 200 MW fire caused by the fire spread from a tanker truck. Other scenarios are possible, but this is the maximum HRR that has been fixed. Based on the model described above the 200 MW can be achieved by a pool fire of approximately 10 m diameter.

#### 4.2.2. POOL DIMENSIONS

The pool dimensions depend on a great number of variables, such as tank leakage hole dimensions, tunnel geometry, accident location and time of ignition. In this subsection a calculation procedure is proposed in order to calculate an equivalent pool diameter for a given scenario.

Two different cases in relation with the paving inclination has been considered:

1. *Flat case*: longitudinal inclination ( $i_l = 0\%$ )-transversal inclination ( $i_t = 2,5\%$ );

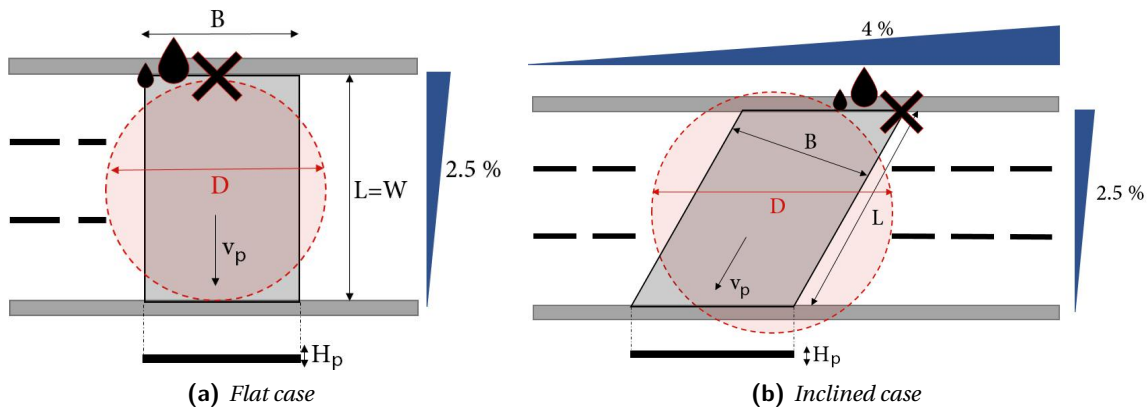


**Figure 4.15**  
Worst spillage location scenarios

2. *Inclined case*: longitudinal inclination ( $i_l = 4\%$ )-transversal inclination ( $i_t = 2,5\%$ ).

In relation with the out-flowed quantities and flow which form the pool, reference is made to the work carried out by TNO in [60]. In Table 4.1, the scenarios considered are shown.

The worst position for a fuel spillage is on the highest point along the tunnel width. In this case, the fuel has to flow towards the opposite side of the tunnel width before reaching the tunnel drainage system. Representation of the flow and reference for the following calculations is given in Fig.4.15, representing the worst scenarios for the spillage location in the inclined and flat case.

Following the calculation procedure suggested in [46], the length along which the flow travels ( $L$ ) is calculated as follow:

$$L = \sqrt{L_l^2 + L_t^2} \quad \longleftrightarrow \quad L_t = W \quad \text{and} \quad L_l = L_t \cdot \sqrt{\frac{i_l}{i_t}}$$

For the width of the out-flowed fuel ( $B$ ), reference is made to the experimental work carried out by Ingason in [24], which found:

$$B = 2.4 \cdot V^{0.46}$$

with:

- $V$ : flow in [ $\text{Ls}^{-1}$ ];
- $B$ : out-flowed fuel width in [m].

The information available are sufficient to calculate the pool area and an equivalent pool diameter:

$$A = B \cdot L \quad \longleftrightarrow \quad D = \sqrt{4 \cdot \frac{A}{\pi}}$$

with:

- $A$ : pool area [ $\text{m}^2$ ];
- $D$ : pool equivalent diameter [m].

**Table 4.1**  
*Pool formation scenarios*

	<b>Scenario</b>	<b>Out-flowed quantity [<math>m^3</math>]</b>	<b>Hole size [<math>m^2</math>]</b>	<b>Flow [<math>l/s</math>]</b>
#1	"Leakage"	0.5	$1.1 \cdot 10^{-4}$	0.3
#2	"Hole"	5	$1.1 \cdot 10^{-2}$	30
#3	"Small drop"	20	0.05	100
#4	"Big drop"	20	0.15	220

In the QRA [46] a calculation procedure to estimate the development of the pool dimensions in time is proposed.

Firstly, the thickness of the pool ( $H_p$ ) is calculated with the formula of Webber taken from [53]:

$$H_p = \left( \frac{6 \cdot v_l \cdot q_s}{\rho_l \cdot \pi \cdot g} \right)^{0.25}$$

with:

- $H_p$ : pool thickness [m];
- $v_l$ : out-flowed liquid [ $\text{kg s}^{-1}$ ];
- $\rho_l$ : liquid density [ $\text{kg/m}^3$ ];
- $g$ : gravitational acceleration [ $\text{m/s}^2$ ].

Secondly, the flow speed ( $v_p$ ) is calculated with the formula of Chézy taken from [53]:

$$v_p = C \cdot R^{0.5} \cdot I^{0.5}$$

with:

- $v_p$ : flow speed [ $\text{m s}^{-1}$ ];
- $C$ : Chézy coefficient ( $C = 18 \cdot \log \frac{12R}{k}$ )<sup>3</sup>;
- $R$ : hydraulic diameter [ $\text{m}$ ]<sup>4</sup>;
- $I$ : slope<sup>5</sup>.

In order to calculate the time needed for the pool to form:

$$t = \frac{v_p}{L}$$

<sup>3</sup>  $k$ [mm] represents the pavement roughness. It is taken equal to 0,002 m;

<sup>4</sup> It can be taken equal to the pool thickness;

<sup>5</sup> In the flat case is equal to the transversal slope. In the inclined case an average between the longitudinal and transversal slope is assumed.

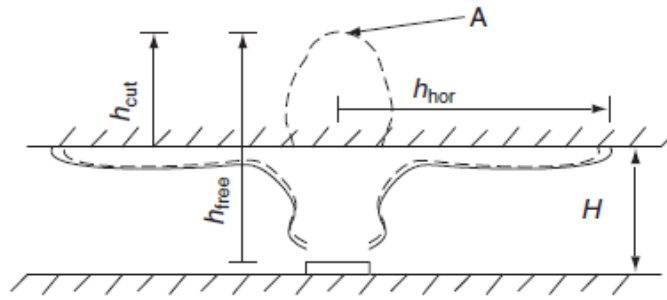


**Figure 4.16**  
Horizontal flame length. Retrieved from [6].

### 4.3. HORIZONTAL FLAME LENGTH

Heselden and Mégret et al. models do not incorporate the effect of horizontal flames caused by big fires. In case the fire generates flames longer than the effective height ( $H_{eff}$ ), the flame must bend and develop along the ceiling. Ventilation has also an influence on the flame behaviour causing a different air mixing process compared to the case of a fire without ventilation.

In order to take into account the effect of the ceiling on the flame behaviour, reference has been made to [6, ch. 13]. In case a fire cause the flame to develop horizontally along the ceiling, the horizontal flame length ( $h_{hor}$ ) can be related to the 'cut-off' flame length ( $h_{cut}$ ). The latter is equal to the difference between the flame height in open space ( $h_{free}$ ) and the effective tunnel height. Once the 'cut-off' flame height is known, the horizontal flame length can be taken equal to 1.5 times larger [6]. The flame height in open space can be calculated as [50]:

$$h_{free} = -1.02D + 0.0148 \cdot HRR^{2/5}$$

with:

- $D$ : Equivalent fire diameter (m);
- $HRR$  in (W).

A representation of the phenomenon described above is shown in Fig.4.16.

In [6, ch. 13] a formula to calculate the flame length taking into account HRR and longitudinal velocity is proposed. The formula, on the other hand, do not include the effect of tunnel width and height and is based upon the observations of full-scale tunnel fire tests. The following formula is proposed:

$$h_{hor} = 20 \cdot \left(\frac{HRR}{120}\right) \left(\frac{u}{10}\right)^{-0.4}$$

with:

- $HRR$  in (MW).

### 4.4. TEMPERATURE DECAY IN THE TUNNEL

In order to estimate the temperature decay along the tunnel reference was found in literature in the studies carried out by TNO [58] and subsequently improved by the SAVE committee [48]. The relation describing the temperature decay has been formulated in terms of a differential equation:

$$\begin{cases} A^* \frac{dT_r(x, t)}{dx} + \alpha_{tot} \cdot (T_r(x, t) - T_a) = 0 \\ T_r(0, t) = T_{r0}(0, t) \end{cases} \longleftrightarrow A^* = \frac{HRR(0, t)/2}{W \cdot (T_{r0} - T_a)}$$

with:

**Table 4.2**  
Convective heat transfer coefficients

Type of convection	$\alpha_c$ [W/m <sup>2</sup> /K]
Natural Convection	1-20
Forced Convection	40-250
Heated Water Vapour	25-100

- $A^*$ : Original heat content of the smoke stream [W m<sup>-1</sup> K<sup>-1</sup>];
- $T_r(x, t)$ : Smoke temperature at location  $x$  and time  $t$  [K];
- $\alpha_{tot}$ : lumped heat transfer coefficient (convection+radiation) [W/m<sup>2</sup>/K];
- $x$ : distance from the fire origin along the tunnel [m];

The solution of the differential equation, giving an estimate of the smoke temperature along the tunnel, is the following:

$$T_r(x, t) = (T_{r0}(0, \tau) - T_a) \cdot e^{-\left(\frac{\alpha_{tot} \cdot (T_{r0}(0, \tau) - T_a) \cdot x}{(HRR(0, \tau)/2/W)}\right)} + T_a \quad (4.9)$$

In eq.4.9 a modification proposed by Ingason in [6] has been implemented. This consists in taking the smoke temperature at the fire location at a time  $\tau$ .

$$T_{r0}(0, \tau) \quad \longleftrightarrow \quad \tau = t - \frac{x}{u}$$

The time needed for the heat to move from the fire location to the location of interest is in this way included. The effect can become important for great fires at far distances from the fire location.

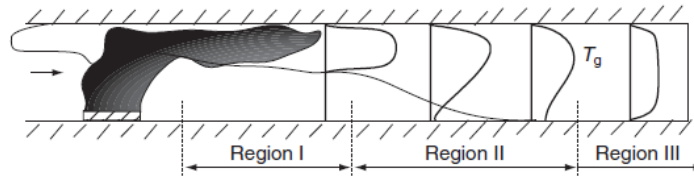
The value of the lumped heat transfer coefficient ( $\alpha_{tot}$ ) is somewhat debatable. The SAVE committee [48] suggests values in the range of 28 – 30 W/m<sup>2</sup>K. In the book of Bonacina et al. [7] the values shown in table 4.2 for the convective heat transfer coefficient are given. In the Eurocode [50] a broad indication is given to take double the value of the convective heat transfer coefficient. As it can be noticed, a lot of discussion and uncertainty is present over an appropriate choice for the lumped heat transfer coefficient value.

In order to still obtain a reasonable value, reference is made to the work conducted by Liu et al.[33]. In this work a theoretical analysis was conducted resulting in a similar formula compared to one of eq.4.9. Successively it was calibrated based on CFD numerical analysis with complementary 1/10 scaled tunnel experiment tests. The study took into account the influence of the cross section through the introduction of a cross sectional coefficient ( $\zeta$ ).

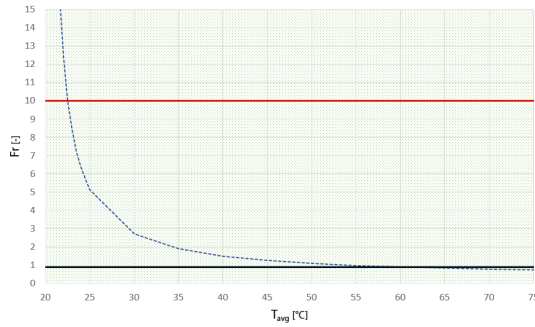
$$\zeta = \frac{A}{H^2}$$

A comparison between the temperature decay expressions of the two models was conducted and keeping the lumped coefficient as the only unknown, a value of around 300 W/m<sup>2</sup>K was found. Ventilation is usually active in a tunnel. The case can be described as a forced convection situation and looking at the values for the convective coefficient proposed in literature (Table 4.2) the found value is considered as a reasonable one.

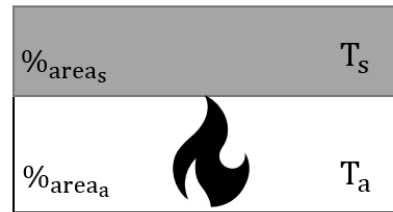
The results presented further on in relation with the temperature decay are related to the work of Liu et al.[33], due to the fact that in addition to what is shown in eq.4.9 it incorporates the effect of the cross section.



(a) Tunnel smoke layer instability schematization. Retrieved from [27].



(b) Froude number



(c) Tunnel cross section schematization

**Figure 4.17**

Smoke layer instability considerations

#### 4.5. SMOKE LAYER INSTABILITY ALONG THE TUNNEL

A theoretical model was proposed by Newman [40] in order to describe the smoke layer instability in tunnels. This was never tested in full-scale tests, but it is anyway investigated in order to have a better understanding and insight of what might happen in terms of smoke instability. At the same time the possible lack of oxygen at the fire location can be studied.

Instability can be schematized as shown in Fig.4.17a. Close to the fire location, where the temperatures are higher, the smoke layer stays stratified at the top part of the tunnel. While cooling down, along the length of the tunnel, the smoke layer tends to mix with the cold air blowing from the opposite direction (which is supplying oxygen at the fire location) and under certain conditions it might become unstable and spread over the entire cross section of the tunnel.

The instability phenomenon, according to Newman [40], can be linked to the Froude number which is related to the tunnel cross sectional average temperature as shown in the equation below:

$$Fr = \frac{u_{avg}^2}{1.5 \cdot (\Delta T_{avg} / T_{avg}) g H}$$

with:

- average gas temperature over the entire tunnel cross-section ( $T_{avg}$ );
- average gas temperature rise ( $\Delta T_{avg} = T_{avg} - T_a$ );
- 

$$u_{avg} = u \cdot \frac{T_{avg}}{T_a}$$

The smoke layer temperature along the tunnel is known. It is assumed that the temperature of the air below the smoke layer is equal to the ambient temperature. Assuming a constant smoke layer thickness equal to the one calculated close to the fire location ( $d_l$ ), it is possible to calculate the average temperature over the cross section. In agreement with Fig.4.17c, the average temperature over the cross section is equal to:

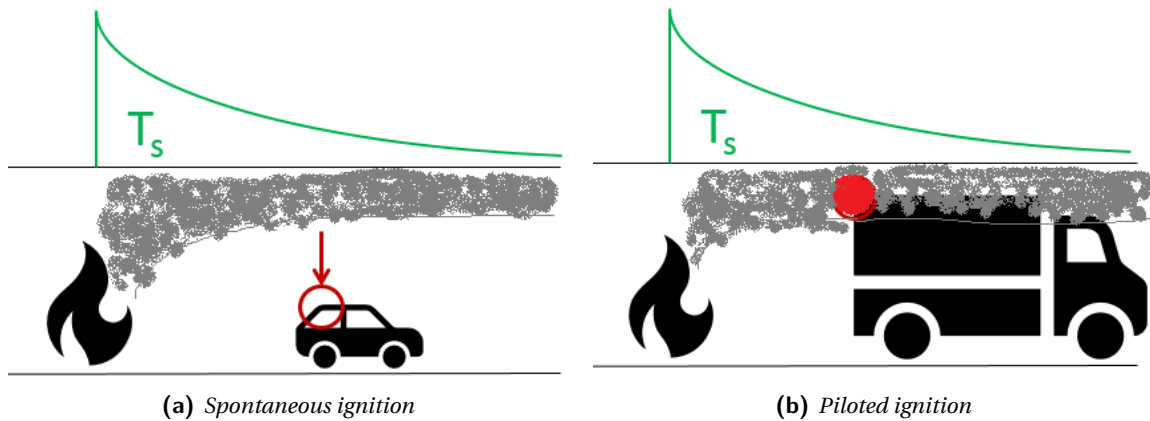


**Figure 4.18**  
Fire spread mechanism representation

$$T_{avg} = \%_{area1} \cdot T_s + \%_{area2} \cdot T_a$$

The assumption of a constant smoke layer thickness along the tunnel is not fully correct, but is conservative and necessary to carry out some preliminary calculations. In reality, the thickness of the smoke layer tends to increase further away from the fire causing the average temperature value to increase. For a higher average temperature the smoke layer keeps stable for a longer distance from the fire.

In Fig.4.17b, the Froude number as function of the temperature for a given tunnel cross section is shown. For Froude numbers larger than a value of 10 a clear stratification is present. For Froude values lower than 0.9 there is instability. In between the two extremes there is an intermediate situation. It is possible to see that further from the fire the average temperature over the cross section will decrease to such a value to cause the smoke layer to become unstable and spread over the whole tunnel cross section.

#### 4.6. FIRE SPREAD AND INCREASED AMBIENT TEMPERATURE

Possible causes of fire spread have been explained in subsection 3.3.1. The most common cause of fire spreading is the *remote ignition* [6]. This can occur due to *spontaneous ignition* or *piloted ignition*, both caused either by convective or radiative heat fluxes. The piloted ignition represents a remote ignition of an already pre-heated material. In literature these mechanisms are commonly related to the minimum smoke layer temperature ( $T_r$ ) above the object causing its ignition. According to [6], for a spontaneous ignition the exposure to convective heat fluxes is governing. A critical smoke layer temperature of 500°C is considered. For the piloted ignition the radiative heat fluxes are governing with a critical smoke temperature of 300°C to 410°C. In [27] critical smoke layer temperatures for specific materials are suggested on the base of the study of full-scale tests results. For wood elements a critical smoke temperature of 700°C is suggested if the object is at the floor level and 600°C if it is located at mid tunnel height. For plastic materials located at the floor level a critical temperature of 490°C is indicated.

Taking into consideration the information given above and referring to Fig.4.18 it is suggested to consider the piloted ignition as a cause of fire spread when part of a vehicle is touched by the smoke layer. In the case of a vehicle of reduced height, entirely located out of the smoke layer, the spontaneous ignition case is considered more representative.

The following critical smoke layer temperatures are considered<sup>6</sup>:

- *Piloted ignition*:  $T_r \approx 355^\circ\text{C}$ ;
- *Spontaneous ignition*:  $T_r \approx 500^\circ\text{C}$ ;

In subsection 4.7 a temperature distribution model in the tunnel during a fire has been proposed. Making use of this model, for every moment in time, it is possible to estimate what is the minimum distance which cause a vehicle to ignite. Eventually it is possible to estimate the minimum distance needed for a vehicle to avoid ignition during an occurring fire.

The ambient temperature at the fire location of a vehicle igniting due to the fire spread from another location can also be estimated. In order to conduct this calculation, the following info need to be retrieved:

- the time at which the vehicle ignite. This occurs when the smoke critical temperature is reached in proximity of the part of the vehicle closer to the fire;
- the vehicle length;
- the temperature distribution in the tunnel at the time of ignition.

In analogy with what has been done in section 4.5, the average gas temperature over the entire tunnel cross-section can be calculated in the portion of the tunnel occupied by the vehicle. Taking the average of this quantity along the length of the vehicle an estimate of the ambient temperature at which the vehicle ignites can be found.

#### 4.7. TEMPERATURE HEAT MAPS

Based on the considerations explained above, it is possible to represent a smoke layer temperature heat map in the tunnel. In order to obtain the heat maps, the following information are required and assumptions have been made:

- for all the type of fires considered (HGV fire, car fire, pool fire), the HRR profile, maximum HRR and time till the maximum HRR need to be known. Those can be found in subsection 4.1.1;
- the vehicles and pool fire dimensions can be modelled according to subsection 4.1.2, 4.2.2. In the case of pool fires, the fire location can be assumed at the level of the ground floor. The vehicle fire location can be assumed assumed at half height of the vehicle considered. From the fire location a coordinate ( $x$ ) can be defined, developing outwards from the fire along the tunnel length. The chosen direction is not relevant. The ventilation is not considered in the model and thus, the smoke layer develops symmetrically;
- the maximum ceiling temperature, related to the maximum HRR, can be calculated according to the Heselden work (subsection 4.1.3) for vehicle fires and Mégret et al. (subsection 4.2.1) for pool fires;
- at the fire location ( $x = 0$ ), the temperature profile in time can be assumed proportional to the HRR profile taking as maximum temperature the one calculated in the previous point;
- the temperature at a given location in the tunnel can be assumed constant along the tunnel width, while the temperature decay along the tunnel can be modelled according to subsection 4.4;

<sup>6</sup>the piloted ignition critical temperature is taken equal to the average between the extreme values proposed in [6]

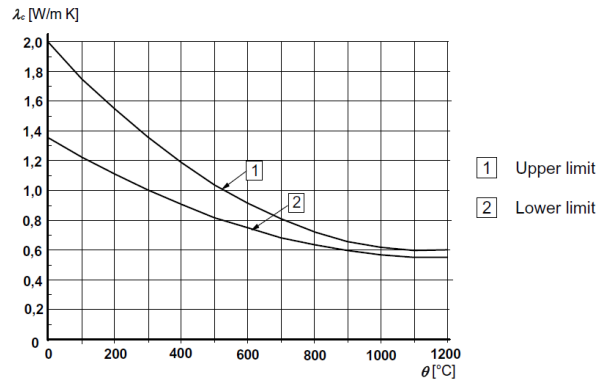


**Figure 4.19**  
Concrete thermal conductivity. Retrieved from [52].

- the results can be plotted in a temperature heat map with time on the axis of abscissae and the distance from the fire location on the axis of ordinates;
- for big fires, the flame develops horizontally along the ceiling. It can be assumed that, in the case of horizontal flames, the maximum temperature keeps constant along the entire ceiling length touched by the flame. The calculation of the horizontal flame length is shown in subsection 4.3. From the tip of the flame, the temperature decay can be modelled.

#### 4.8. LINING TEMPERATURE PROFILE

The heat flux through a concrete tunnel element can be modelled by Fourier's law, which is represented with a differential equation. For the case under examination, the one dimensional version of the differential equation is sufficient and can be written as [8]:

$$\frac{\delta(\rho_c c_c T)}{\delta t} - \frac{\delta^2(\lambda_c T)}{\delta^2 x} = 0 \quad (4.10)$$

The concrete density and specific heat capacity are assumed constants with temperature. The density is taken equal to  $2400 \text{ kg/m}^3$  according to [52] and the specific heat equal to  $800 \text{ J kg}^{-1} \text{ K}^{-1}$  [52]. The concrete thermal conductivity can be taken equal to  $1,5 \text{ W m}^{-1} \text{ K}^{-1}$  [52].

Considering the above mentioned constant quantities, eq.4.10 can be rewritten as:

$$\rho_c c_c \cdot \frac{\delta T}{\delta t} - \lambda_c \cdot \frac{\delta^2 T}{\delta^2 x} = 0 \quad (4.11)$$

In the following thesis the possibility of modelling a temperature dependent concrete thermal conductivity ( $\lambda_c(T)$ ) has also been investigated. Reference has been made to Eurocode 2, part 1-2 [52] and an average between the proposed upper and lower limit has been taken. The temperature dependent thermal conductivity is shown in Fig.4.19. In this case eq.4.10 is rewritten as:

$$\rho_c c_c \cdot \frac{\delta T}{\delta t} - \left( \frac{\delta \lambda_c}{\delta x} \cdot \frac{\delta T}{\delta x} + \lambda_c \cdot \frac{\delta^2 T}{\delta^2 x} \right) = 0 \quad (4.12)$$

The analytical solution of the differential equation can be found imposing one initial condition and two boundary conditions. In case of fire, the initial condition is represented by an ambient temperature applied to the element. Three different types of boundary conditions are usually applied:

1. the smoke temperature is applied directly at the edge of the element;

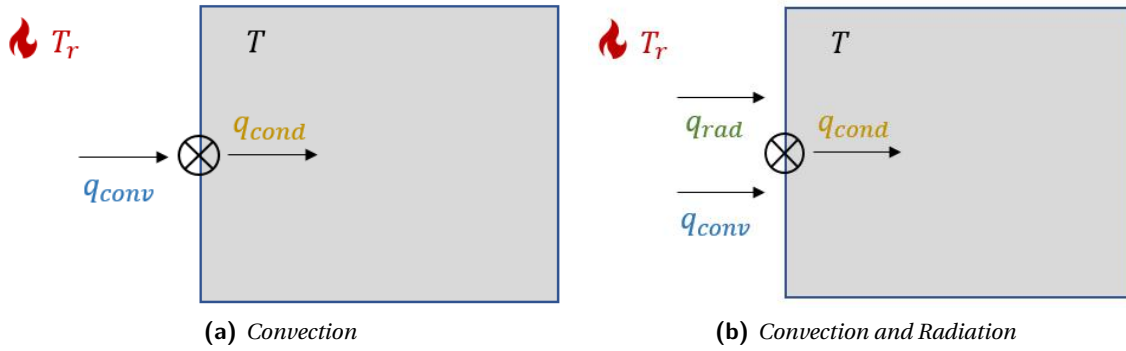


**Figure 4.20**  
Heat transfer B.C.

2. the convective boundary condition is applied, imposing a heat transfer from the smoke to the element surface through convection. A sketch representing the equilibrium used to write down the B.C. is shown in Fig.4.20a. The B.C. can be written as such:

$$\underbrace{-\lambda_c \frac{\delta T}{\delta x}}_{cond} = \underbrace{\alpha_c (T_s - T)}_{conv} \quad (4.13)$$

3. the convective and radiative boundary condition is applied, imposing a heat transfer from the smoke to the element surface through convection and radiation. A sketch representing the equilibrium used to write down the B.C. is shown in Fig.4.20b. The B.C. can be written as such:

$$\underbrace{-\lambda_c \frac{\delta T}{\delta x}}_{cond} = \underbrace{\alpha_c (T_r - T)}_{conv} + \underbrace{\alpha_r (T_r^4 - T^4)}_{rad} \quad (4.14)$$

with:

$$\alpha_r = F_{s-c} \cdot \sigma_n$$

where:

- the smoke-concrete view factor ( $F_{s-c}$ ) being assumed as equal to one;
- $\sigma_n = 5,67 \times 10^{-8} \text{ W/m}^2/\text{K}^4$ .

The radiation from the concrete surface to the smoke is neglected.

#### 4.8.1. NUMERICAL SOLUTION

The system of differential equations and B.C. is approximated numerically using the Finite Difference Method. In such a way the solution of the system is possible through its implementation in a commercial software such as Excel.

Considering an increasing coordinate system going from left to right, with the smoke acting on the left side and on its right the concrete element, the following approximations can be done:

- the D.E. of eq.4.11 can be rewritten as such:

$$\rho_c c_c \cdot \frac{T_i^{t+1} - T_i^t}{\Delta t} - \lambda_c \cdot \frac{T_{i+1}^t - 2T_i^t + T_{i-1}^t}{\Delta x^2} = 0$$

with a numerical stability condition:

$$\frac{\lambda_c}{\rho_c c_c} \cdot \frac{\Delta t}{\Delta x^2} < 0.5$$

- the D.E. of eq.4.12 can be rewritten as such:

$$\rho_c c_c \cdot \frac{T_i^{t+1} - T_i^t}{\Delta t} - \left( \frac{\lambda_{i+1}^t - \lambda_{i-1}^t}{2\Delta x} \cdot \frac{T_{i+1}^t - T_{i-1}^t}{2\Delta x} + \lambda \cdot \frac{T_{i+1}^t - 2T_i^t + T_{i-1}^t}{\Delta x^2} \right) = 0$$

- the B.C. of eq.4.13 can be rewritten as such:

$$-\lambda_c \frac{T_{i+1}^t - T_i^t}{\Delta x} = \alpha_c (T_r^t - T_i^t)$$

- the B.C. of eq.4.14 can be rewritten as such:

$$-\lambda_c \frac{T_{i+1}^t - T_i^t}{\Delta x} = \alpha_c (T_r^t - T_i^t) + \alpha_r (T_r^{4t} - T_i^{4t})$$

- the B.C. for the smoke temperature directly applied on the concrete surface:

$$T_r = T_i$$

#### 4.8.2. VERSIONS

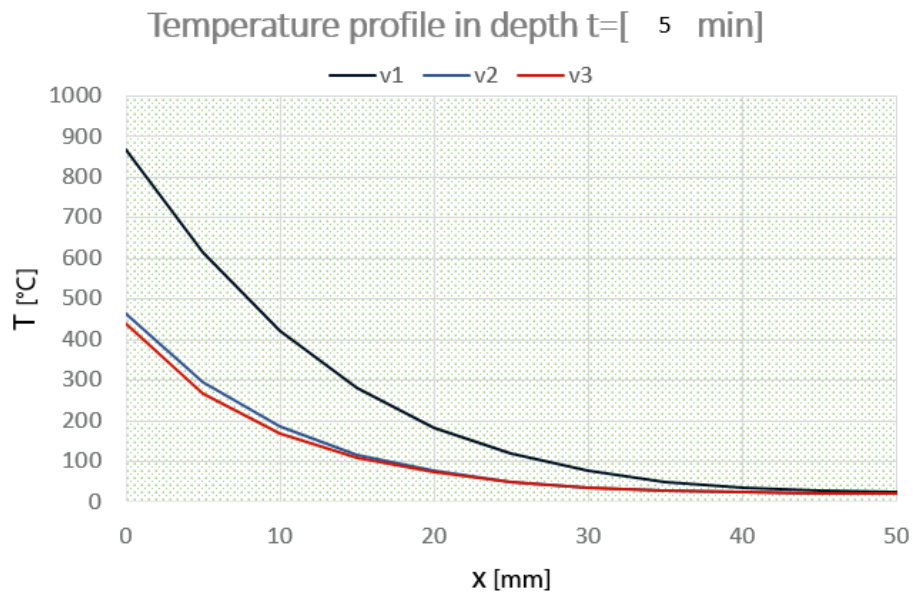
Three different temperature profiles have been considered. Each one taking into consideration different B.C. The different versions differs as follows:

- $\nu 1$ : Temperature development in time (Fire curve) directly applied at the surface;
- $\nu 2$ : introduction of the convective and radiative fluxes boundary conditions at the lining surface exposed to the fire;
- $\nu 3$ : same as  $\nu 2$ , but with the temperature dependent concrete thermal conductivity included ( $\lambda(T)$ ).

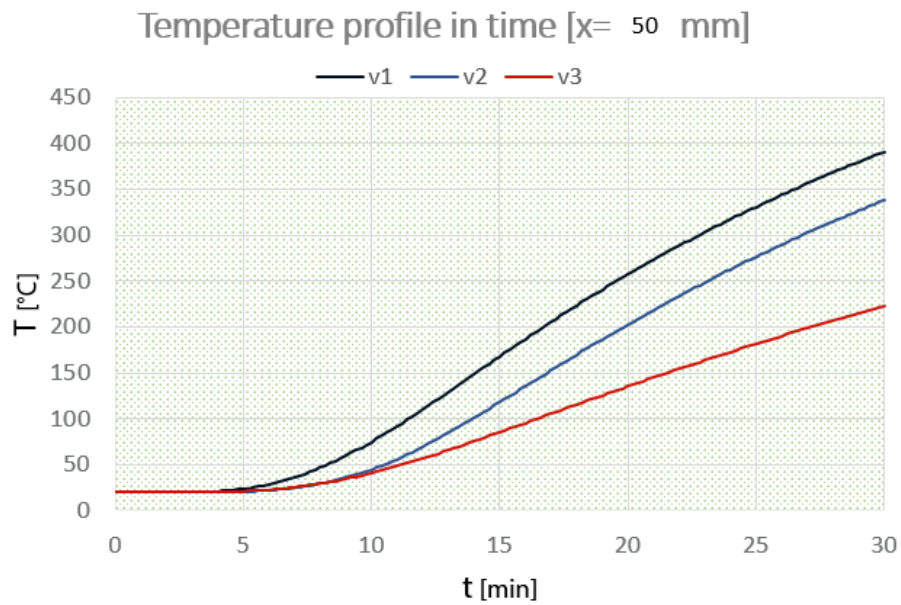
In Fig.4.21 the results obtained using the three different versions using the same assumptions are shown. The following assumptions apply for the elaboration of the results:

- .....

*The  $\nu 3$  version of the temperature profile is the one including more aspects and modelling the reality in a more realistic way. Comparing the 3 versions, a great advantage can be achieved from the 3rd version in terms of reduced temperature profiles in the concrete. It was then decided to only use the  $\nu 3$  version. The analysis and results that will be shown further on in the thesis will be based on the  $\nu 3$  version.*



(a) Temperature profile along cross section at given time



(b) Temperature profile in time at given location

**Figure 4.21**  
Cross section temperature gradients

## 4.9. RESULTS

In this section the results of the different fire dynamics aspects exposed in this chapter are shown. The scenarios that have been considered in the elaboration of the following results are mostly based on a flat 2 lanes tunnel and the events considered are:

- car fire;
- HGV-Low Q fire;
- HGV-High Q fire;
- Pool fire of 10,3 m diameter;
- Pool fire of 12,3 m diameter.

The choice of the two pool fires considered is based upon the considerations made in subsection 4.9.2. Firstly a diameter equivalent to the tunnel width (10,3 m) has been considered. Secondly, a worst-case scenario with the maximum equivalent pool fire diameter in a flat two lane tunnel generated by a leakage from a hole (scenario #2) with ignition time fixed after 1 min has been elaborated.

### 4.9.1. TEMPERATURE DEVELOPMENT

The vehicle temperature development of different vehicles has been investigated using the modified "Heselden" approach exposed in subsection 4.1.3. In Fig.4.22 the maximum temperature development of a car and both an HGV with low and high energy content have been compared. It can be noted that the temperature development of a car is negligible when compared with HGVs. The following hypothesis were used:

- HRR from subsection 4.1.1;
- $T_a = 20^\circ\text{C}$ ;
- $\rho_a = 1,217\text{ kg/m}^3$ ;
- $c_a = 1\text{ KJ/kg/K}$ ;
- two lanes tunnel ( $W = 10,3\text{ m}, H = 5,1\text{ m}$ ).

The effect of the tunnel cross section, in particular tunnel height and width, has been studied. In Fig.4.23 the results of this study are shown. It can be noted that the cross section has a considerable effect on the maximum temperature, in particular the height.

### 4.9.2. POOL DIMENSIONS

The maximum pool dimensions under different scenarios have been calculated according to the procedure shown in subsection 4.2.2. In Table 4.3 the maximum diameter for different scenarios are shown, where the scenarios causing the pool diameter to be lower than 15 m are highlighted in bold characters. This is related to the limits set by the fire development model described in subsection 4.2.1 where only pool with a diameter lower than 15 m can be calculated. The following scenarios variations have been investigated:

- **w1**: 1 lane tunnel ( $W=6.8\text{ m}$ );
- **w2**: 2 lane tunnel ( $W=10.3\text{ m}$ );
- **w3**: 3 lane tunnel ( $W=13.8\text{ m}$ );

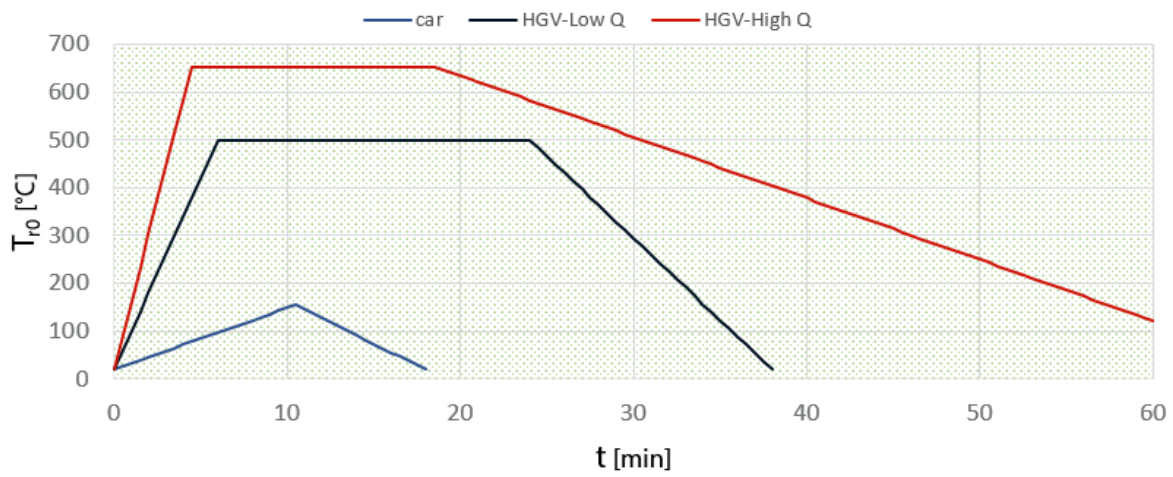
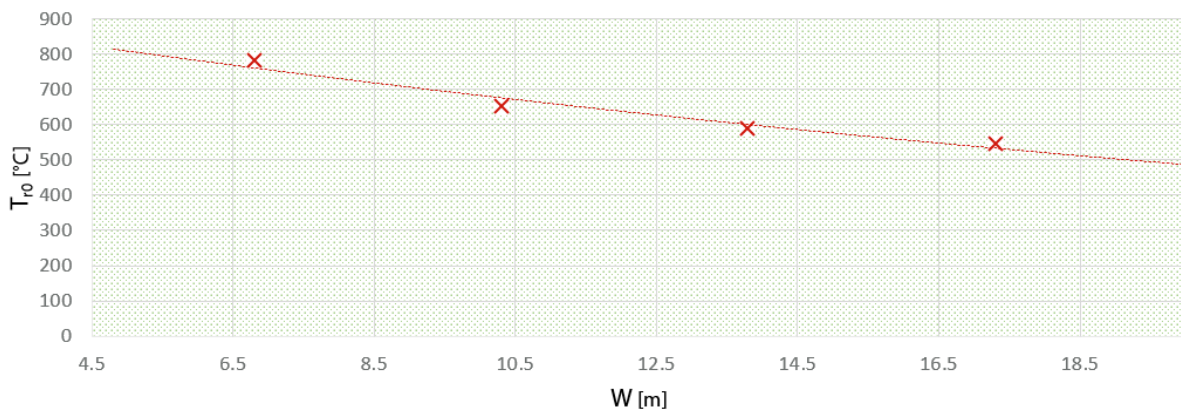
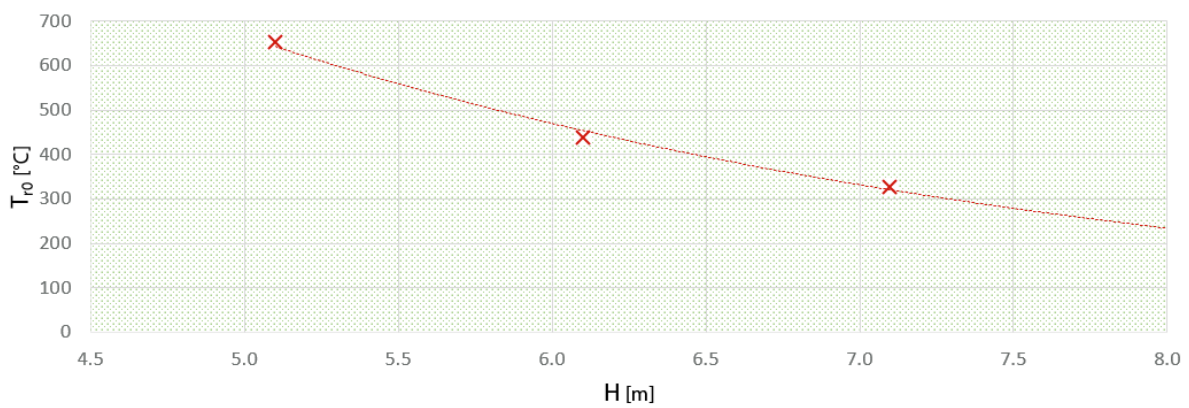


**Figure 4.22**  
*Vehicles maximum temperature*



**(a)** *Tunnel width variation*



**(b)** *Tunnel height variation*

**Figure 4.23**  
*Maximum ceiling temperatures-Cross section variations*



**Table 4.6**  
*Horizontal flame length-Vehicle fire and pool fire*

Fire	Hor. Flame Length [m]
Car	0
HGV-Low Q	4
HGV-High Q	6.2
Pool (D=10.3 m)	26.1
Pool (D=12.3 m)	30.6

is shown. The following hypothesis were used:

- $T_a = 20^\circ\text{C}$ ;
- $\rho_a = 1,217\text{kg/m}^3$ ;
- $H = 5,1\text{m}$ .

4

#### 4.9.4. HORIZONTAL FLAME LENGTH

The horizontal flame length has been compared between vehicle fires and pool fires according to the analytical model shown in subsection 4.3. In Table 4.6 the results are shown. It can be noted that pool fires cause a significantly bigger flame length compared to vehicle ones. This is related to the higher HRR that pool fires of 10.3 and 12.3 m diameter have. The following hypothesis were used:

- vehicles HRR from subsection 4.1.1;
- pool HRR from subsection 4.2.1;
- vehicles dimensions from subsection 4.1.2;
- $H = 5,1\text{m}$ .

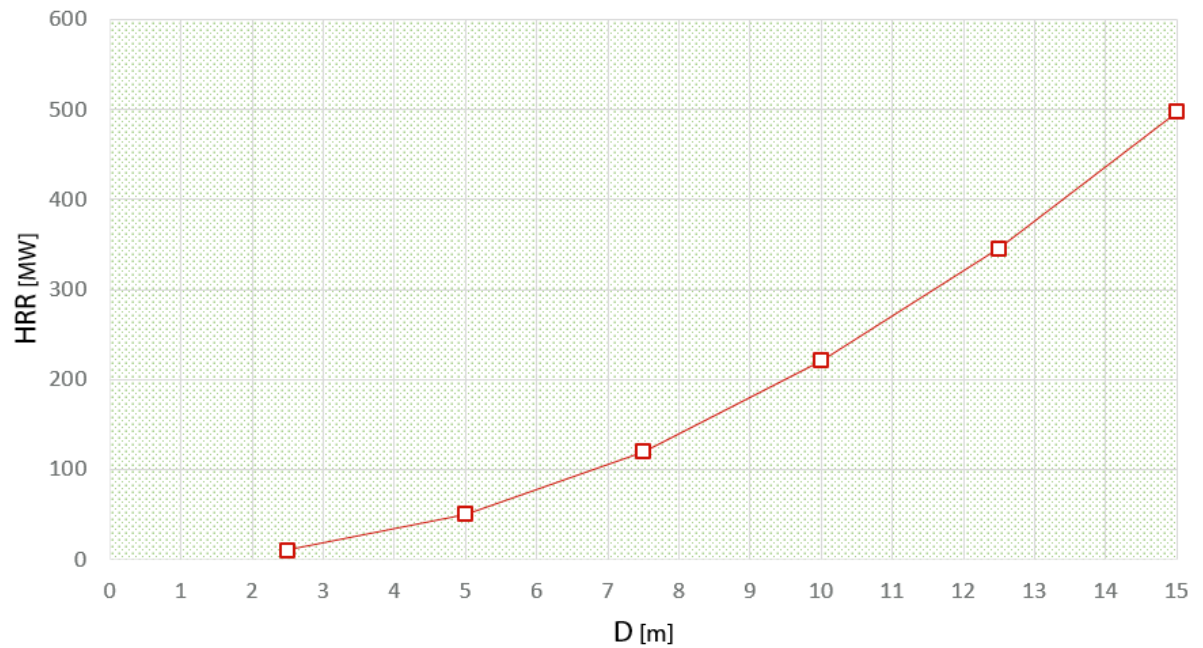
#### 4.9.5. TEMPERATURE DECAY

The temperature decay of the smoke layer along the tunnel is shown in Fig.4.25 for different fire scenarios. The following hypothesis were used:

- temperature profile corresponding to the moment in time when the highest maximum temperature was calculated for the different vehicles;
- vehicles HRR from subsection 4.1.1;
- pool HRR from subsection 4.2.1;
- $T_a = 20^\circ\text{C}$ ;
- $\rho_a = 1,217\text{kg/m}^3$ ;
- $c_a = 1\text{KJ/kg/K}$ ;
- two lanes tunnel ( $W = 10,3\text{m}$ ,  $H = 5,1\text{m}$ ).



(a) Maximum temperature



(b) Maximum HRR

**Figure 4.24**  
*Pool fire development*

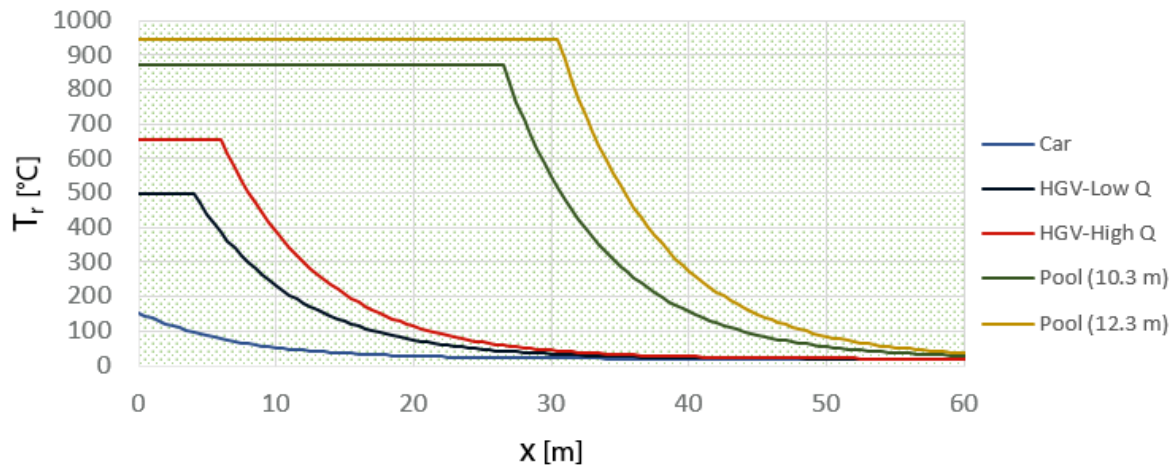


**Figure 4.25**  
*Temperature decay-Different scenarios*

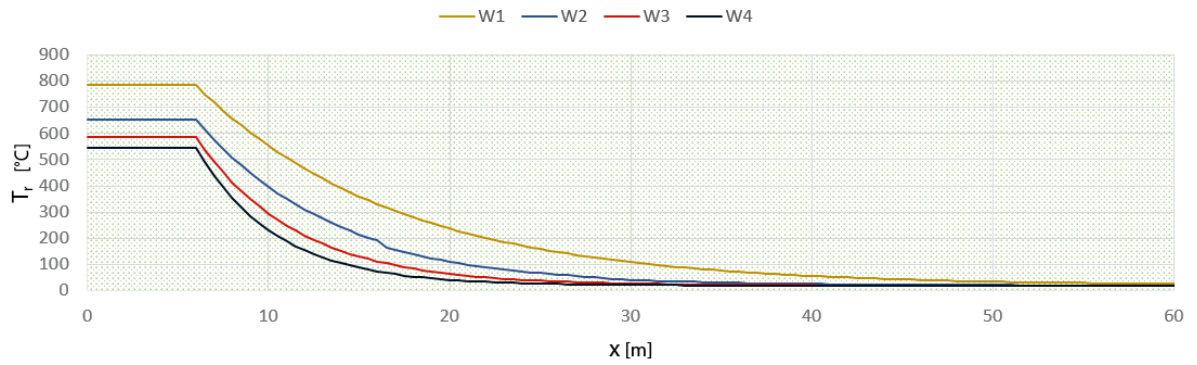
A study taking into consideration the effect of different cross sections has been carried out and the results are shown in Fig.4.26. The analytical model exposed in subsection 4.4 has been used to elaborate this calculations. The following hypothesis were used:

- HGV-High Q HRR from subsection 4.1.1;
- temperature profile corresponding to the moment in time when the highest maximum temperature;
- $T_a = 20^\circ\text{C}$ ;
- $\rho_a = 1,217\text{kg/m}^3$ ;
- $c_a = 1\text{KJ/kg/K}$ ;
- two lanes tunnel with either the height or width fixed ( $W = 10,3\text{m}, H = 5,1\text{m}$ ).

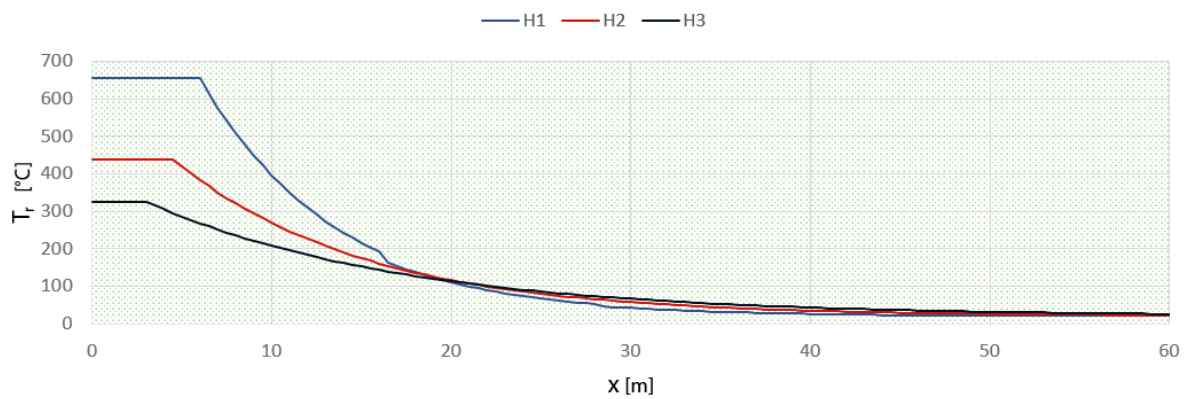
#### 4.9.6. SMOKE LAYER INSTABILITY

The smoke layer instability phenomenon has been studied making use of the analytical model exposed in subsection 4.5. A study indicating the maximum tunnel length above which clear smoke stratification is not present any more ( $l1$ ) and length above which smoke layer instability is predicted ( $l2$ ) has been conducted. The scenario considers a tunnel fire igniting at half tunnel length. In Table 4.7 the tunnel lengths for different fire typologies are listed. The following hypothesis were used:

- vehicles HRR from subsection 4.1.1;
- pool HRR from subsection 4.2.1;
- $T_a = 20^\circ\text{C}$ ;
- $\rho_a = 1,217\text{kg/m}^3$ ;
- $c_a = 1\text{KJ/kg/K}$ ;
- $u = 0,5\text{ms}^{-1}$ ;



(a) Width variation



(b) Height variation

**Figure 4.26**

Temperature decay-Cross section variation

**Table 4.7**

Smoke layer instability for different fire typologies

Vehicle	l1 [m]	l2 [m]
Car	69	105
HGV-Low Q	97	133
HGV-High Q	106	142
Pool (10.3 m)	151	186
Pool (12.3 m)	160	196

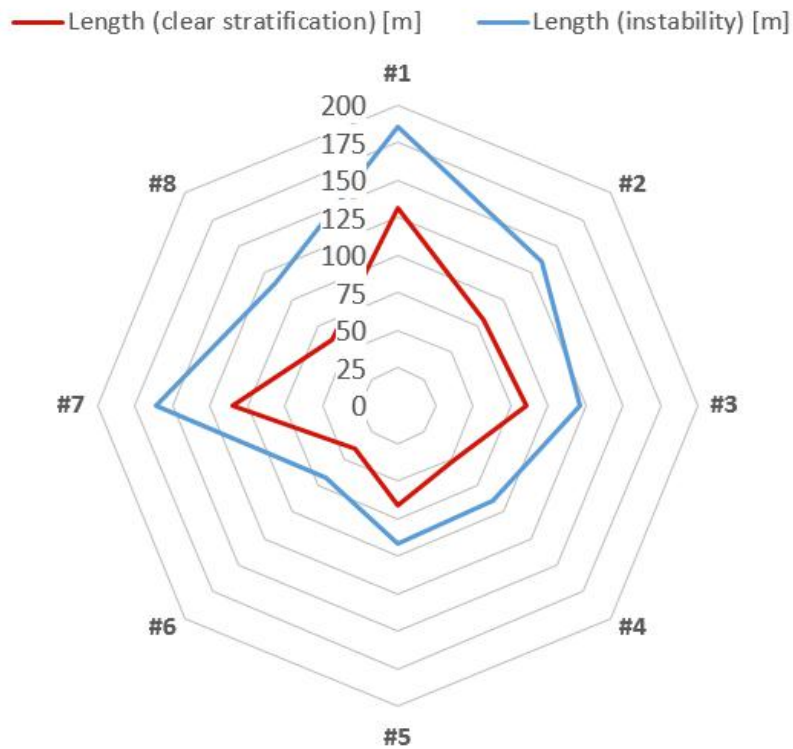


**Figure 4.27**  
Smoke layer instability for different scenarios

- two lanes tunnel ( $W = 10,3\text{ m}, H = 5,1\text{ m}$ ).

In Fig.4.27 a radar chart showing the smoke instability behaviour for different scenarios involving an HGV-High Q fire is shown. The characteristics of the considered scenarios are:

- #1:  $H=5,1\text{ m}, W=6,8\text{ m}, v=0,5\text{ m s}^{-1}$ ;
- #2:  $H=5,1\text{ m}, W=6,8\text{ m}, v=1,5\text{ m s}^{-1}$ ;
- #3:  $H=5,1\text{ m}, W=10,3\text{ m}, v=0,5\text{ m s}^{-1}$ ;
- #4:  $H=5,1\text{ m}, W=10,3\text{ m}, v=1,5\text{ m s}^{-1}$ ;
- #5:  $H=5,1\text{ m}, W=13,8\text{ m}, v=0,5\text{ m s}^{-1}$ ;
- #6:  $H=5,1\text{ m}, W=13,8\text{ m}, v=1,5\text{ m s}^{-1}$ ;
- #7:  $H=6,1\text{ m}, W=10,3\text{ m}, v=0,5\text{ m s}^{-1}$ ;
- #8:  $H=6,1\text{ m}, W=10,3\text{ m}, v=1,5\text{ m s}^{-1}$ .

In Fig.4.28 a parametric study over the smoke layer instability has been conducted. The following hypothesis were used:

- HGV-High Q HRR from subsection 4.1.1;
- $T_a = 20^\circ\text{C}$ ;

- $\rho_a = 1,217 \text{ kg/m}^3$ ;
- $c_a = 1 \text{ KJ/kg/K}$ ;
- the independent parameter of the different graphs fixed to: ( $u = 0,5 \text{ ms}^{-1}$ ,  $W = 10,3 \text{ m}$ ,  $H = 5,1 \text{ m}$ ).

#### 4.9.7. FIRE SPREAD

The fire spread mechanism has been studied making use of the procedures explained in subsection 4.6. In Fig.4.29 the HGV High Q ignition time as a function of the distance from a fire already occurring is shown. Various initial fire source have been considered and namely are: HGV-High Q, pool(10.3m), pool(12.3m). The scenarios considered are:

- **HGV-HGV**: fire originating from a HGV with high energy content spreading to a second vehicle with the same characteristics;
- **pool(10.3)-HGV**: fire originating from a pool fire of 10,3m diameter spreading to a second vehicle being an HGV with high energy content;
- **pool(12.3)-HGV**: fire originating from a pool fire of 12,3m diameter spreading to a second vehicle being an HGV with high energy content.

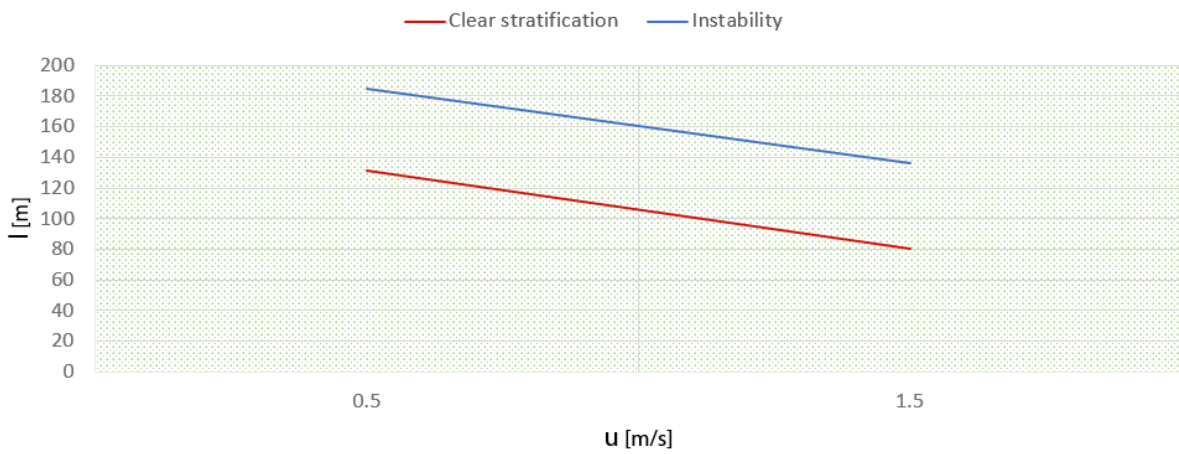
The following hypothesis were used:

- vehicles HRR from subsection 4.1.1;
- pool HRR from subsection 4.2.1;
- $T_a = 20^\circ\text{C}$ ;
- $\rho_a = 1,217 \text{ kg/m}^3$ ;
- $c_a = 1 \text{ KJ/kg/K}$ ;
- two lanes tunnel ( $W = 10,3 \text{ m}$ ,  $H = 5,1 \text{ m}$ ).

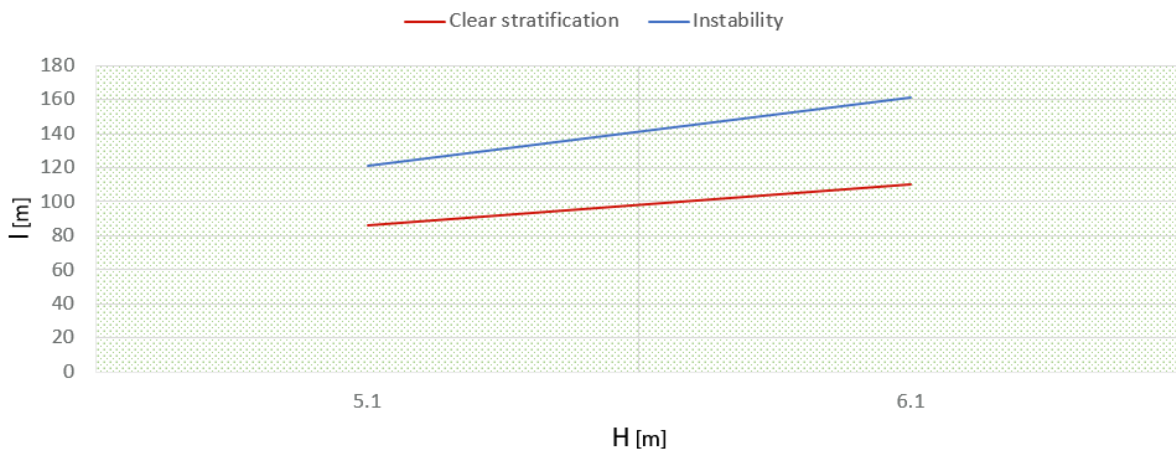
In the particular scenario HGV-HGV, the highest ambient temperature at the moment of ignition of the second vehicle has been calculated according to what has been highlighted in subsection 4.6. Based upon this starting temperature, the temperature development of the second vehicle has been calculated using the modified version of "Heselden" model. In Fig.4.30 the comparison between the HGV igniting at two different ambient temperatures is shown. For the vehicle igniting at an ambient temperature of  $20^\circ\text{C}$ , the following hypothesis were used:

- HGV-High Q HRR from subsection 4.1.1;
- $T_a = 20^\circ\text{C}$ ;
- $\rho_a = 1,217 \text{ kg/m}^3$ ;
- $c_a = 1 \text{ KJ/kg/K}$ ;
- two lanes tunnel ( $W = 10,3 \text{ m}$ ,  $H = 5,1 \text{ m}$ ).

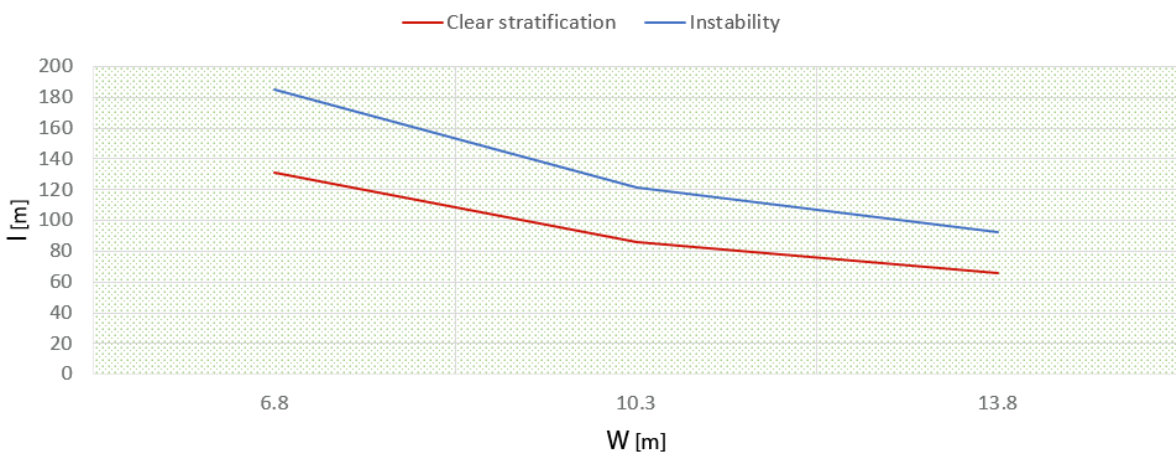
For the vehicle igniting at an ambient temperature of  $70^\circ\text{C}$ , the same hypothesis were applied with the exception of the following:



(a) Ventilation variation



(b) Tunnel height variation



(c) Tunnel width variation

**Figure 4.28**  
Smoke layer instability parametric study

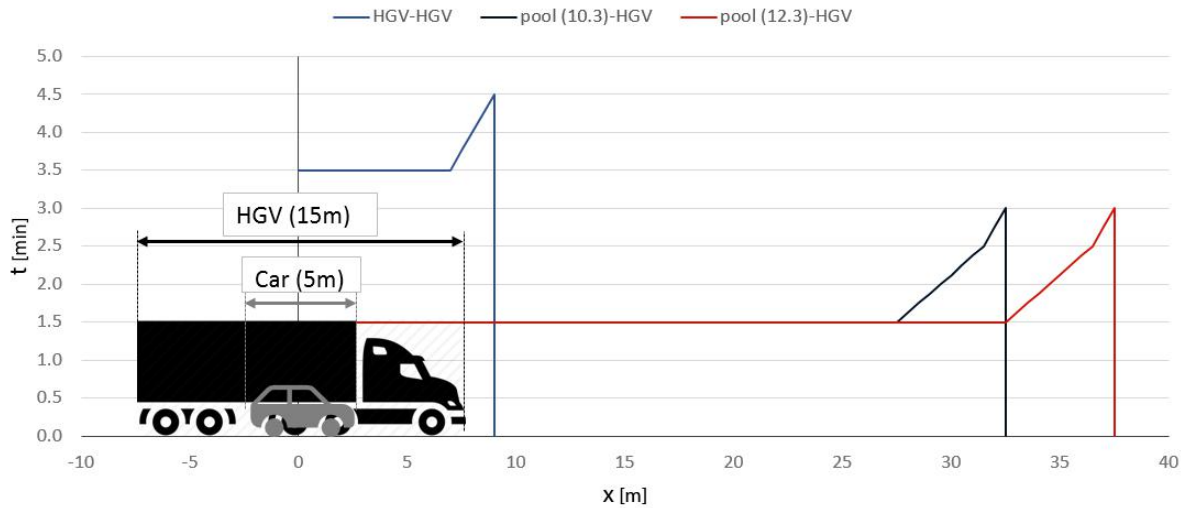


**Figure 4.29**

*Space-time graph representing the fire spread for different scenarios*

- $T_a = 70^\circ\text{C}$ ;
- $\rho_a = 1,03\text{ kg/m}^3$ ;
- $c_a = 1,012\text{ KJ/kg/K}$ .

#### 4.9.8. TEMPERATURE HEAT MAPS

Following the indications explained in subsection 4.7, the heat maps of a HGV with high energy content fire in a two lanes tunnel is shown in Fig.4.31. The following hypothesis were used:

- HGV-High Q HRR from subsection 4.1.1;
- $T_a = 20^\circ\text{C}$ ;
- $\rho_a = 1,217\text{ kg/m}^3$ ;
- $c_a = 1\text{ KJ/kg/K}$ ;
- two lanes tunnel ( $W = 10,3\text{ m}, H = 5,1\text{ m}$ ).

#### 4.9.9. LINING TEMPERATURE PROFILE

In this subsection the temperature gradients of concrete elements exposed to different worst-case temperature curves caused by different scenarios are shown. The graphs exposed below are based upon the numerical model explained in section 4.8 and consider concrete elements on the tunnel ceiling exposed to the maximum temperature caused by each scenario. In Table 4.8 the average temperature over a thickness of both 16 and 32 mm on the fire exposed side of the concrete element is shown. Different scenarios were used and the listed values correspond to the average temperature after 5 min of fire exposure. The following hypothesis were used:

- temperature curve calculated with the vehicles HRR from subsection 4.1.1 according to the modified "Heselden" approach exposed in subsection 4.1.3;

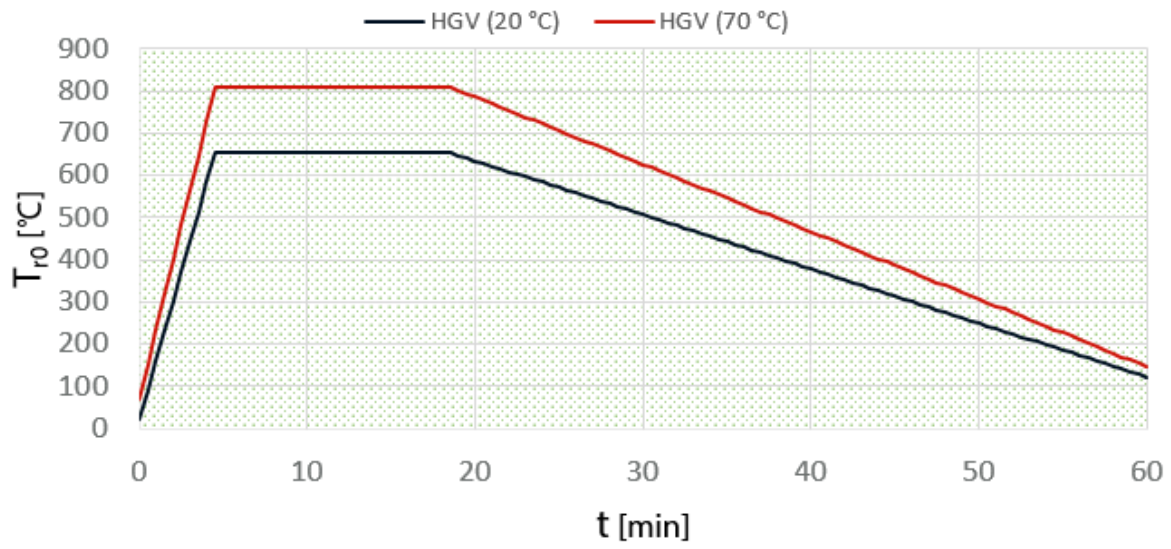


**Figure 4.30**  
 Temperature development of HGV for different initial ambient temperatures

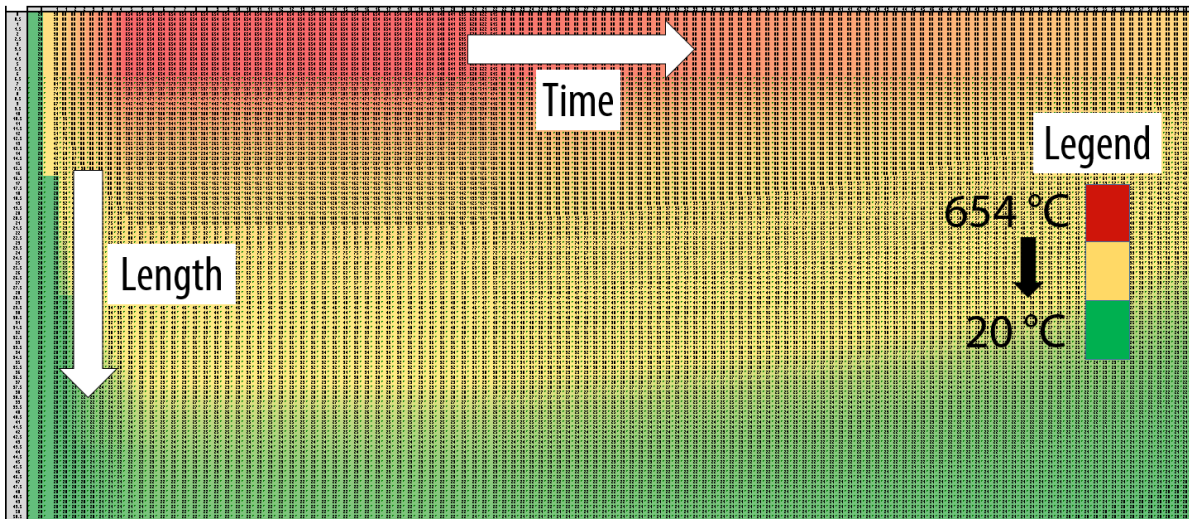


**Figure 4.31**  
 HGV high Q-Heat map

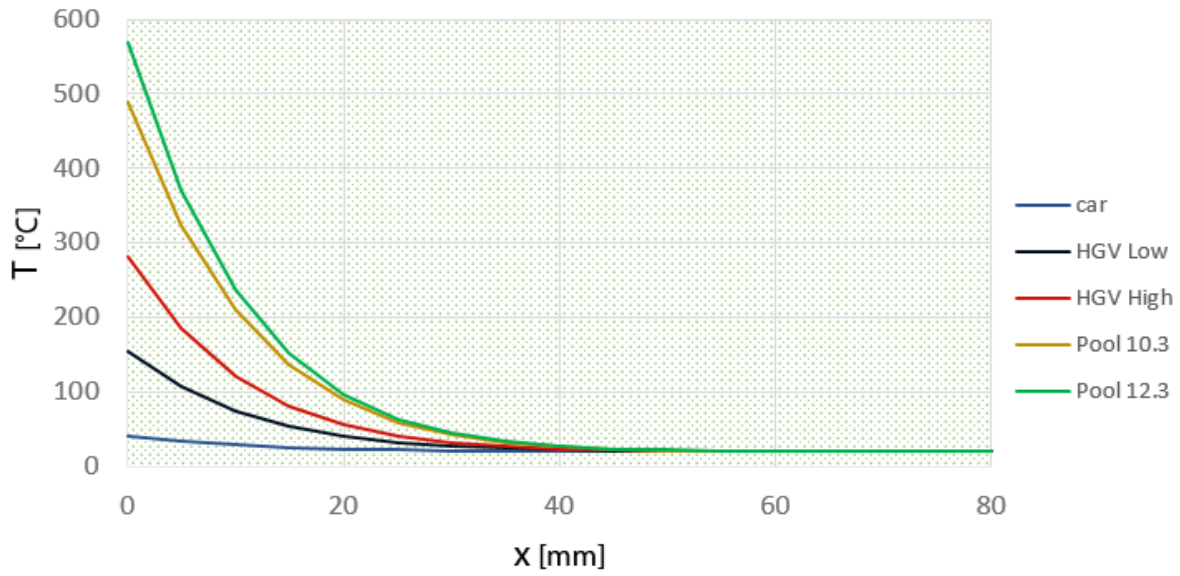
**Table 4.8**  
Average temperature after 5 min exposure

	20 mm	32 mm
<i>Car</i>	43°C	37°C
<i>HGV Low</i>	86°C	70°C
<i>HGV High</i>	145°C	114°C
<i>Pool (10.3 m)</i>	250°C	193°C
<i>Pool (12.3 m)</i>	285°C	219°C

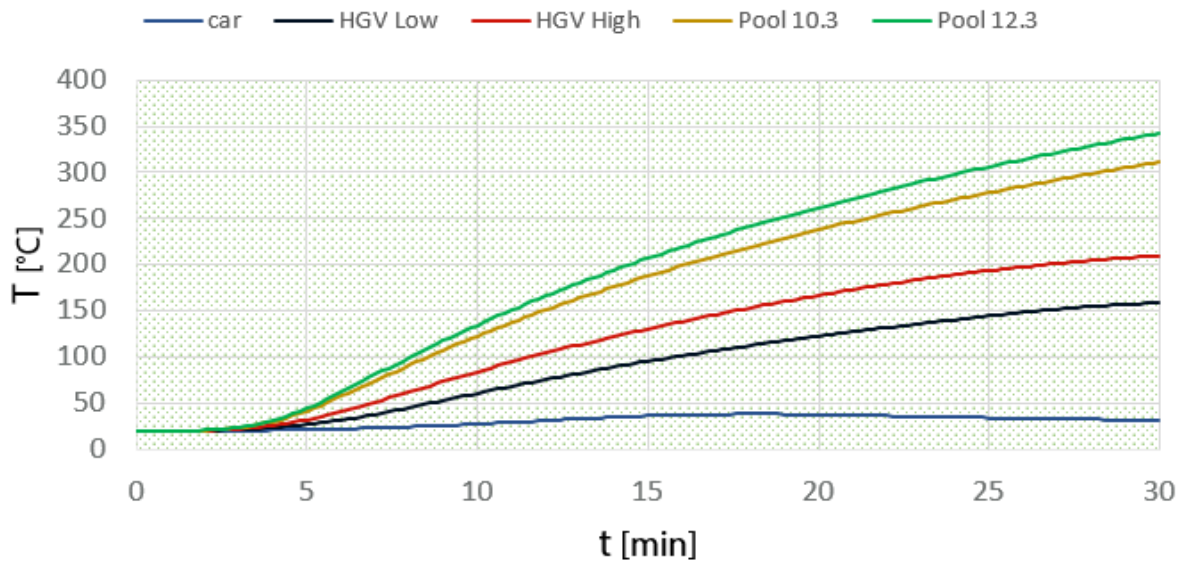
## 4

- temperature curve calculated using the pool HRR from subsection 4.2.1, with the additional assumptions of an initial linear growth of the HRR in the growth phase. Based on the results of the pool fire full-scale test explained in subsection 4.2.1, the HRR was modelled as increasing from a value of 0 MPa at the ignition time till the maximum calculated HRR in 3,75 min;
- $T_a = 20^\circ\text{C}$ ;
- two lanes tunnel ( $W = 10,3\text{ m}$ ,  $H = 5,1\text{ m}$ ).

In Fig.4.32a the temperature gradient after 5 min exposure is shown. The development of the temperature at a depth of 32 mm is also shown in Fig.4.32b. The same hypothesis exposed above applies.



(a) Temperature gradient after 5 min



(b) Temperature at 32mm depth

**Figure 4.32**  
Temperature development

## 4.10. CONCLUSIONS

Based on theory exposed and the results obtained in this chapter, with respect to the thesis objectives, the following conclusions can be drawn:

### 1-DERIVE MOST PROBABLE FIRE SCENARIOS

- an analytical calculation procedure to predict the maximum ceiling temperature and temperature along the tunnel in time for vehicle fires (cars, HGVs,...) has been successfully found. The results are in good agreement with the output of a CFD simulation carried out with analogous inputs. The simulation results are shown in Chap.5;
- an analytical calculation procedure capable of estimating the pool diameter, given the tunnel characteristics, ignition time and tank leaking conditions, has been found in literature, re-elaborated and proposed;
- the theoretical Heat Release Rate of a given pool fire can be calculated using an analytical model found in literature and re proposed in this thesis;
- additional analytical calculation procedures have been found in literature and modified to estimate the following parameters, when both the maximum ceiling temperature and tunnel characteristics are known:
  1. Horizontal flame length;
  2. Smoke layer instability;
  3. Fire spread.
- a vehicle igniting under the conditions of an already burning fire, causes a more severe scenario compared to the ignition of the same vehicle at the ambient temperature. In Fig.4.30 an example of the fire curve describing the maximum temperature for an HGV in both cases is shown;
- both tunnel cross section and length have a great influence on the maximum temperature, temperature distribution along the tunnel and smoke layer instability;
- in the unidimensional Fourier heat transfer model, boundary conditions including the convective and radiative heat transfer have been included. Adding these heat fluxes in the model show a reduction in the temperature gradient experienced by the concrete compared to the case where they are neglected.

# 5

## FIRE DYNAMICS SIMULATOR

*The focus of this chapter is the simulation with a CFD software of a series of representative scenarios. The software used to carry out the calculations is: Fire Dynamics Simulator (FDS). Two scenarios not including ventilation have been investigated. These scenarios have also been analytically studied in Chapter 4 and are here compared with the numerical results. Additionally two scenarios including ventilation have been investigated.*

*In the first section the description of the inputs information used to carry out the simulations is described in detail. Subsequently a section describing the output quantities that have been set and some insight on the procedures followed to elaborate the results is given. The results are then presented for the following simulations:*

- *HGV (no ventilation);*
- *Pool (no ventilation);*
- *Pool ( $u = 2,5 \text{ ms}^{-1}$ );*
- *Pool ( $u = 3,5 \text{ ms}^{-1}$ ).*

*The simulations carried out in this thesis are then compared with a similar representative CFD calculation that has been found in literature. Finally conclusions are drawn over the results presented in this chapter.*

### 5.1. INPUTS

The simulations of the considered scenarios involve vehicle and pool fires. The hypothesis that have been used in the simulations are similar to the one used for the analytical calculations of the scenarios in section 4.9. The following additional common inputs and hypothesis have been taken into account:

- the Large Eddy simulation (LES) hydrodynamic model has been used. This model is less computational demanding compared to the Reynolds-averaged Navier–Stokes equations (RANS) model;
- a single step combustion model has been used and the HRR was directly applied on properly defined surfaces. The HRR applied is the one coming from full-scale tests that has been used for the analytical models showed in Chap.4;

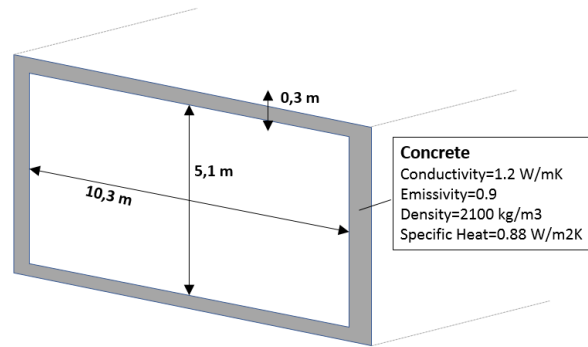


**Figure 5.1**

*Cross section used in the FDS simulations*

5

- the fuel has been defined as an n-Heptane ( $C_7H_{16}$ ) with the following characteristics:
  - soot yield = 0.1;
  - CO yield = 0.1;
  - Heat of combustion = 29903,9 kJ/kg.

For the pool fire simulation this choice was done in order to compare the results directly with the analytical calculation that have been carried out considering the same fuel. For the HGV this choice is considered an appropriate one to model a vehicle containing different materials based on common practice in the fire safety engineering industry;

- the cross section chosen is the one representing a unidirectional tunnel with two lanes and shown in Fig.5.1. The length of the tunnel has been fixed upon smoke layer instability considerations. In real scenarios the friction, caused by obstacles and the distance of the fire from the portals, limits and reduce the oxygen supply to the fire location. Reference was made to the maximum tunnel length for which there is a clear smoke stratification (section 4.5). This length was considered a good choice to account for the effect of the friction but at the same time account for the possibility of the fire to be reached by the oxygen. Considering the uncertainties of this analytical model a reduced length of approximately 80 m for the HGV fire and 100 m for the pool fire was fixed;
- the mesh was subdivided into three zones as shown in Fig.5.2. An inner part consisting of a finer mesh was chosen close to the fire location. And two zones at the extremes of the tunnel with a courser mesh were applied. For the HGV and pool fire simulations the length shown in Table 5.1 have been used. The maximum dimension of the grid cell ( $\delta x$ ) was fixed equal to 0,3 m and this is the value assumed for the course mesh. In [17], an equation that can be used for the grid sensitivity study is proposed. The equation is the following:

$$\delta x \approx \frac{D^*}{16} \quad \text{with} \quad D^* = \left( \frac{HRR}{\rho_a c_a T_a \sqrt{g}} \right)^{2/5}$$

with:

- HRR in [kW].

where  $D^*$  is a characteristic fire diameter. The value obtained with this equation was used in the finer mesh. For the HGV fire a grid cell size of 0,15 m was applied while for the pool fire the same value as the courser mesh has been used (0,3 m).

**Table 5.1**  
*Mesh dimensions*

	<b>l1</b>	<b>l2</b>	<b>l3</b>
<i>HGV fire</i>	24 m	27 m	78 m
<i>Pool fire</i>	12 m	45 m	102 m

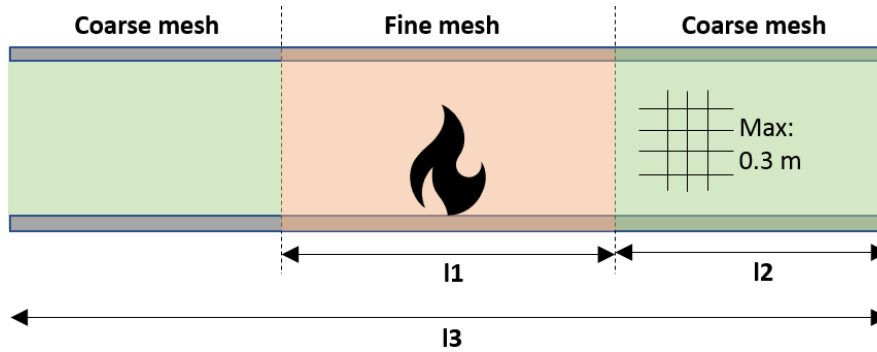


**Figure 5.2**  
*Mesh subdivision*

- the boundaries have been set open for the simulations that do not include ventilation. The simulations including ventilation have an open boundary and a boundary supplying air with a given velocity. To simulate real scenarios the ventilation is activated after 80 s from the fire ignition and the time needed to activate the fans at full regime is taken equal to additional 30 s. A linear increase of the supplied air velocity has been modelled in this second interval.

The maximum ventilation value that could be used can be estimated calculating the value of the critical velocity ( $v_{cr}$ ). According to Ingason et al. [27], the non dimensional model for the estimation of the critical velocity is the most appropriate to be used. This model fits particularly well the full-scale tests data. The following equation can be used to calculate the critical velocity:

$$Q^* = \frac{HRR}{\rho_a c_a T_a \sqrt{g} H^{5/2}} \quad v_c^* = \begin{cases} 0.81 \cdot Q^{*1/3}, & \text{if } Q^* \leq 0.15 \\ 0.43, & \text{if } Q^* > 0.15 \end{cases}$$

$$v_{cr} = v_c^* \sqrt{gH}$$

with:

- HRR in [kW].

- the overall configuration and representation of the applied fire surfaces applied in the simulations is shown in Fig.5.3. In the HGV fire cases an obstacle above which the fire surface is positioned has been used. The obstacle represents the vehicle and its height is equal to half the vehicle height. This follows the assumption of the fire origin being located at half of the height of the vehicle. The pool fire has been represented with a surface positioned on the floor level,

## 5.2. OUTPUTS

The selection of the outputs has to be carried out prior to the simulation. This is necessary in order to limit the amount of information to be stored considering the heavy computational demand of a fire simulation. The following quantities have been selected:

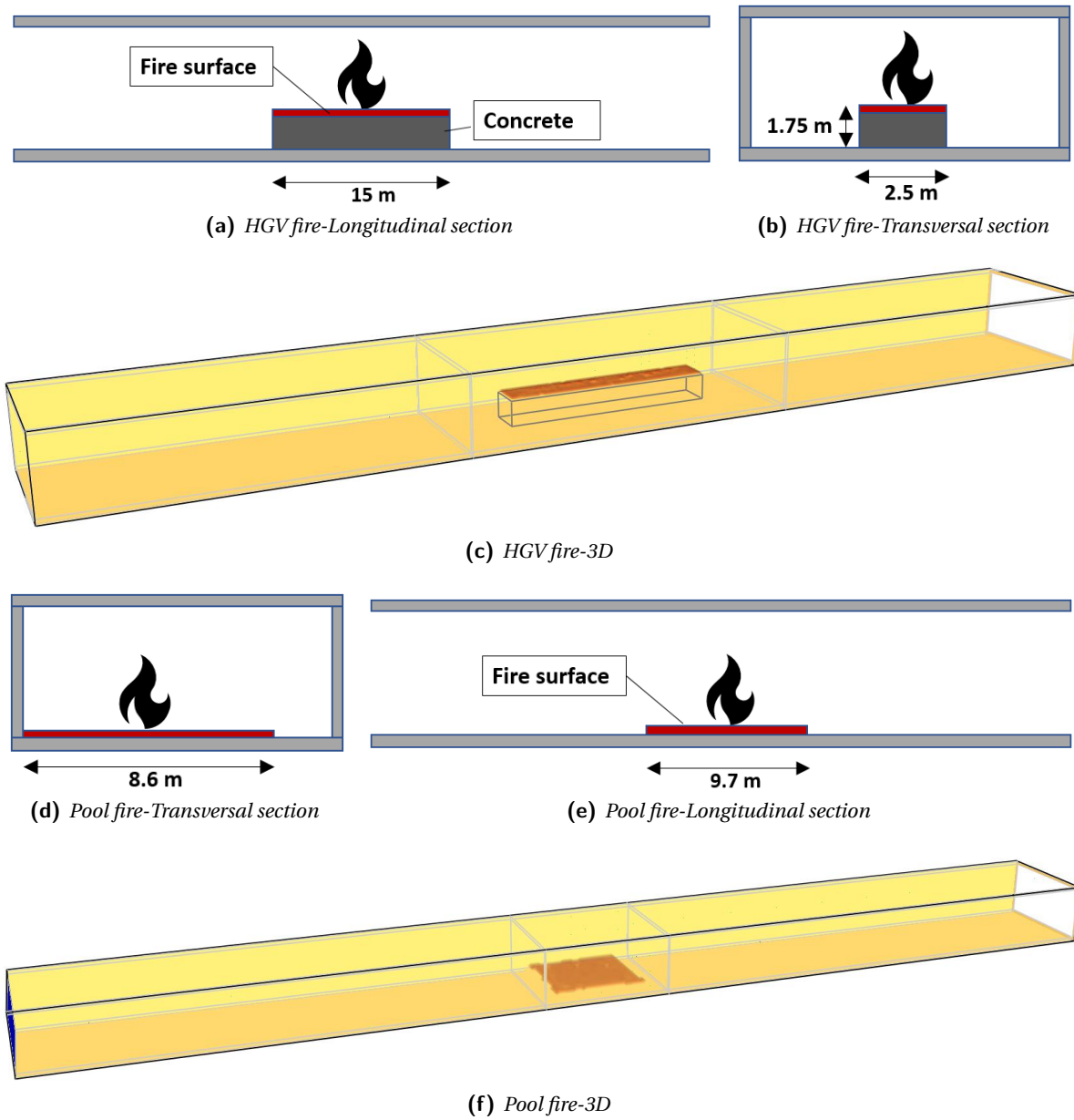


**Figure 5.3**

*FDS simulations geometry overview*

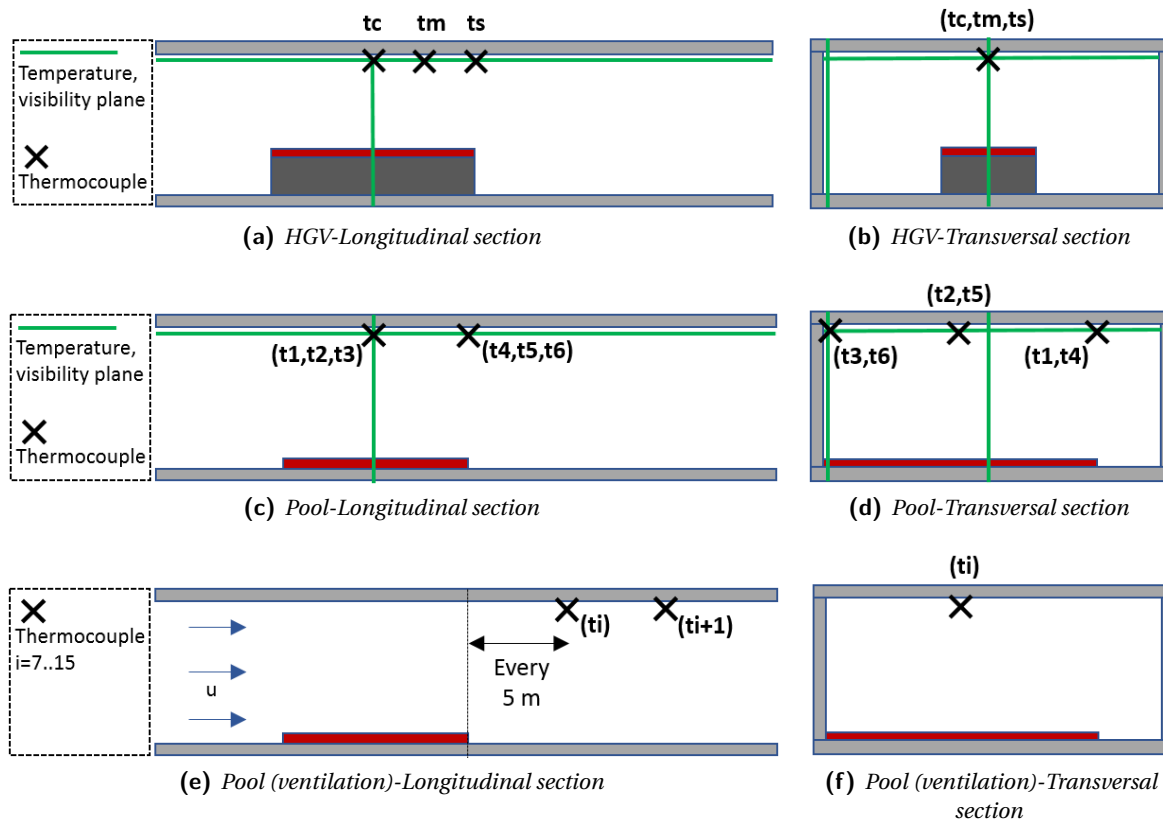


**Figure 5.4**  
Temperature outputs

- a three dimensional field representing the cell values of temperature, visibility and velocity along the three main directions;
- a series of surfaces and punctual thermocouples measuring the temperature have been positioned in the model. In Fig.5.4 a representation of their positions is shown. The pool fire has been modelled with and without ventilation. For the pool fire ventilated simulations additional thermocouples were added compared to the pool fire without ventilation. In Fig.5.4e,5.4f their location is shown. These were necessary to measure the temperature downstream of the fire location. In particular the use of ventilation deviates the flames and cause parts of the tunnel downstream of the fire to experience the maximum temperatures;
- a series of mass fraction detectors have been positioned in the model. These detectors acquire information regarding the fuel and oxygen mass fraction at a given location. This information let us calculate the air entrainment ratio and compare it with the stoichiometric one. This information is relevant for the understanding of the fire development in a fuel or ventilation controlled manner. In Fig.5.5 the devices location for HGV and pool fire simulations is shown;

### 5.2.1. FUEL VS VENTILATION CONTROLLED FIRE

To better understand the fire dynamics there is the need to characterize a fire and in particular have control over the combustion development. This development can be characterized by a ventilation or fuel controlled situation as explained in Chap.3. This phenomenon can be studied at a local or global scale.

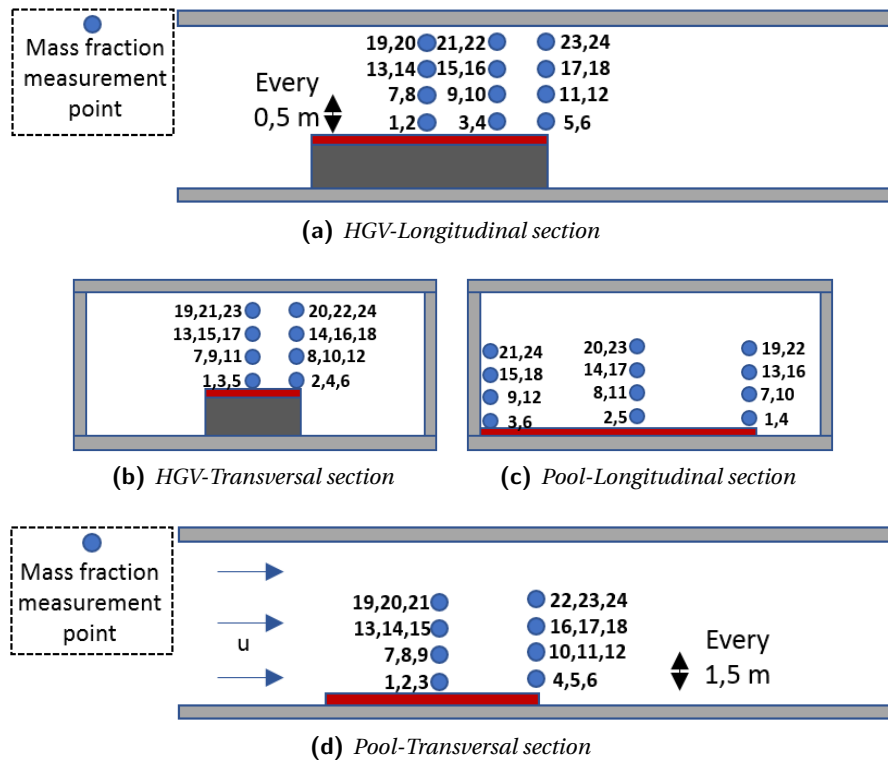
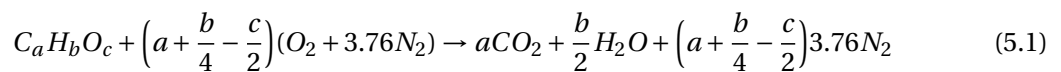


Figure 5.5

Mass fractions outputs

According to Ingason [6] it is possible to calculate the optimal air entrainment ratio. This can be compared with the effective air entrainment ratio present at a certain location. The effective ratio gives an indication of the fire typology development. The air entrainment ratio represents the balance between air and fuel. From the stoichiometric chemical equation describing the combustion of a generic fuel (eq.5.1) it is possible to calculate the optimal air entrainment ratio as shown in eq.5.2.



$$n = \frac{137.8[a + (b/4) - (c/2)]}{12a + b + 16c} \quad (5.2)$$

Using this information, a local indication of the conditions of the fire in the FDS model can be estimated.

At a global scale the Air/Fuel equivalence ratio ( $\Phi$ ) can be used to understand the combustion behaviour. This can be calculated as follows [6]:

$$\Phi = 3000 \cdot \frac{\dot{m}_a}{HRR} \quad \rightarrow \quad \dot{m}_a = \rho_a u H_{eff} W_{eff}$$

where:

- $\dot{m}_a$  [kg/m<sup>2</sup>/s] is the mass flow rate of supplied air;
- $u$  [m s<sup>-1</sup>] is the average velocity of the supplied air;

- $H_{eff}$  [m] is the effective height over which the air is supplied. It is usually the height of the tunnel reduced of the smoke layer thickness. The smoke layer thickness cause only outflow of combustion products from the tunnel;
- $W_{eff}$  [m] is the effective width over which the air is supplied. It is usually the whole width of the tunnel;
- HRR in [kW].

The Air/Fuel equivalence ratio can be used in the following way:

$$\begin{aligned}\Phi \geq 1 & \quad \text{Fire fuel controlled} \\ \Phi < 1 & \quad \text{Fire ventilation controlled}\end{aligned}$$

The Air/Fuel equivalence ratio can be alternatively expressed as follows:

$$\Phi = \frac{\dot{m}_a}{n\dot{m}_f}$$

which can be rearranged in the following way:

$$n = \frac{\dot{m}_a}{\Phi\dot{m}_f} \quad (5.3)$$

For ventilation controlled fires the HRR is directly proportional to the mass flow of supplied air [6]. Assuming that the fuel mass rate loss is constant, the HRR can be taken proportional to the air entrainment ratio. Using the effective air entrainment ratio an estimate of the effective HRR can be calculated. In the specific case of a pool fire eq.4.8 can be used to estimate the fuel mass rate loss.

### 5.3. RESULTS

This chapter highlights results obtained simulating fire scenarios with the use of FDS. The theoretical background and hypothesis used have been shown previously in this chapter. All the simulations are carried out considering a two lane tunnel and a combustible material being n-Heptane ( $C_7H_{16}$ ). The following scenarios have been analysed:

- HGV with high energy content fire without ventilation;
- pool fire (D=10.3 m) without ventilation;
- pool fire (D=10.3 m) with a ventilation of  $2,5 \text{ m s}^{-1}$ ;
- pool fire (D=10.3 m) with a ventilation of  $3,5 \text{ m s}^{-1}$ .

#### 5.3.1. HGV SIMULATION (NO VENTILATION)

In this subsection the results of the HGV simulation are highlighted. In Fig.5.6 the HRR produced by the HGV fire is shown. It can be seen that the HRR output is the same as the one modelled and imposed to the simulation. This is explained by the fact that in the simulation combustion process there is enough oxygen. For the n-Heptane the optimal air entrainment ratio is:

$$n = 15.158$$

In Table 5.2 the air entrainment after 5 minutes from ignition is listed for the mass fraction outputs points. Most of the points receive enough oxygen for the optimal combustion to take place. In

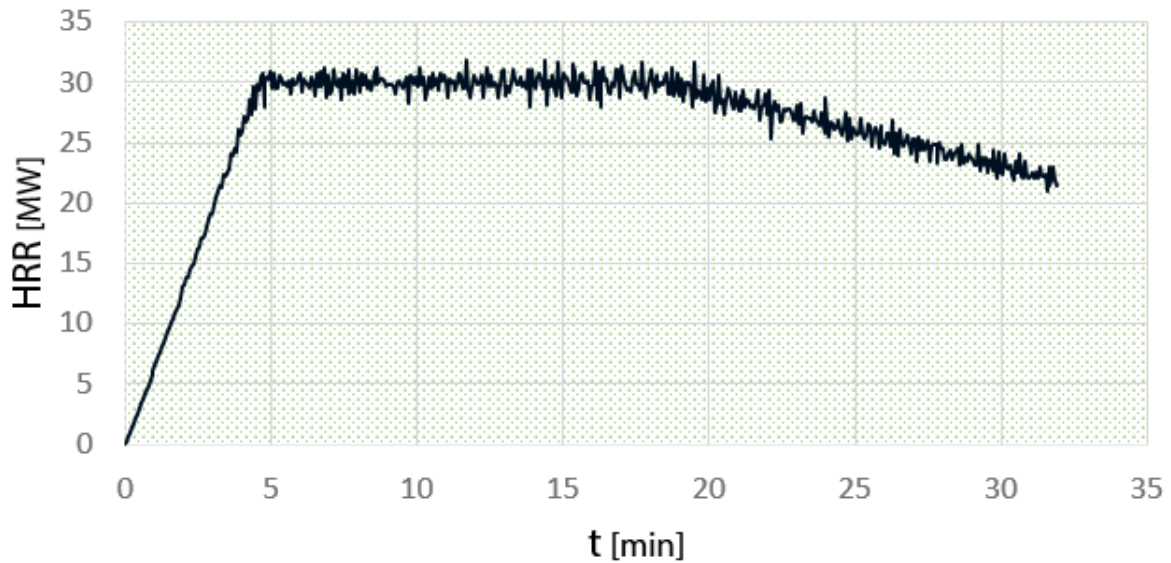


**Figure 5.6**  
*HRR-HGV High Q (no ventilation)*

Fig.5.11 a visual representation of this points and their air entrainment values is shown. It can be noted that only the inner points above the combustion surface do not reach the optimal level.

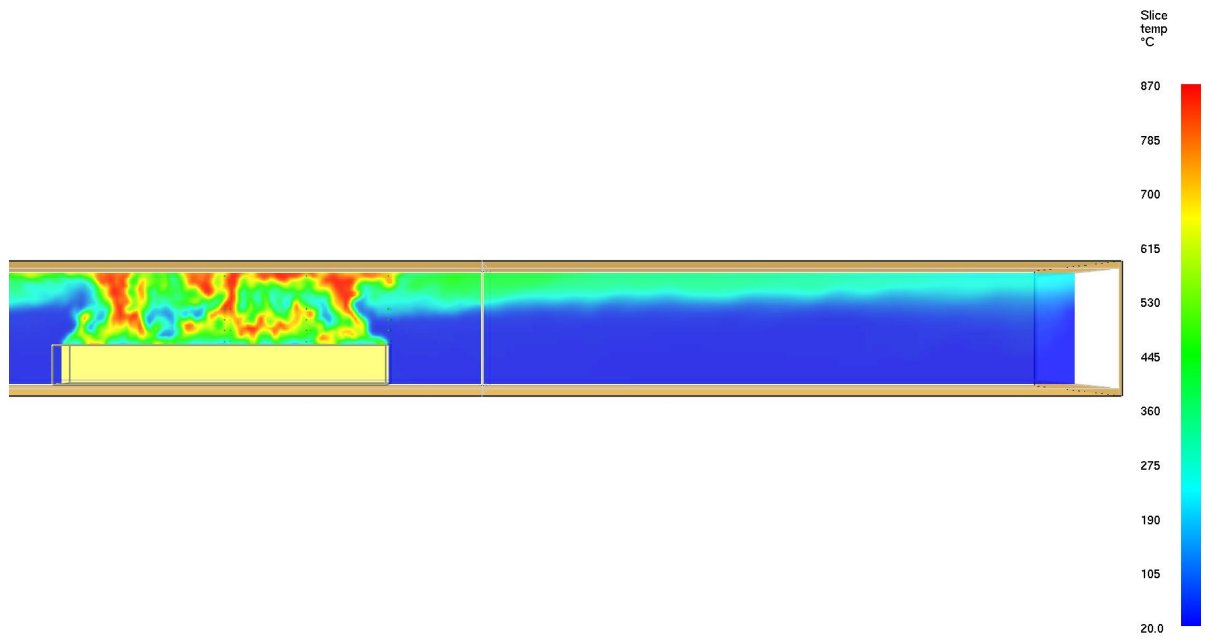
Fig.5.7 confirms the assumptions and predictions of the modified "Heselden" model. The smoke stratifies on the top part of the tunnel while in the bottom part an inward air flow feeds the fire. This two zone characterization is the base over the analytical calculations and finds confirmation in the results obtained from this simulation. In particular, Fig.5.7a shows a representation of the smoke development while Fig.5.7b represent the longitudinal air velocity vector field on a plane positioned along the half tunnel width.

In Fig.5.8,5.9 a representation of the temperatures of the fluid in the tunnel after 5 minutes from ignition is shown. At first sight, the flames development in the tunnel can clearly be noted. In Fig.5.9b, the flames touching the ceiling at that particular time are clearly visible in the area marked by the high temperature contour. Additionally, from Fig.5.8a,5.8b it can be noted that the smoke layer on the top part of the tunnel cross section traps the majority of the heat. This phenomenon results in an area characterized by high temperature on the top part of the tunnel and an area on the bottom part which maintains similar temperature compared to the initial ambient one. Anyway, the effect of radiation should not be forgotten. Heat from the fire source can still reach the tunnel walls and in particular for the bottom part, the smoke layer is not acting as an intermediate barrier layer. The structure does not need to be checked using reduced material properties caused by high temperatures over its cross-section surface. Different fire loads, considered as both high smoke temperatures and radiation, should be applied to different parts of the tunnel cross section.

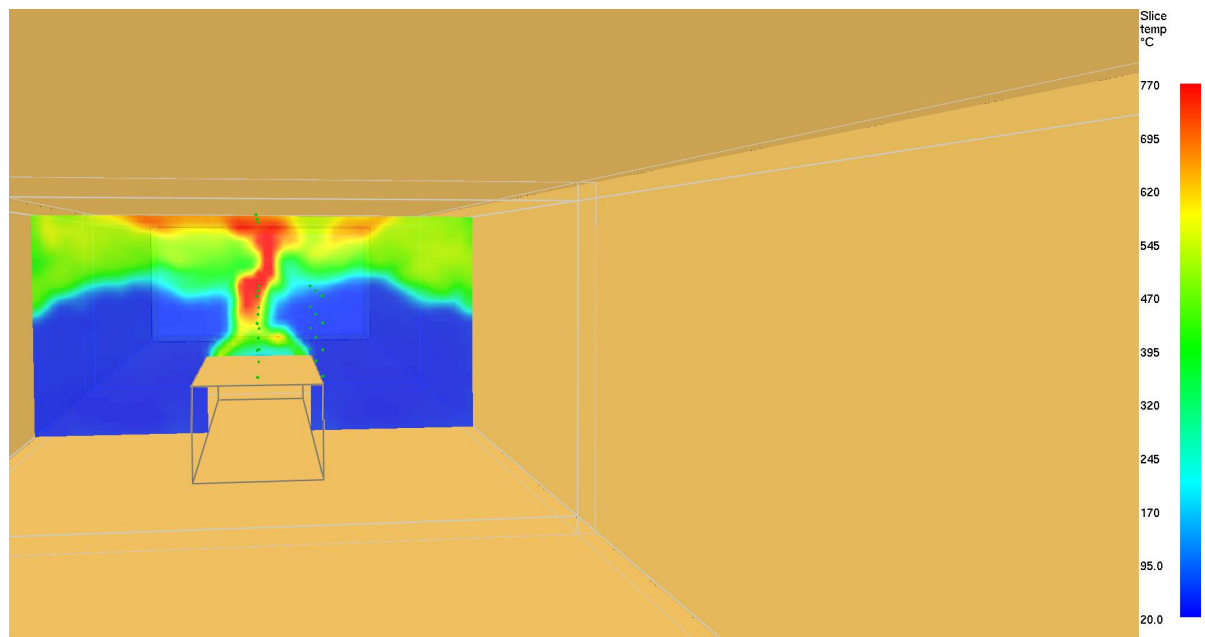
In Fig.5.10 the maximum ceiling temperatures between the analytical model predictions and the simulation results are compared. It can be seen that the analytical model gives extremely good results, which have been confirmed by the FDS simulation. The simulation results shows an oscillatory behaviour around the values calculated with the analytical model. This can be explained by the flames, which cause the points where the temperature outputs have been positioned to experience an oscillatory behaviour depending to the presence or not of the flame at that location at a certain moment in time.



5



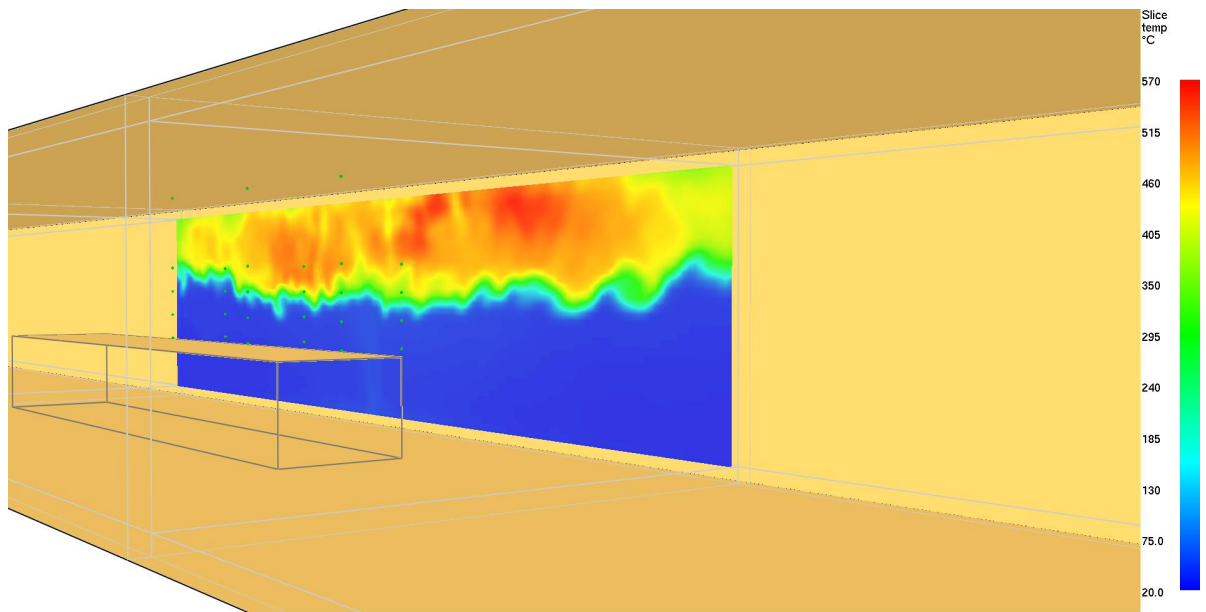
(a) Longitudinal plane at half width



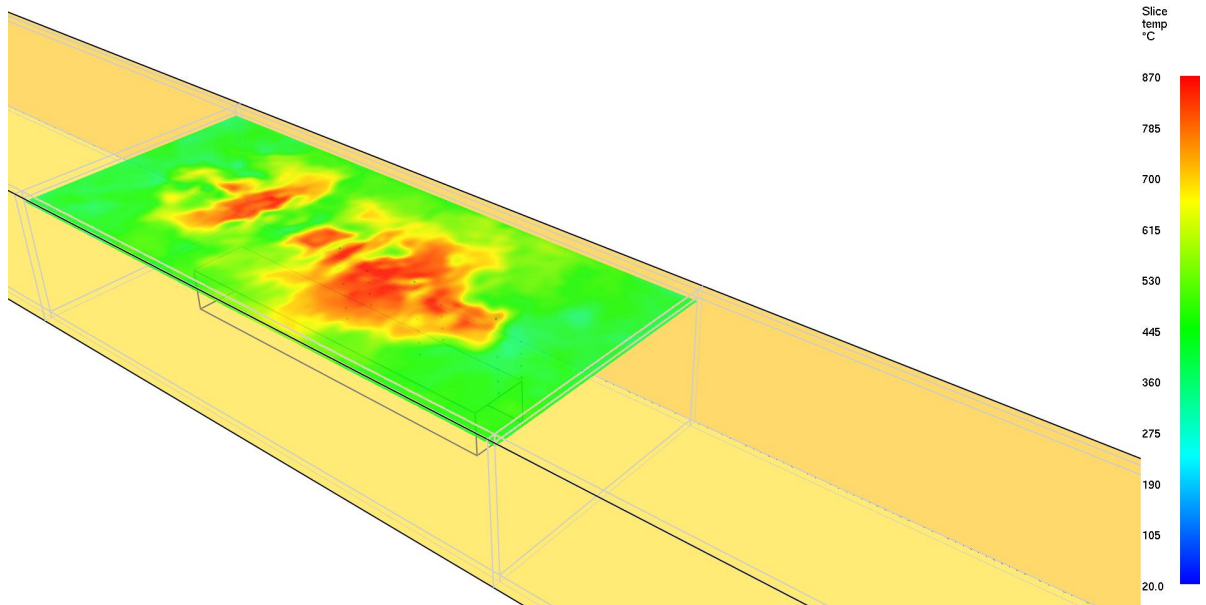
(b) Transversal plane at half length

**Figure 5.8**

*HGV High Q (no ventilation)-Fluid temperature [5 min after ignition]*



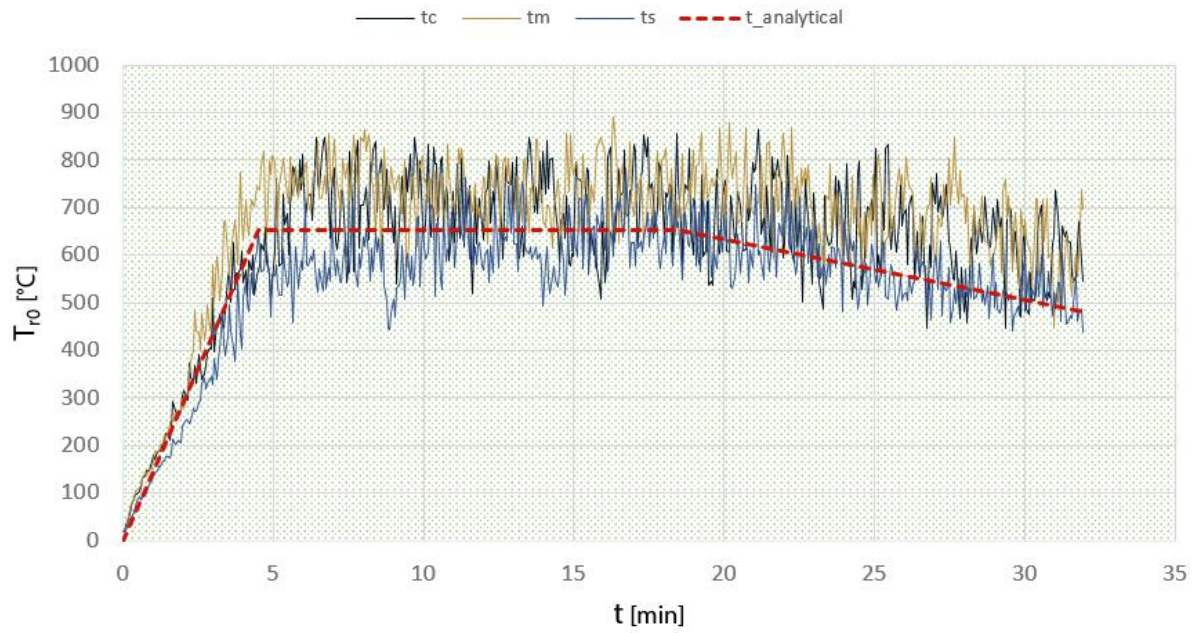
(a) Side wall



(b) Ceiling

**Figure 5.9**

*HGV High Q (no ventilation)-Fluid temperature [5 min after ignition]*



5

**Figure 5.10**  
*HGV High Q (no ventilation)-Maximum temperature*

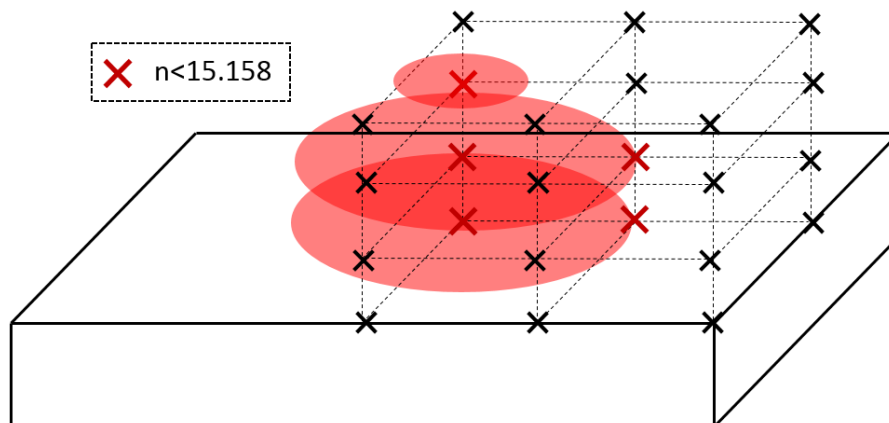


**Figure 5.11**  
*HGV High Q (no ventilation)-Mass fraction outputs points visualization*

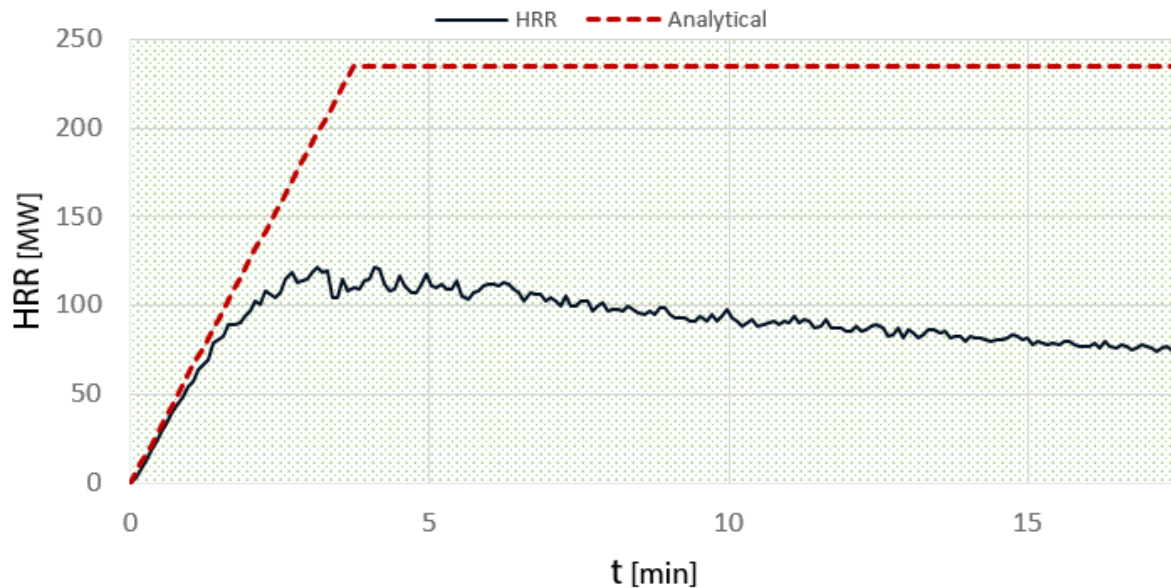


**Figure 5.12**  
*HRR-pool fire (no ventilation)*



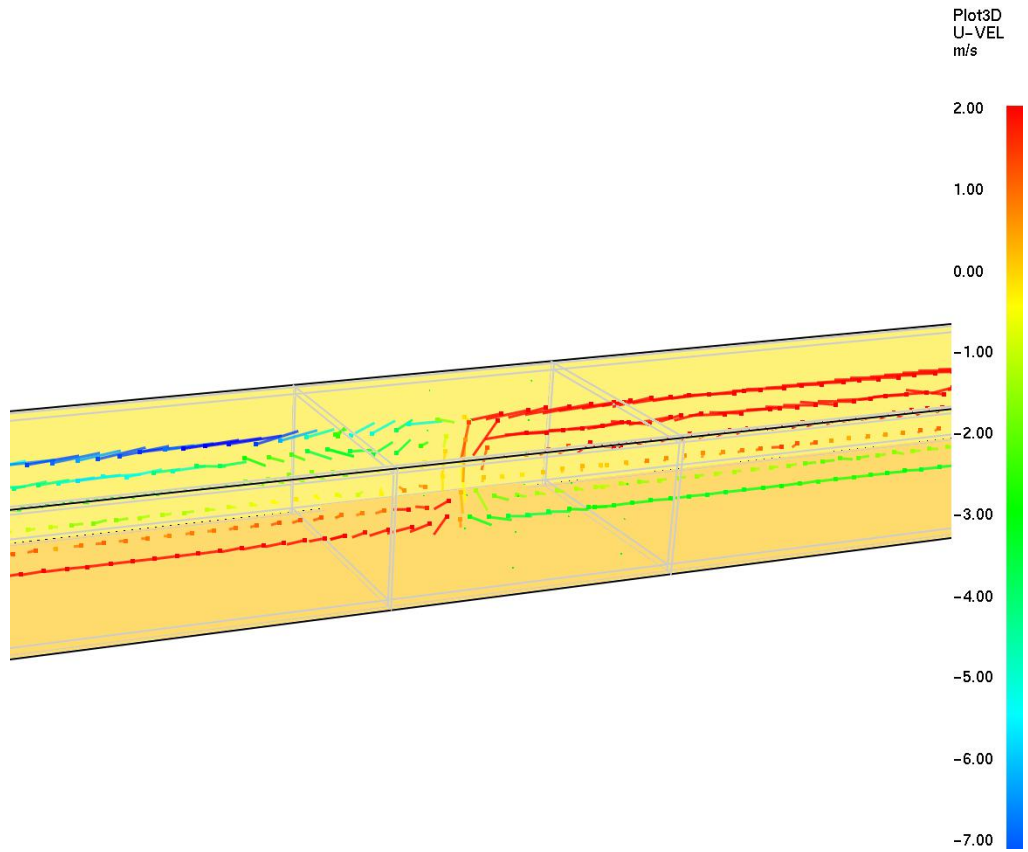
**Figure 5.13**  
*Pool fire (no ventilation)-Smoke development [2 min after ignition]*

### 5.3.2. POOL SIMULATION (NO VENTILATION)

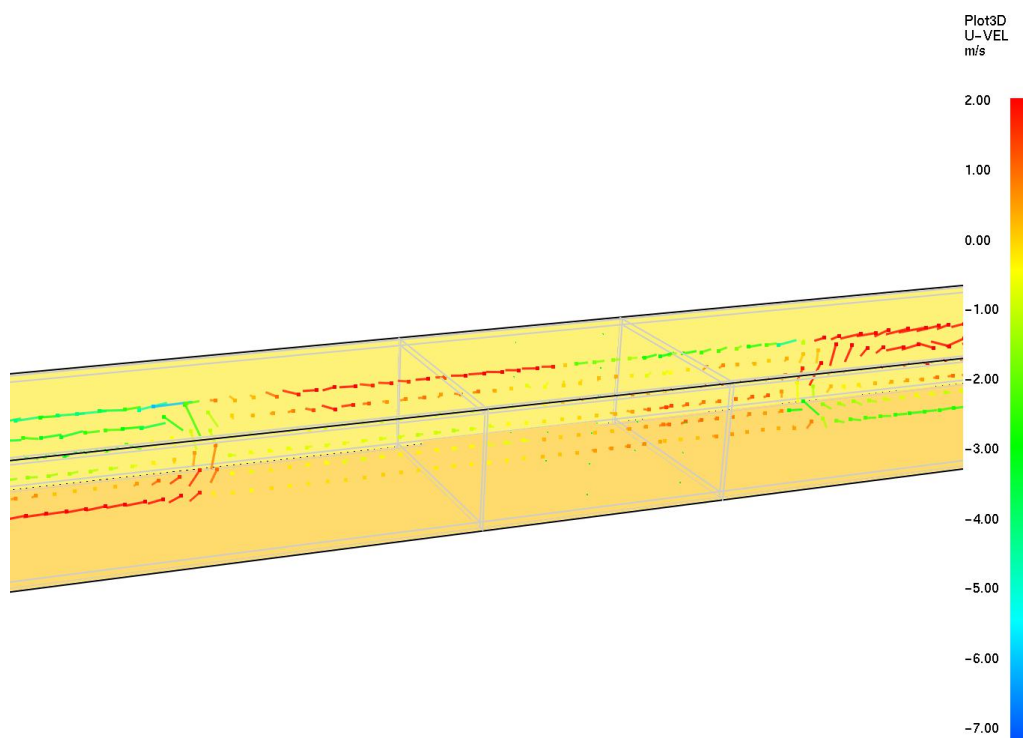
This subsection shows the results of a pool fire of 10.3 meters diameter in a tunnel without the use of ventilation. This simulation is purely conducted for academic purposes, since in actual practice the ventilation is most of the times used in case of fire. This is related to considerations involving human safety in case of fire occurrence in a tunnel. It is in any case important to investigate the effects caused by the fire in absence of the ventilation.

In Fig.5.12 the HRR of the pool fire is shown. It can immediately be seen that the HRR of the simulation does not follow the imposed one. In particular, after approximately 3,5 min the HRR increase suddenly stops and after a short phase of constant development, enters a decaying phase till reaching a lower constant value. This fact can be clearly explained by the lack of sufficient oxygen feeding the fire. In Fig.5.13 it can be seen that already after 2 minute from the fire ignition, the tunnel is engulfed with smoke which creates an obstacle for the input of fresh air from the portals. In Fig.5.14 the longitudinal air flow at 2 minutes and 5 minute from ignition is shown. It can be seen that while in the first 2 minutes the oxygen is able to reach the middle section of the tunnel, feeding the combustion process along the entire length, this is not the case after 5 minute. The combustion at this time step can take place only in a part of the tunnel due to the oxygen depletion before it can reach the initial fire location. This explains and justify the HRR decrease as being caused by the absence of a sufficient oxygen supply.

To further investigate and determine whether the oxygen depletion phenomena is the cause of the results obtained with the simulation, two additional checks have been conducted:



(a) 2 min after ignition



(b) 5 min after ignition

**Figure 5.14**  
*Pool fire (no ventilation)-Air flow*

1. the air entrainment ratio development in time has been checked;
2. the Air/Fuel equivalent ratio has been roughly calculated to understand the conditions of the fire.

In Fig.5.16 the air entrainment ratio in time in some mass fraction output points is shown. It can be seen that after approximately 3,5 min the air entrainment ratio of all the points falls below the optimal value. This confirms the HRR behaviour in time. At a global level, the amount of air feeding the fire has been estimated. Fig.5.15 shows the longitudinal air flow after 10 minutes from ignition along a plane positioned at half width of the tunnel. Assuming that the same behaviour applies for the points along the width of the tunnel ( $W_{eff} = W = 10,2\text{m}$ ), the following parameters have been estimated:

- $H_{eff} = 3\text{m}$ ;
- $u = 1,02\text{ms}^{-1}$ .

Following the procedure exposed earlier in subsection 5.2.1, the calculation below can be conducted:

$$\begin{aligned}\dot{m}_a &= 2 \cdot \rho_a u H_{eff} W_{eff} = 2 \cdot (1.2 \cdot 1.02 \cdot 3 \cdot 10.2) = 74 \text{ kg s}^{-1} \\ \Phi &= 3000 \cdot \frac{\dot{m}_a}{HRR} = 3000 \cdot \frac{74.9}{235000} = 0.95 \\ n &= \frac{\dot{m}_a}{\Phi \dot{m}_f} = \frac{74.9}{0.95 \cdot 6.664} = 11.8 \\ 15.158 : 100\% &= 11.8 : x \quad \Rightarrow \quad x \approx 78\%\end{aligned}$$

The calculation suggests that the HRR cannot develop fully and after 10 minutes only 78% of its potential can be released. This reduction is not the one seen in the HRR output, but this is a reasonable result considering the many assumptions that has been taken and the rough check that has been conducted. This result highlights that the scenario under consideration is in a ventilation control situation and that the results of the FDS simulation are valid and can be justified. This should raise awareness over the improper use of HRR and maximum temperature fire curves derived from full-scale tests that are conducted under different conditions compared to the tunnel under consideration.

In Fig.5.17,5.18 the fluid temperature profiles along the half width of the tunnel and on the ceiling are shown for different moments in time. In the first 2 minutes, oxygen is available and the combustion takes place along the entire length of the tunnel resulting in the highest temperatures above the fire location. While time increases and oxygen supply reduces due to the engulfment of the tunnel cross section by the smoke, the combustion can only take place at the sides of the initial fire location. Oxygen is depleted before reaching the initial fire location, thus the points located in its vicinity experience a decrease of the fluid temperature due to the interruption of the combustion process.

In Fig.5.19 the temperature profiles at different locations are shown. Additionally the analytical result and a worst-case temperature curve model (pool0) for this simulation are shown. The modelled temperature curve follows the maximum values recorded for all the points located above the pool fire.

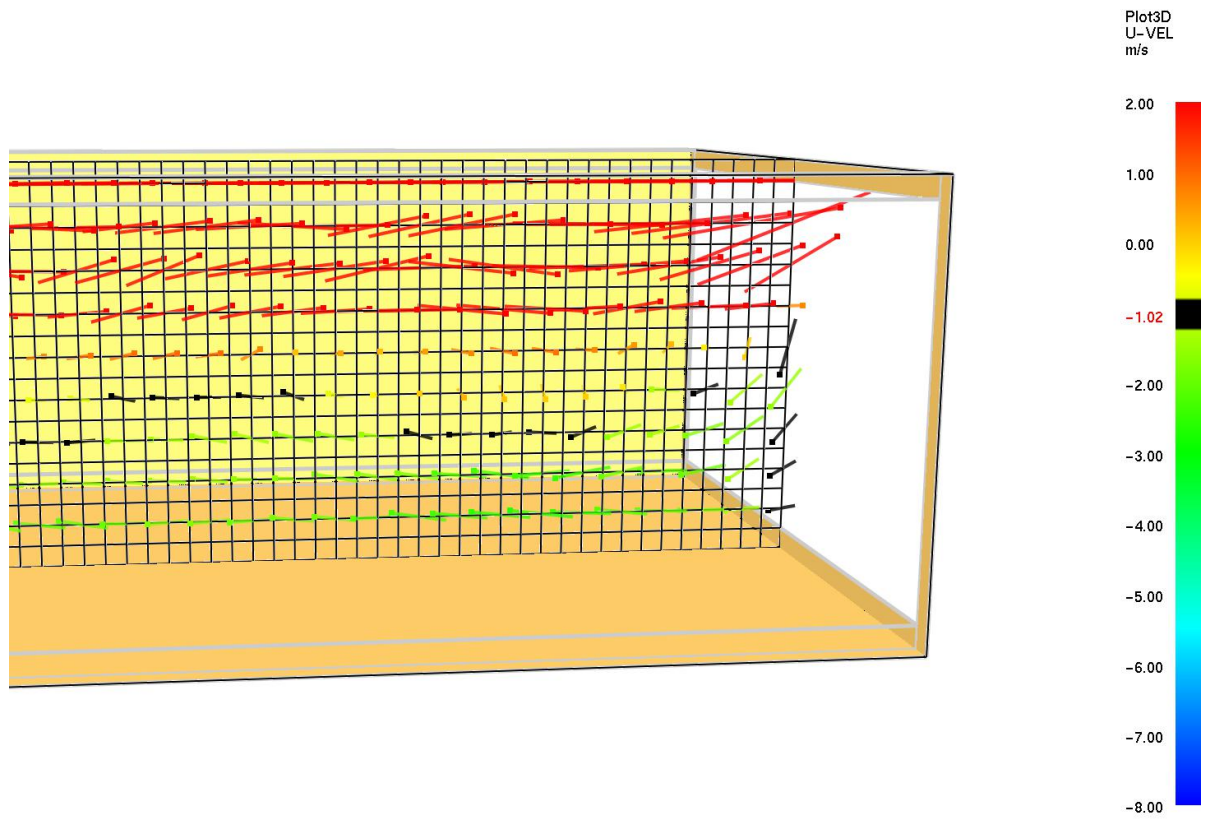


**Figure 5.15**  
*Pool fire (no ventilation)-Longitudinal air flow [10 min after ignition]*

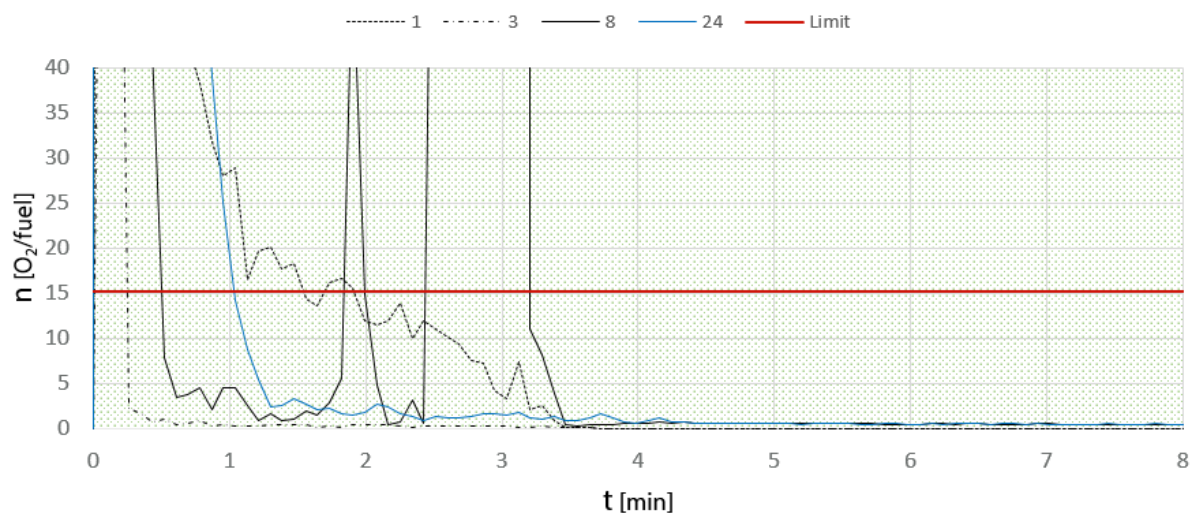
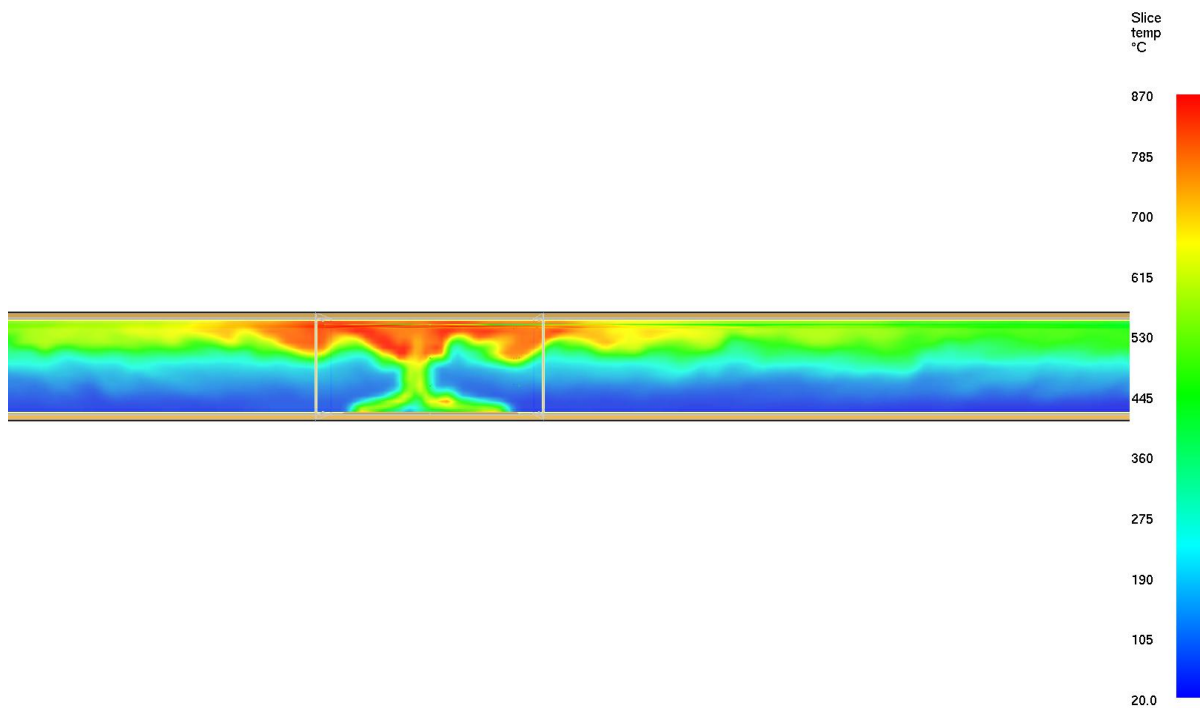
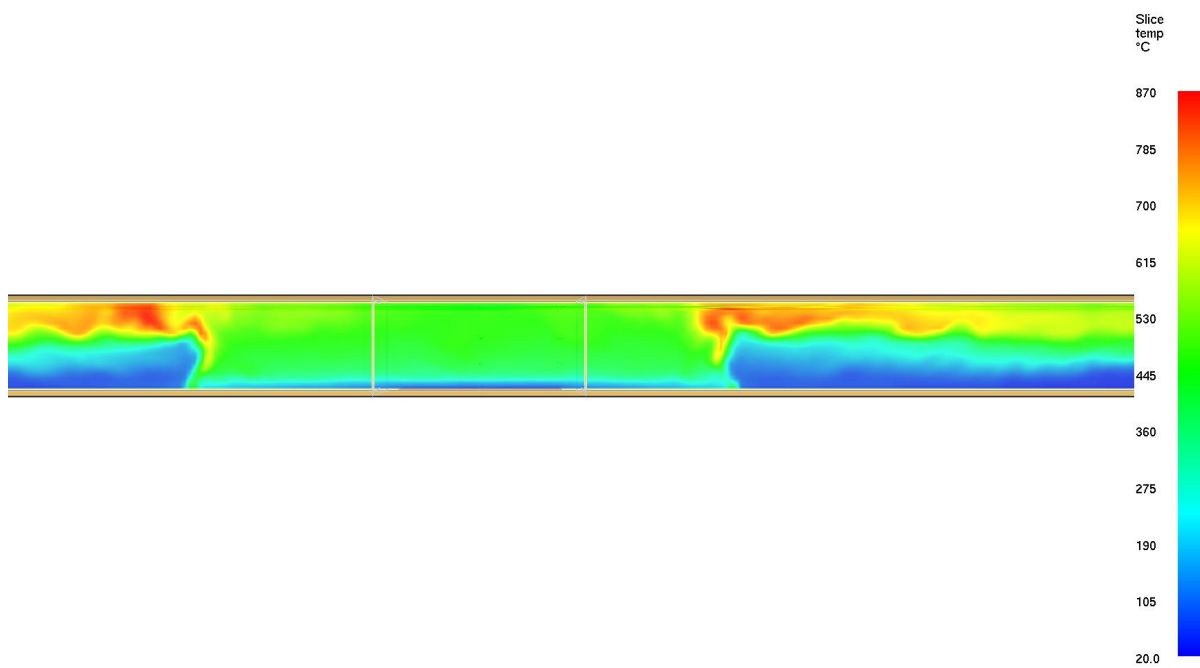


**Figure 5.16**  
*Pool fire (no ventilation)-Air entrainment ratio in time*



(a) 2 minute after ignition



(b) 5 minute after ignition

**Figure 5.17**  
*Pool fire (no ventilation)-Fluid temperature along tunnel half width*

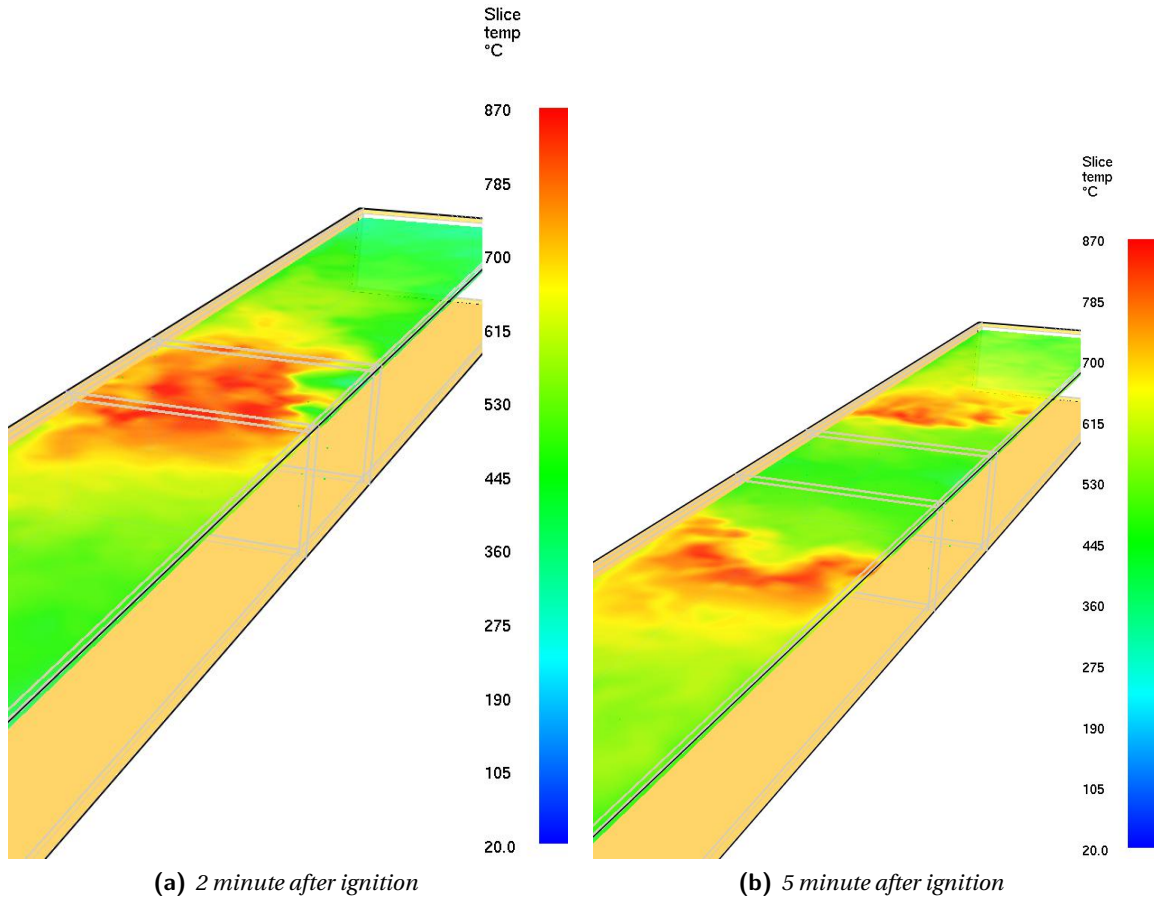


**Figure 5.18**  
Pool fire (no ventilation)-Fluid temperature along the ceiling

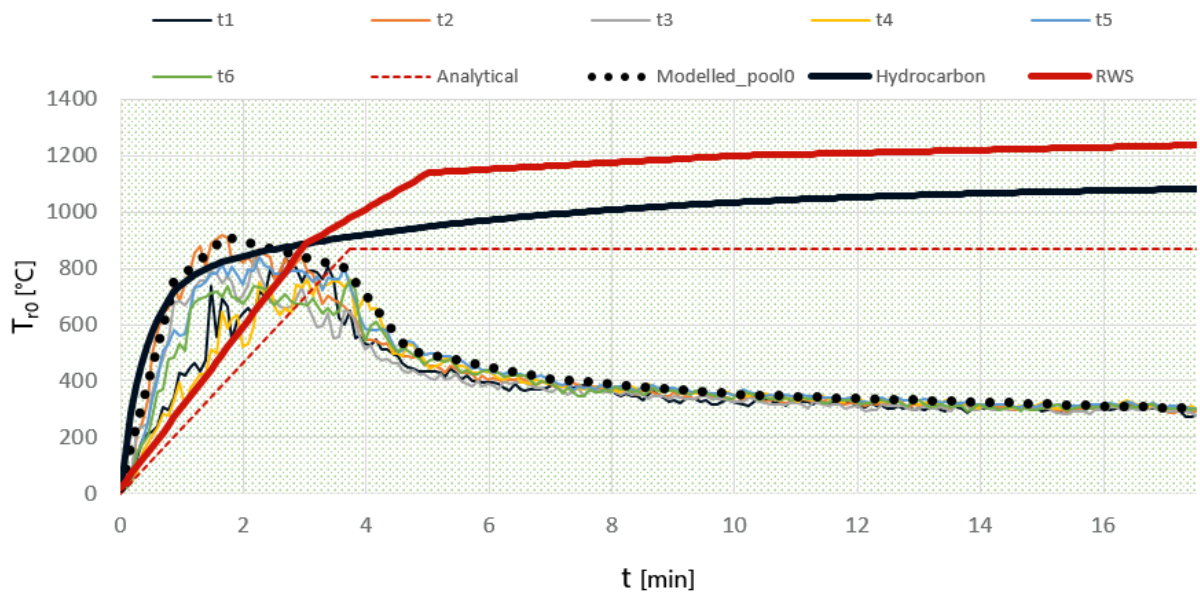


**Figure 5.19**  
Pool fire (no ventilation)-Maximum temperature

### 5.3.3. POOL SIMULATION (v=2.5 M/S)

In this subsection the analysis of the same pool fire discussed in the previous subsection has been conducted with the only difference being the addition of ventilation to the scenario. A ventilation of  $2,5 \text{ ms}^{-1}$  has been imposed at one of the portals. To simulate real conditions, a delay of 80 s before ventilation activation and additional 30 s before full regime conditions was chosen. A graph representing the applied ventilation is shown in Fig.5.23b. The chosen maximum speed is slightly lower compared to the critical velocity calculated for this specific case ( $v_{cr}$ ). The calculations expressed earlier in this chapter have been used to estimate a value of the critical velocity:

$$Q^* = \frac{HRR}{\rho_a c_a T_a \sqrt{gH^{5/2}}} = \frac{235000}{1.217 \cdot 1 \cdot 293.15 \cdot \sqrt{9.81 \cdot 5.1^{5/2}}} = 3.58 > 0.15$$

$$v_{cr} = v_c^* \sqrt{gH} = 0.43 \cdot \sqrt{9.81 \cdot 5.1} = 3,04 \text{ ms}^{-1}$$

In Fig.5.20 the HRR is shown. It can be seen that the imposed maximum HRR is not reached, but a considerable increase compared to the case with no ventilation is recorded. The ventilation supplies enough oxygen for the combustion to take place. An explanation for the HRR being slightly lower compared to the imposed one can be seek considering the smoke development downstream of the fire. Points located on the downstream side of the pool surface might not receive sufficient oxygen for the combustion to take place following the stoichiometric combustion equation.

Fig.5.21 shows both the smoke behaviour and longitudinal air flow after 5 minutes from the pool fire ignition. In contrast with the scenario without ventilation, the use of ventilation push both the smoke and the air along the same direction. A small back-layering originating from the fire is clearly visible in Fig.5.21a. The ventilation speed is strong enough to avoid the smoke propagation upstream of the fire and the estimated value of approximately  $3,04 \text{ ms}^{-1}$  finds confirmation in the simulation results about its ability to prevent back-layering of the smoke.

In Fig.5.22 a representation of the temperature of the fluid in the tunnel after 5 minutes from ignition is shown. The ventilation deviates the flames downstream of the fire and causes the highest temperature to occur at a certain distance from the initial pool fire location.

In Fig.5.23 the maximum temperature together with the ventilation in time of points above and downstream of the fire location are shown. The graph suggests two possible worst-case temperature curve, one being the temperature development above the fire location and the other for points downstream of the original fire location in the vicinity of the flame tip. What is more, Fig.5.24 shows the maximum temperature of the points located in these two positions. These have been modelled considering the maximum recorded temperature. The two modelled worst-case temperature curves represents the following situations:

1. points above fire location experiencing steep initial temperature gradients (**pool2.5(#1)**);
2. points downstream of the fire experiencing constant temperature increase reaching the highest maximum temperature recorded in the tunnel (**pool2.5(#2)**).

### 5.3.4. POOL SIMULATION (v=3.5 M/S)

In this subsection the analysis of the same pool fire discussed in the previous subsection has been conducted with the only difference being the use of a ventilation of  $3,5 \text{ ms}^{-1}$ . The chosen maximum speed is slightly higher compared to the critical velocity calculated previously. The results of this FDS simulation are shown in the following pages. Two main differences have been recorded between the case using  $2,5 \text{ ms}^{-1}$  and  $3,5 \text{ ms}^{-1}$  ventilation:

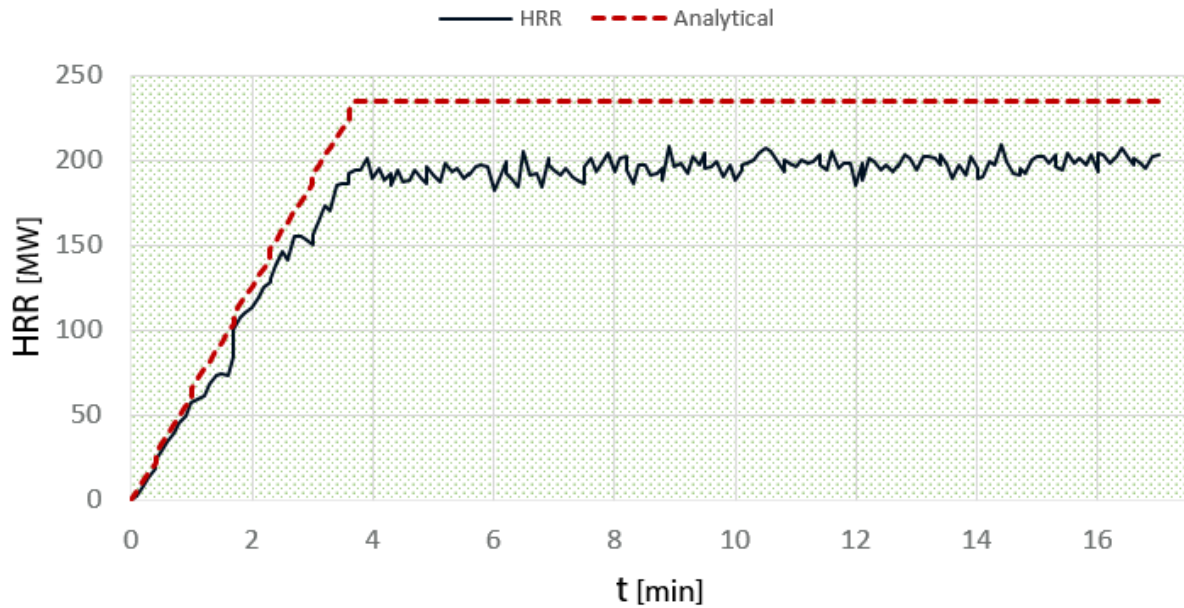


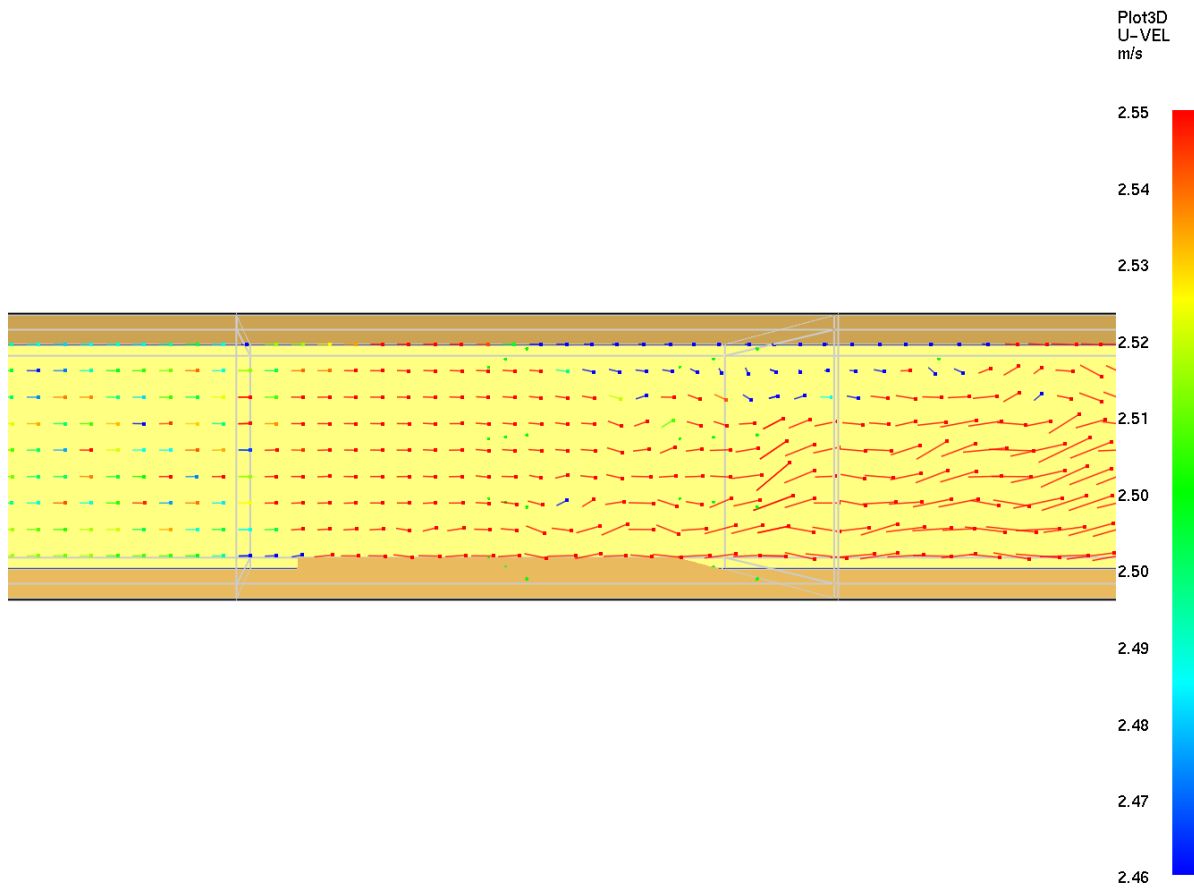
**Figure 5.20**

*HRR-pool fire (2.5 m/s)*

1. the use of an higher ventilation speed brings more oxygen towards the fire and enhances the combustion process. This is reflected by the higher HRR obtained in the simulation with  $3,5\text{ m s}^{-1}$  ventilation speed (Fig.5.26) compared to the one obtained with the simulation using a ventilation of  $2,5\text{ m s}^{-1}$  (Fig.5.20);
2. at the same time an higher ventilation helps both the heat to be extracted from the tunnel and the mixing of cold air with the hot smoke layer. This results in lower fluid temperature recorded downstream of the fire location. This phenomenon is confirmed by the results of the CFD calculations carried out by TNO in [59] for Rijkswaterstaat. In Fig.5.25 the maximum temperature calculated for the same scenario with the only difference being the ventilation velocity is shown. It can be noted that higher ventilation speeds cause a considerable reduction in the maximum temperature.

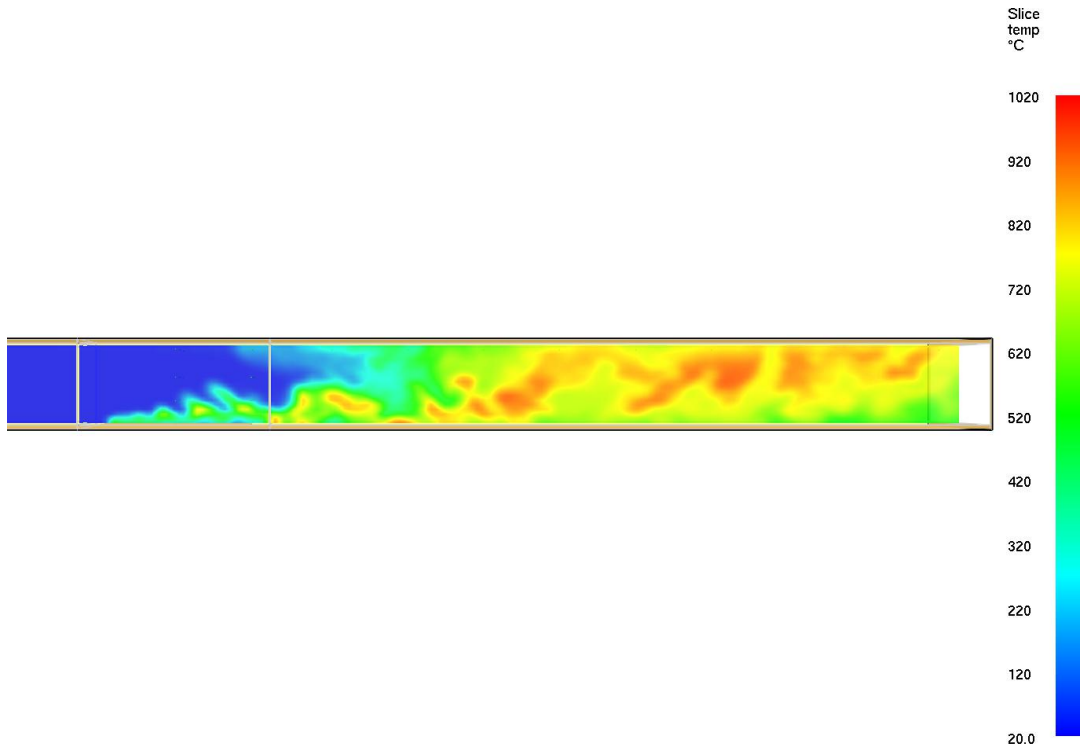


(a) Smoke development

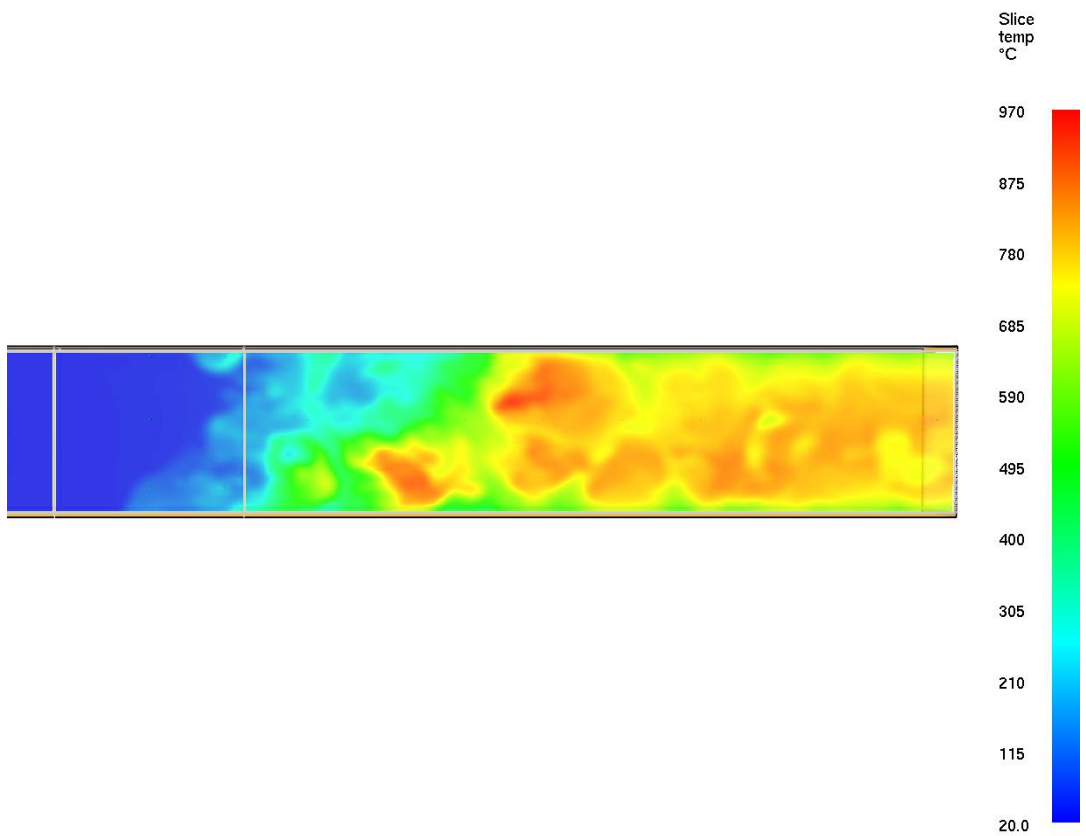


(b) Longitudinal air velocity

**Figure 5.21**  
Pool fire (2.5 m/s)-Smoke and air flow [5 min after ignition]



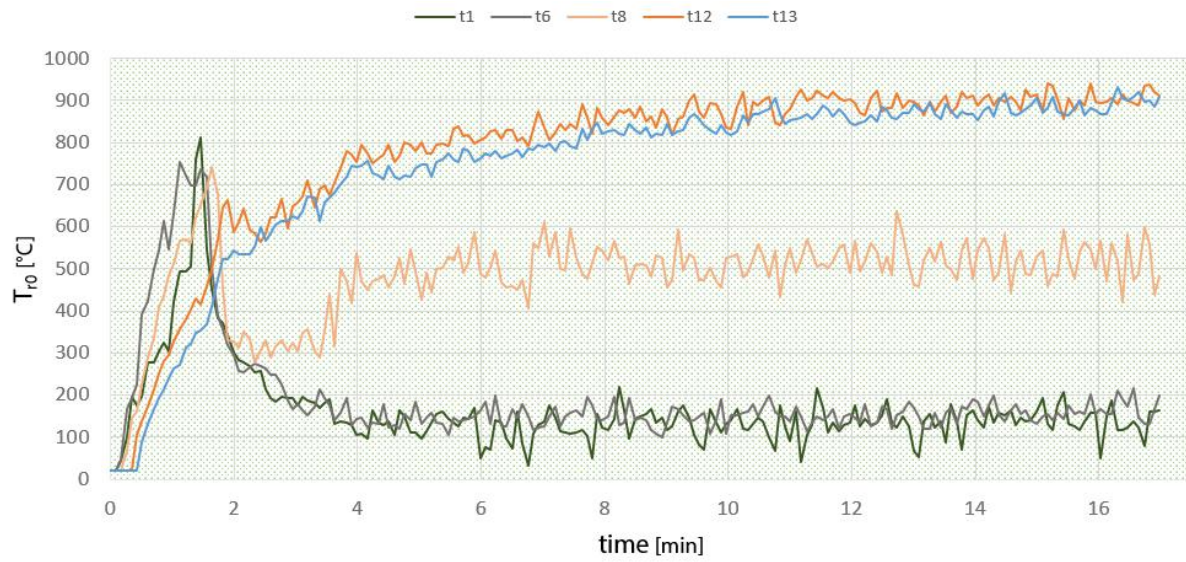
(a) Longitudinal plane at half width



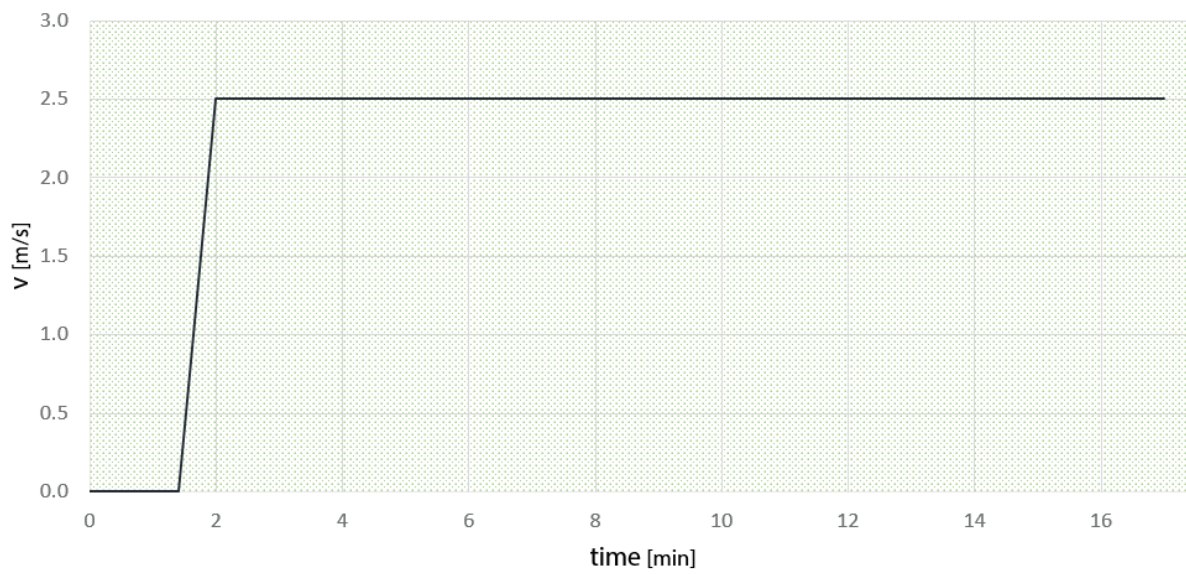
(b) Ceiling

**Figure 5.22**

*Pool fire (2.5 m/s)-Fluid temperature [5 min after ignition]*



(a) Maximum temperature



(b) Ventilation speed

**Figure 5.23**

*Pool fire (2.5 m/s)-Maximum temperature and ventilation*



**Figure 5.24**  
Pool fire (2.5 m/s)-Maximum temperature curves

Tijd [s]	inlaatsnelheid				
	1 [m/s]	2 [m/s]	3 [m/s]	5 [m/s]	10 [m/s]
0	10.0	10.0	10.0	10.0	10.0
30	71.5	77.6	53.7	38.6	29.6
60	625.0	457.0	267.0	162.0	100.0
100	1660.0	1270.0	835.0	516.0	291.0
200	2070.0	1570.0	1020.0	626.0	351.0
300	2180.0	1660.0	1080.0	652.0	362.0
400	2210.0	1690.0	1100.0	663.0	365.0
600	2230.0	1700.0	1120.0	669.0	367.0

**Figure 5.25**  
Maximum ceiling temperature-CFD simulation. Retrieved from [59]

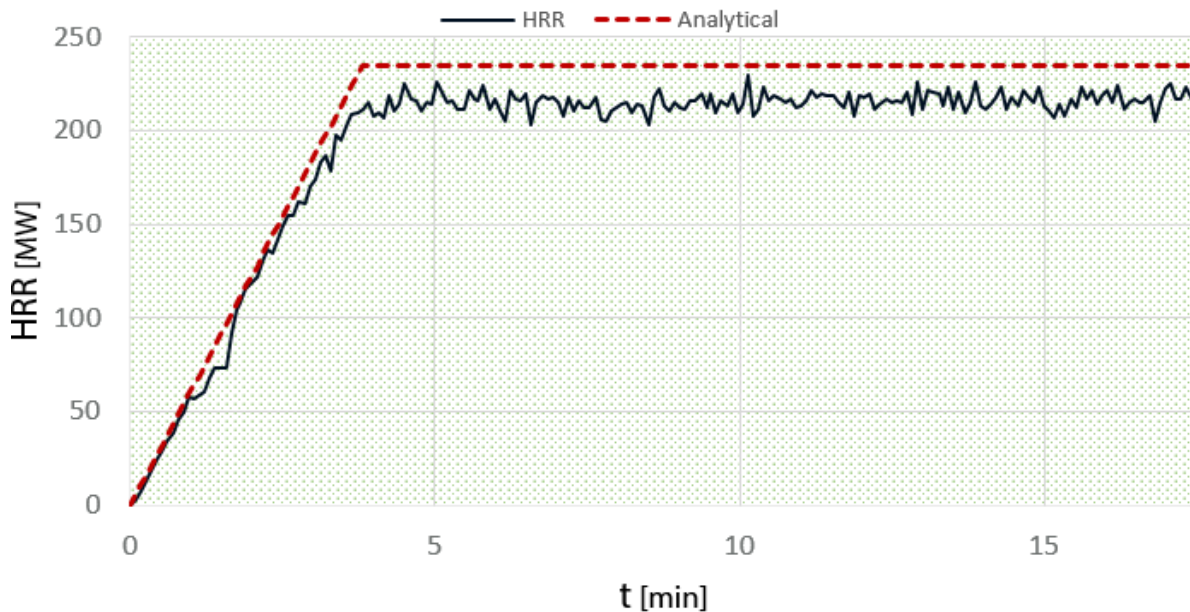


**Figure 5.26**  
*HRR-pool fire (3.5 m/s)*

### 5.3.5. DISCUSSION AND COMPARISON WITH PREVIOUS SIMULATIONS

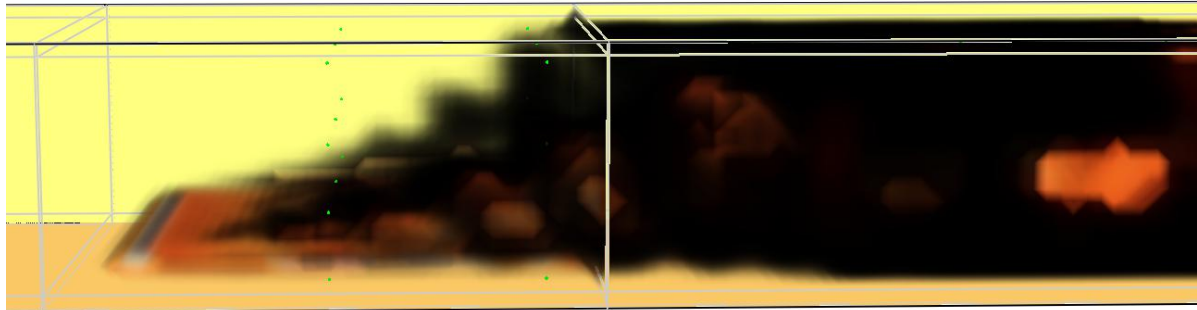
A discussion over the results obtained in this chapter in comparison with a representative simulation carried out in the past is carried out. In particular, we will focus on the results obtained by TNO and highlighted in [59]. This series of calculations was carried out for Rijkswaterstaat in order to better understand and study the worst-case fire scenarios in a tunnel and their consequences in terms of maximum temperature. It has to be pointed out that at the time it was carried out, the calculation was conducted in 2D and not 3D due to excessive computational time required.

In Fig.5.25 the maximum recorded temperature for a pool fire with the following characteristics are shown:

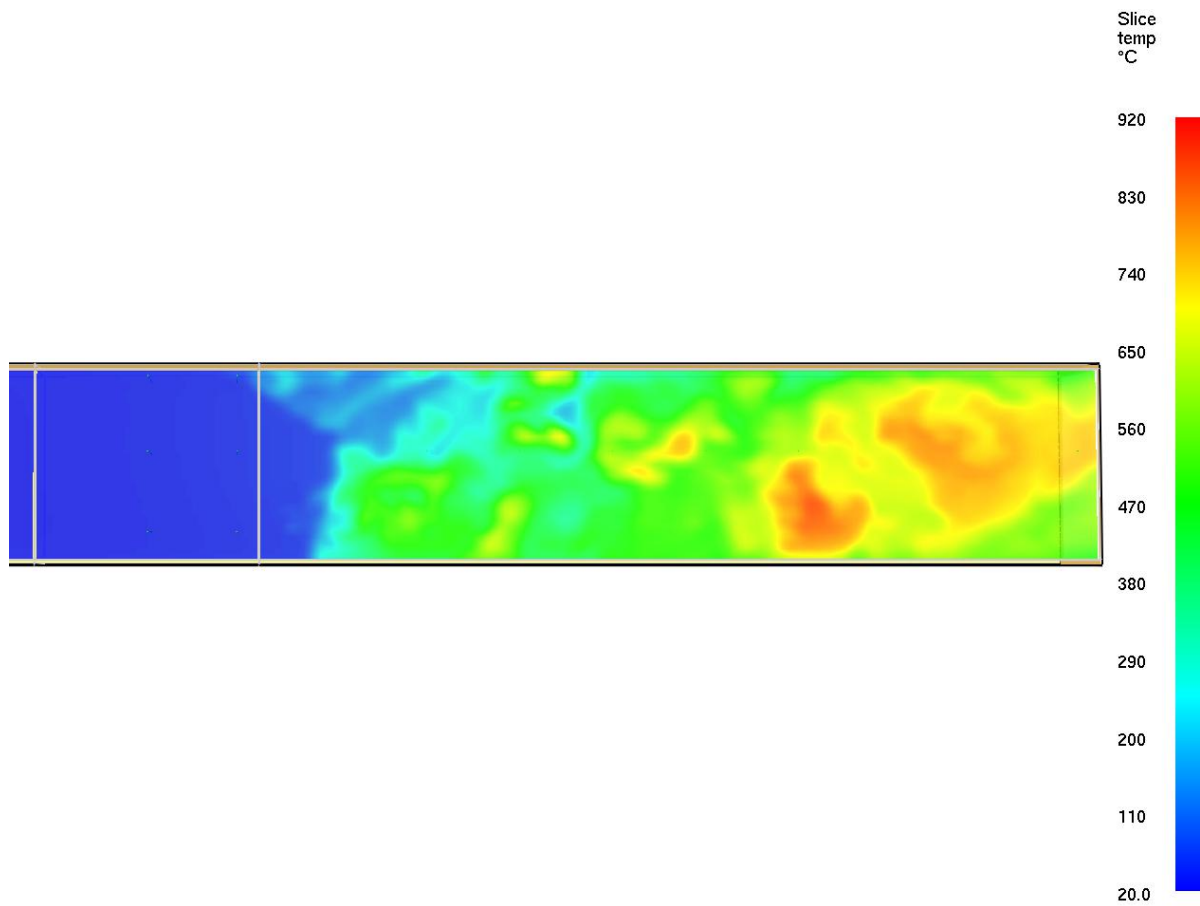
- 2 lanes tunnel, 10m wide and 5 m high;
- tunnel of total length of 600m, composed by two inclined sections at the sides (4%) of 200 m and a flat section of 200 m in the middle;
- pool fire of 301 MW with a surface of 142 m<sup>2</sup>, which is equivalent to a pool of approximately 13,4 m diameter;
- fire duration of 37 min;
- fire occurring in the middle of the tunnel;
- the leakage is described by a "Hole" condition (Table 4.1);
- fuel heat of combustion equal to 44 100 kJ kg<sup>-1</sup>.

The tunnel cross section of the above mentioned simulation and the one used for the simulations of this thesis, highlighted earlier in this chapter, are approximately the same. At the same time, the pool fires have a similar diameter. These hypothesis allow us to compare and discuss the results coming from the two simulations. We will only focus on the maximum temperature.

5



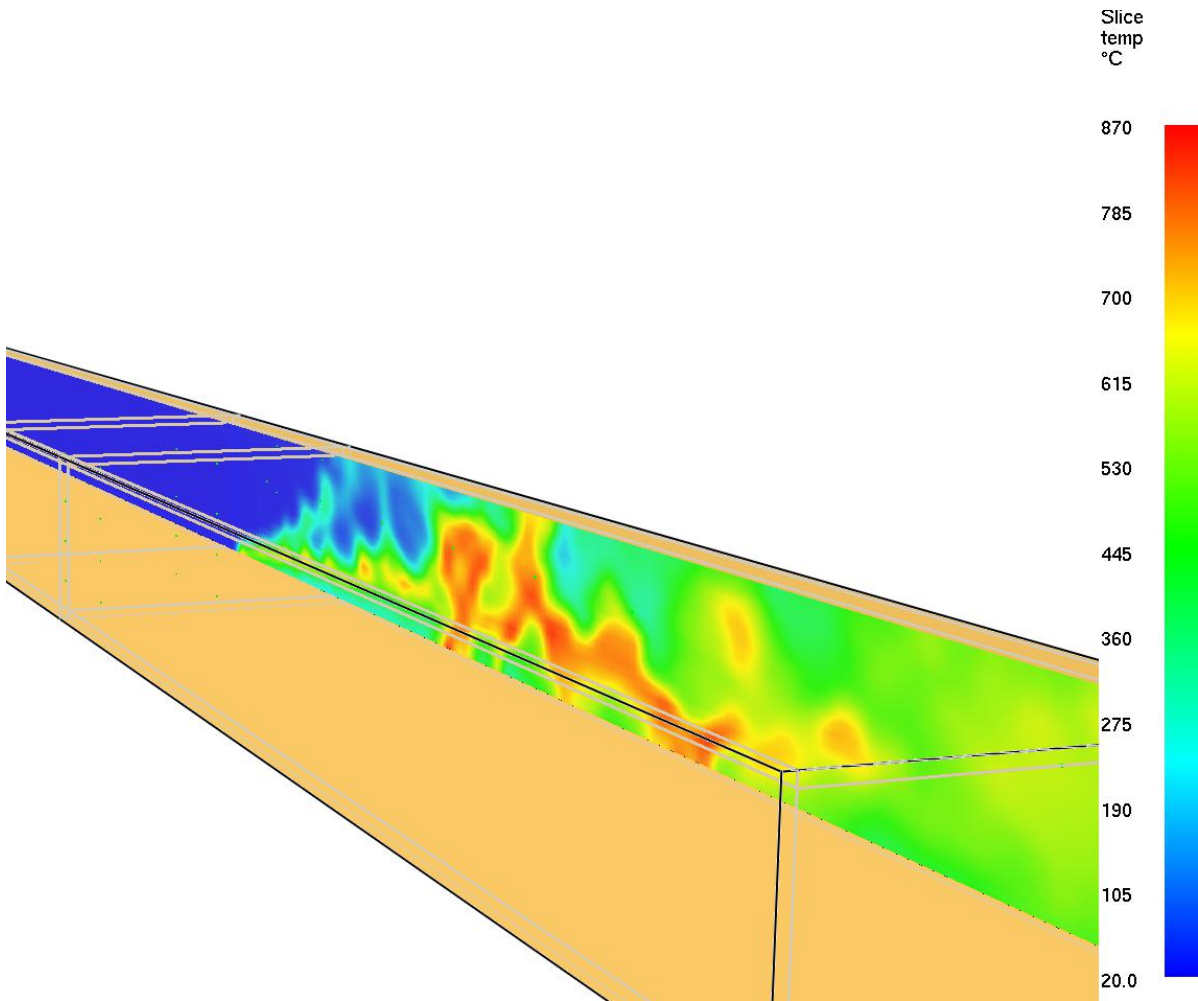
(a) *Smoke development*



(b) *Ceiling fluid temperature*

**Figure 5.27**

*Pool fire (3.5 m/s)-Smoke and ceiling fluid temperature [5 min after ignition]*



5

**Figure 5.28**  
Pool fire (3.5 m/s)-Side wall fluid temperature

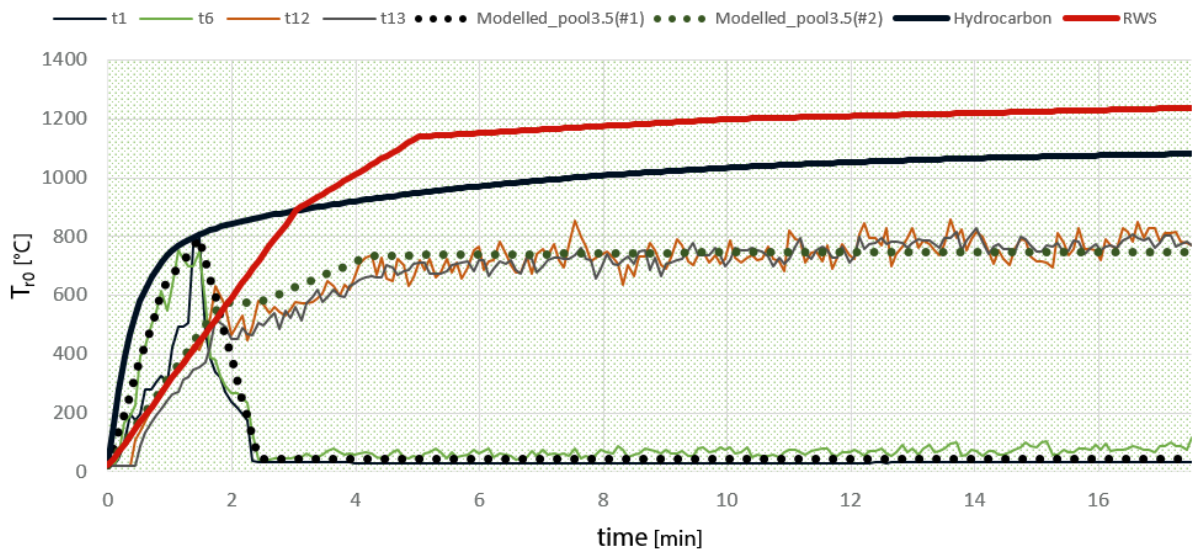


**Figure 5.29**  
Pool fire (3.5 m/s)-Maximum temperature curves

The results of the calculations in [59], from now on defined as "*Simulation I*", suggest that for ventilation speeds between  $2 - 3 \text{ m s}^{-1}$  the maximum temperature lies in the range between  $1700 - 1120^\circ\text{C}$ . These temperature are quite severe and for the former case it overshoots the maximum temperature used in the RWS curve of more than  $200^\circ\text{C}$ . On the other hand, looking at the results obtained in this thesis for a pool fire with  $2,5 \text{ m s}^{-1}$  in subsection 5.3.3, from now on defined as "*Simulation II*", the maximum temperature recorded is considerably lower. In the first 17 min of simulation the maximum recorded temperature was  $911^\circ\text{C}$ .

The huge difference in the maximum temperature highlighted above might raise doubts over the validity of the results obtained in this thesis. This is not the case if a detailed analysis is carried out over the hypothesis used in the two simulations and their differences. The following points highlights the differences:

- *Simulation I* is carried out considering a 2D model while *Simulation II* a 3D one;
- the pool diameters and consequently the HRR are different between the 2 simulations. One being 235 MW and the other 301 MW;
- *Simulation I* uses a tunnel 600 m long with inclined parts, while *Simulation II* uses a flat tunnel of 100 m length;
- *Simulation I* uses a heat of combustion of  $44\,100 \text{ kJ kg}^{-1}$ , while *Simulation II* of  $29\,903 \text{ kJ kg}^{-1}$ .

The different hypothesis that have been used, in particular the different heat of combustion, explain the results. It has to be noted that the two simulations run for different time frames. There is the possibility that *Simulation II*, if run for 37 min it would cause a higher temperature to be present in the tunnel. On the other hand, the temperature development of *Simulation II* seems to stabilize around a temperature that is considerably lower compared to the RWS and *Simulation I* value.

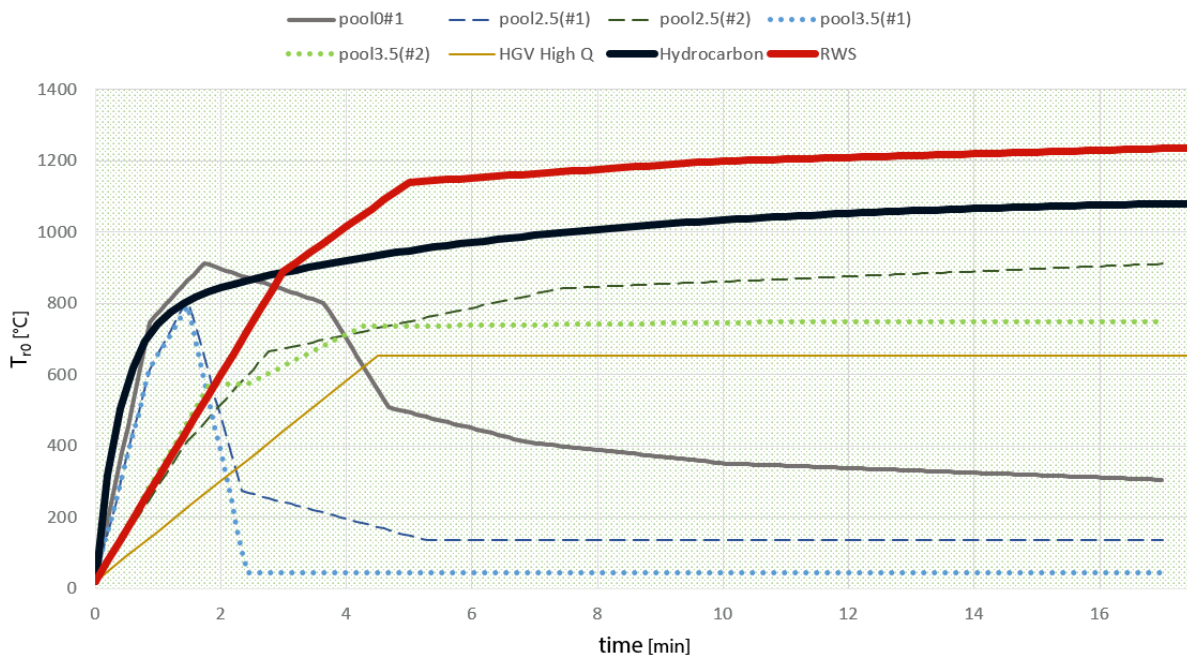


**Figure 5.30**  
*Fire curves comparison*

## 5.4. CONCLUSIONS

Based on theory exposed and the results obtained in this chapter, with respect to the thesis objectives, the following conclusions can be drawn:

### 1-DERIVE MOST PROBABLE FIRE SCENARIOS

- both analytical calculations and CFD simulations confirm that not the whole cross-sectional internal surface of a tunnel is exposed to the high temperatures caused by the fire at the same time;
- oxygen availability is one of the most fundamental parameters to be taken into consideration when designing a tunnel against fire;
- oxygen availability and distribution within the tunnel during a fire are interconnected to many other aspects, such as cross section dimensions, energy content of the fire source and ventilation. Following the work carried out in this thesis, these three aspects have shown the biggest influences in defining the temperature output of a given fire;
- the use of ventilation in a fire causes different points along the tunnel to experience significantly different fire loads. This leads to the possible need to use multiple worst-case fire temperature curves to check the tunnel structural safety against fire.

### 3-COMPARE STANDARD DESIGN FIRE CURVES WITH PROBABLE FIRE SCENARIOS

- in general terms, comparing the scenarios considered in this thesis and the design fire curves (Fig.5.30), the following points can be concluded:
  - the initial temperature gradient of the design fire curves finds confirmation in the worst scenario gradients that have been calculated in this thesis;
  - the maximum temperature predicted by the design fire curve seems to be an overestimate of approximately 200-400 °C;

- later in Chap.6 the importance of the combined effect on the spalling mechanism of both temperature gradient and elevated maximum temperature for long periods of time is discussed. The scenarios considered above suggest that a concrete element could only experience one of the above mentioned phenomena and never both at the same time. This is not the case for the design fire curves used in current practice, which have both a steep temperature gradient and elevated maximum temperature.
- a proper definition of the hypothesis to be used in the CFD simulations is fundamental. These must represent in the proper way the scenario under consideration. As highlighted in subsection 5.3.5, different hypothesis can result in outcomes that could be quite dissimilar.

# 6

## NSC SPALLING MECHANISM - 1ST VERSION

*This chapter is dedicated to the development of a spalling model based upon the idea of describing the phenomenon as an equivalent buckling instability failure. The whole spalling model is based upon the idea of a series of two failures:*

- *Buckling failure treated in the "Preliminary approach" section;*
- *Crack failure treated in the "Detailed approach" section.*

*Initially a section dedicated to the development of the model in agreement with full-scale test results is described. Subsequently, the NSC spalling mechanism model is described. The model is composed of two parts, namely Preliminary approach and Detailed approach, and they make use of the following models:*

### *PRELIMINARY APPROACH:*

1. *Column spalling model.*

### *DETAILED APPROACH:*

1. *Stress model;*
2. *Optimal thickness model;*
3. *Crack model.*

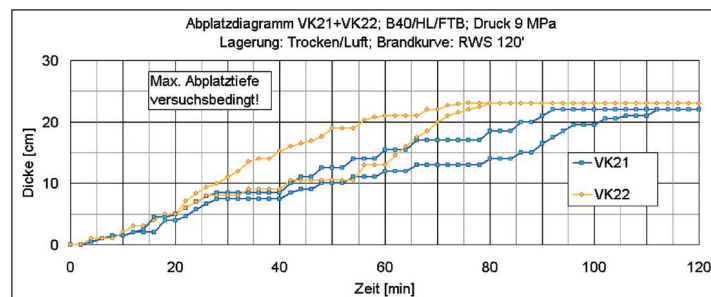
*A section is then dedicated to the elaboration and discussion over the results obtained with the model proposed in this chapter. Finally conclusions over the topics treated in this chapter are drawn.*

### **6.1. SPALLING TEST RESULTS**

In order to have info and data regarding the spalling mechanism, test results were searched in literature. A series of tests carried out by FSV [31] was found valuable and of interest to base the spalling model upon. The tests mentioned earlier are carried out on concrete elements (1400x1800x500 mm) with a load applied in the longitudinal direction through prestress. In the transverse direction, prestress is also applied. The transversal prestress load is applied with a magnitude such to simulate a fully clamped condition in that direction. In this way a plane strain situation simulating an infinitely long cross section can be achieved. In Fig.6.1a an example of the test setup is shown. The



(a) Test setup



(b) Spalling test results

**Figure 6.1***FSV544 Spalling Tests [31]*

tests were carried out on multiple elements with different characteristics. In particular: different loads applied, different concrete types, different aggregate types, different fire curves used.

The initial focus of this thesis is on the data coming from NSC elements. A list of the considered test results used with the different characteristics of each test is shown in Table 6.1. In particular, of great importance are the results showing the behaviour of the spalling mechanism in time. In Fig.6.1b an example of it is shown, where the spalling depth in time is shown.

In order to understand and model the spalling mechanism we will only focus on the first piece that spall. In Table 6.1 the first spalling depth ( $t$ ) and time of occurrence ( $t_1$ ) are listed.

## 6.2. PRELIMINARY APPROACH

In order to model the spalling mechanism, a preliminary approach based on the buckling behaviour of the spalled piece regarded as a column was chosen. The idea of modelling the spalling mechanism as a buckling problem comes from the work done by Lottman [34] and explained in Chap. 3. Modelling the problem as a buckling instability failure allows to include in the model the effect of the imposed thermal deformations in the spalling mechanism. On the other hand, the proposed model does not take into account the effect of the pore pressure. This follows the considerations over the limited influence on the spalling mechanism of the pore pressure in a cracked element as highlighted in subsection 3.5.2.

### 6.2.1. COLUMN SPALLING MODEL

In order to model the spalling mechanism as a buckling problem, we refer to Fig.6.2a. For the moment it is assumed that the concrete is cracked at a certain known depth ( $t$ ). This detached piece, modelled as a rectangular beam, is the piece prone to spall. It is assumed that the piece has a known

**Table 6.1**  
List of spalling test results

Test	Fire Curve	Calc/Silic	$f_{cm}$ [Mpa]	$\sigma_{ext}$ [Mpa]	t [mm]	t1 [min]
VK01	RWS 120 (red.)	C	33	1.16	21	12
VK02	RWS 120	C	33	1.16	20	6
VK05	RWS 120	C	33	1.16	18	4
VK06	RWS 120	C	33	1.16	22	3
VK11	RWS 120	C	33	9	26	2
VK12	RWS 120	C	33	9	31	1.5
VK19	ETK 240	C	33	1.16	21	7
VK20	ETK 240	C	33	1.16	16	4
VK21	RWS 120	C	38	6.5	15	4
VK22	RWS 120	C	38	6.5	10	2
VK33	Lainz 180	S	33	1.16	15	3
VK34	Lainz 180	S	33	1.16	32	2.5
VK43	RWS 120	S	33	1.16	17	3
VK44	RWS 120	S	33	1.16	17	3
VK58	Lainz 180	S	33	1.16	16	4
VK59	Lainz 180	S	33	1.16	33	4

buckling length ( $l_{buc}$ ), which will be searched later on. The detached piece is part of the element, which is in general subjected to an external load ( $F$ ) and on the external side exposed to a fire curve. The fire curve causes the element to be subjected to a temperature gradient which decreases into the cross section.

Assuming the spalling mechanism can be studied as a buckling problem, the spalled piece is regarded as a column of rectangular cross section, with dimensions equal to the thickness of the spalled piece ( $t$ ) and the width of the element. In general the acting load ( $F_{Ed}$ ) is composed by the external load ( $F$ ) and the thermal load ( $F_{\Delta T}$ ) caused by the imposed deformation. The spalled piece (column) is regarded as fully clamped at the supports. The resistance ( $F_{Rd}$ ) is given by the Euler buckling resistance ( $F_{buc}$ ). In the equations below the acting load and the resistance are related to each other.

$$F_{Ed} \geq F_{Rd} \quad (6.1)$$

$$F + F_{\Delta T} \geq F_{buc} \quad (6.2)$$

$$\sigma \cdot A + E_c(T) \cdot \varepsilon_c(T) \cdot A \geq \frac{\pi^2 \cdot E_c(T) \cdot I}{l_{buc}^2} \quad (6.3)$$

$$\sigma \cdot bt + E_c(T) \cdot \varepsilon_c(T) \cdot bt \geq \frac{\pi^2 \cdot E_c(T) \cdot bt^3}{l_{buc}^2 \cdot 12} \quad (6.4)$$

In order to take into account the imposed deformation caused by the temperature into the calculation procedure, it is decided to take a constant temperature. Since the temperature profile has a gradient, it is decided to take an average of the temperature over the spalled piece thickness. This is shown in Fig. 6.2b. At the same time, the Young's Modulus ( $E_c(T)$ ) and the thermal elongation ( $\varepsilon_c(T)$ ) are temperature dependent. The behaviour with temperature of this quantities is shown in Fig. 6.3.

The model is independent of the width of the spalled piece ( $b$ ) as can be seen in eq. 6.4, where the width is present at both sides of the equation.

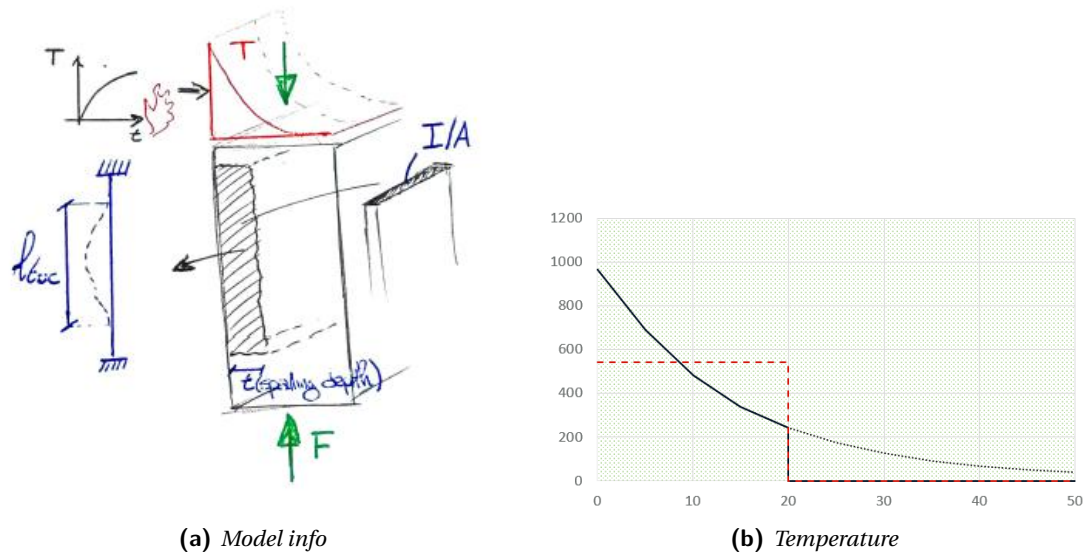


**Figure 6.2**  
Column spalling model

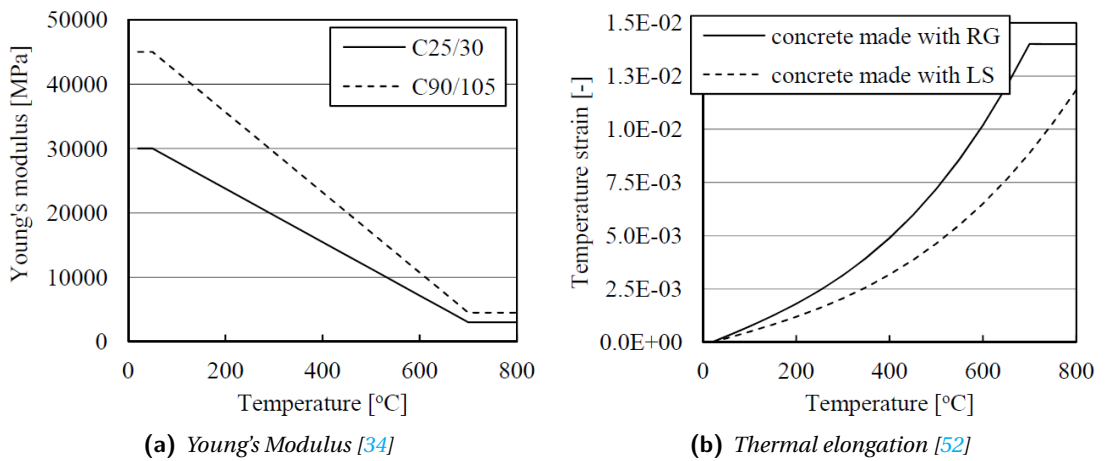


**Figure 6.3**  
Concrete characteristics with temperature



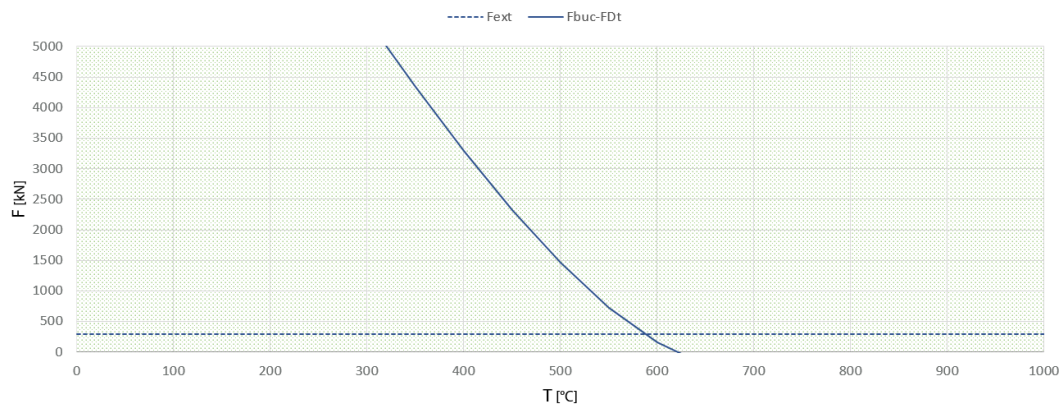
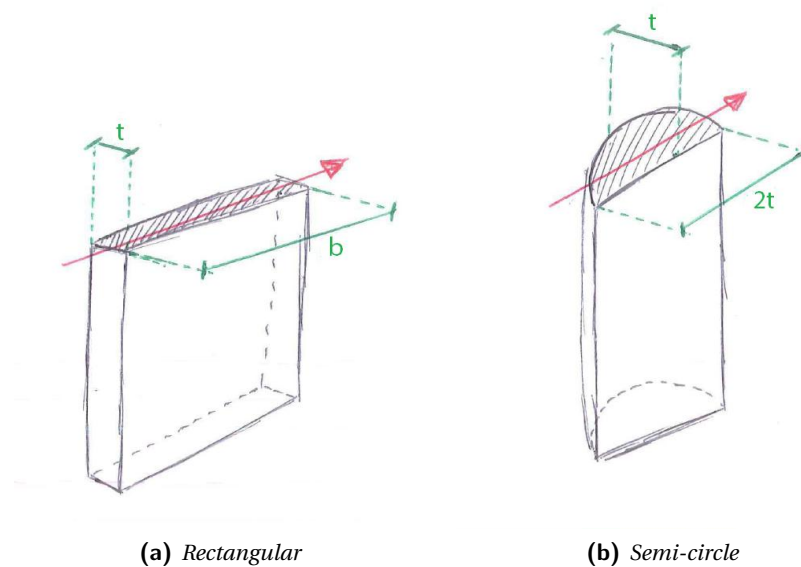


**Figure 6.5**  
*Example result using column spalling model*



(a) *Rectangular*

(b) *Semi-circle*

**Figure 6.6**  
*Column cross sectional shapes*

#### CROSS SECTION SENSIBILITY CHECK

In order to check whether the model is dependent on the chosen rectangular column shape, the same procedure was followed for a column modelled as a semi-cylinder (Fig. 6.6b). The model calibration was repeated with the new buckling length values and the same characteristics used above (thickness, concrete and aggregate type, etc.). The result was compared with the previously obtained result using the rectangular section. The minimum temperature for the piece to spall, differs by only 2.5 %. Considering the numerical approximations that have been carried out, the difference is considered negligible and the column spalling model is considered independent from the chosen shape.

#### PARAMETRIC STUDY

In order to explore the possibilities and the results offered by the column spalling model, a parametric study was carried out varying the following parameters:

- buckling length (Fig. 6.7);

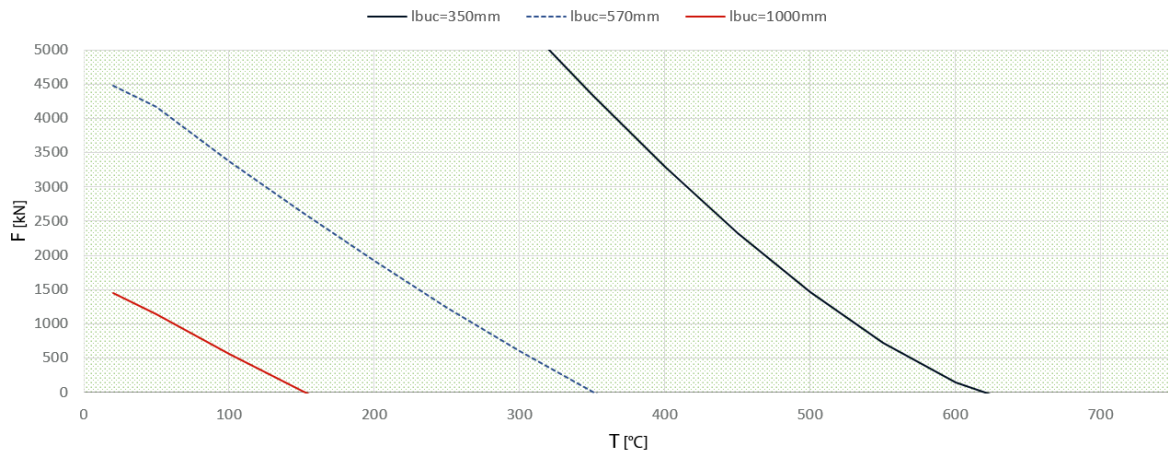


**Figure 6.7**  
*Buckling length variation*

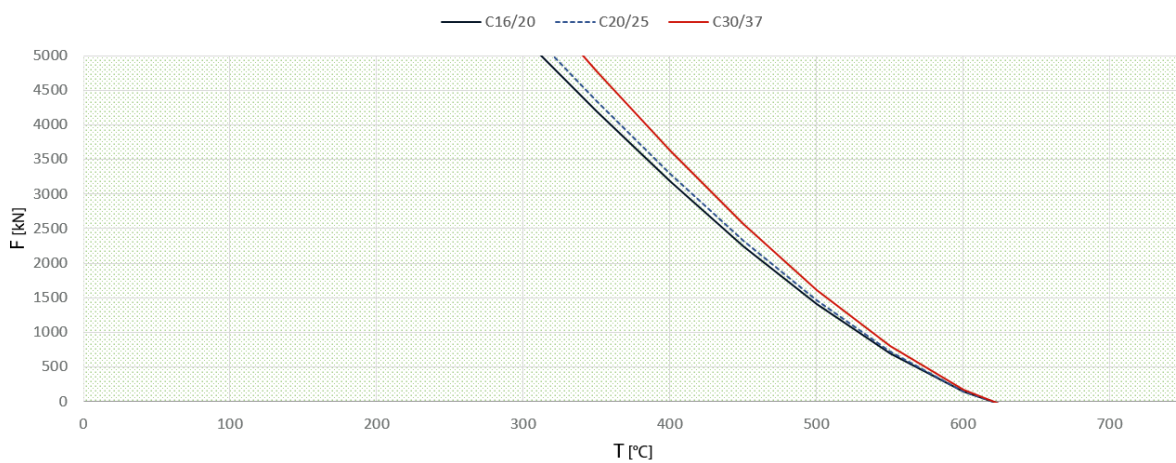


**Figure 6.8**  
*Initial Young's modulus variation*

- Young's modulus (Fig. 6.8);
- Aggregate type (Fig. 6.9);
- thickness (Fig. 6.10);
- external load (Fig. 6.11).

The following results are highlighted:

1. as expected, a longer buckling length and smaller thickness causes the piece to spall at a lower averaged temperature. This means sooner in time;
2. initial Young's modulus have almost no influence on the temperature causing spalling. This is related to the same reduction with temperature of the Young's modulus in both the buckling resistance ( $F_{buc}$ ) and in the force resulting from imposed deformations ( $F_{\Delta T}$ );
3. as experienced in practice, for a higher load, the average spalling temperature reduces and spalling occurs sooner in time;

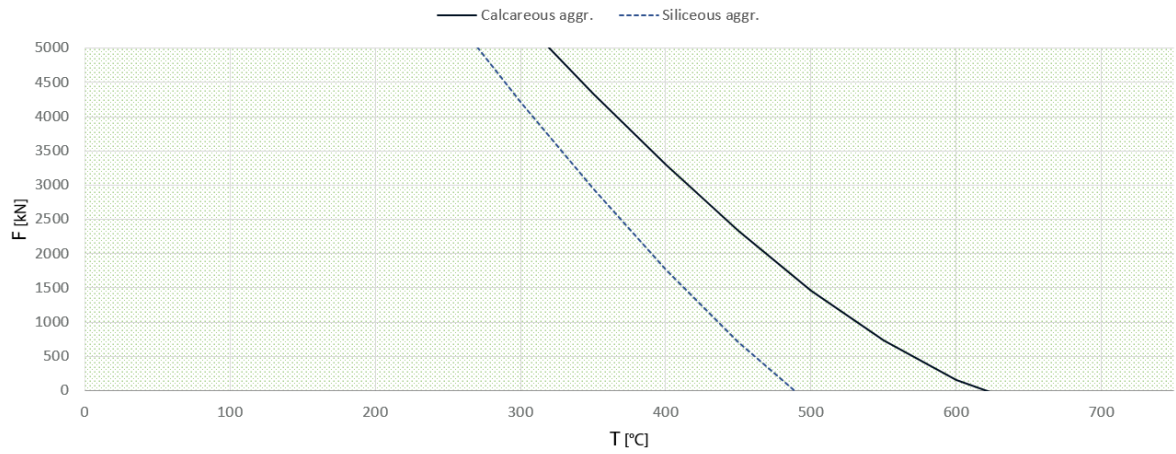


**Figure 6.9**  
*Aggregate type variation*

6

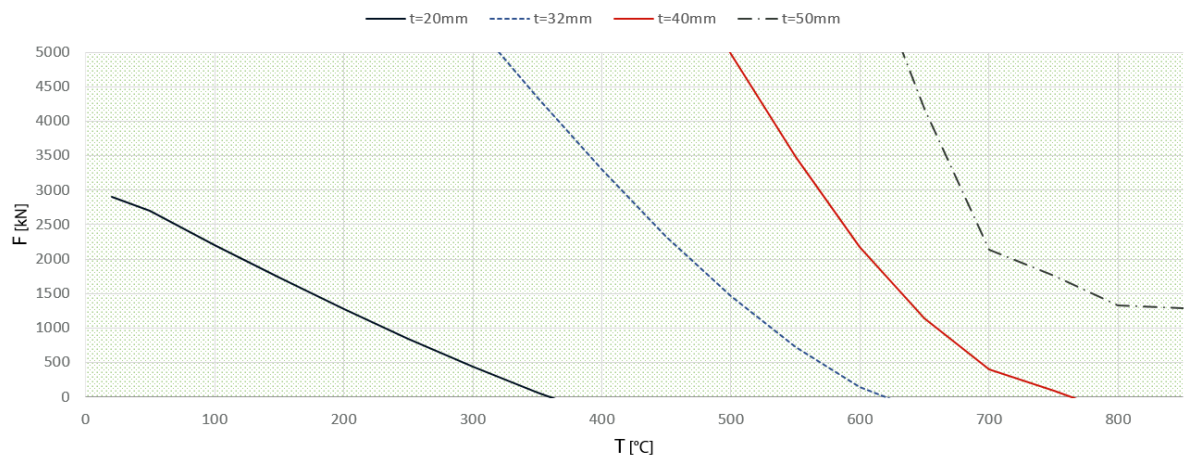


**Figure 6.10**  
*Thickness variation*

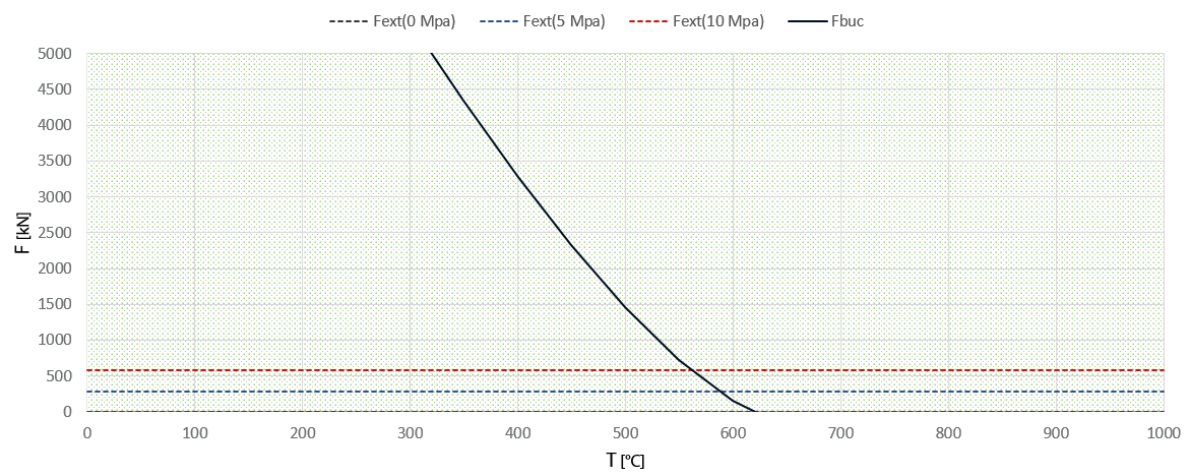


**Figure 6.11**  
*External force variation*

4. the aggregate type plays a major role in the spalling behaviour. This is related to the thermal expansions experienced by different aggregates subjected to elevated temperatures.

### 6.3. DETAILED APPROACH

The preliminary approach explained earlier obtains promising results in terms of describing the spalling mechanism for NSC. But, 2 important questions arise and need additional considerations:

1. *What thickness should be considered for the spalled piece? Is the aggregate size an appropriate choice? Is there an optimal thickness that has a higher probability to spall?*
2. *Given a certain thickness, is it true that the surface at that depth is cracked and the spalled piece is indeed free to spall? Is it possible to check whether or not a crack is present?*

In order to answer the above mentioned questions an additional part is added to the preliminary approach. This *detailed approach* will focus on understanding if a crack is present at the rear of the spalled piece as well as research if an optimal thickness is prone to spall.

#### 6.3.1. STRESS MODEL

In order to answer to the questions above the mechanics involved for a fire exposed concrete element need to be considered. For this reference is made to Lottman [34] which gives formulas to calculate the stresses in the cross section exposed to a single sided fire while subjected to external load and support conditions.

An overview of the model is shown in Fig.6.12a. In Fig.6.12b an example of the stresses present in the concrete element partially restrained subjected to external loading is shown.

#### PARAMETRIC STUDY

In order to explore the possibilities and the results offered by the stress model, a parametric study was carried out varying the following parameters:

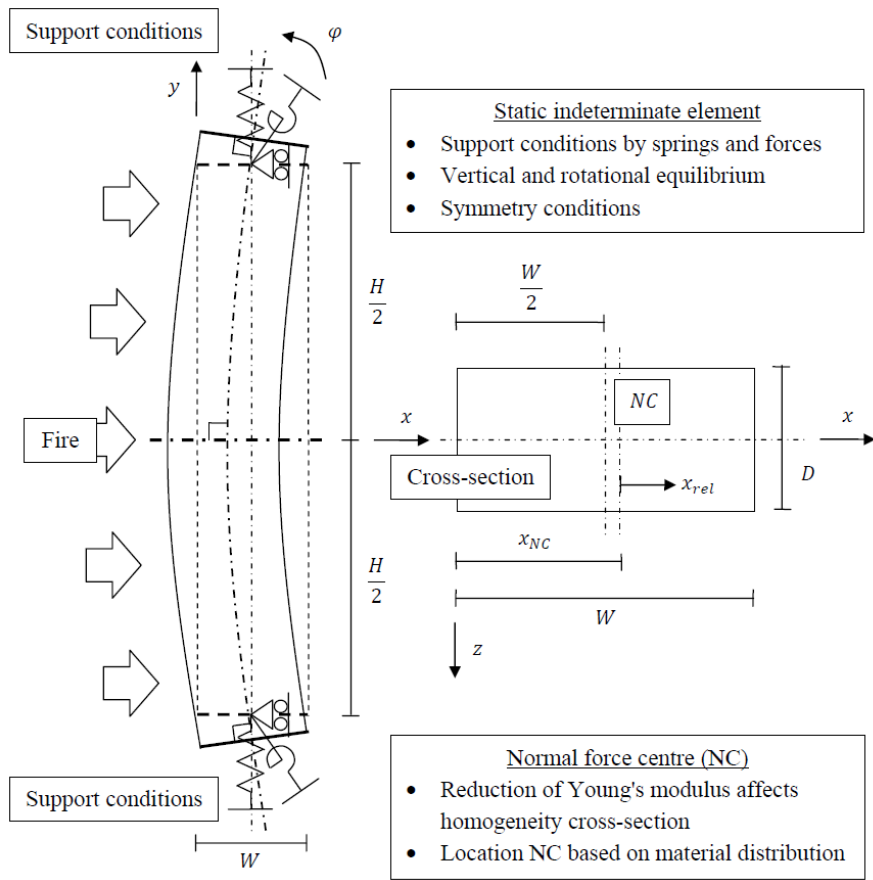
- springs stiffness (Fig.6.13a);
- external load (Fig.6.13b).

The following results can be highlighted:

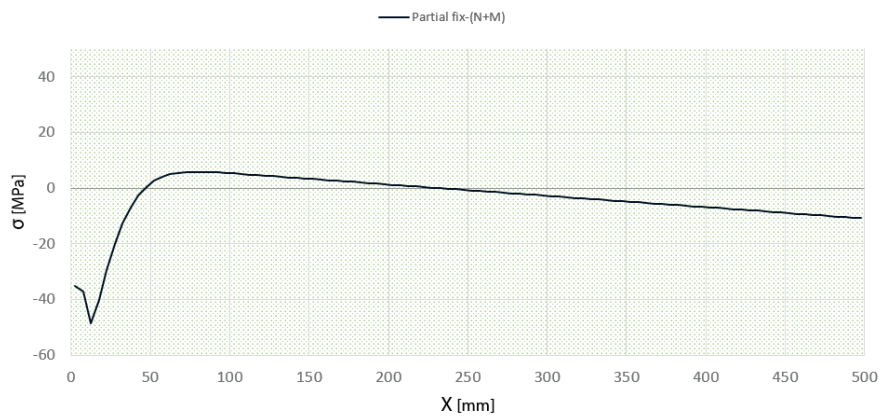
1. increased compression shifts the stresses towards the compressive side. So the point at which the stresses change sign shifts away from the fire exposed side (Fig.6.13b);
2. a fully restrained element cause higher compression stresses to be present on the fire exposed surface compared to a partial restrained one. At the same time, a reduction of the level of restraint cause the non exposed surface to experience higher tensile stresses.

#### 6.3.2. OPTIMAL THICKNESS MODEL

With the knowledge of the stresses in the cross section calculated with the model explained above (*Stress model*), we are now able to do some considerations regarding the optimal thickness prone to buckle and cause spalling. Referring to eq.6.2 it can be stated that the force acting on the spalled piece ( $F + F_{\Delta T}$ ) is related to the stress acting over a certain area, which represent the spalled piece. The *Stress model* allows us to have a more precise estimate of this force taking into account the structural restraint. *If we now compare, for every possible thickness, the buckling force resistance ( $F_{Rd}$ ) and the acting load ( $F_{Ed} = \sigma \cdot A$ ), which includes both external load and thermal expansion, we can find for which thicknesses the load overcomes the resistance and spalling can occur. The optimal*

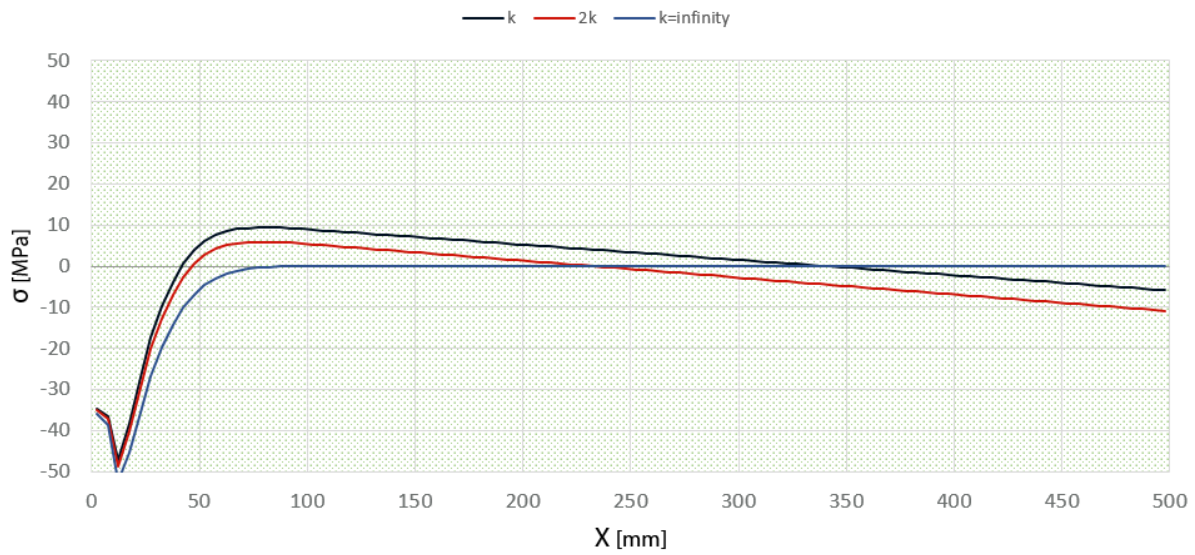


(a) Stress model idealization [34]

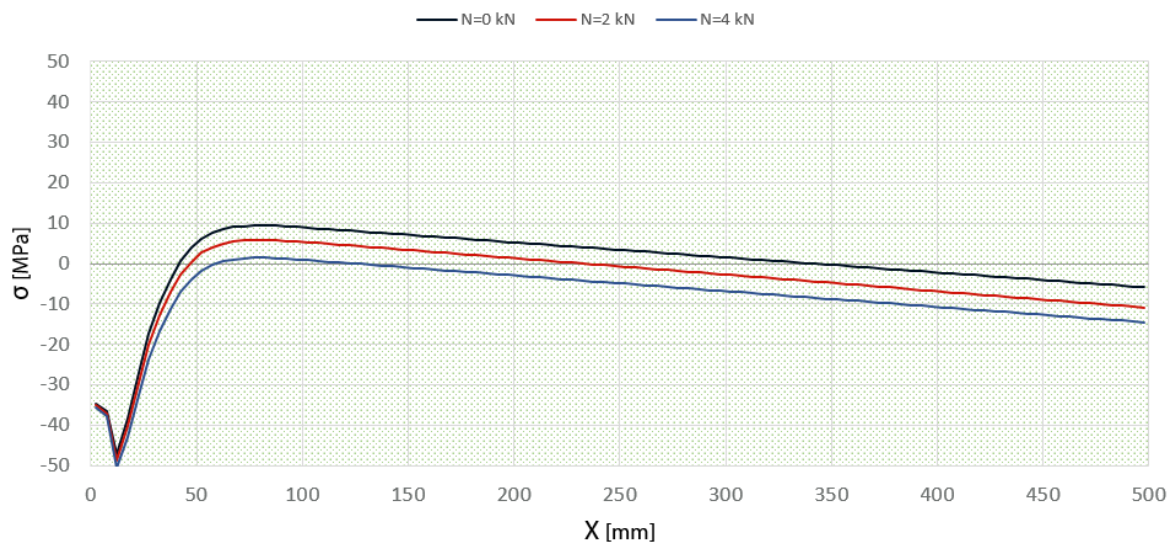


(b) Example stress-partially restrained element

**Figure 6.12**  
Stress model info



(a) Boundary spring stiffness



(b) External force

**Figure 6.13**  
Stress model-parametric study

thickness is the one that has the higher probability to cause buckling and is in this case the thickness with a higher difference between the load and the resistance ( $\Delta F$ ).

$$\Delta F = F_{buc} - F_{Ed}$$

In order to carry out this calculation there is the need to discretize the section, as shown in Fig.6.14a, and for every thickness knowledge of the following quantities is needed:

- the average temperature over a given thickness, calculated using the Lining temperature profile (section 4.8);
- the average Young's modulus, based on the average temperature of every thickness;
- the average thermal elongation, based on the average temperature of every thickness;
- the average stress, calculated based on the stress model (subsection 6.3.1).

In Fig.6.14b an example showing the optimal thickness for a partially restrained concrete element is shown.

## 6

### 6.3.3. CRACK MODEL

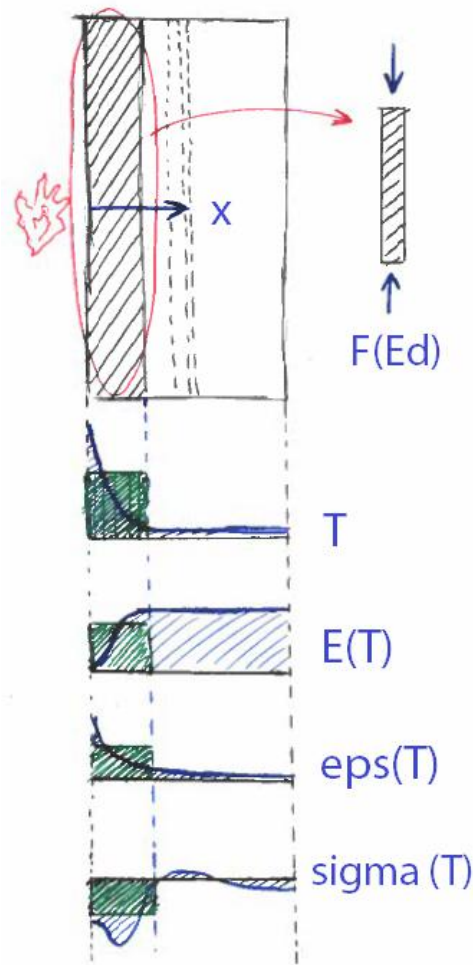
In order to explain the cracking mechanism and whether or not the concrete is cracked along the internal side of the spalled piece, a model based on strut & tie has been developed. The model idealization can be seen in Fig.6.15 and is composed of a double triangular truss. The width of the truss is equal to two times the spalled piece thickness. This is due to the fact that the crack is assumed at the middle of the horizontal truss since this direction is in tension. The length of the truss is taken equal to the buckling length (fixed and coming from the model calibration) and the force acting at the nodes is proportional to the average stress over the thickness. The stress comes from the previously mentioned *Stress model* (subsection 6.3.1). In the case the average stress results in tension, the force acting is assumed to be null. This is related to the fact that in that case the horizontal truss is subject to compression which do not give rise to cracks in the concrete.

An additional feature of the model is the load spreading from the 2 side nodes of the truss subjected to tension. It is assumed that the tension force spreads in the direction of the middle cracked surface of the model forming an angle of 45°. This can be better visualized checking Fig.6.16a. In the same figure the expressions to calculate the loads acting on the strut & tie model are highlighted. The angle  $\alpha$  depends on the geometry of the spalled piece consisting of the fixed buckling length ( $l_{buc}$ ) and the thickness ( $t$ ) and can be calculated as follows:

$$\alpha = \arctan \frac{2t}{l_{buc}} \quad (6.5)$$

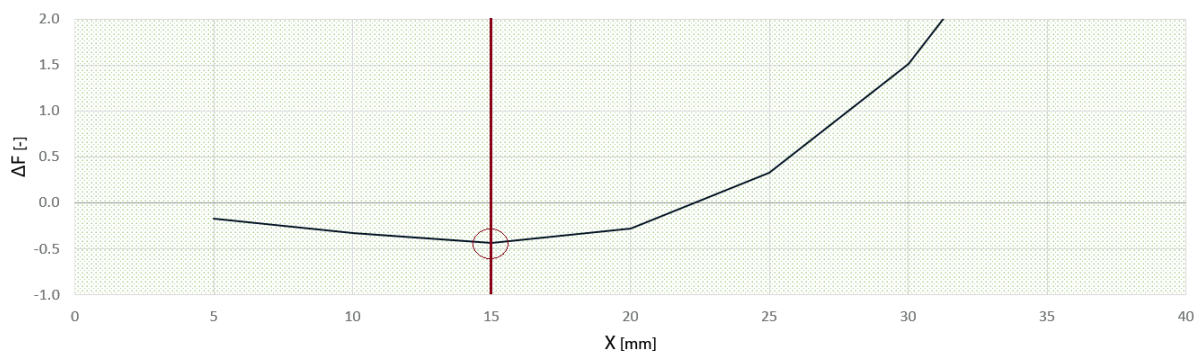
In a nutshell, the tension force is determined based on the spalling piece angle ( $\alpha$ ) while the tensile stress governing the crack formation is based on the 45° spreading angle. This implies that an initial crack of smaller length compared to the buckling length forms first. Subsequently, during the continued compression, the crack propagates till the formation of the spalled piece. This can be visualized in Fig.6.16b.

The tensile stress is compared to the tensile strength of the concrete which is temperature dependent. Based on the Lining temperature profile shown in section 4.8, an average temperature can be calculated for all thickness. In Fig.6.17 an example showing the tensile stress and tensile strength for different thickness of a partially restrained element is given. It can be noted that above a certain thickness, the element becomes too thick and the crack cannot develop anymore. This effect limits the maximum thickness of a piece that could be prone to spalling.



6

(a) Element thickness discretization



(b) Optimal thickness example

**Figure 6.14**  
Optimal thickness model info

6

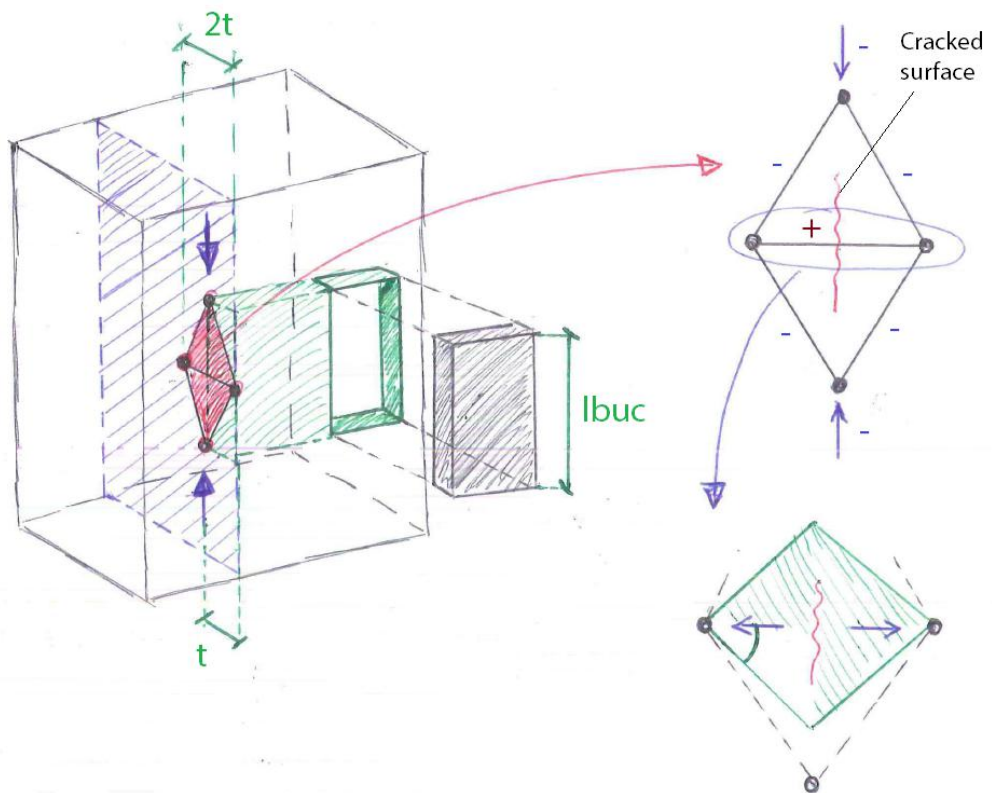


**Figure 6.15**  
*Crack model idealization*

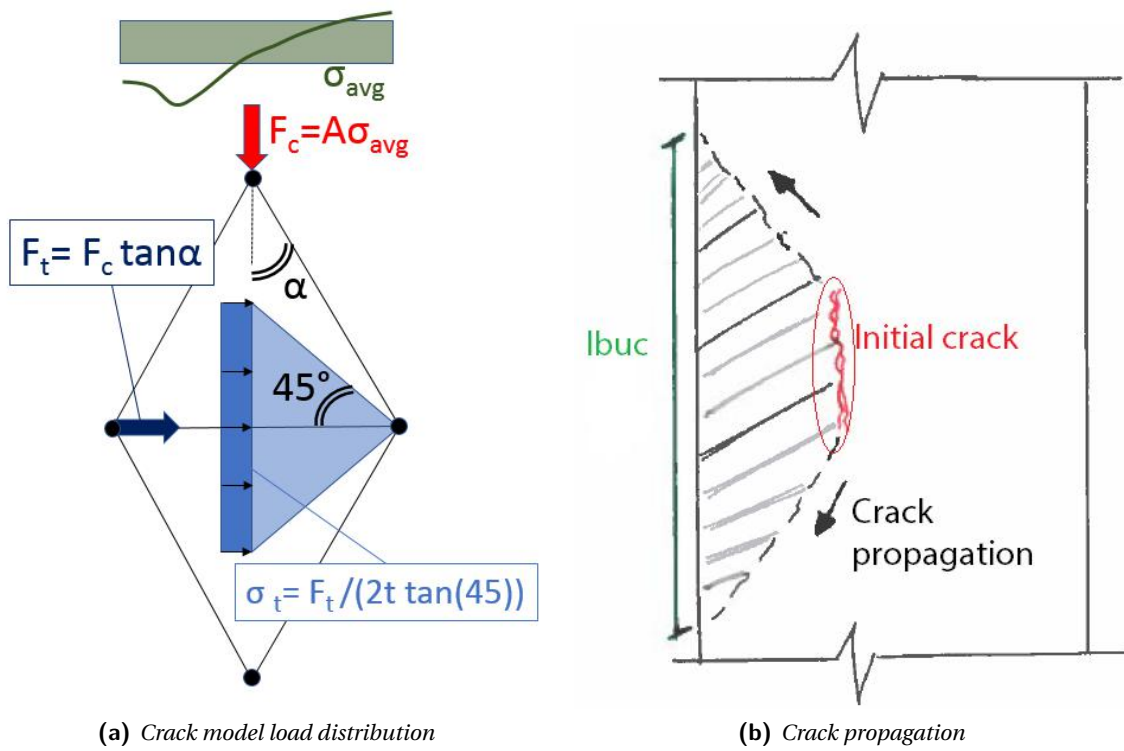


**Figure 6.16**  
Crack model visualization

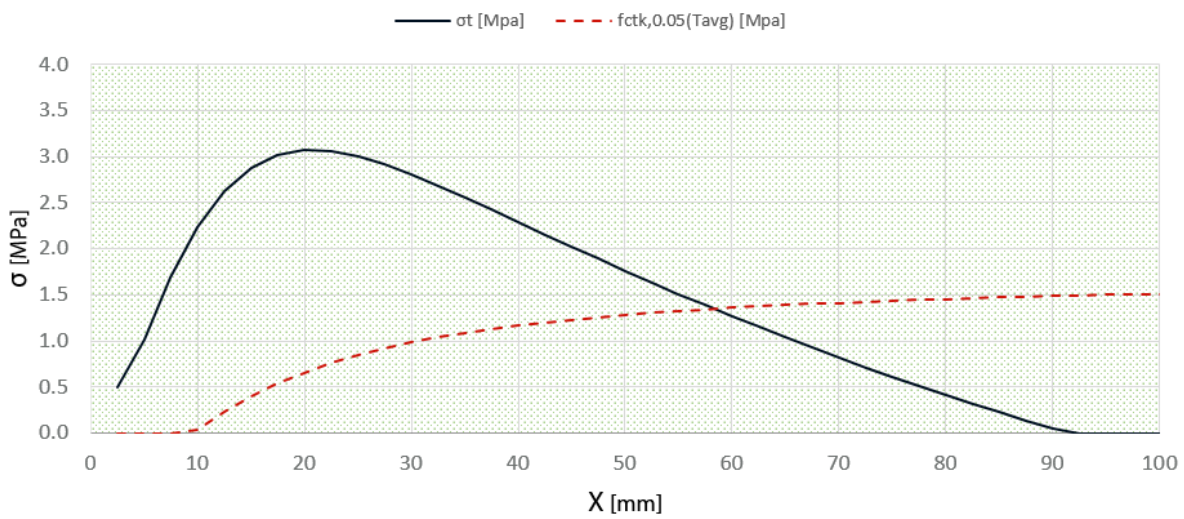


**Figure 6.17**  
Crack model example

#### 6.4. SPALLING MECHANISM CALCULATIONS OVERVIEW

In Fig.6.18 the overview of the proposed spalling calculation approach is shown. This approach is composed by the different models that have been proposed above.

The calculation method is composed of two parts. In the *preliminary part*, given an initial assumption over the spalling thickness (equal to the aggregate size), an estimate for the occurrence or not of spalling is given. In the former case an estimate of the time of occurrence of spalling can be found. This time is dependent on the fire curve that the element is facing.

Based on this result, a more accurate calculation can be carried out which is subsequently inserted into the *detailed approach*. Based on the fire curve and the time of spalling, knowledge of the stress in the cross section is possible through the *Stress model*. Once this is known the presence of a crack is checked. An optimal thickness can also be calculated. In case the optimum required thickness is smaller than the aggregate size, the initial estimate for the thickness is found to be valid. If the opposite holds true then the optimal thickness is chosen and an iteration is carried out.

#### 6.5. RESULTS

This section is dedicated at showing the results of the model developed in this chapter. Firstly the *column spalling model* has been investigated. In this section the following standard element is chosen as reference and will be analysed in detail:

- **A:** concrete element C20/25 with 16 mm calcareous aggregate subjected to an external axial stress of 5 MPa with a 350 mm fixed buckling length;

In Table 6.2 the minimum average temperature over the element thickness required for the element to spall is reported for different variations of the standard elements. This temperature is independent of the fire load. The following different variations have been investigated:

- different aggregate sizes: 16/32 mm;
- different external stresses: 0/5/10 MPa;
- different aggregate: Calcareous/Siliceous;
- different concrete types: C20/25-C25/30-C30/37;
- the first and the second buckling length derived from the model calibration: 350/570 mm.

Considering the results and the big difference in temperature between elements with different aggregate thickness, it is chosen to introduce a second reference element with the following characteristics:

- **B:** concrete element C20/25 with 32 mm calcareous aggregate subjected to an external axial stress of 5 MPa with a 350 mm fixed buckling length;

Subsequently the predicted spalling time for the reference elements exposed to different scenarios have been calculated and shown in Table 6.3. This table include also cases where no spalling occurs (Never) or where the spalling time was not calculated since the analytical or numerical set time limit was reached without spalling occurrence (>). The considered scenarios and consequent maximum temperature fire curves used are the following:

- **ISO:** the cellulosic curve is based upon building materials burning rates;
- **Hydrocarbon:** the hydrocarbon design fire curve proposed in the ROK [2] to model the worst scenario temperature curve to be used to design open tunnel parts;

### SPALLING MECHANISM CALCULATIONS OVERVIEW

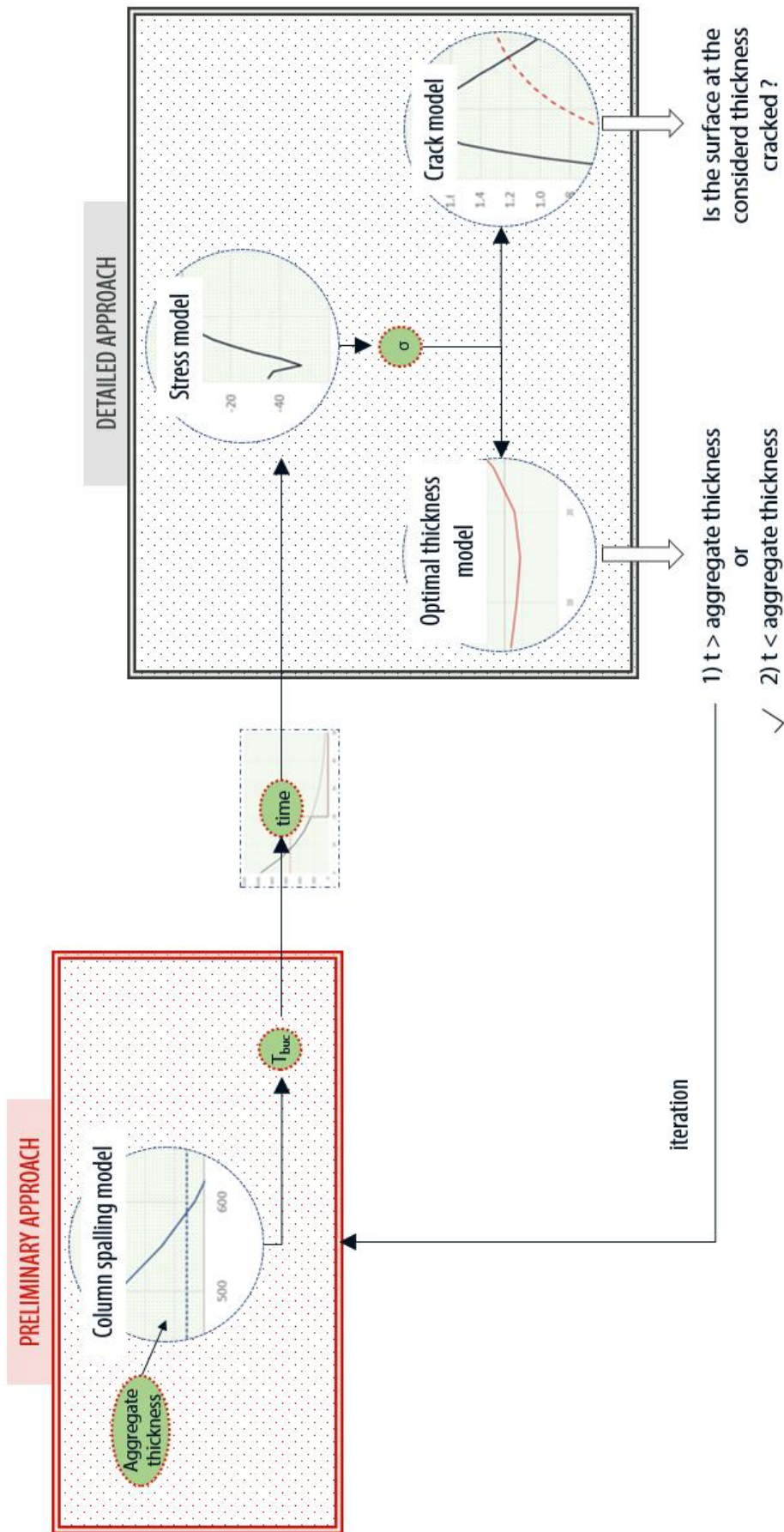


Figure 6.18

Spalling calculation approach

**Table 6.2**  
Average spalling temperature over the spalled thickness

$t$ [mm]	$\sigma_{ext}$ [MPa]	Aggregate type	Concrete	$l_{buc}$ [mm]	T-avg
16	5	Calcareous	C20/25	350	<b>238</b>
32	5	Calcareous	C20/25	350	<b>586</b>
32	0	Calcareous	C20/25	350	<b>617</b>
32	5	Calcareous	C20/25	350	<b>586</b>
32	10	Calcareous	C20/25	350	<b>562</b>
32	5	Calcareous	C20/25	350	<b>586</b>
32	5	Siliceous	C20/25	350	<b>472</b>
32	5	Calcareous	C20/25	350	<b>586</b>
32	5	Calcareous	C25/30	350	<b>588</b>
32	5	Calcareous	C30/37	350	<b>589</b>
32	5	Calcareous	C20/25	350	<b>586</b>
32	5	Calcareous	C20/25	570	<b>326</b>

**Table 6.3**  
Spalling time

	ISO	Hydrocarbon	RWS	HGV	pool0	pool2.5(#2)
A (16mm)	8.2 min	2.6 min	3.4 min	7.8 min	2.2 min	5.2 min
B (32mm)	>30 min	21.2 min	14.2 min	Never	Never	>17 min

- **RWS**: the RWS design fire curve proposed in the ROK [2] to model the worst scenario temperature curve to be used to design closed tunnel parts;
- **HGV**: the analytically modelled HGV with high energy content fire curve with ignition at ambient temperature (Fig.4.22). It has been shown in Chap.6 that for a vehicle fire igniting at ambient temperature in a two lanes standard tunnel, this is the most severe fire curve both in terms of initial steepness and maximum temperature. At the same time CFD simulations confirms that the following curve is pretty accurate in describing an HGV fire with an HRR of 30MW;
- **pool0** and **pool2.5(#2)** are the most severe fire curves among the pool fire simulations carried out for a two lanes standard tunnel (Chap.5). In Fig.6.19 the modelled fire curves coming from the pool simulations are shown together and it can be noted that **pool0** simulation is the one showing the steeper temperature development while **pool2.5(#2)** simulation shows the highest temperature. This is the reason upon which the choice of this two fire curves as model to be used for the spalling mechanism checks is based;

In Fig.6.20 the stress state in the concrete element at the spalling moment for the different fire curve exposure is shown.

Finally, the detailed approach of the spalling calculation approach has been carried out on the 2 reference elements subjected to different fire curves. The results are shown in Table 6.4.

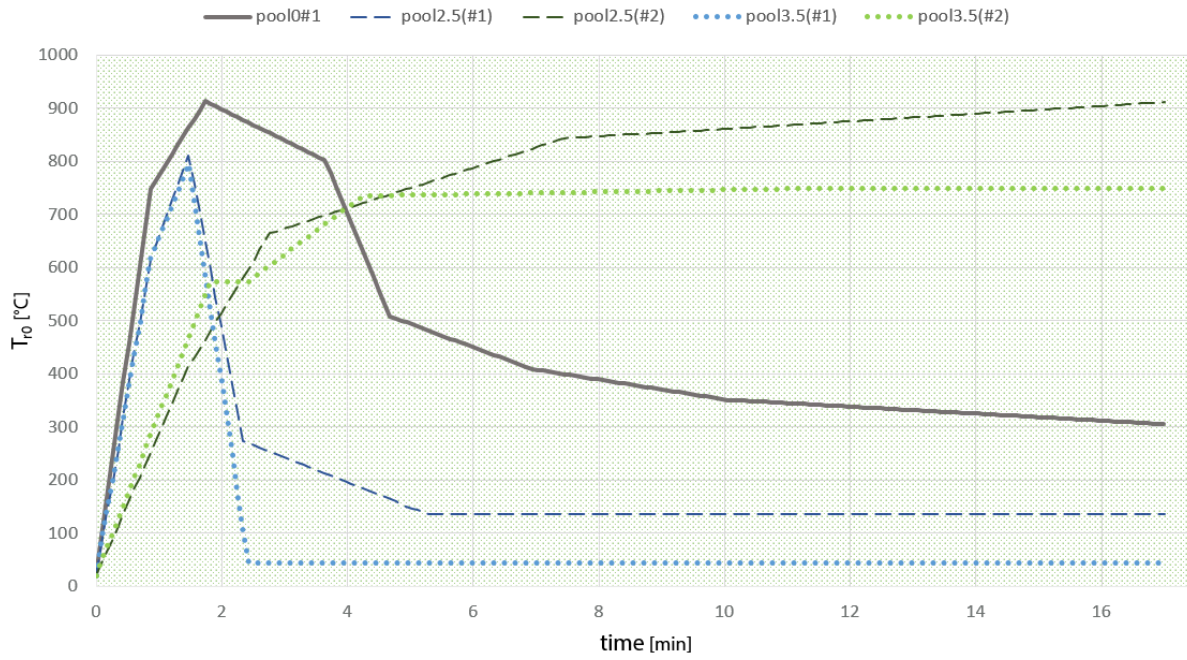
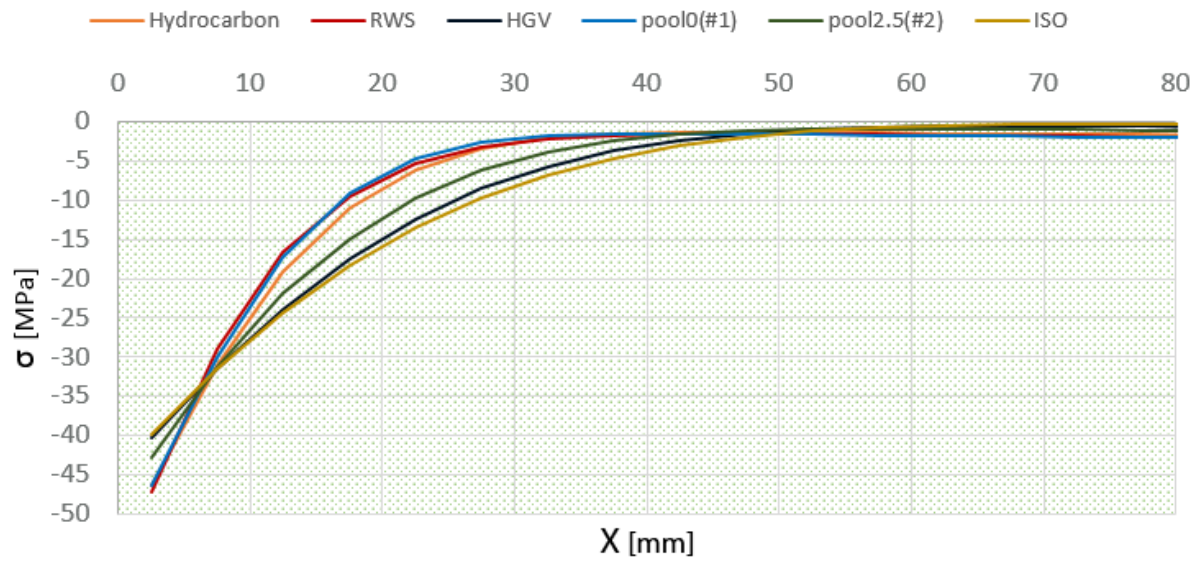


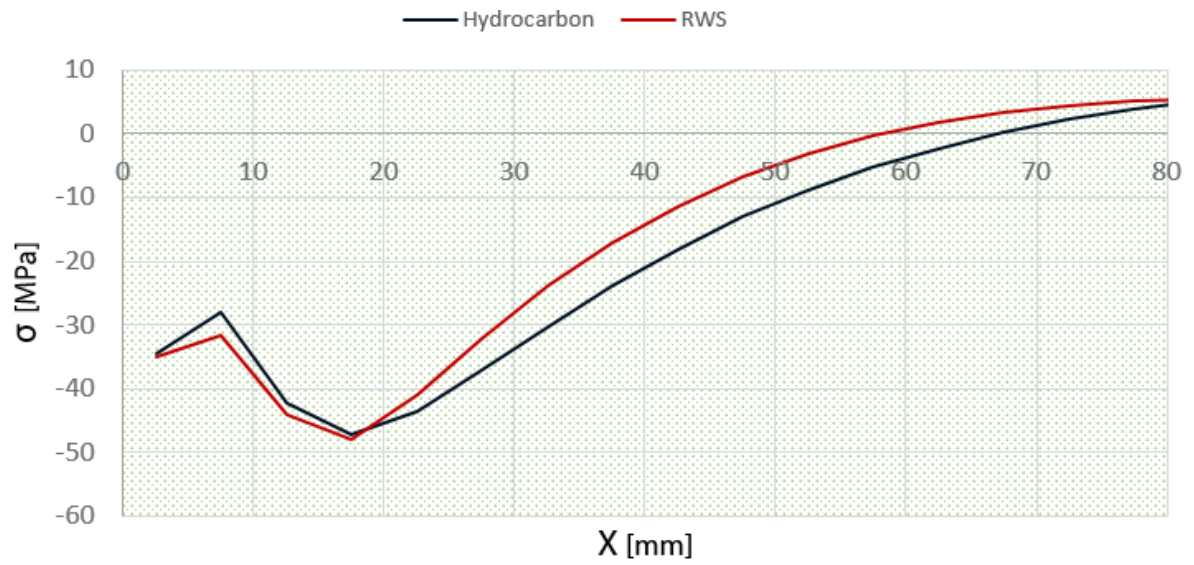
**Figure 6.19**  
*Modelled pool fire curves*

**Table 6.4**  
*1st model-Detailed approach results*

Case	t [mm]	Fire curve	$t_{opt}$ [mm]	Crack	Iteration needed
A	16	ISO	10	Yes	No
	16	Hydrocarbon	10	Yes	No
	16	RWS	10	Yes	No
	16	HGV	10	Yes	No
	16	pool0	10	Yes	No
	16	pool2.5(#2)	10	Yes	No
B	32	ISO	Spalling over 30 min delayed, not calculated		
	32	Hydrocarbon	20	Yes	Yes
	32	RWS	15	Yes	Yes
	32	HGV	Spalling does not occur		
	32	pool0	Spalling does not occur		
	32	pool2.5(#2)	Spalling over 17 min delayed, not calculated		



(a) Stresses at spalling time of 16 mm aggregate concrete



(b) Stresses at spalling time of 32 mm aggregate concrete

**Figure 6.20**

Concrete element stress state at buckling failure

## 6.6. CONCLUSIONS

Based on theory exposed and the results obtained in this chapter, with respect to the thesis objectives, the following conclusions can be drawn:

### 2-DEVELOP SPALLING MECHANISM MODEL

- an analytical model able to describe the spalling mechanism called '*NSC spalling mechanism-1st version*' has been successfully developed. The model estimates the initial spalling time of NSC elements subjected to the fire, gives an indication over the optimal thickness of the first concrete piece prone to spalling and it also checks whether the cracked surface necessary for the occurrence of the mechanism forms. The model describes the spalling mechanism as a series of 2 failure mechanisms:
  1. crack failure is the necessary first step for the spalling mechanism modelled as a buckling problem to happen. The spalled piece needs to be detached from the element before having the possibility of being suddenly pushed out because of a buckling failure. The crack failure is checked making use of the *Crack model*;
  2. buckling failure is the second step of the spalling mechanism resulting in the detachment of concrete pieces and is checked using the *column spalling model*.

In this thesis an approach which first checks the possibility of a piece to fail under buckling instability and subsequently checks the occurrence of the necessary crack failure is followed. This reversed procedure has been carried out due to the complexity of the problem, involving a relation between time, temperature, material properties and stresses, which could not result in a crack failure check without previously estimating the buckling failure time;

- the aggregate thickness is, according to the proposed model, one of the most important parameters influencing the NSC spalling mechanism. It has been found that taking an aggregate of double the thickness can considerably delay or under certain circumstances prevent the buckling failure as highlighted in Table 7.3. On the other hand, this does not reflect the evidence of better spalling performance shown in practice by concrete mix containing aggregates of reduced sizes. This could be related to the micro structural behaviour and its influences in the crack failure mechanism (section 7.3) which are not included in this model;
- the use of calcareous aggregates over siliceous one has been found to be beneficial on reducing the effects of the spalling mechanism;
- both the analytical model and the test results show worse spalling performances of NSC elements subjected to increasing external load. In the analytical model the external load plays a role only in the buckling failure, but in a revised version of the model it should also be included in the crack failure;
- the analytical model indicates that the aggregate size and type have a considerably higher impact on the spalling mechanism occurrence compared to the external load.



# 7

## SPALLING MECHANISM: 2ND VERSION AND HSC/PPFRC

*In this chapter an improved version of the spalling mechanism model is proposed and the results predicted with the use of this 2nd version model are discussed. Subsequently the limits and possibilities offered by the spalling model are investigated and in particular its use for the description of HSC and PPFRC elements spalling is discussed. Additionally a section is dedicated to a detailed description of the crack failure and the limits of the crack model are investigated. Finally conclusions over the topics treated in this chapter are drawn.*

### 7.1. SPALLING MECHANISM IMPROVEMENTS (2NS VERSION)

The NSC spalling mechanism - 1st version proposed in Chapter 6 has shown great potential in describing the spalling failure. Nevertheless, there are aspects that still raise questions or demand for improvements. The following points require additional attention:

- *the predicted spalling times seems to be too delayed if they are compared with the experimental spalling time of a NSC element. In the particular case of a NSC element exposed to RWS curve and Hydrocarbon the spalling time of the reference element **B** in Chap.6 appears to be excessively delayed compared to the full-scale test results recorded in [31] which range in the interval (1.5-12) min;*
- *Is the choice of calibrating the model (subsection 6.2.1) with a finite series of buckling lengths appropriate? Which one should be considered?*

To answer the above mentioned questions and seek for a possible different calculation approach, the full-scale test results summarized in Table 6.1 have been further studied. Analysing the data in Table 6.1 and the buckling lengths coming from the model calibration (subsection 6.2.1) it was found that there is a repetitive relation between the length and depth of the spalled piece. As shown in Fig.7.1 and Table 7.1, at a macroscopic level the spalled piece forms an averaged angle of 85° between the spalling depth and the buckling length. This is the case for all the tests of Table 6.1. Based on this result it was then assumed that there is a fixed relation between the length and depth. These are related to each other through the 85° angle as shown in Fig.7.1. The spalling calculation approach schematized in Fig.6.18 was consequently modified in order to account for this fact. The main difference lies in the choice of the buckling length. While in the 1st-version is taken as a constant value, in the 2nd-version is directly related to the spalling depth.

**Table 7.1**  
Spalling test results-Depth/length relation

Test	t [mm]	t1 [min]	$l_{buc}$ [mm]	$\beta$ [Deg]	$\beta_{avg}$ [Deg]
VK01	21	12	350	83	
VK02	20	6	300	82	
VK05	18	4	390	85	
VK06	22	3	640	86	
VK11	26	2	950	87	
VK12	31	1.5	1290	87	
VK19	21	7	560	86	
VK20	16	4	510	86	
VK21	15	4	280	84	
VK22	10	2	320	86	
VK33	15	3	460	86	
VK34	32	2.5	1380	87	
VK43	17	3	360	85	
VK44	17	3	360	85	
VK58	16	4	370	85	
VK59	33	4	1050	86	

$$\beta = \arctan\left(\frac{l_{buc}}{2 \cdot t}\right)$$

7

For the *column spalling model*, the same approach of subsection 6.2.1 was followed with the only difference being the fact that the value of the buckling length was now related to the spalled piece thickness. This resulted in higher values of the buckling length for the pieces with a thickness larger than approximately 15 mm compared with the predicted 1st-version model values. A higher value of the buckling length causes an earlier buckling failure as can be calculated with eq. 6.4.

Similarly the *optimal thickness model* was modified. In the same way as done in subsection 6.3.2 the acting load can be compared with the buckling resistance for every thickness. Relating the length to the thickness of the spalled piece a similar graph as the one of Fig. 6.14b can be obtained. The results show a tendency towards a slightly bigger value of the optimal thickness compared to the one predicted in the 1st-version.

The concepts behind the *crack model* were not varied. The only difference present in the new model is the introduction of the relation between buckling length and thickness of the spalled piece while previously a fixed value of the buckling length was taken. As a result, the tension force is determined based on a different double triangular truss which has a fixed value for the angle  $\alpha = 5^\circ$  (see Fig. 6.16a), while the tensile stress is calculated in the same way as done in the 1st-version model with a  $45^\circ$  spreading angle.

### 7.1.1. RESULTS

This subsection shows the results obtained using the improved spalling model explained in this chapter. The same approach followed in Chap. 6 has been conducted, making use of 2 reference concrete elements (A and B) and a series of representative fire temperature curves. The same elements and curves as the one used in Chap. 6 have been here examined. Both results from the improved preliminary and detailed approaches are here highlighted.

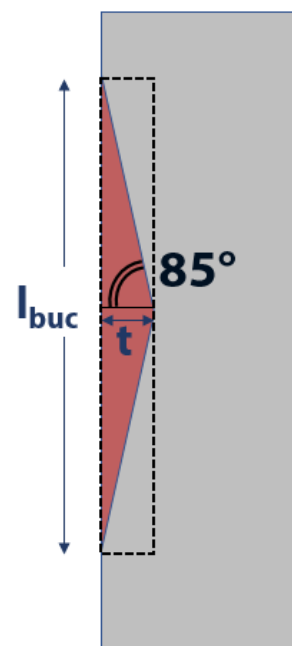


**Figure 7.1**  
Depth-Length relation

**Table 7.2**  
Average spalling temperature over the spalled thickness

$t$ [mm]	$\sigma_{ext}$ [MPa]	Aggregate type	Concrete	$l_{buc}$ [mm]	T-avg
16	5	Calcareous	C20/25	366	<b>221</b>
32	5	Calcareous	C20/25	732	<b>221</b>
32	0	Calcareous	C20/25	732	<b>247</b>
32	5	Calcareous	C20/25	732	<b>221</b>
32	10	Calcareous	C20/25	732	<b>195</b>

**Table 7.3**  
Spalling time

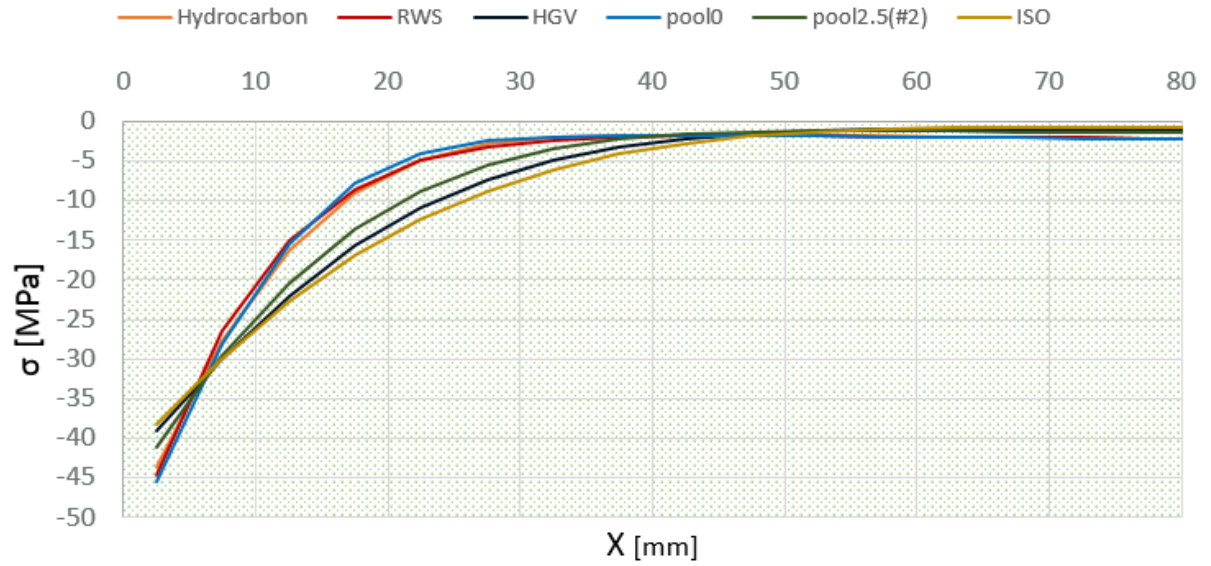
	ISO	Hydrocarbon	RWS	HGV	pool0	pool2.5(#2)
A (16mm)	7.4 min	2.2 min	3.2 min	7 min	2 min	4.8 min
B (32mm)	11 min	4 min	4.4 min	11.6 min	Never	7.2 min

Table 7.2 shows the average temperatures for which the *column spalling model* forecasts buckling failure. The tendency shown in Chap.6 for different external loads is still followed. The major difference lies in the fact that in this model the average buckling temperatures of the wide aggregate size reference element are considerably reduced. In fact, the same average temperature causing buckling both for the reference element **A** and **B** is predicted. This can be explained analysing eq.6.4 which describes the buckling failure and in particular: considering that a fixed relation is present between thickness ( $t$ ) and buckling length ( $l_{buc}$ ) and dividing at both sides of the equation for the thickness, the equation becomes independent of the aggregate thickness and the same spalling temperature is predicted. In any case, this result does not imply that both element buckle at the same time. A wider element thickness, require much more time to be heated till the critical average temperature.

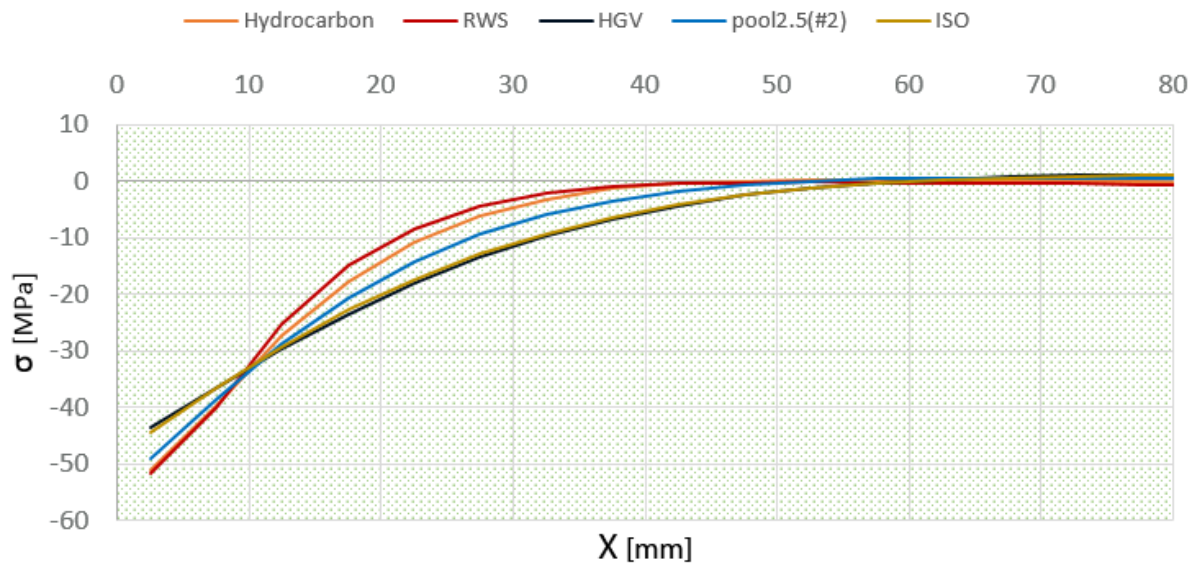
Table 7.3 shows the times at which the 2 reference elements buckle while exposed to different fire temperature curves. It can be highlighted that lower buckling times for the reference element **B** are predicted in this 2nd version model. This is more in line with the results of full-scale tests [31]. It must be noted that the exposure of elements to the ISO fire curve causes buckling. Even if this is considerably delayed compared to the more severe fire curves, it does not fully describe what is seen in practice. The exposure of concrete elements to the ISO curve does often not cause the spalling failure to occur. As will be explained more in detail in section 7.3, the reason for this can most likely be attributed to the crack failure mechanism. This cause the element to be prone to buckling failure, but the crack has not fully developed impeding the spalled piece to be detached from the concrete element.

In Fig.7.2, the stresses over the concrete element at the time in which buckling failure is predicted are shown. It can be noted that most of the stresses profile caused by the fire temperature curves follows a similar trend. An exception to that is represented by the stress profile of the reference elements exposed to the HGV and ISO curve. These curves cause the element to experience a more distributed stress state along the element.

Table 7.4 summarises the results of the detailed approach applied to the reference elements. It can be noted that for wider aggregate size elements the crack failure is suggested to be governing over the buckling failure causing a delay or prevention of the spalling occurrence. In this case the spalling occurrence has to be calculated using the *crack model*. Starting from the spalling time predicted by the *column spalling model*, time has to be increased gradually until the time (if any) of



(a) Stresses at spalling time of 16mm aggregate concrete



(b) Stresses at spalling time of 32mm aggregate concrete

**Figure 7.2**

Concrete element stress state at buckling failure

**Table 7.4**  
2nd model-Detailed approach results

Case	t [mm]	Fire curve	$t_{opt}$ [mm]	Crack	Iteration	Fig.
A	16	ISO	5	Yes	No	
	16	Hydrocarbon	5	Yes	No	
	16	RWS	5	No	No	
	16	HGV	5	Yes	No	
	16	pool0	5	No	No	
	16	pool2.5(#2)	5	Yes	No	
B	32	ISO	10	No	No	a1
	32	Hydrocarbon	10	No	No	
	32	RWS	10	No	No	
	32	HGV	10	No	No	a2
	32	pool0		Spalling does not occur		
	32	pool2.5(#2)	10	No	No	

cracking failure occurring. An example showing a similar calculation procedure is shown in subsection 7.3. Following that, in Fig.7.3 2 examples of the results at the time for which buckling is predicted and obtained with the 2nd-version of the *crack model* are shown. It can be seen that for the examined depth the tensile strength ( $f_{ctk,0.05}$ ) is still higher than the tensile stress ( $\sigma_t$ ) applied and the spalling failure cannot occur at that time.

7

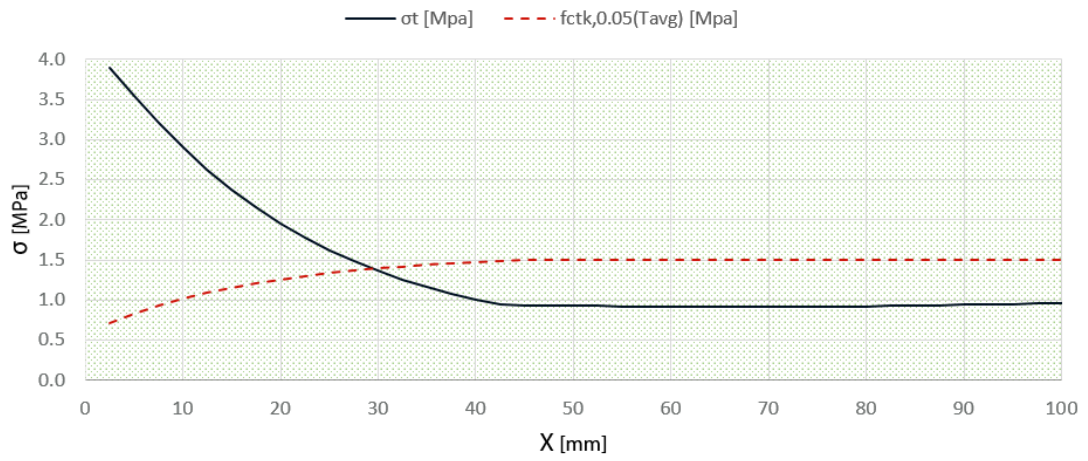
## 7.2. HSC AND PPFRC

In this section some considerations regarding the applicability of the NSC spalling mechanism model for the description of the spalling failure of HSC and PPFRC elements are expressed. In literature, available and appropriate full-scale test results over the spalling failure of HSC and PPFRC elements are missing. Documented knowledge over the shape and dimensions of the spalled pieces of these elements is essential to describe and model properly the failure mechanism. It is thus difficult to use the same spalling mechanism approach proposed in Chap.6 to model these elements spalling failure.

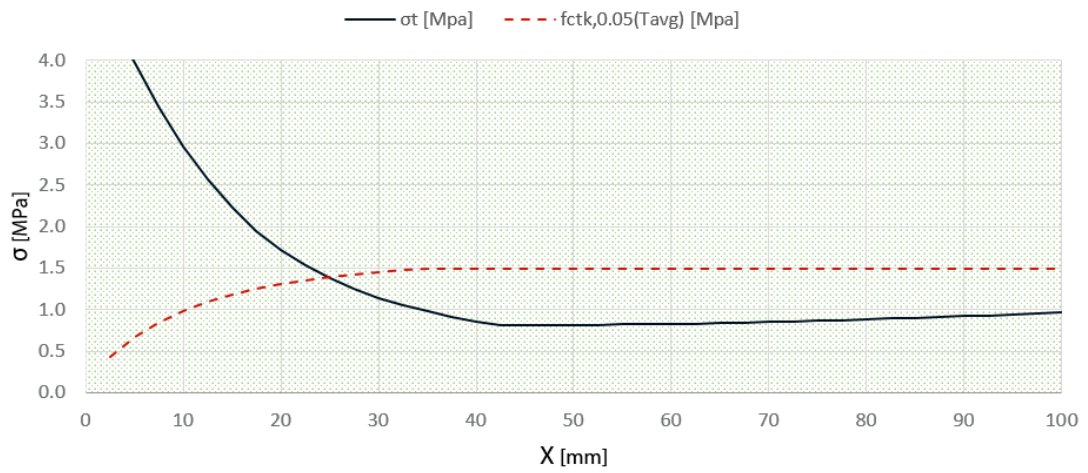
The spalling mechanism proposed in Chap.6 can be synthetically summarized as a series of two failure mechanisms: crack failure and buckling failure. While considerations over the crack failure are difficult to express without sufficient full-scale test results available, some analytical ones can be conducted over the buckling failure of HSC and PPFRC elements. The buckling failure has been modelled using the *column spalling model*, which is described by eq.6.4. While using the model, it was here chosen to assume an external load equal to zero in order to better understand which are the internal parameters (subsection 3.5.3) that while changing can describe the behaviour shown by the High Strength Concrete (HSC) and Polypropylene Fibre Reinforcement Concrete (PPFRC) in terms of spalling failure. Under the assumptions remarked above, the equation describing the buckling failure can be re-written as:

$$F_{Rd} - F_{Ed} \leq 0$$

$$\frac{\pi^2 \cdot E_c(T) \cdot bt^3}{l_{buc}^2 \cdot 12} - E_c(T) \cdot \varepsilon_c(T) \cdot bt \leq 0 \quad (7.1)$$



(a) Figure a1



(b) Figure a2

**Figure 7.3**  
Crack model results

In the following subsections the parameters that can play a role in the description of HSC and PPFRC using the *column spalling model* will be discussed. Considerations over the influence of the parameters that differs between NSC and HSC/PPFRC will also be highlighted.

### 7.2.1. HIGH STRENGTH CONCRETE

For the High Strength Concrete, the parameters that can change comparing it with NSC are highlighted in eq.7.2.

$$\frac{\pi^2 \cdot E_c(T) \cdot bt^3}{l_{buc}^2} - E_c(T) \cdot \varepsilon_c(T) \cdot bt \leq 0 \quad (7.2)$$

These parameters play a different role in relation to the spalling behaviour. The following considerations can be done:

- the thickness of the spalled piece ( $t$ ) and the buckling length ( $l_{buc}$ ) are in relation with each other. This has been highlighted in section 7.1. They represent the shape of the spalled piece, which varies significantly between NSC and HSC. With the former showing a shorter and thicker piece shape, while the latter showing a thinner but longer one [34]. In general, the relation found in the previous chapter for NSC can not be used. This is derived on the base of full-scale test experiments carried out on NSC elements.

Considering the fact that the HSC spalled pieces are thinner, it is possible to show that for a constant value of all the other parameters a reduced value of the thickness causes spalling failure to occur earlier. This is in agreement with the full-scale tests experiments carried out so far, where HSC is considered more susceptible to show spalling earlier in time [34];

- the Young's Modulus ( $E_c(T)$ ) has the same behaviour with temperature compared to NSC according to Kodur [29]. The Initial Young's Modulus at ambient temperature of HSC is higher compared to NSC, but this has a negligible influence on the spalling behaviour as shown in Fig.6.8;
- the thermal elongation ( $\varepsilon_c(T)$ ) has a similar behaviour with temperature compared to NSC as highlighted by Kodur in [29];

### 7.2.2. POLYPROPYLENE FIBRE REINFORCEMENT CONCRETE

For the Polypropylene Fibre Reinforcement Concrete, the parameters that can change comparing it with NSC are the same as for HSC and are highlighted in eq.7.2. The parameters play a different role in relation to the spalling behaviour. The following considerations can be done:

- the Young's Modulus ( $E_c(T)$ ) has the same behaviour with temperature compared to NSC. The NSC behaviour, shown in Fig.6.3a, has been compared with the Young's Modulus temperature behaviour proposed by Aslani et al. [5]. The graph comparing the 2 results is shown in Fig.7.4. The same concrete class has been used, with the PPFRC containing a fibers volume fraction ( $V_f$ ) of 0.2%.

The temperature behaviour of the PPFRC Young's Modulus can be described with the following equations:

$$E_{PPFRC} = E_c - 31.177 \cdot V_f$$

$$E_{PPFRC}(T) = E_{PPFRC} \cdot \begin{cases} 1 & 20^\circ\text{C} \\ 1.01 - 0.0013T + 10^{-7}T^2 & 100^\circ\text{C} \leq T \leq 800^\circ\text{C} \end{cases}$$

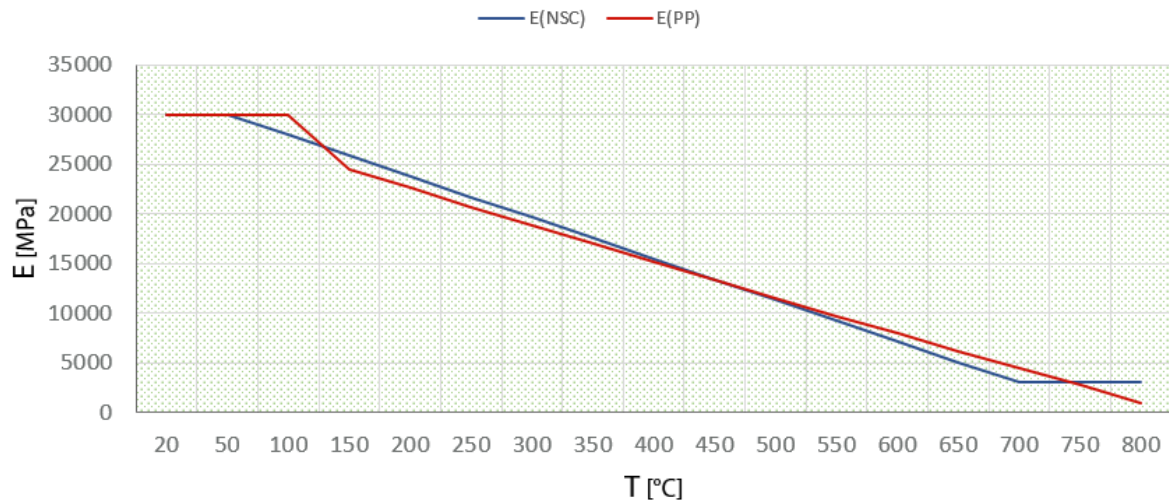


**Figure 7.4**  
*Young's Modulus: NSC vs PPFRC*

- the thermal elongation ( $\varepsilon_c(T)$ ) shows a different behaviour compared to the NSC. The PPFRC shows lower thermal elongation until 600 °C with a maximum reduction of approximately 5% at 500 °C according to the research carried out by Aslani et al. [5]. After this temperature there is a sudden increase in the elongation. This can be linked to the transformation of sand and gravel from quartz  $\alpha$  to quartz  $\beta$ . In the concrete mixture this gives rise to a strong volumetric expansion at around 575 °C. In Fig.7.5 the thermal elongation of PPFRC ( $\varepsilon_{cT}$ ) has been compared with the thermal elongation of NSC ( $\varepsilon_c$ ).

The PPFRC thermal elongation behaviour cause the element to delay the spalling failure due to the reduced thermal elongation. This phenomenon is in agreement with the results obtained applying PP fibers in the concrete mixture when exposed to fire. The addition of fibers is known to have a beneficial effect on the spalling failure, delaying its occurrence [11]. Nonetheless, thermal elongation according to this data only has a small influence and cannot alone describe the better performance of PPFRC elements.

### 7.2.3. PARAMETRIC STUDY

The considerations expressed in the previous subsection contribute in developing the understanding over the spalling mechanism model and its possible extension towards the description of other concretes compared to the NSC. Nevertheless this is not sufficient to prove or assess the applicability of such a model in that direction. It was then decided to carry out a parametric study in which some representative parameters, based upon the considerations over eq.7.1, are varied. The reference case is the standard element **B** and the variations concerns the following parameters:

- thermal elongation (Fig.7.6). The standard element thermal elongation with temperature was increased and decreased of 25%;
- Young's modulus (Fig.7.7). The standard element Young's modulus with temperature was increased and decreased of 25%;
- Depth/Buckling length relation (Fig.7.8). The relation between the depth and buckling length of the spalled piece was varied from the 85° of the standard element to 83° and 87°. Meaning that for a given thickness the spalled piece length is respectively smaller and bigger compared to the standard element length.

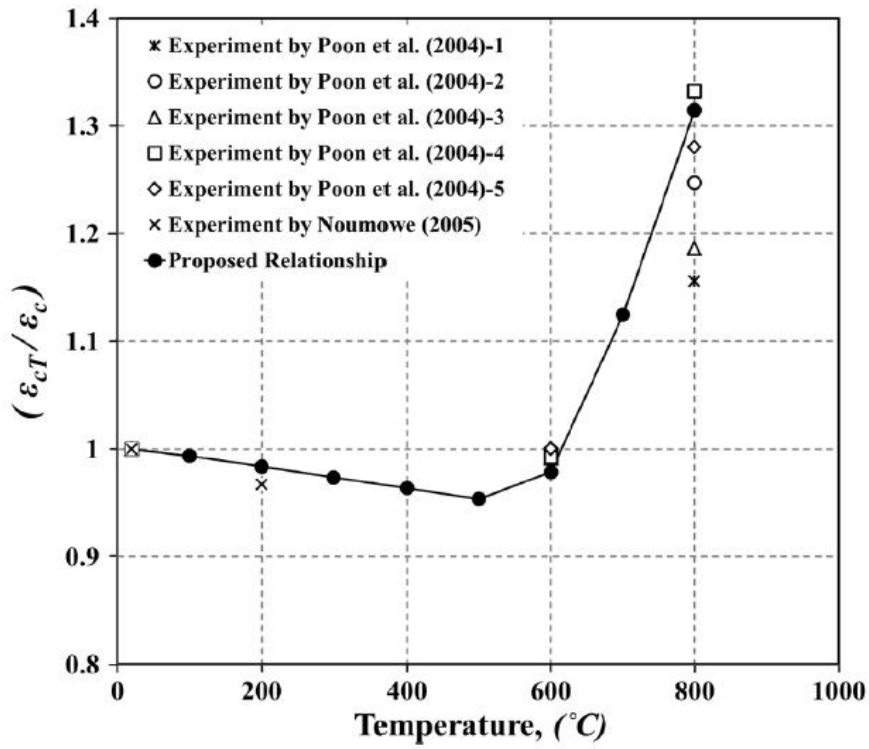


**Figure 7.5**  
 Thermal elongation: NSC vs PPFRC. Retrived from [5]

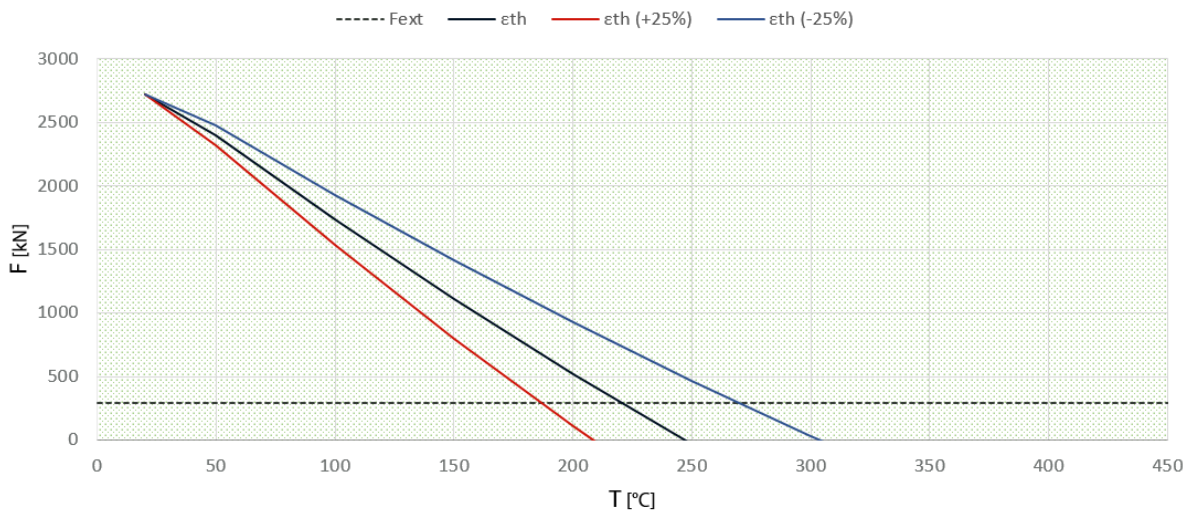


**Figure 7.6**  
 Thermal elongation variation

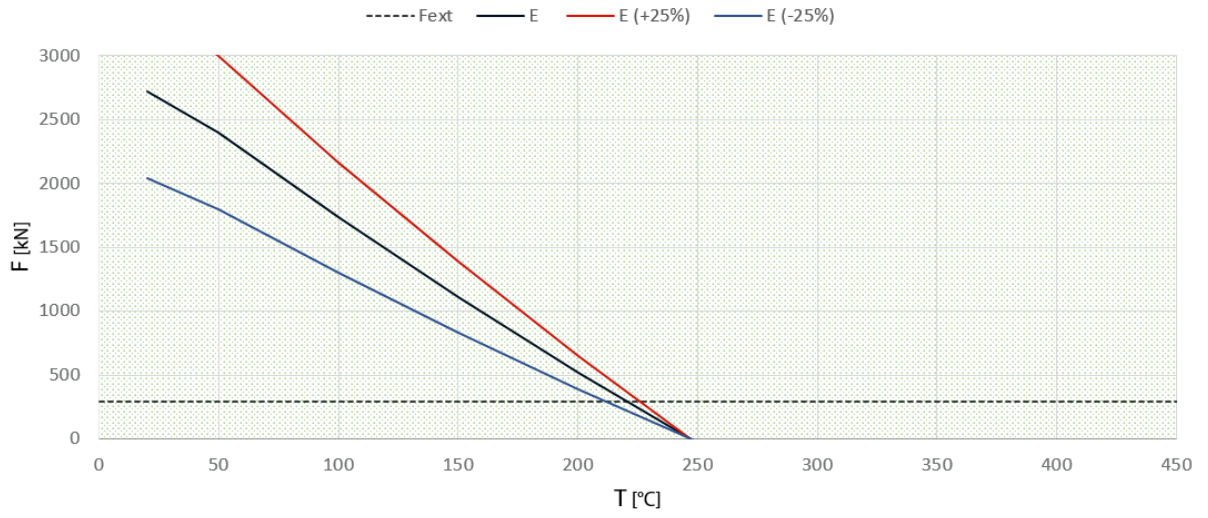


**Figure 7.7**  
*Young's modulus variation*

7

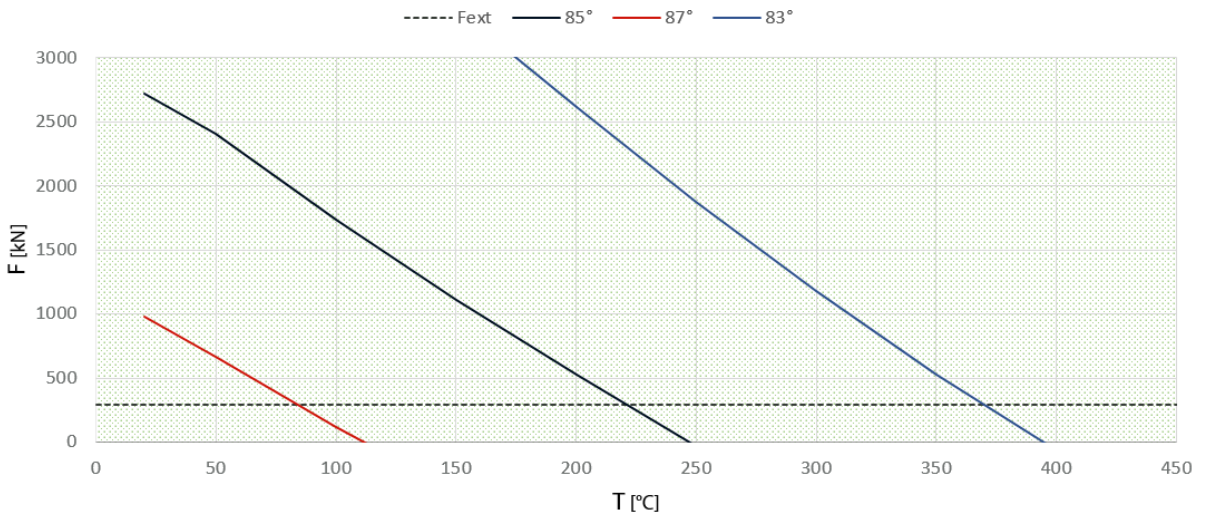


**Figure 7.8**  
*Depth/Buckling length relation variation*

In general terms, according to [11], HSC elements shows worst performances and PPFRC elements improved ones in terms of spalling failure prevention. Referring to this known behaviours, the following results are highlighted:

1. the thermal elongation behaviour seems to play an important role in the occurrence of the spalling mechanism. Based on the results of Fig.7.6, it is suggested that PPFRC should show a reduced thermal elongation compared to NSC. This is partially suggested by the result shown in Fig.7.5 and could be explained by the restraining effect that the melted PP fibers could have while the concrete mixture tries to expand due to exposure to high temperatures. On the other hand it is suggested that HSC should show an increased thermal elongation compared to NSC. This is not suggested by the study carried out by Kodur in [29];
2. the Young's modulus have almost no influence on the temperature causing spalling. This is in agreement with the results of section 6.2.1. It has also to be noted that Aslani et al. [5] for PPFRC and Kodur [29] suggest that the reduction of the young's modulus with temperature do not vary if compared with NSC;
3. the Depth/Buckling length relation seems to play a fundamental role in the spalling mechanism. It is suggested that PPFRC shows spalled pieces that are of reduced dimensions while HSC shows pieces that are slices of considerable length. The latter statement is in agreement with the spalled pieces of tested HSC elements.

The proposed NSC spalling model has potential to capture the spalling behaviour seen in practice for HSC and PPFRC elements. The *column spalling model* seems to capture and describe parts of their behaviours, but in the view of the author it cannot be considered the only part that defines the differences between NSC and the other elements. The *crack model* describing to the crack failure, must also play an important role and at the same time explain the performances of HSC and PPFRC elements. The crack mechanism must be of fundamental importance and should be therefore more carefully studied both for NSC elements and for the other concrete typologies. In the following section attention will be given to the crack failure and the model proposed to treat it (*crack model*).

### 7.3. CRACK FAILURE

The previous sections showed the great potential of the spalling mechanism both for NSC and HSC/PPFRC elements. For the latter it was highlighted that the crack failure might play a big role in describing the whole spalling failure problem.

Both the 1st version and 2nd version of the NSC spalling mechanism make use of similar assumptions in the *crack model* used to describe the crack failure. The tensile stress governing the crack formation was calculated under certain assumptions over the tensile load spread. As a consequence of the importance of the crack mechanism in the spalling mechanism, the following point is put under discussion:

- *the chosen angle (45°) for the spreading of the tensile load in the strut & tie crack model (subsection 6.3.3) raises some doubts. The mentioned value is an engineering common practice choice whenever no additional research or information are available, but the validity of this choice in this case has yet to be proven in literature*

In order to better understand the cracking phenomenon, two variations studies (Study 1/Study 2) have been conducted. These studies make use of the strut & tie model of Fig.6.15, but some quantities are fixed to a constant value while the others are varied.

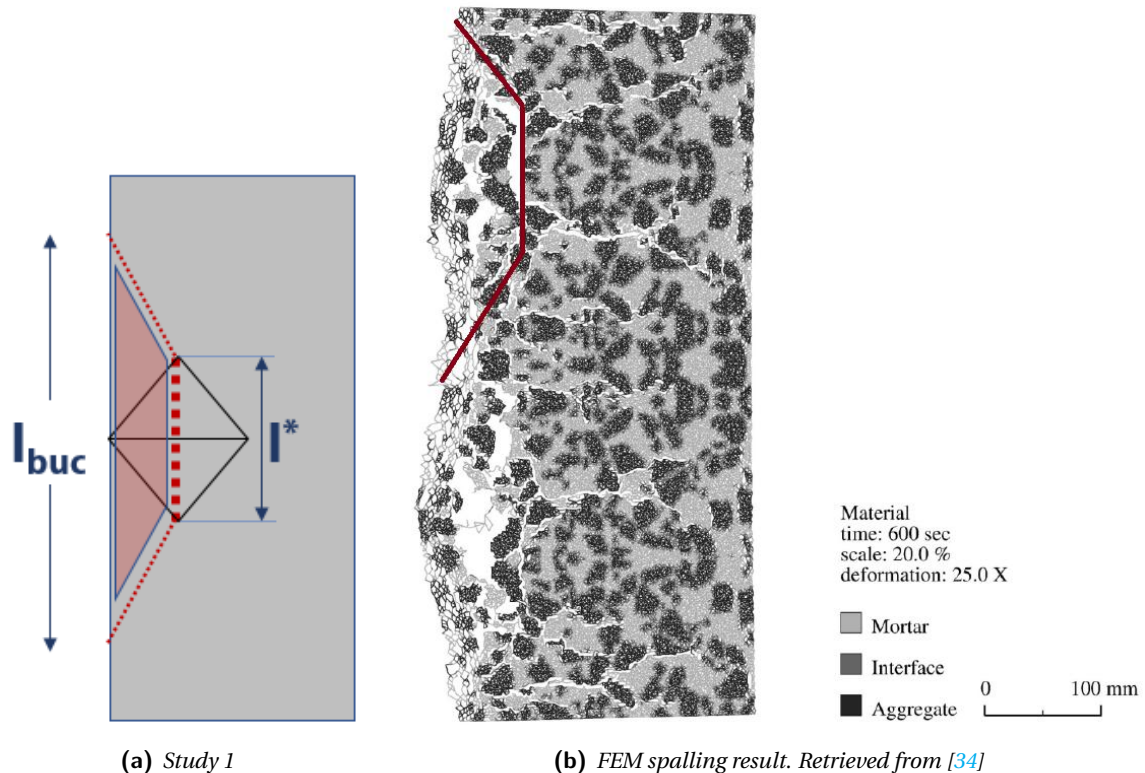


**Figure 7.9**  
Crack failure visualization

Study 1 uses as a starting assumption that the two strut& tie models used for the calculation of the tension force and tensile stress are the same. In case the crack failure, at the moment in time in which buckling failure is predicted, does not occur then the value of the length over which the tension force is spread is subsequently reduced. This is repeatedly done until the length for which the tensile stress overcomes the tensile strength. In order to better visualize this procedure, we refer to Fig.7.9a.

In study 2 a different approach has been followed. The strut& tie models used to calculate the tension force and tensile stress have been kept the same. In case the crack failure, at the moment in time in which buckling failure is predicted, does not occur then the time was subsequently increased. The time was increased until the moment that crack failure occurs. Increasing the time causes the tensile stress to increase due to the more severe compression acting on the fire exposed concrete surface. At the same time, the temperature gradient progresses and increases into the cross section causing the tensile strength to reduce.

#### STUDY 1

In this study the following hypothesis were used:

- aggregate thickness of 32 mm;
- Concrete C20/25 with calcareous aggregate;
- External stress of 5 MPa in compression;
- RWS fire curve exposure causing buckling failure after 4,4 min;

- starting strut & tie length ( $l = l_{buc} = 732 \text{ mm}$ ).

The value of the tensile strength ( $f_{ctk,0.05}$ ) is constant due to the assumption of keeping the time fixed. At the same time the length of the strut & tie model was taken as a variable and the tensile stress ( $\sigma_t$ ) is consequently varying for different lengths. In Fig. 7.10a the result of this study is shown. It was found that for lengths smaller than 237 mm a crack is predicted. This value is considerably smaller than the buckling length of 732 mm which is used to determine the tensile force acting on the spalled piece. The angle over which the tensile force spreads in the case of a 237 mm long spalled piece is  $\approx 75^\circ$ . It is a value in between the  $45^\circ$  angle used to determine the tensile stress and  $85^\circ$  angle to determine the tensile force in the spalling mechanism. This results suggests and confirms the previous assumption used in the original *crack model*, which suggested a cracking length on the inner side of the concrete element which is smaller than the buckling length visible on the surface. Fig. 7.9b shows the result obtained by Lottman [34] in a FEM calculation conducted to model the spalling mechanism. A similar crack pattern compared to the one proposed is visible.

*This study suggests that the initial crack develops at the internal side of the spalled piece with a length smaller than the buckling length. While the imposed deformation caused by the fire develops, a crack propagation phenomenon take place. This causing as a final result the complete detachment of the spalled piece from the element and allowing the spalled piece to buckle.*

#### STUDY 2

In this study the following hypothesis were used:

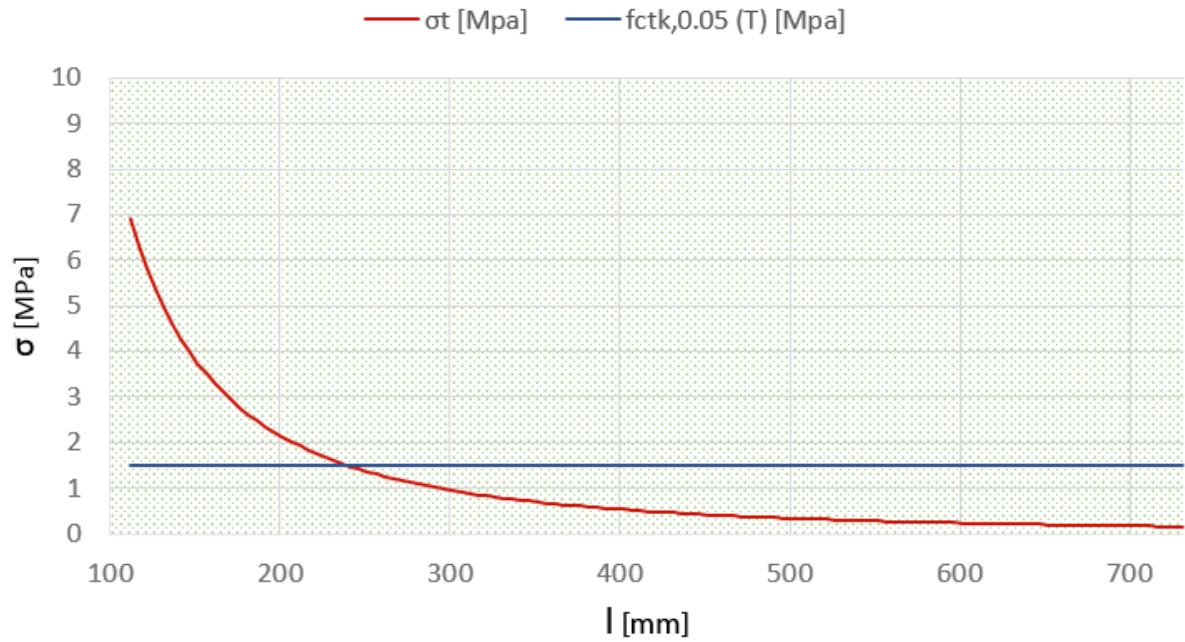
- aggregate thickness of 32 mm;
- Concrete C20/25 with calcareous aggregate;
- External stress of 5 MPa in compression;
- strut & tie length ( $l = l_{buc} = 732 \text{ mm}$ );
- initial time: 4,4 min.

In this study the stru & tie length is fixed and the time is considered as a variable. Assuming the time as a variable both the tensile strength ( $f_{ctk,0.05}$ ) and tensile stress ( $f_{ctk,0.05}$ ) vary in time. The former due to the changing temperature profile and the latter caused by the different compressive load applied in the strut & tie model due to a changing stress state in time. Fig. 7.10b shows the result of this study. The crack failure occurs more than 25 min later compared to the predicted buckling failure time.

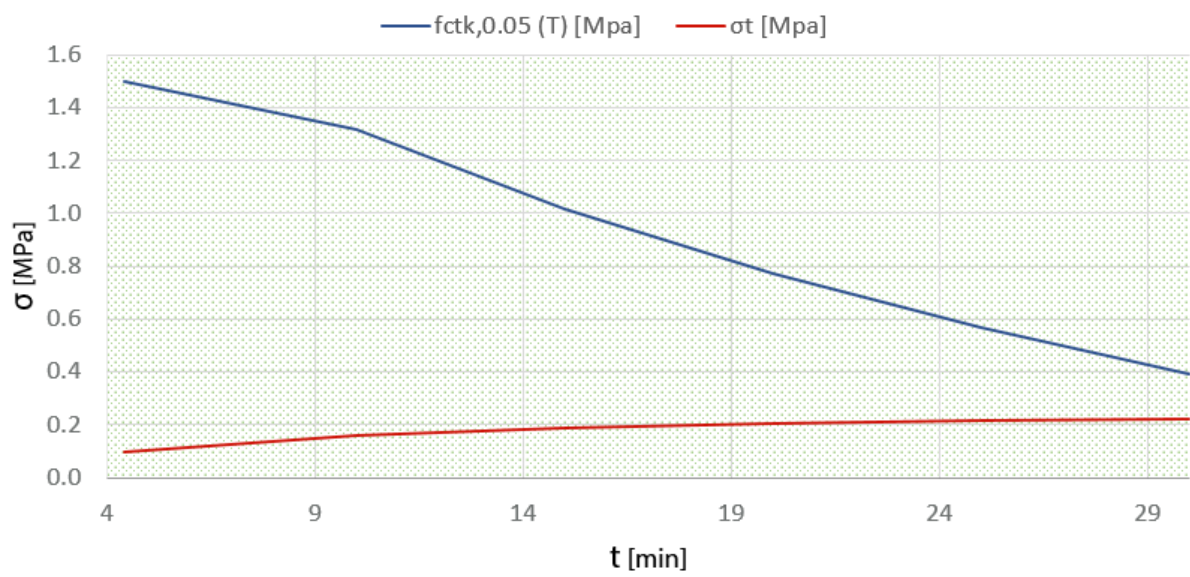
*This result suggests that the crack failure could be governing over the buckling failure under certain circumstances. This effect could explain the sudden and violent detachment of concrete pieces at a certain moment in time that some full-scale test show. The concrete piece could be seen as a spring accumulating load and prone to fail under buckling, but still prevented from spalling by the fact that the crack is not fully formed and the piece is still connected with the concrete element. Once the full crack has develop, the piece is free to spall and release the accumulated energy.*

#### ADDITIONAL CONSIDERATIONS

This section confirms the importance of the crack failure in the spalling mechanism. This thesis gave an indication on a methodology that could be applied to check the formation of the initial crack (Fig. 6.16b). When this occurs, it is then assumed that the crack propagation towards the element surface will take place instantaneously. Nonetheless, the crack propagation is an important aspect to investigate further. Both from this thesis work and from Lottman [34] FEM results it is suggested that this propagation might in some cases govern the spalling mechanism.



(a) Study 1 result



(b) Study 2 result

**Figure 7.10**  
Studies over the crack failure results

Further research and full-scale tests are needed to better understand in detail this phenomenon. In the view of the author, the introduction into the *crack model* of the stress gradient in depth is of great importance. Considering the stresses at buckling failure of Fig.7.2, the different stress state of elements exposed to the ISO or HGV fire temperature curve might explain the results seen in practice. In this sense, the exposure to ISO curve sometimes does not cause spalling in practice, while the actual version of the model predicts its occurrence (Table 7.4).

Additionally, the external load should be included in the crack failure mechanism. An higher external load causes a more distributed initial crack pattern. During heating the cracks will extend the existing pattern due to thermal deformation [38]. It can be said that the external load predefines the spalled piece crack pattern and the subsequent spalled piece shape.

The micro-structure and in particular the different thermal behaviour of aggregate and mortar are considered relevant to the development of the spalling mechanism. In particular, for the crack failure description the introduction of these aspects could be necessary. While the proposed model describes concrete mixes with large aggregate as beneficial for spalling, this is not always the case in practice. This could be explained briefly analysing the micro-structural behaviour of concrete components:

1. for NSC with calcareous/siliceous aggregate, the thermal deformation of the aggregate is considerably greater compared to the mortar [15]. This causes the aggregate to push against the mortar causing internal crack patterns;
2. NSC shows a greater stiffness reduction with temperature of the aggregate compared to the mortar [54],[13]. This causes the aggregate to take a higher share of the applied external load and subsequently experience higher elastic and inelastic deformations compared to the mortar resulting in additional internal cracks.

The two behaviours mentioned above suggest that great sized aggregate have a bigger impact on the crack formation and propagation causing spalling to occur.

## 7.4. CONCLUSIONS

Based on theory exposed and the results obtained in this chapter, with respect to the thesis objectives, the following conclusions can be drawn:

### 2-DEVELOP SPALLING MECHANISM MODEL

- an improved model based upon the model exposed in Chap.6 has been developed, named '*NSC spalling mechanism-2nd version*'. The results of this model find better agreement with the data coming from full scale tests and results mentioned in literature;
- this model suggests that, in some cases, the crack formation might be governing over the buckling failure spalling mechanism;
- the NSC spalling model shows great potential for being expanded further towards the description of the spalling behaviour of HSC and PPFRC elements.

### 4-COMPARE SPALLING TEST PROCEDURES WITH SPALLING MECHANISM MODEL

- the spalling times predicted by the 2nd version of the *column spalling model* are in the same values range as the ones seen in full-scale test reports;
- the model predicts spalling for NSC elements exposed to the ISO curve. This is not in agreement with the full-scale tests results where this often does not occur. A possible explanation can be sought in the crack formation mechanism in relation to the temperature gradient experienced in time by the concrete element. In Fig.7.2 it can be noted that a fire curve like the ISO curve gradually heats up the concrete surface and causes a less severe temperature gradient in the concrete. This could eventually lead to a different crack formation mechanism that impedes the piece to develop a full crack;
- the optimal thicknesses are often lower than the aggregate size. Nonetheless, the aggregate size taken as the minimum thickness along which crack can form is considered a good choice for NSC elements. For this concrete typology the matrix is the weakest part of the mixture and the crack could freely form and expand. On the other hand, for HSC the aggregate substitutes the matrix on being the weakest part and could allow the crack to develop at a lower depth than the aggregate size. This phenomenon agrees with evidences seen in practice of HSC spalled pieces having a thinner depth compared to NSC ones;
- for small thicknesses the buckling failure is often the governing failure mode while for bigger ones the crack failure is governing. This suggests that for concrete with large aggregate sizes, the buckling could occur but is prevented by the fact that the crack is not yet formed;
- the spalling model hold high potential for being extended towards the description of the spalling mechanism of HSC and PPFRC elements.

# 8

## CONCLUSIONS AND RECOMMENDATIONS

*This chapter focuses on the conclusions of this thesis. In particular, the conclusions are structured upon the answers given to the research question. In addition, this chapter will culminate in a section providing recommendations regarding future research and practice.*

### 8.1. CONCLUSIONS

The research question proposed in this thesis aims at bridging the knowledge between fire safety engineering and structural engineering and improving the design of underground infrastructures by combining these two fields. At the same time, the formulation of new models and methodologies is carried out to achieve this goal. The following conclusions in relation to this thesis research question can be drawn:

- in general terms, a better understanding of the fire dynamics and spalling mechanism allows engineers to have better control over the underground infrastructure design process. For the particular subject of design under fire circumstances, this control is sometimes missing in the current design methodology, where prescribed design fire curves which do not account for the specific tunnel characteristics are used and a trial and error test procedure for concrete spalling free linings approval is carried out;
- improved knowledge concerning the fire dynamics allows the designer to take a more realistic fire scenario into account during the design. Lower and less severe temperature developments imply the use of fewer protective measures and consequently a reduced budget to be accounted for fire safety actions. Valuable resources could be used for other purposes within or outside the same project. As a reference, a narrow 2 track railway tunnel of 1,5km has an estimated heat resistance cladding cost of 4.3 million euros according to [45]. Part of this cost could be saved by using fire curves based on specific tunnel scenarios;
- this thesis underlines the importance of the tunnel cross section and oxygen availability in defining the worst fire curves under a given scenario. Under these circumstances the applicability of the RWS curve for the design of all the tunnels is put under discussion. The conditions under which the RWS has been derived and the consequent design fire curve that has been proposed do not always model the conditions of the specific tunnel design under consideration. A cross section of 2x2 meters with unlimited fuel supply, as the one used in the tests used for the derivation of the RWS curve, provokes extremely high temperatures to develop in the trial tunnel. The high temperatures are caused both by the confined conditions and the

continuous oxygen supply that a short tunnel without obstacles and of reduced length (8m) causes;

- the use of ventilation to control the fire scenario and prevent the spalling mechanism to be more severe can be applied. In Fig.8.1 the worst fire curves above the fire location and downstream for the cases of a  $2,5\text{m s}^{-1}$  and  $3,5\text{m s}^{-1}$  pool fire in a two lane tunnel are shown. It can be noted that two important achievements can be accomplished using the ventilation in a proper way:
  1. improving the fire recognition and activating the ventilation earlier in time can reduce the temperature peak that the points above the fire location experiences;
  2. a higher ventilation speed seems to contribute to cooling down the points located downstream of the fire. This implies a lower maximum temperature for the worst fire curves.
- this thesis suggests that the spalling mechanism is something that cannot be prevented for NSC elements without the use of protective measures. These measures are indeed currently necessary in The Netherlands. According to the Dutch regulations contained in the ROK [2], the tunnel design must be carried out guaranteeing that no spalling occurs during a fire. On the other hand, the use of reduced and tunnel specific fire curves helps in reducing the amount of protective measure that are necessary to prevent spalling. This resulting in a reduction of the costs;
- in case the design accounting for spalling occurrence is allowed, the results obtained from this thesis give the opportunity to achieve a dual objective:
  - the *NSC spalling model* allows engineers to estimate the concrete cross section reductions caused by spalling and consequently design the tunnel in accordance with these conditions;
  - considering a tunnel specific worst-case fire scenario might result in reduced fire temperature curve compared to the design fire curves currently used. This is beneficial for the spalling failure and can result in a more economical design.

The development of spalling is already allowed by Eurocode 2, part 1-2 under the condition that '*the influence of spalling on performance requirements (R and/or EI) shall be taken into account*' [52, p. 30].

- PPFRC elements are good candidates to prevent spalling. This is confirmed by full scale results and suggested by the analytical studies carried out in this thesis. It is necessary to conduct more research on this topic in order to understand the PPFRC mechanism. This could lead to a design which prevents spalling without the use of additional protective measures;
- the fire curve steepness, the time of exposure and the maximum temperature all have a great influence on the spalling mechanism. This effect can be better understood analysing the results of Table 7.3. Reference element **B** does not spall when exposed to the temperature curve representing the worst-case fire scenario: *pool0* (Fig.6.3). This temperature curve shows a steep temperature gradient and a severe maximum temperature, but the duration of time that the element is exposed to this temperature is not sufficient for the buckling failure to take place.

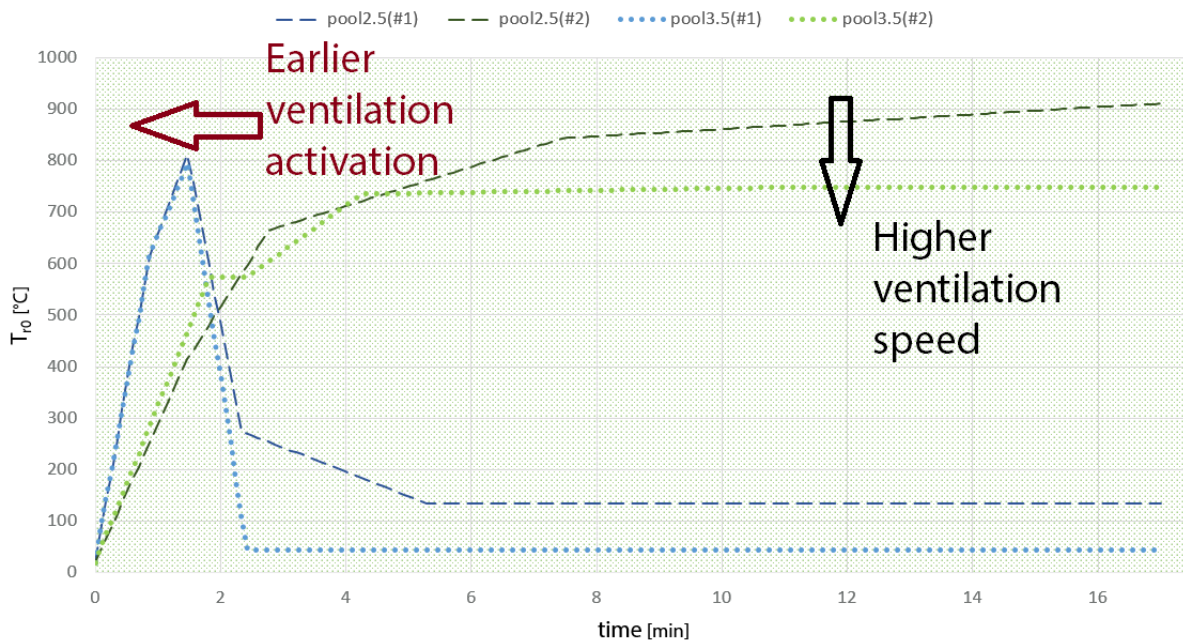


**Figure 8.1**  
*Ventilation use in defining fire scenarios*

## 8.2. RECOMMENDATIONS

The conclusions of this thesis help to broaden the knowledge and have a better insight into the topics involved in the design of underground infrastructures under fire conditions. To further develop the understanding of this topic additional research is needed and some recommendations are given in this section. On top of that, this thesis showed that many possibilities to further improve the design process in the engineering practice are possible. Some recommendations in this sense are given.

### 8.2.1. RECOMMENDATIONS FOR FUTURE RESEARCH

The following research possibilities are suggested:

- the conduction of full-scale tests aimed at studying the HRR of different fires. In particular the influence of the tunnel cross section, vehicle type, pool dimensions, fuel depletion and ventilation on the HRR development must be further improved and studied at a real scale;
- additional research both analytical and experimental of fires caused by explosions, BLEVE and VCE;
- a better theoretical understanding of the smoke instability phenomenon supported by full scale tests results;
- study analytically the early phase of pool fire in order to be able to predict its development under different conditions such as pool diameter, ventilation and tunnel characteristics;
- experimental and probabilistic research in terms of fire ignition conditions, fuel leakage, probable fire scenarios;
- spalling full-scale test of NSC, HSC and PPFRC elements focusing on recording the spalled pieces thicknesses and lengths in time. Additional attention should be paid to understand and possibly visually capture the crack development in time during spalling. Zeiml in [64]

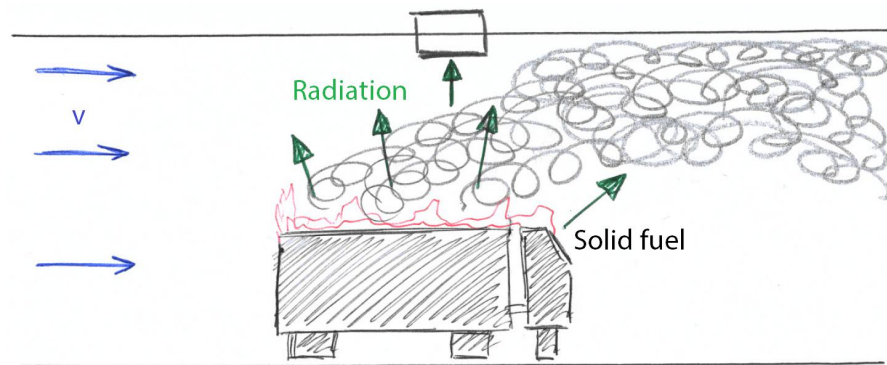


**Figure 8.2**  
*Radiation from solid phase pyrolysis*

recorded the spalling failure of concrete elements using high speed camera images. This experimental method could be used to collect a series of spalling results;

- supported by full scale experiments new analytical models should be developed to understand and predict the cracking behaviour under spalling conditions of concrete elements. A first idealization of a possible mechanism occurring during spalling has been described and is shown in Fig.7.9;
- analytical and numerical research over the effect of the radiation coming from objects located far away from the concrete element under consideration should be carried out. Currently the temperature development of the fluid close to the concrete surface is the base over which the fire curves are built upon. From the fluid, conductive, convective and radiative heat fluxes transfer heat from the fluid to the concrete element as shown in Fig.4.20. This approach do not considers the effect of the radiation coming from objects located in the tunnel that irradiate a considerable amount of heat due to the high temperatures involved in a fire. As an example the solid fuel material releases heat during its pyrolysis. In Fig.8.2 a representation of this effect is shown.

## 8

### 8.2.2. RECOMMENDATIONS FOR PRACTICE

The following suggestions for the improvement of the engineering practice are given:

- in order to avoid spalling occurrence without protecting the concrete element surface, a PPFRC concrete mix seems the only viable option able to achieve this goal. If partial spalling is considered acceptable, then NSC could be used. HSC shows thinner spalled slices and is more prone to spall and therefore less obvious to include for the design process;
- the automotive industry should be made aware of the importance of the design of vehicles which make use of materials and solutions limiting the heat of combustion of the materials itself and the global HRR of the vehicle;
- as mentioned in Chap.3 the HRR is the most fundamental parameter determining the fire development, but at the same time highly complicated to calculate and estimate due to its close relation with many other parameters. In the current practice, the HRR is used as an input in fire numerical simulations. Its magnitude is based upon analytical calculations or more often full-scale experiments. It is in the view of the author that the use of a multi-step combustion model, as showed in Fig.3.8, could lead to more reliable and tunnel specific HRR. Using this model and introducing the appropriate material properties, the whole combustion problem could be modelled (solid fuel pyrolysis and fluid combustion) and the HRR obtained as

an output. This type of simulations require more computational time compared to the actual procedure, but with both the constant improvements in the processors speed within the computer industry and the improvements of the numerical models used to solve the equations behind the CFD calculations this problem could be overcome in the near future.



## REFERENCE LIST

- [1] Rijkswaterstaat. ROK 1.3:2015. *Richtlijn ontwerp kunstwerken*. 2015.
- [2] Rijkswaterstaat. ROK 1.4:2017. *Richtlijn ontwerp kunstwerken*. 2017.
- [3] National Fire Protection Association. NFPA 502:2017. *Standard for Road Tunnels, Bridges and Other Limited Access Highways*. 2017.
- [4] B.C.M. Bierenbroodspot-van Agtmaal. *Fire Development [PowerPoint Slides]*. Lecture delivered in Fire Safety, CIE5131. Delft University of Technology, 24 November 2016.
- [5] Farhad Aslani and Bijan Samali. “High strength polypropylene fibre reinforcement concrete at high temperature”. In: *Fire Technology* 50 (5) (2014), pp. 1229–1247.
- [6] Alan Beard and Richard Carvel. *Handbook of Tunnel Fire Safety*. 2nd. London: ICE, 2012.
- [7] Cesare Bonacina, Alberto Cavallini, and Lino Mattarolo. *Trasmissione del calore*. Cleup, 1991.
- [8] K van Breugel et al. *Betonconstructies onder temperatuur-en krimpvervormingen (BP2)*. 's Hertogenbosch: BetonPrisma, 1996.
- [9] AJ Breunese, C Both, and GM Wolsink. *Fire testing procedure for concrete tunnel linings*. Report. Efectis, 2008.
- [10] Alberto Cavallini and Lino Mattarolo. *Termodinamica applicata*. Cleup, 1992.
- [11] The International Federation for Structural Concrete. *Fire design of concrete structures-materials, structures and modeling*. Report-bulletin 38. fib, 2007.
- [12] SOLIT2 Consortium. *Engineering Guidance for a Comprehensive Evaluation of Tunnels with Fixed Fire Fighting Systems using the example of water based Fixed Fire Fighting Systems*. Engineering guidance. 2012.
- [13] Alekseĭ Pavlovich Dmitriev. *Physical properties of rocks at high temperatures*. Springfield: National Aeronautics and Space Administration, 1972.
- [14] F Figueiredo et al. *Recycled Tyre Polymer Fibres to Mitigate Heatinduced Spalling of Concrete*. Borås, Sweden, Proceedings from 5th International Workshop on Concrete Spalling due to Fire Exposure., 2017.
- [15] Daniel R. Flynn et al. *Response of high performance concrete to fire conditions : review of thermal property data and measurement techniques*. NIST GCR ; 99-767. Gaithersburg, MD: National Institute of Standards, Technology, Building, and Fire Research Laboratory, 1999.
- [16] M Fragkopoulou. “Road Tunnel Fire Safety. Determining the effect of the performance of technological systems for fire detection on fire detection time and on the total evacuation time”. MSc Thesis. Delf University of Technology, 2016.
- [17] E Gissi. *An introduction to Fire Simulation with FDS and Smokeview*. 2009. URL: <http://www.emanuelegissi.eu>.
- [18] Andreas Häggkvist. “Fixed fire fighting systems in road tunnels: an overview of current research, standards and attitudes”. MSc Thesis. Luleå University of Technology, 2009.
- [19] T.Z. Hermathy. “Effect of moisture on the fire endurance of building materials. Moisture in Relation to Fire Tests”. In: *ASTM Special Technical Publication* 385 (), pp. 74–95.

- [20] A Heselden. "Studies of Fire and Smoke Behaviour Relevant to Tunnel". In: *Proc. of the 2nd Int. Symp. Aerodynamics & Ventilation of Vehicle Tunnels*. Cambridge, 1976.
- [21] J. Horvath, U Schneider, and U Diederichs. *Beiträge zum Abplatzverhalten von Hochleistungs-betonen*. Heft 11. TU Wien, 2004.
- [22] Youbo Huang et al. "Numerical investigation on the maximum ceiling temperature and longitudinal decay in a sealing tunnel fire". In: *Tunnelling and Underground Space Technology incorporating Trenchless Technology Research* 72 (2018), pp. 120–130.
- [23] Morgan J Hurley et al. *SFPE handbook of fire protection engineering*. Springer, 2015.
- [24] Haukur Ingason. "Small scale test of a road tanker fire". In: *International Conference on Fires in Tunnels*. Borås: SP Swedish National Testing and Research Institute, 1994, pp. 238–248.
- [25] Haukur Ingason. "State of the art of tunnel fire research". In: *Fire Safety Science* 9 (2008), pp. 33–48.
- [26] Haukur Ingason, Ying Zhen Li, and Anders Lönnermark. "Runehammar tunnel fire tests". In: *Fire Safety Journal* 71 (2015), pp. 134–149.
- [27] Haukur Ingason, Ying Zhen Li, and Anders Lönnermark. *Tunnel fire dynamics*. Springer, 2014.
- [28] Alexander Khoury and Yngve Anderberg. *Fire safety design—Concrete spalling review*. Report submitted to the Swedish National Road Administration. 2000.
- [29] Venkatesh Kodur. "Properties of Concrete at Elevated Temperatures". In: *ISRN Civil Engineering 2014* (2014).
- [30] Karl Kordina. "Institut für Baustoffe, Massivbau und Brandschutz, IBMB, der Technischen Universität Braunschweig - Materialprüfanstalt für das Bauwesen - MPA Braunschweig". In: vol. 2. Braunschweig: Institut für Baustoffkunde und Stahlbetonbau, 1963. Chap. Verhalten von Stahlbeton- und Spannbetonbauteilen unter Feuerangriff.
- [31] W Kusterle et al. *Brandbeständigkeit von Faser-, Stahl- und Spannbeton [Fire resistance of fiber-reinforced, reinforced, and prestressed concrete]*. Heft 544. Bundesministerium für Verkehr, Innovation und Technologie, 2004.
- [32] Ying Zhen Li, Bo Lei, and Haukur Ingason. "The maximum temperature of buoyancy-driven smoke flow beneath the ceiling in tunnel fires". In: *Fire Safety Journal* 46.4 (2011), pp. 204–210.
- [33] Fang Liu et al. "Study on longitudinal temperature distribution of fire-induced ceiling flow in tunnels with different sectional coefficients". In: *Tunnelling and Underground Space Technology incorporating Trenchless Technology Research* 54 (2016), pp. 49–60.
- [34] B.B.G. Lottman. "The spalling mechanism of fire exposed concrete". Doctoral dissertation. Delft University of Technology, 2017.
- [35] RJ McNamee et al. *Screening test methods for determination of fire spalling of concrete – an international comparison*. Borås, Sweden, Proceedings from 5th International Workshop on Concrete Spalling due to Fire Exposure, 2017.
- [36] C. Meyer-Ottens. *Zur frage der abplatzungen an bauteilen aus beton bei brandbeanspruchungen*. Deutscher Ausschuss für Stahlbeton ; 248. Berlin: Ernst, 1975.
- [37] O. Mégret and O. Vauquelin. "A model to evaluate tunnel fire characteristics". In: *Fire Safety Journal* 34 (4) (2000), pp. 393–401.
- [38] Jean-Christophe Mindeguia. "Contribution expérimentale à la compréhension des risques d'instabilité thermique des bétons". Doctoral dissertation. Université de Pau et des Pays de l'Adour, 2009.

- [39] *National Annex (NL)-EN 1991-1-2: Actions on structures: General actions-Actions on structures exposed to fire*. Report. European Committee for Standardization, 1991.
- [40] Jeffrey S. Newman. "Experimental evaluation of fire-induced stratification". In: *Combustion and Flame* 57 (1) (1984), pp. 33–39.
- [41] The European Parliament and the council of the European Union. 2015/719:2015. *Maximum authorised dimensions in national and international traffic and the maximum authorised weights in international traffic*. 2015.
- [42] The SOLIT Research Project. *Water Mist Fire Suppression Systems for Road Tunnels*. Research Report. 2007.
- [43] The UPTUN Research Project. *Engineering Guidance for Water Based Fire Fighting Systems for the Protection of Tunnels and Subsurface Facilities*. Engineering Guideline. 2007.
- [44] I Rickard et al. *Predictive testing for heat induced spalling of concrete tunnel linings – The potential influence of sustained mechanical loading*. Borås, Sweden, Proceedings from 5th International Workshop on Concrete Spalling due to Fire Exposure., 2017.
- [45] Rijkswaterstaat. *Aanvullend advies tunnel technische installaties Betuweroute*. Document 6917-2003-0034. Bouwdienst Rijkswaterstaat, 2003.
- [46] Rijkswaterstaat. *QRA-tunnels 2.0: Achtergronddocument*. Report. 2012.
- [47] W. Ulises Rojas Alva, Grunde Jomaas, and Anne S. Dederichs. "The influence of vehicular obstacles on longitudinal ventilation control in tunnel fires". In: *Fire Safety Journal* 87 (2017), pp. 25–36.
- [48] SAVE. *Handleiding risicoanalyse voor brandveiligheid van Ondergrondse, Bijlage 3*. Rapport van Ministerie van V&W. 1993.
- [49] European Committee for Standardization. EN 1363-2:1999. *Fire resistance tests - Part 2: Alternative and additional procedures*. 1999.
- [50] European Committee for Standardization. EN 1991-1-2:1991. *Actions on structures: General actions-Actions on structures exposed to fire*. 1991.
- [51] European Committee for Standardization. EN 1992-1-1:2005. *Design of concrete structures: General rules and rules for buildings*. 2005.
- [52] European Committee for Standardization. EN 1992-1-2:2004. *Design of concrete structures: General rules-Structural fire design*. 2004.
- [53] Committee for the Prevention of Disaster caused by Dangerous Substances. *Methods for the calculation of physical effects : resulting from releases of hazardous substances (liquids and gases)*. 2nd. Voorburg: Ministry of Social Affairs and Employment, Directorate-General of Labour, 1992.
- [54] RILEM TC-HTC. *Behaviour of concrete at high temperatures - part 1 - ordinary concrete*. State of the Art Report. RILEM publications S.A.R.L., 2004.
- [55] TNO. *Beproeving van het gedrag bij verhitting van twee isolatiematerialen ter bescherming van tunnels bij brand*. Report. Instituut TNO voor Bouwmaterialen en Bouwconstructies, 1979.
- [56] TNO. *Beproeving van het gedrag van twee isolatiematerialen ter bescherming van tunnels tegen brand*. Report. Instituut TNO voor Bouwmaterialen en Bouwconstructies, 1980.
- [57] TNO. *Brawat 3: Onderzoek naar het afspatgedrag van een op druk belaste wand in afgezonken tunnels*. Report. Instituut TNO voor Bouwmaterialen en Bouwconstructies, 2001.
- [58] TNO. *Toepasbaarheid fysische effectmodellen t.b.v. ongevalscenario's in tunnels*. Report. TNO Milieu, Energie en Procesinnovatie, 2003.

- [59] TNO. *Tunnelbrand Simulaties voor Rijkswaterstaat*. Report. Instituut TNO voor Bouwmaterialen en Bouwconstructies, 1992.
- [60] TNO. *VERVOER VAN BRANDBARE VLOEISTOFFEN DOOR TUNNELS. Detaillering van uitstroomhoeveelheid en uitstroomkans en de gevolgen voor het resultaat van het beslismodel*. Report. Hoofdgroep Maatschappelijke Technologie TNO, 1988.
- [61] Trafikministeriet. *Sikkerhet ved Transport gennem Storebealtstunneler*. Report. 1995.
- [62] N Vagiokas, A Bletsas, and RML Nelisse. "Methodological approaches for tunnel classification according to ADR agreement". In: *World Tunnel Congress 2013*.
- [63] N.V. Waubke. "Transportphänomene in Betonporen". Doctoral dissertation. Technische Hochschule Braunschweig, 1966.
- [64] Matthias Zeiml. "Concrete subjected to fire loading-From experimental investigation of spalling and mass-transport properties to structural safety assessment of tunnel linings under fire". Doctoral dissertation. Technischen Universität Wien, 2008.
- [65] V.V. Zhukov. *Explosive failure of concrete during a fire*. Translation No. DT 2124. Borehamwood: Joint Fire Research Organization, 1975.

**A**

**APPENDIX**

**Table A.1**  
*List of fires in road tunnels*

<i>TUNNEL</i>						<i>FIRE</i>				
<b>Location</b>	<b>Year</b>	<b>Length [m]</b>	<b>Location</b>	<b>Cause</b>	<b>Damage</b>	<b>Starting vehicle</b>	<b>Duration [h]</b>	<b>Vehicles involved</b>	<b>Fatalities</b>	<b>Injured</b>
Oslofjord (Norway)	2017	7310	Water	Vehicle	Serious	HGV	1	3	0	0
Fjæerland (Norway)	2017	6400	Ground	Vehicle	Serious	HGV	1	1	0	13
Sangju (South Korea)	2015	400	Ground	Collision/Explosion	Serious	Tank	6	12	0	21
Gudvanga (Norway)	2015	11430	Ground	Vehicle	Serious	Bus	2	1	0	5
Skatestraum (Norway)	2015	1902	Water	Vehicle	Serious	Tank	2	2	0	0
Chanel Tunnel (UK/France)	2008	51000	Water	Vehicle	Serious	HGV	16	-	0	14
Newhall Pass Tunnel (USA)	2007	166	Ground	Collision/Explosion	Serious	HGV	24	-	3	23
San Marino Tunnel (Italy)	2007	4800	Ground	Crash	-	Lorry	-	-	2	10
Burnley Tunnel (Australia)	2007	3500	Ground	Collision/Explosion	-	Lorry	-	7	3	-
Viamala Tunnel (Switzerland)	2006	700	Ground	Crash	-	Bus	-	5	9	5
Frejus Tunnel (France/Italy)	2005	12900	Ground	Vehicle	-	HGV	-	4	2	-